

Characterization of the sequential nature of neuronal dynamics: Experimental recordings, computational models and novel stimulation neurotechnologies

By

Alicia Garrido Peña



PhD thesis

Doctorado en Ingeniería Informática y Telecomunicaciones

Supervisor

Pablo Varona Martínez

Departamento Ingeniería Informática
Escuela Politécnica Superior (EPS),
Universidad Autónoma de Madrid (UAM)
Madrid, Spain.

(July 2024)

Acknowledgments

“That is all as it should be, for in a question like this truth is only to be had by laying together many varieties of error.” - Virginia Woolf

Abstract

In the context of the multidisciplinary and combined efforts to understand the brain, we focus in a bottom-up approach to explain neural dynamics at low description levels. In particular, we study the sequential nature of neuronal dynamics, an essential point of view since many neural processes at different time and spatial scales occur in a sequential manner. To explore this sequentiality at different scales we need adequate cases of study, approaches and techniques. In this thesis, we have addressed this topic using neurons and circuits of Central Pattern Generators (CPGs) to explore their robust sequential rhythm generation. and a novel neurotechnology for the noninvasive modulation of neural dynamics: continuous-wave near-infrared laser stimulation. Throughout this work, we have combined electrophysiology and computational techniques, exploiting the advantages of their joint use.

First, we examined the presence of robust linear relationships between intervals that build up the cycle-by-cycle bursting sequence of the feeding CPG of the great pond snail (*Lymnaea stagnalis*) characterizing emerging coordination constraints in the form of sequential dynamical invariants, which were recently reported in the pyloric CPG of *Carcinus maenas*. We assessed the universality of this phenomenon by exploring it in another system and in a modeling study. We discuss its role in motor coordination under different contexts. We also discuss the necessity of reproducing intrinsic functional variability in computational models for a complete characterization of the system and the associated sequential dynamical features. Finally, in this first part of the thesis, we propose the validation of sequential dynamical invariants as a dynamical coordination mechanisms for effective locomotion in biohybrid robotics.

In the aim of finding novel techniques and approaches to noninvasively modulate sequential neural activity, we present in the second part of the thesis a study of the effect of continuous-wave NIR laser in the neuronal dynamics of single neurons. First, we show its effect on single neurons, proving its effectiveness in sustained stimulation to modulate neuronal dynamics by accelerating the action potentials and the spiking rate. We analyzed the different biophysical candidates to explain the results

with the help of a theoretical study that explored both the effect of each candidate and the global key role of temperature in the observed modulation. To assess the change in the sequential evolution of the spike generation, we designed a novel activity-dependent technique to deliver the illumination at specific time instants. This protocol allowed to dissect the effect of the CW-NIR illumination on the action potential. Beyond its potential as a research tool, we believe that this closed-loop protocol will become a widely used neurotechnology in clinical applications, allowing the design of personalized treatments.

Overall, this work provides a comprehensive study of neural dynamics exploring its sequential nature. The identification of dynamical invariants and the non-invasive stimulation through CW-NIR laser will be key for future applications in neurorhabilitation for assisted locomotion and treatments in neural disorders.

Resumen

En el contexto de los esfuerzos multidisciplinares y combinados para entender el cerebro, en esta tesis nos centramos en un enfoque *bottom-up* para explicar la dinámica neuronal desde una descripción a bajo nivel. En particular, estudiamos la naturaleza secuencial de la dinámica neuronal, un punto de vista esencial ya que muchos procesos neurales ocurren de manera secuencial en diferentes escalas temporales y espaciales. Para explorar esta secuencialidad en diferentes escalas, necesitamos casos de estudio, enfoques y técnicas adecuadas. Por tanto, abordamos este tema utilizando neuronas y circuitos Generadores Centrales de Patrones (CPGs, por sus siglas en inglés) para explorar la generación de sus ritmos secuenciales robustos, y una novedosa neurotecnología para la modulación no invasiva de la dinámica neuronal: la estimulación con láser infrarrojo cercano de onda continua. A lo largo de este trabajo, combinamos técnicas de electrofisiología y modelos computacionales, explotando las ventajas de su uso conjunto.

En primer lugar, examinamos la presencia de relaciones lineales robustas entre intervalos que componen la secuencia de las ráfagas ciclo a ciclo del CPG alimentario del gran caracol de estanque (*Lymnaea stagnalis*), caracterizando las restricciones de coordinación emergentes en forma de invariantes dinámicos secuenciales, recientemente reportados en el CPG pilórico de *Carcinus maenas*. Evaluamos la universalidad de este fenómeno explorándolo en otro sistema y en un estudio teórico, abordando su papel en la coordinación motora bajo diferentes contextos. También discutimos la necesidad de reproducir la variabilidad funcional intrínseca en modelos computacionales para una caracterización completa del sistema y las características dinámicas secuenciales asociadas. Finalmente, en esta primera parte de la tesis, proponemos la validación de los invariantes dinámicos secuenciales como mecanismos de coordinación dinámica para la locomoción efectiva en robótica biohíbrida.

Con el objetivo de encontrar nuevas técnicas y enfoques para una modulación no invasiva de la actividad neural secuencial, presentamos en la segunda parte de la tesis un estudio del efecto del láser infrarrojo continuo (CW-NIR) en la dinámica neuronal de neuronas individuales. Primero, ilustramos

su efecto en estas neuronas, demostrando su eficacia con iluminación sostenida para modular la dinámica neuronal al acelerar los potenciales de acción y e incrementar su frecuencia. Analizamos los diferentes candidatos biofísicos para explicar los resultados con la ayuda de un estudio teórico en el que se explora tanto el efecto de cada candidato como el papel clave de la temperatura en la modulación observada. Para evaluar el cambio en la evolución secuencial de la generación de *spikes*, diseñamos una novedosa técnica dependiente de actividad para entregar la iluminación en instantes de tiempo específicos. Este protocolo permitió diseccionar por etapas el efecto de la iluminación CW-NIR en el potencial de acción. Más allá de su potencial como herramienta de investigación, creemos que este protocolo de ciclo cerrado puede convertirse en una neurotecnología ampliamente utilizada en aplicaciones clínicas, permitiendo el diseño de tratamientos personalizados.

En resumen, este trabajo proporciona un estudio exhaustivo de la dinámica neuronal explorando su naturaleza secuencial. La identificación de invariantes dinámicos y la estimulación no invasiva a través de láser CW-NIR pueden ser claves para futuras aplicaciones en neurorrehabilitación para la locomoción asistida y tratamientos en trastornos neurológicos.

Contents

1	Introduction and State of the Art	1
1.1	Neuroscience, neurons and their dynamics	1
1.1.1	Neuronal dynamics	2
1.1.2	Network dynamics	5
1.2	The sequential nature of neural dynamics	6
1.3	Studying neural dynamics in computational models.	10
1.3.1	Conductance-based models	11
1.3.2	Variability in computational models	15
1.4	Vertebrate and invertebrate animal studies	16
1.5	Neural stimulation	18
1.5.1	Stimulation techniques	18
1.5.2	Neuromodulation and its need for clinical applications	19
2	Introducción y Estado del Arte	21
2.1	Neurociencia, neuronas y su dinámica	21
2.1.1	Dinámica neuronal	23
2.1.2	Dinámicas de redes	26
2.2	La naturaleza secuencial de la dinámica neuronal	27
2.3	Estudiando la dinámica neuronal en modelos computacionales.	30
2.3.1	Modelos basados en conductancia	32
2.4	Estudios de animales vertebrados e invertebrados	34

CONTENTS

2.5 Estimulación neuronal	37
2.5.1 Técnicas de estimulación	37
2.5.2 Neuromodulación y su necesidad para aplicaciones clínicas	37
3 Motivation and Objectives	39
4 Materials and Methods	41
4.1 The neural system of <i>Lymnaea stagnalis</i>	41
4.2 Feeding CPG in <i>L. stagnalis</i>	42
4.3 Electrophysiology in <i>Lymnaea Stagnalis</i>	43
4.4 Conductance based models	44
4.4.1 Feeding CPG model	45
4.4.2 CGC neuron model	48
4.5 Neural data analysis	49
4.6 CW-NIR laser	53
5 Sequential constrains in CPG circuits: Dynamical invariants	55
5.1 Introduction	55
5.2 Methods	57
5.2.1 Time references, intervals and CPG sequence	57
5.2.2 Inducing variability in the model by current injection	59
5.2.3 Experimental recordings and stimulation	61
5.2.4 Models with chaotic activity	62
5.2.5 Hybrot structure	64
5.3 Sequential dynamical invariants in computational models	66
5.3.1 N1M driven variability	66
5.3.2 N3t driven variability	68
5.3.3 SO driven variability	69
5.3.4 Time intervals relations cycle-by-cycle beyond period	71

CONTENTS

5.3.5	Comparison with two-phase intervals	71
5.4	Experimental results in <i>Lymnaea Stagnalis</i>	77
5.4.1	Invariants in spontaneous activity	78
5.4.2	Invariants in SO driven activity	86
5.4.3	Invariants in MLN stimulation driven activity	92
5.4.4	Invariants in CVa1 driven activity induced by electrical stimulation	95
5.4.5	Invariant reseting	101
5.5	Characterization of variability in bursting models and its functionality	103
5.6	Transformation of sequential intervals into effective robot movement	105
5.7	Discussion	108
6	CW-NIR laser as an effective neuromodulation technique	113
6.1	Introduction	113
6.2	Methods	115
6.2.1	Sustained CW-NIR stimulation protocol	115
6.2.2	Activity-dependent laser stimulation protocol	116
6.2.3	Spike waveform characterization parameters	118
6.2.4	Statistical Analysis	119
6.3	Temperature estimation for analyzing laser neuromodulation	121
6.4	Sustained CW-NIR laser stimulation effect on single neuron dynamics	121
6.4.1	CW-NIR laser effect on spike waveform	121
6.4.2	CW-NIR laser effect on spiking rate	126
6.4.3	Effect of CW-NIR stimulation in a minimal circuit	128
6.4.4	Effect of CW-NIR stimulation at different wavelengths	129
6.5	Model analysis for constraining candidates to explain the effect of CW-NIR laser illumination in the spike dynamics	132
6.5.1	Parameter range modification for the biophysical candidates in the model	132
6.5.2	Change of spike dynamics considering temperature modulation in the model	137

CONTENTS

6.6 Activity-dependent stimulation to assess the laser effect at distinct stages of the spike dynamics	141
6.6.1 Model simulation of activity-dependent stimulation	142
6.6.2 Experimental activity-dependent stimulation	142
6.7 Discussion	146
6.7.1 Singularity of the sustained and activity-dependent CW-NIR stimulation on neural dynamics	146
6.7.2 Biophysical explanation of the CW-NIR modulation through modeling and activity-dependent stimulation	147
6.7.3 Applications for research and clinical use	149
7 Conclusion and Discussion	151
8 Conclusiones y Discusión	157
A Publications	187
B Supplementary figures for chapter 4	191

List of Tables

5.1	List of i_{inj} values that yield realistic bursting rhythms for each neuron in the model CPG used in the stimulation protocols reported in this paper. The left section of the table displays the i_{inj} values applied to each neuron (columns) during each simulation condition (rows). Ramp values on the right section refer to the minimum and maximum values of the ramp variable c in each simulation, increasing i_{inj} in the specified step every 4.6 seconds (the approximate duration of two N3t burst) to induce variability.	61
5.2	Time reference boundaries for the three phases in the feeding CPG	78

LIST OF TABLES

List of Figures

1.1	Illustration by Ramon y Cajal intended to show the probable course of currents in the bee retina. (A) rods; (B) second visual neuron (giant monopolar); (C) ganglionic corpuscle (third visual neuron); (B,C) short centrifuges; (M,S) T cell or interzonal connection cell; (F,G) basal dendrites destined to articulate with centrifugal fibers (Ramón y Cajal and Sánchez, 1915). Copyright Serrano-Herrera and Espinosa-Sánchez serrano-herrera_domingo_2024 (CC BY-SA 4.0	2
1.2	Representation of the sequential phases and terminology of an action potential. (Adapted from Chris73, Wikimedia Commons, CC BY-SA 3.0). In each of these phases of the action potential generation, different ionic channels are activated sequentially, e.g. the sodium channel is involved during the depolarization phase and its activity decays as the potassium channel activates mostly in the repolarization phase.	4
1.3	Examples of different spike shapes. Representation of two recordings from two different cells in the right parietal ganglion of <i>Lymnaea stagnalis</i> . Left: symmetrical spike; right: shoulder shaped spike.	4
1.4	Representation of two examples of different spiking neuronal activity. Left: two simultaneous intracellular recordings in <i>Lymnaea stagnalis</i> showing tonic firing at two different frequencies. Right: Two examples of bursting activity, from <i>Lymnaea stagnalis</i> (top panel) and from <i>Carcinus maenas</i> (bottom panel).	5
1.5	Representation of synapses types. Left. Example of electrical synapse between two cells and diagram of gap junction (Adapted from Wikimedia Commons). Right. Example of chemical synapse structure (Adapted from Wikimedia Commons)	6
1.6	Left. gastric and pyloric circuit scheme of <i>Carcinus Maenas</i> (Huerta et al., 2001). Right. Conectome in human brain rendered from 20 subjects (By Andreashorn CC BY-SA 4.0)	6

LIST OF FIGURES

1.7 Illustration of the sequential feeding process at different time scales in <i>Lymnaea stagnalis</i>	8
1.8 Superimposition of bursts at different time instants aligned by the first spike in the burst for intracellular recordings of an LP neuron in the sthomatogastric CPG.	9
1.9 Neural and network models classified by biophysical detail, structure modeled and size of the network. Figure adapted from Fig. 2 Gleeson et al., 2019 under Creative Commons CC-BY license. Models are classified by the biophysical detail, by y-axes being the models in the bottom the less specific ones; by the size of the network modeled, from left to right one cell to hundreds of cells; and by the brain-structure they model, represented in colored boxes. The shape of the box also classifies the model in network model or individual cell model. A third category was here included from the original work, representing by an spiral in the box the ability of the model to produce chaotic activity without external alterations, i.e, reproduce spontaneous variability. Although the figure does not contain all model approaches, it illustrates key milestones in neuronal modeling.	12
1.10 Electrical circuit describing the membrane voltage in a conductance based neuron model.	13
1.11 Electrical circuit representing the scheme for intracellular recordings.	13
1.12 Simulation of two distinct spike types: no shoulder (a) and shoulder shaped (b), described by equations in Hodgkin and Huxley, 1952b and Vavoulis et al., 2010, respectively	14
1.13 Imagen of <i>Lymnaea Stagnalis</i>	18
1.14 Representation of <i>L. stagnalis</i> life cycle. Figure 2A from Fodor et al., 2020 (Creative Commons license).	18
2.1 Ilustración de Ramón y Cajal que muestra el probable curso de las corrientes en la retina de la abeja. (A) bastones; (B) segunda neurona visual (monopolar gigante); (C) corpúsculo ganglionar (tercera neurona visual); (B,C) centrífugas cortas; (M,S) célula T o célula de conexión interzonal; (F,G) dendritas basales destinadas a articularse con fibras centrífugas (Ramón y Cajal y Sánchez, 1915). Copyright Serrano-Herrera y Espinosa-Sánchez serrano-herrera_domingo_2024 (CC BY-SA 4.0) . . .	22

LIST OF FIGURES

LIST OF FIGURES

2.9 Modelos neuronales y de red clasificados por detalle biofísico, estructura modelada y tamaño de la red. Figura adaptada de la Fig. 2 Gleeson et al., 2019 bajo licencia Creative Commons CC-BY. Los modelos están clasificados por el detalle biofísico, siendo los modelos en la parte inferior los menos específicos; por el tamaño de la red modelada, de izquierda a derecha, una célula a cientos de células; y por la estructura cerebral que modelan, representada en cajas de colores. La forma de la caja también clasifica en modelo de red o célula individual. Se incluyó una tercera categoría a partir del trabajo original, representada por una espiral en la caja, que indica la capacidad del modelo para producir actividad caótica sin alteraciones externas, es decir, reproducir variabilidad intrínseca espontánea. Aunque la figura no contiene todos los enfoques de modelos, ilustra hitos clave en el modelado neuronal.	32
2.10 Circuito eléctrico que describe el potencial de membrana en un modelo de neurona basado en conductancia.	33
2.11 Circuito eléctrico que representa el esquema para registros intracelulares.	33
2.12 Imagen de <i>Lymnaea Stagnalis</i>	36
2.13 Represnetación del ciclo de vida de <i>L. stagnalis</i> . Figura 2A de Fodor et al., 2020 (Creative Commons license).	36
4.1 <i>L. stagnalis</i> buccal ganglia (top) and parietal ganglia and visceral ganglion (bottom).	42
4.2 <i>L. stagnalis</i> nervous system diagram representing all ganglia.	42
4.3 Example of a sharp micro-electrode glass in the SUTTER puller.	44
4.4 Panel (a). Ionic channel distribution in the two-compartment description for the individual neurons in the Vavoulis et al. model used in this study. At the soma: I_{ACh} , acetylcholine ionic channel; I_{NaL} , slowly inactivating sodium ionic channel; I_T , low-threshold calcium current; I_{inj} , injected current; $I_{L,S}$, leakage current in the soma; I_{syn} , synaptic current. At the axon: I_{NaT} , fast inactivating sodium current; I_K , delayed rectifier potassium current; $I_{L,A}$, leakage current in the axon. The color for each I_X current represents the CPG neuron that includes it at the soma, N1M, N2v and N3t, respectively. Panel (b). Connection scheme for the <i>Lymnaea</i> feeding CPG circuit model. The colors indicating each neuron in the circuit match those in the representation of their corresponding somatic membrane potential traces in section 4.4.1.	47

LIST OF FIGURES

4.5 Triphasic feeding rhythm as produced by the circuit CPG model described in Fig. 4.4. In this simulation, i_{inj} values applied to each neuron are 8.5, 6, 2 and 0 mV, respectively.	47
4.6 Simulation of the CGC-model representing the voltage dynamics during an action potential and the corresponding ionic currents defined in the model ($I_{NaP}, I_{NaT}, I_A, I_D, I_{LVA}, I_{HVA}$). The units in the y-axis are specified in the legend.	49
4.7 Illustration of the laser beam focused on a neuron in the right parietal ganglia.	53
4.8 Image of the NIR-laser stimulation setup. On the left there is the micromanipulator with the electrode and the glass micropipette for the intracellular recording. In the center of the image in the base there is the preparation of the CNS of <i>Lymnaea stagnalis</i> . On the right side the laser fiber is attached to the collimator and at the end of the holder there is the lenses to focus the laser beam. This is also attached to another micromanipulator for a precise focusing.	53
5.1 Example of robust sequential bursting dynamics in CPGs. Representation of burst duration in 3 neurons in a CPG model, the sequential activation of the three neurons conform cycles (transparent grey boxes in the sequence). The connections between the three neurons are represented in the diagram on the right side of the panel.	56
5.2 Panel A. Individual neuron sequence interval definitions. Each BD label represents the burst duration, defined as the time interval from the first spike to the last spike in the neuron's burst. Period was measured as the interval from the first spike of N1 burst to the first spike of the next N1 burst, covering three phases in relation to the activity of the other neurons. IBI represents the interburst interval, defined as the time from the last spike of a neuron's burst to the first one of the next burst in the same neuron. Panel B. Definition of intervals involving pairs of neurons. NXNY interval represents interval from NX start to NY start. NXNY delay represents interval from NX end to NY start. Period was measured from N1 start to N1 start, covering the three phases of the CPG rhythm.	58
5.3 Illustration of the CPG activity when a current ramp i_{inj} is applied to N3t. Variability in the sequence intervals was induced by applying two consecutive ramps as the one shown in this figure into different cells.	59

LIST OF FIGURES

5.4 Top panel: illustration of the experimental setup for the FLC-Hybrot implementation: A) Computer that controls the closed-loop interaction between the living CPG and the robot. B) DAQ and signal amplifiers; C) Microscope; D) Testing track with light and shadows regions. Middle panel: detail of the elements of the setup: E) Hexapod robot, receives the neural information from the computer and sends back the sensory feedback through a Bluetooth connection; F) <i>In vitro</i> pyloric CPG preparation with three electrodes, one to record extracellular activity from the nerve which includes the activity from the LP neuron (blue), one to record intracellular activity from the PD neuron (green) and another to introduce the feedback current into a PD neuron (red). Electrodes and computer are connected through the DAQ device. Bottom panel: detail of the elements of the robot and the preparation. PD neuron (intracellular recording, green trace) and LP neuron (extracted from the extracellular recording, blue trace) behavior is analyzed online by the computer and used to modulate the movement of the robot. Meanwhile, robot's light sensor detects the presence of light or shadow over it and the Arduino board sends that information to the computer, which injects feedback current into the PD neuron (red trace).	65
5.5 N1M stimulation: a) Box-plots of the sequence intervals under N1M neuron stimulation. b) Interval correlations to period for N1M-driven simulation. First row: Burst duration. Second and third row: Two-neuron intervals. Forth and fifth row: Two-neuron delays. Linear relationships are quantified by the R^2 values of the linear regression.	67
5.6 N3t stimulation: a) Box-plots of the sequence intervals under N3t neuron stimulation. b) Interval correlations to Period for N3t-driven simulation. First row: Burst duration. Second and third row: Two-neuron intervals. Forth and fifth row: Two-neuron delays.	69
5.7 SO stimulation: a) Box-plots of the sequence intervals under SO neuron stimulation. b) Interval correlations to Period for SO-driven simulation. First row: Burst duration. Second and third row: Two-neuron intervals. Forth and fifth row: Two-neuron delays.	70
5.8 N1M stimulation: Pairplot with all possible combination between time intervals within a cycle.	72
5.9 N3t stimulation: Pairplot with all possible combination between time intervals within a cycle.	73

LIST OF FIGURES

5.10 SO stimulation: Pairplot with all possible combination between time intervals within a cycle.	74
5.11 a) Representation of the intervals for each cycle when considering three or two phases (left and right, respectively). b) Interval correlations to period for SO-driven simulation for 3 phases. First row: Burst duration. Second and third row: Two-neuron intervals. Forth and fifth row: Two-neuron delays (Data shown in Fig. 5.5). c) Interval correlations to period for N1M-driven simulation for 2 phases. First row: Burst duration. Second row: Two-neuron intervals. Third row: Two-neuron delays. For b) and c) the linear relationships are quantified by the R^2 values of the regression.	76
5.12 Delimitation of phases in the feeding CPG of <i>Lymnaea stagnalis</i> based on different recordings. Panel a) intracellular recordings for motoneurons B4,B3,B1 and B8 and the interneuron N1M. Phases are delimited by N1M and B1, that have the same activation time for phase N1, the inhibition of N1M and the start of the depolarization in B8 for phase N2 and the first and last spike of burst B8 for phase N3. Panel b) intracellular recordings for motoneurons B3,B4,B5, B1 and B8. Phases are delimited by B1 depolarization for phase N1, the strong inhibition of B5 for phase N2 and the first and last spike of burst B8 for phase N3.	79
5.13 Representation of the distributed system of the feeding CPG. Dots indicate inhibitory chemical synapses, bars excitatory chemical synapses and resistor symbols electrotonic (electrical) synapses. Colors indicate the function of the neuron classified in modulatory or initiator (yellow and orange, respectively) and the three phases protraction, rasp and swallow (green, blue and red, respectively). From left to right food detection represented by Lips that stimulate CGC, SO CBIs and N1M neurons and initiate the rhythm. The ongoing activity is then modulated by those neurons but also by OC neurons and N1 and N3t neuron. Some examples of motor neurons are represented on the right side of the panel, associated to each feeding phase. This figure was adapted from Panel C from Figure 1 in P. R. Benjamin, 2012 (work under license Creative Commons Attribution)	80

LIST OF FIGURES

5.14 Spontaneous case 1: Panel of intervals distribution and dynamical invariants for the three phases in the CPG for spontaneous activity. a) Voltage traces for the intracellular recording analyzed for this panel. b) Representation of the time-intervals described. c) Duration of each time interval (<i>y – axis</i>) at each cycle. d) Box-plot with the variability distribution of the duration of each time-interval. e) Time-intervals duration against the period for NX-duration (blue), NXNY-Interval (green) and NXNY-Delay (red)	82
5.15 Spontaneous case 2: Panel of intervals distribution and dynamical invariants for the three phases in the CPG for spontaneous activity. a) Voltage traces for the intracellular recording analyzed for this panel. b) Representation of the time-intervals described. c) Duration of each time interval (<i>y – axis</i>) at each cycle. d) Box-plot with the variability distribution of the duration of each time-interval. e) Time-intervals duration against the period for NX-duration (blue), NXNY-Interval (green) and NXNY-Delay (red)	83
5.16 Spontaneous case 3: Panel of intervals distribution and dynamical invariants for the three phases in the CPG for spontaneous activity. a) Voltage traces for the intracellular recording analyzed for this panel. b) Representation of the time-intervals described. c) Duration of each time interval (<i>y – axis</i>) at each cycle. d) Box-plot with the variability distribution of the duration of each time-interval. e) Time-intervals duration against the period for NX-duration (blue), NXNY-Interval (green) and NXNY-Delay (red)	84
5.17 Panel of the pairplots for all possible combinations between the time intervals for two phases (N1 and N3) in the CPG recordings for the three examples of spontaneous activity recordings.	85
5.18 Representation of the spontaneous recording with lapses of SO modulation. The parts of the recording with yellow background highlight were the activity was modulated by the SO neuron. From top to bottom, intracellular recording of a neuron from the B4 cluster, B3 motoneuron, B1 motoneuron, B8 motoneuron, and N1M interneuron.	86

LIST OF FIGURES

5.19 Spontaneous SO neuron driven: Panel of intervals distribution and dynamical invariants for the two phases in the CPG for spontaneous activity driven by SO neuron. a) Voltage traces for the intracellular recording analyzed for this panel. b) Representation of the time-intervals described. c) Duration of each time interval (<i>y – axis</i>) at each cycle. d) Box-plot with the variability distribution of the duration of each time-interval. e) Time-intervals duration against the period for NX-duration (blue), NXNY-Interval (green) and NXNY-Delay (red)	88
5.20 Spontaneous activity when the SO-driven modulation ceases: Panels illustrate the interval distribution and dynamical invariants for the three phases in the CPG during spontaneous activity. a) Voltage traces for the intracellular recording analyzed for this panel. b) Representation of the time-intervals described. c) Duration of each time interval (<i>y – axis</i>) at each cycle. d) Box-plot with the variability distribution of the duration of each time-interval. e) Time-intervals duration against the period for NX-duration (blue), NXNY-Interval (green) and NXNY-Delay (red)	89
5.21 Spontaneous SO neuron modulation restarts: Panel of intervals distribution and dynamical invariants for the two phases in the CPG for spontaneous activity driven by SO neuron. a) Voltage traces for the intracellular recording analyzed for this panel. b) Representation of the time-intervals described. c) Duration of each time interval (<i>y – axis</i>) at each cycle. d) Box-plot with the variability distribution of the duration of each time-interval. e) Time-intervals duration against the period for NX-duration (blue), NXNY-Interval (green) and NXNY-Delay (red)	90
5.22 Induced SO neuron modulation: Panel of intervals distribution and dynamical invariants for the two phases in the CPG for activity driven by SO neuron induced by its electrical stimulation. a) Voltage traces for the intracellular recording analyzed for this panel. b) Representation of the time-intervals described. c) Duration of each time interval (<i>y – axis</i>) at each cycle. d) Box-plot with the variability distribution of the duration of each time-interval. e) Time-intervals duration against the period for NX-duration (blue), NXNY-Interval (green) and NXNY-Delay (red)	91
5.23 Panel of the pairplots for all possible combinations between the time intervals for two phases in the CPG recordings for (left) spontaneous SO rhythm modulation and (right) the induced SO rhythm modulation	92

LIST OF FIGURES

5.24 MLN stimulation: Panel of intervals distribution and dynamical invariants for the three phases in the CPG under MLN Medium Lip Nerve (MLN) stimulation. a) Voltage traces for the intracellular recording analyzed for this panel. b) Representation of the time-intervals described. c) Duration of each time interval (<i>y – axis</i>) at each cycle. d) Box-plot with the variability distribution of the duration of each time-interval. e) Time-intervals duration against the period for NX-duration (blue), NXNY-Interval (green) and NXNY-Delay (red)	93
5.25 MLN stimulation: Pairplot of the invariants reset within cycles.	94
5.26 CV1a driven case 1: Panel of intervals distribution and dynamical invariants for the two phases in the CPG under CV1a stimulation. a) Voltage traces for the intracellular recording analyzed for this panel. b) Representation of the time-intervals described. c) Duration of each time interval (<i>y – axis</i>) at each cycle. d) Box-plot with the variability distribution of the duration of each time-interval. e) Time-intervals duration against the period for NX-duration (blue), NXNY-Interval (green) and NXNY-Delay (red)	96
5.27 CV1a driven case 2: Panel of intervals distribution and dynamical invariants for the two phases in the CPG under CV1a stimulation. a) Voltage traces for the intracellular recording analyzed for this panel. b) Representation of the time-intervals described. c) Duration of each time interval (<i>y – axis</i>) at each cycle. d) Box-plot with the variability distribution of the duration of each time-interval. e) Time-intervals duration against the period for NX-duration (blue), NXNY-Interval (green) and NXNY-Delay (red)	97
5.28 CV1a driven case 3: Panel of intervals distribution and dynamical invariants for the two phases in the CPG under CV1a stimulation. a) Voltage traces for the intracellular recording analyzed for this panel. b) Representation of the time-intervals described. c) Duration of each time interval (<i>y – axis</i>) at each cycle. d) Box-plot with the variability distribution of the duration of each time-interval. e) Time-intervals duration against the period for NX-duration (blue), NXNY-Interval (green) and NXNY-Delay (red)	98

LIST OF FIGURES

5.29 CV1a driven case 4: Panel of intervals distribution and dynamical invariants for the two phases in the CPG under CV1a stimulation. a) Voltage traces for the intracellular recording analyzed for this panel. b) Representation of the time-intervals described. c) Duration of each time interval (<i>y – axis</i>) at each cycle. d) Box-plot with the variability distribution of the duration of each time-interval. e) Time-intervals duration against the period for NX-duration (blue), NXNY-Interval (green) and NXNY-Delay (red)	99
5.30 Panel of the pairplots for all possible combinations between the time intervals for two phases (N1 and N3) in the CPG recordings for the four examples of induced CV1a neuron modulation recordings.	100
5.31 Panel representing the reset cycle-by-cycle of dynamical invariants. For each pairplot the lower triangle represent a cycle and the upper triangle represents the intervals of that cycle against the intervals of next cycle. The examples showed here are from top left to right: Spontaneous activity example 1 (Fig. 5.14), SO induced modulation (Fig. 5.22), MLN stimulation (Fig. 5.24) and CVa1 stimulation (Fig. 5.26)	102
5.32 Example of variability in waveforms from intracellular recordings of the LP and PD neurons in the pyloric CPG	103
5.33 Example of bursts with no variability in waveforms from model simulation of neuron from Ghigliazza and Holmes, 2004 model in chaotic mode and N1M neuron from Vavoulis, Straub, et al., 2007a with no ramp stimulation in the CPG circuit. The equations for both models can be found in Secs. 5.2.4 and 4.4.1, respectively.	104
5.34 Example of variability in waveforms from model simulation of neuron from Nowotny et al., 2008 model in chaotic mode and N1M neuron from Vavoulis, Straub, et al., 2007a under current stimulation in the CPG circuit. The equations for both models can be found in Secs. 5.2.4 and 4.4.1, respectively.	104

LIST OF FIGURES

- 5.35 Representation of the FLC-Hybrot paradigm design. Neural dynamics from a functional living CPG circuit are recorded online and used to coordinate the robot movement in real-time. Activity from the PD neuron is recorded intracellularly (green trace), while the LP bursts are extracted from the nerve's extracellular signal (blue trace). This robot walks through a trial track with interspersed light and shadow regions. When the robot's light sensor detects that it is located under a shadow, it sends feedback current to the living circuit. CPG dynamics change as a reaction to the injected current, thus modifying the robotic locomotion. The following video shows an example of this experiment <https://youtu.be/ny2dJGbG8lo>. 106
- 5.36 Flexible hybrot adaptation to environmental changes when noticed by the robot sensors and associated coordinated locomotion. When the robot entered a shadow section, it sent sensory feedback to the living CPG in the form of positive electrical current (red trace). Blue and green traces are recordings of the extracellular and intracellular (PD neuron) activity of the circuit and display the change caused by the feedback current injection in the PD neuron, slowing down the CPG rhythm. The oscillatory movement of the robot legs is represented in the brown trace and it can be observed that a variation in the CPG rhythm leads to a change in the robotic locomotion, modifying both the period and the amplitude of the oscillation. 107
- 5.37 **Left:** dynamical invariant present in the living CPG activity during the validation test, represented as a linear relation between the LP neuron bursting period and the LPPD interval cycle-by-cycle. **Right:** dynamical invariant present in the FLC-Hybrot locomotion during the validation test, represented as a linear relation between its legs oscillation period and amplitude cycle-by-cycle. The dynamical invariant property is effectively translated from the living CPG to the robot locomotion, codified as: Robot period = LP period, Robot amplitude = LPPD interval * factor. 108
- 6.1 CW-NIR laser stimulation protocol sequence: Control, laser stimulation and recovery. 116
- 6.2 Activity-dependent protocol scheme. Neurons were recorded intracellularly and their voltage signals were processed in real-time with the RTXI software. Using the spike prediction algorithms, the shutter was triggered at the desired action potential phase illuminating the neurons. 117
- 6.3 Examples of illumination offset, defined as the time interval from the end of the illumination to the peak of the spike. 118

LIST OF FIGURES

- 6.4 Representation of waveform shape's metrics: a) Spike duration at half width. b) Spike amplitude between the maximum and minimum voltage values. c) Depolarization slope at half width. d) Repolarization slope at half width. 119
- 6.5 Open-pipette temperature estimation method. Each row in the panel represents pulsed and continuous current delivery for the estimation, respectively. For both examples: left column, temperature and voltage relation. Right column filtered mean of voltage recordings from short illumination intervals in the pipette. 122
- 6.6 Effect of sustained CW-NIR laser stimulation on the spike waveform for two distinct neuron types. For all panels: control, laser and recovery are color coded in blue, red and green, respectively. Panel A. Characterization of no shoulder shape type neuron. Panel B. Characterization of shoulder shape type neuron. Ai) and Bi) Superimposition of spike waveforms in a single trial recording corresponding to a symmetrical and shoulder spike neuron, respectively. The spikes were aligned to the peak for the x axis and to the onset for the y axis, the mean is depicted in darker colors. Aii) and Bii) barcharts quantify the change using the difference from laser to control normalized by the mean control value for metrics: duration, depolarization and repolarization slopes, and amplitude. Panel C, violin plots representing the variation of the experiments with respect to the control ($N = 23$) for shoulder and symmetrical types together. For each metric of the waveform, the control, laser and recovery recordings are normalized to the first control. From left to right: duration, depolarization slope, repolarization slope and amplitude. Asterisks over the violins indicate that the metric change was highly significant (Bonferroni correction, $(\rho < 0.01/4)$, see Statistical Analysis Sec. 6.2.4 in Materials and Methods). 123
- 6.7 Segregation of data into shoulder and symmetrical neural types. Violin plots for the four metrics -duration, depolarization slope, repolarization slope and amplitude- grouped by control, laser and recovery trials. Spikes metrics are normalized to the first control, as in Fig. 6.6 panel C 125

LIST OF FIGURES

6.8 Firing rate and interspike interval (ISIs) analysis for the CW-NIR laser stimulation. A. Absolute firing rate in all experiments (N=23). B. Absolute firing rate for cases from the experiments in A with no change during laser illumination (N=11); C. Absolu- tute firing rate for experiments from A showing an increase in the firing rate (N=12); D. ISI histograms for control, laser and recovery for each experiment. Cases showing increased excitation in their firing rate (sample in panel C) when illuminated by the CW-NIR laser are highlighted in a red square.	127
6.9 Microscope image of the three cases of illumination. From left to right illumination of VD1 neuron, RPD2 neuron and the gap junction of their electrical coupling. In the images it can be appreciated the electrode recording each cell, form the bottom right and from the top left.	129
6.10 Electrically coupled neurons illumination, superimposition of the averaged wave- form for control, laser and recovery in three different examples. For each case, it is the spike waveforms of VD1 and RPD2 illuminating first VD1; waveforms of VD1 and RPD2 illuminating then RPD2 and finally both waveforms illuminating the gap junction. Each plot follows the previous color code for control, laser and recovery of blue, red and green, respectively).	130
6.11 Water absorption for different wavelengths values.	131
6.12 Representation of the effect of sustained laser stimulation at 830nm at 90mW and 1450nm at 120mW. In terms of power density the corresponding values are: 194.88 W/cm ² and 315.78 W/cm ² , respectively. The left panel in each row is the superim- position of the spike waveforms aligned to the first point, during a control recording with no stimulation, a laser recording during the illumination at the specific wave- length and a recovery control, again with no stimulation. The four panels in each row correspond to the mean value for each trial of control, laser and recovery for the spike waveform metrics: duration, amplitude, depolarization and repolarization slopes.	131

LIST OF FIGURES

- 6.13 Modeling study of the CW-NIR laser stimulation effects due to isolated biophysical changes that alter the spike waveform. Panels A, B, C and D: Superposition of spike waveforms in each model by modulating a single biophysical candidate. The background colors correspond to each simulated model. In Panel A, the capacitance is changed for the HH and CGC neuron models, and in the two compartments for the N3t neuron model. Panel B shows the spike waveforms changing the conductances of Na channel currents: I_{Na} from the HH-model, I_{NaP} and I_{NaT} , from the CGC-model. Panel C, displays the modulation of K conductances in ionic currents: I_K in the HH-model and I_D and I_A for the CGC-model (from left to right). Panel D shows the modification of the calcium current conductances in the CGC-model (I_{HVA} and I_{LVA}). Table in panel E represents the quantification of the changes in the spike metrics when tuning each parameter for every model. Each cell contains the waveform change normalized to the maximum. The color gradient represents similarity based on the standard deviation of the normalized experimental change. Dark purple corresponds to low similarity ($2\sigma_{MEC}$ or larger) and white to high similarity. The quantified experimental reference (MEC) is annotated in the first row of the table. . . 133

LIST OF FIGURES

6.15 Simulation of the effect of individual channels on the spike waveform under temperature modulation. Panel A.i) Waveform modulation in the CGC-model excluding temperature dependency in one channel at a time, from left to right: I_{NaT} , I_A , I_{HVA} , I_{LVA} , I_D respectively. Panel A.ii) Waveform modulation in the CGC-model with temperature dependency only in one channel at a time, from left to right: I_{NaT} , I_A , I_{HVA} , I_{LVA} and I_{NaP} , respectively. Note that I_{NaP} is not in panel A.i) and neither is I_D in A.ii), as for these two particular simulations there was no spike generation. Panels B.i) and B.ii) show the quantification of the waveform change for $\Delta T = 5^\circ\text{C}$ in duration, depolarization slope, repolarization slope and amplitude for all channels in panel A. Both figures include, as reference, the experimental mean and STD (showed in black) and, for case B.ii) (only one channel at a time), the quantification when all channels have the same temperature dependency (all with $\Delta T = 5^\circ\text{C}/3^\circ\text{C}$, data used in Figure 5) is depicted in light and dark red bars.	140
6.16 Simulation of the effect of CW-NIR laser in the CGC-model. Stimulating only during the depolarization or only during repolarization phases for first and second rows respectively.	142
6.17 Results in the spike waveform for the simulation of the effect of CW-NIR laser in the CGC-model. Stimulating only during the depolarization or only during repolarization phases for first and second rows respectively.	143
6.18 Study of the laser effect at different stages of the spike waveform with an activity-dependent stimulation protocol. The panels quantify the change induced by the laser stimulation at distinct illumination offsets, –time intervals from the end of the illumination to the peak of the spike–. Top panel shows a spike waveform from the experiment as a time reference for the offset –time 0 corresponds to the spike peak. Boxplots represent the difference of each metric with respect to the control. All illumination intervals, pictured in the blue boxes, had the same duration of 58 ms and spikes were grouped by the illumination offset. Recovery and continuous laser reference are also shown in green and red boxes at left and right in the figure, respectively. The spike metrics selected here were duration, depolarization and repolarization slopes, –second, third and fourth rows, respectively.	144

LIST OF FIGURES

6.19 Normalized change for grouped values of spike duration, depolarization and repolarization slopes at distinct illumination offsets in the activity-dependent stimulation protocol. Each value in each group was normalized to the mean of its corresponding day controls as minimum value and the mean of the continuous laser recordings for each day as the maximum value. The maximum value for each metric is marked by a black circle.	145
7.1 Schematic summary of the results presented in this work. In the feeding CPG of <i>Lymnaea stagnalis</i> we explored in (1) experimental and (2) computational data the presence of dynamical invariants (Secs. 5.4 and 5.3), showing strong linear relations and associating this to the possible functional role of this indicator. The experimental results were complemented exploring the transformation of (3) robot movement into effective robot movement maintaining strong linear relations (Sec. 5.6). We also showed the (4) importance of reproducing the functional variability in computational models (Sec. 5.5. As a way to modulate neural dynamics we characterized the effect of the CW-NIR laser in single neurons in a sustained and activity dependent protocol. We showed (5) the spike waveform is modified during the laser illumination, as well as the firing rate (Sec. 6.4), and discussed the effect at (6) different wavelengths (Sec. 6.4.4). We showed also (7) preliminary results in the stimulation of a minimal circuit (Sec. 6.4.3). The computational model analysis (8) revealed the combination of candidates to reproduce the effect and the importance of the temperature role (Sec. 6.5). (9) The activity-dependent protocol (10) allowed to assess the action potential generation at different phases (Sec. 6.6).	156
B.1 N1M stimulation: Pairplot of the invariants no reset within cycles. Lower triangle represents the intervals within the same cycle. Upper triangle represents the intervals of one cycle within the next cycle.	191
B.2 Spontaneous case 1: Panel of intervals distribution and dynamical invariants for the three phases in the CPG for spontaneous activity.	192
B.3 Spontaneous case 2: Panel of intervals distribution and dynamical invariants for the three phases in the CPG for spontaneous activity.	193
B.4 Spontaneous case 3: Panel of intervals distribution and dynamical invariants for the three phases in the CPG for spontaneous activity.	194

LIST OF FIGURES

B.5 CV1a driven case 4: Panel of intervals distribution and dynamical invariants for the three phases in the CPG under CV1a stimulation.	195
B.6 Table of R^2 values for the linear regression between the period and each interval for all experimental recordings showed in this section.	195

CHAPTER 1

Introduction and State of the Art

1.1 Neuroscience, neurons and their dynamics

Neuroscience is a wide and challenging field in science. It faces crucial questions, such as the study of the neural mechanisms underlying brain activity, how can those mechanisms outcome as human cognition or behavior, how is the information processed and transferred through neural activity, how are neural diseases generated and how can we detect and treat them. These questions and many more have been open problems that have intrigued scientific community since the first steps on the field. Neuroscience was born as a discipline from anatomy, physiology, biochemistry and biophysics. As a broad field, it is approached from distinct perspectives and it is usually referred to by its subfields, e.g. Neurobiology, Neuropharmacology, Clinical Neuroscience, Developmental Neuroscience, Systems Neuroscience, Cognitive Neuroscience, Computational Neuroscience, Neurotechnology, etc. All these fields aim to explain or repair the brain function either as a whole or in parts. They use different techniques and approaches where some of which give rise to entirely new fields, like Neuroimaging.

We cannot think or discuss about neuroscience without highlighting the work by Santiago Ramón y Cajal, crucial in the firsts steps on the understanding the brain (De Carlos & Borrell, 2007; de Castro, 2019; de Castro & Merchán, 2016; Delgado-García, 2015; Ramón y Cajal, 1899). The idea of the "neuron doctrine" was a boost on the study of the brain, explaining and describing the structure of individual cells called *neurons* that are able to connect and thus communicate by *synapses*. Figure 1.1 shows one of Cajal's drawings describing the bee retina and a first approximation to the possible flow of currents on it.

The brain is a complex system that we can study from many different prisms. In this thesis, we follow a bottom-up approach. So we will analyze experimentally and theoretically the neural activity at ionic channels and small circuits (with few synapses). Moreover, we will follow a Neurocomputational

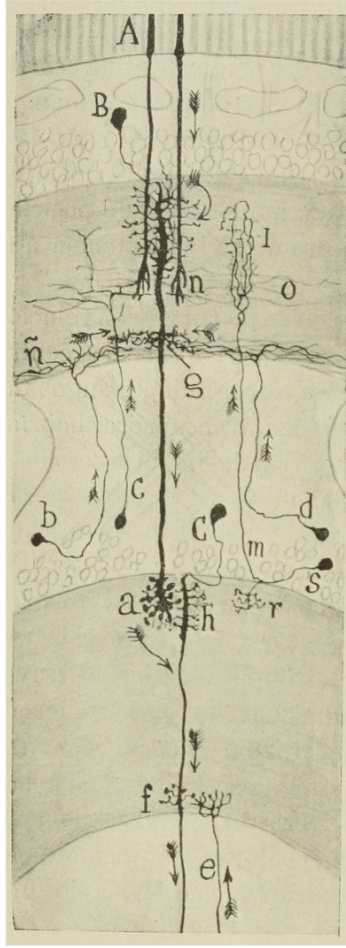


Figure 1.1: Illustration by Ramon y Cajal intended to show the probable course of currents in the bee retina. (A) rods; (B) second visual neuron (giant monopolar); (C) ganglionic corpuscle (third visual neuron); (B,C) short centrifuges; (M,S) T cell or interzonal connection cell; (F,G) basal dendrites destined to articulate with centrifugal fibers (Ramón y Cajal and Sánchez, 1915). Copyright Serrano-Herrera and Espinosa-Sánchez [serrano-herrera_domingo_2024](#) (CC BY-SA 4.0)

perspective based on hierarchical sequential information processing, which will be defined in detail in subsection 1.3. In the following lines we will approach the basis of neural activation from a computational perspective necessary for the reading flow of this document. We will focus not in their molecular properties but in the change of voltage that they are able to produce and how that inter-operates to give rise to neural activity.

1.1.1 Neuronal dynamics

Neurons are cells morphologically composed by dendrites, where the connections from other neurons are received through synapses), a soma or cellular body (where information is typically integrated) and an axon (where the information is conveyed as output). Since neurons are the cells that present

the largest diversity in morphology, this description does not apply to all neuronal types but serves to start highlighting the importance of spatial scales in the nervous system.

Neuronal electrical activity is often described in terms of the evolution of membrane voltage caused by the flow of ionic channels between the inside and outside of the cell (Kandel et al., 2012). The characteristic fast change in the membrane voltage when a neuron fires an output signal is called an action potential or a spike. They are often seen as the minimal pieces of information for reception, processing and transmission carried out by neurons. A more concrete definition of spike could be "an abrupt and transient change of membrane voltage that propagates to other neurons via a long protrusion called an axon" (Izhikevich, 2007). Thus, when no inputs are received, the membrane potential of a neuron is negative and it is called resting potential. When this potential is altered by an input that makes the voltage increase, it is known as depolarization. After reaching a peak of voltage, typically a positive value of around 40mV, the potential starts decreasing again. When the potential is more negative than the resting potential, it is known as hyperpolarization. Figure 1.2 illustrates the sequential phases of the action potential generation.

The neural activity is generated by the flow of different ionic channels that counterbalance the voltage value generating the action potential (Koch, 1999). The membrane can be composed by different ionic channels, and their dynamics are conditioned by that combination and the possible synaptic connections. These changes in dynamics can be manifested in different ways, but the most notorious ones are the shape and temporal evolution of the action potential. For example, in Fig. 1.3 there is an example of two distinct action potentials with visible differences in their shape, one of them presents a symmetrical shape, where depolarization and repolarization slopes are similar, whereas in the right waveform, there is a notable shoulder in the repolarization and its timescale is almost double in comparison of the example shown in (a).

If spikes are considered minimal pieces of information when coding the neural activity, the combination of these minimal information leads to new forms of information, also known as bursts. Although there is not a fixed description of a burst, and depending on the animal and system a burst might look different (Lundqvist et al., 2016; Palmu et al., 2010; Russell & Hartline, 1978), there are some common features in bursts: they typically consists of a group of spikes(more than two) on top of a sustained depolarization, and these groups are separated by a hyperpolarization quiescent period called inter-burst interval (IBI). Figure 1.4 shows several examples of distinct neuronal activities observed in intracellular recordings. Depending on the specific neuron and the circuit, neurons can present tonic firing (first column), at different rates, or bursting activity (second column).

Traditionally, neural codes have been studied focusing on the single spike activation, e.g., by the

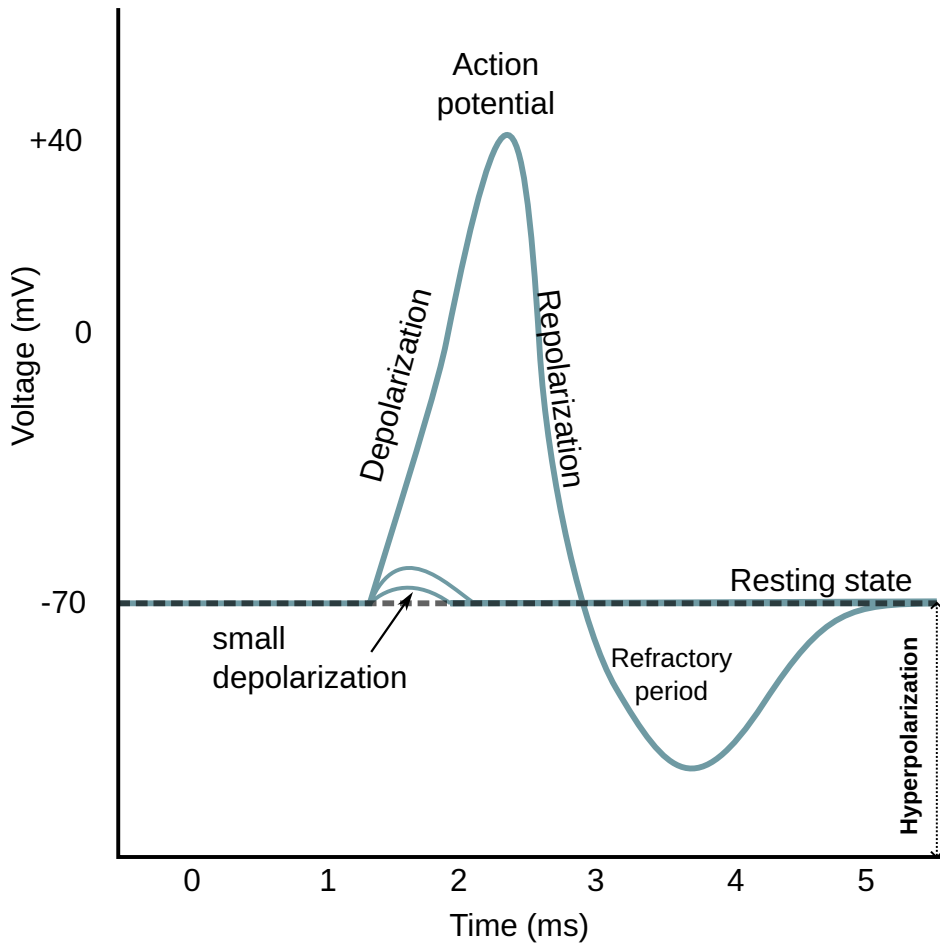


Figure 1.2: Representation of the sequential phases and terminology of an action potential. (Adapted from Chris73, Wikimedia Commons, CC BY-SA 3.0). In each of these phases of the action potential generation, different ionic channels are activated sequentially, e.g. the sodium channel is involved during the depolarization phase and its activity decays as the potassium channel activates mostly in the repolarization phase.

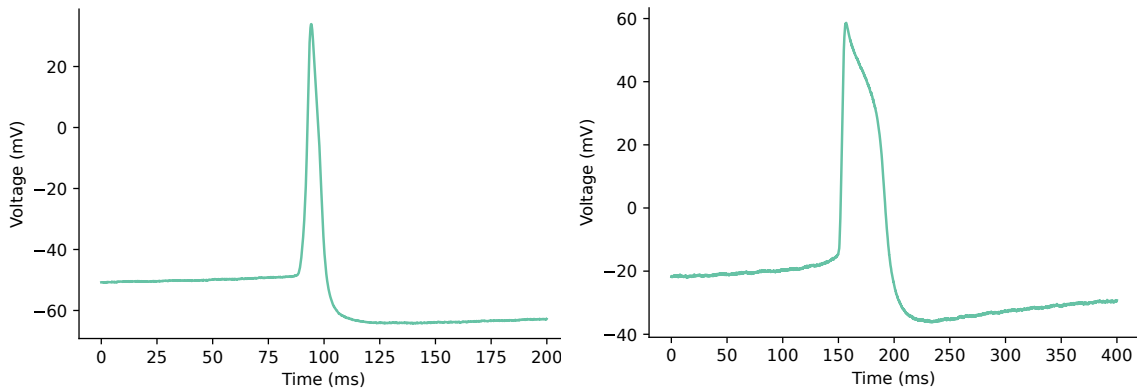


Figure 1.3: Examples of different spike shapes. Representation of two recordings from two different cells in the right parietal ganglion of *Lymnaea stagnalis*. Left: symmetrical spike; right: shoulder shaped spike.

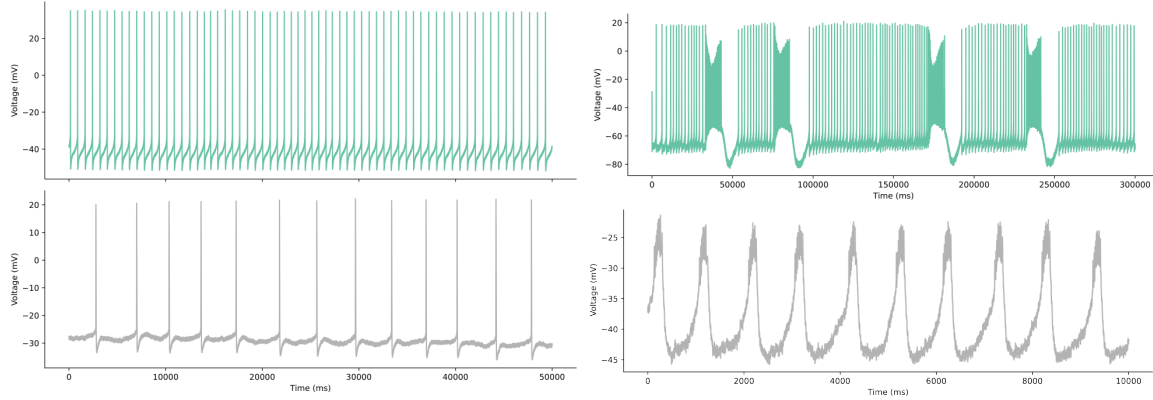


Figure 1.4: Representation of two examples of different spiking neuronal activity. Left: two simultaneous intracellular recordings in *Lymnaea stagnalis* showing tonic firing at two different frequencies. Right: Two examples of bursting activity, from *Lymnaea stagnalis* (top panel) and from *Carcinus maenas* (bottom panel).

binarization of the activity (the neuron generates a spike or it does not). Burst can also be informative in terms of the neural activity, either as a whole piece of information or as a complex box of data itself: "bursts are a family of firing patterns that trigger physiological mechanisms not engaged by the same number of spikes in relative isolation" (Friedenberger et al., 2023). Bursts can be originated either by internal activation, mostly by calcium channels or by the synaptic dynamics involving the corresponding cell (inhibition/excitation) (for an extended review see (Friedenberger et al., 2023)). This is the case in many Central Pattern Generators (CPGs) (Katz, 2016; Steuer & Guertin, 2018), which will be discussed in detail below and in Chapter 5.

1.1.2 Network dynamics

Although analyzing the activity of a single neuron is important in terms of characterizing its dynamics, when talking about information processing and behavior, it is also crucial to study the overall circuit dynamics. A circuit of neurons is defined by nervous cells interconnected by synapses. There are two main types of synapses in the nervous system: electrical and chemical connections, see Fig. 1.5. The main difference between them relies on how the communication takes place. Chemical synapses occur through the mediation of *neurotransmitters*, where a presynaptic neuron liberates these molecules that are bound to neuroreceptors to produce an alteration in the postsynaptic neuron. Thus, this connection is asymmetrical and unidirectional, whereas in electrical synapses we find a symmetrical and bidirectional connection. In those synapses, the neurons are almost attached by a structure called *gap junction*, which "pipes" both neurons, in a tissue structure that constrains the leakage to the extracellular space. This communication allows electric charge to flow from one neuron to the other and is then faster than the chemical synapses, which in comparison has no delay. The

activity of neurons electrically coupled is usually synchronous (Levitin & Kaczmarek, 2002).

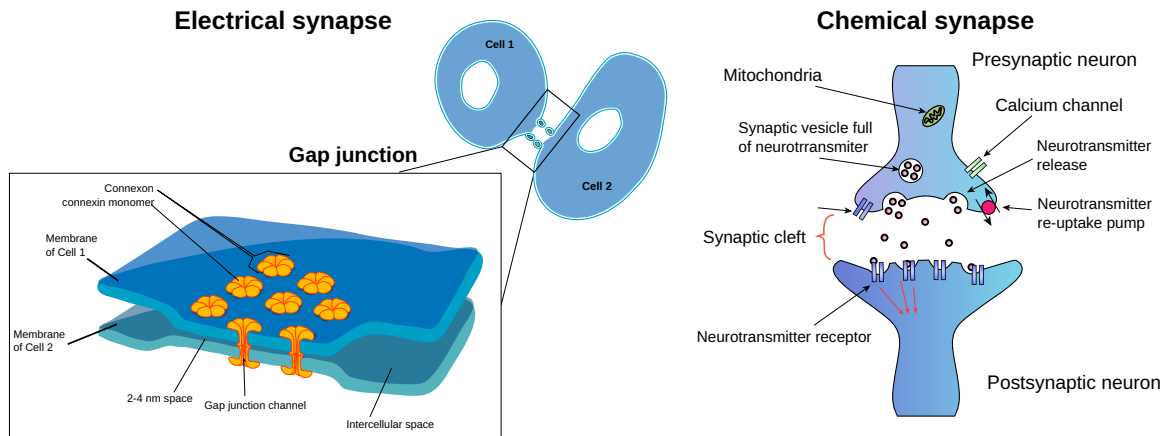


Figure 1.5: Representation of synapses types. Left. Example of electrical synapse between two cells and diagram of gap junction (Adapted from [Wikimedia Commons](#)). Right. Example of chemical synapse structure (Adapted from [Wikimedia Commons](#))

In neural circuits, cells can be connected by one or both types of chemical and electrical synapses, and they usually are also connected to other circuits or modulatory neurons. In Figure 1.6 illustrates two examples of circuits at the cellular and macroscopic levels. In this context, there are formed complex system of networks of networks, that might work at different time scales and can take part in one or several functionalities. This interconnection of networks and, from a lower level, cells, leads to sequential activations and transfers of actions into sequences of sequences.

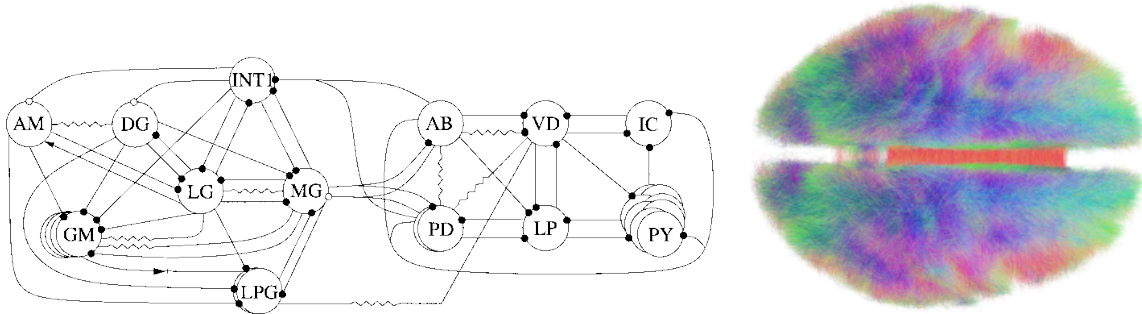


Figure 1.6: Left. gastric and pyloric circuit scheme of *Carcinus Maenas* (Huerta et al., 2001). Right. Conectome in human brain rendered from 20 subjects (By Andreashorn [CC BY-SA 4.0](#))

1.2 The sequential nature of neural dynamics

Brain dynamics can be described as sequences of interactions, from molecules, to neurons, to motor movement and behavior, within a coordinated hierarchy of temporal and spatial scales (Kiebel

CHAPTER 1: INTRODUCTION AND STATE OF THE ART

et al., 2008; Rabinovich et al., 2023; Rabinovich & Varona, 2018; Yuste et al., 2005), from ionic channel activations to sensory encoding, processing, and decision making. Its study reveals fundamental aspects of brain function and cognition, e.g., impulse transmission, executive function, spatial processing or memory.

A common example of sequential processing is speech, where sequential patterns are present in the structure of phrases, as sequences of sequences of syllables, words and silences (Kiebel et al., 2009). In this line, an extended case of study is the birdsong, which has similarity to human's speech, as they involve sequences of coordinated sounds (Fishbein et al., 2019; Prather et al., 2017). Beyond speech, sequential processing is also present in motor movement, from muscle activation to repetitive coordinated actions such as rhythmic tapping or music performance (N. Ding et al., 2017). Also, there are many important cognitive processes that rely in sequential mechanisms such as perception, memory, decision making, attention and emotion (He, 2018; Rabinovich et al., 2020; Varona & Rabinovich, 2016).

However, it is not clear how exactly the brain processes time. In contrast to the theory of a central clock that manages time for every behavioral task, the theory of a distributed time processing (Buonomano & Merzenich, 1995; Ivry, 1996) is well accepted. In this framework, especially in movement coordination, there is a need for circuits that manage the sequential rhythmic activity. This is the case of Central Pattern Generators (CPGs), circuits of neurons with closed-topology that sequentially activate neurons and generate coordinated motor activity (Selverston et al., 2000). They are present in many systems, from insects to humans (MacKay-Lyons, 2002; Marder & Bucher, 2001; Minassian et al., 2017; Pearson, 1972). There are several key aspects that make these circuits an interesting case of study. First, their neurons are organized in closed-topologies receiving all feedback from companion cells (Huerta et al., 2001). These circuits are able to maintain a rhythmic activity in an autonomous manner, typically by mutual inhibitory interactions (Katz, n.d.). Second, their activity is flexible enough to adapt to changes in the context, e.g., variations in the terrain while walking. Finally, they are present in many systems and in some of them there is a direct relationship between the activity of the neurons in the circuit and the motor movement that they produce. For example, in the stomatogastric CPG in the crab *C. maenas*, in charge of the pylorus movement, the PD (pyloric dilator), LP (Lateral Pyloric) and PY (PYloric) neurons correspond to the pylorus dilatation, pylorus close and contraction of the rostral constrictor to move food in the digestive system (Moulins & Selverston, 1987; Selverston & Ayers, 2006).

The sequential activity in the brain goes from the sub-millisecond scale to days (the time scale of circadian rhythms (Mauk & Buonomano, 2004)). Figure 1.7 shows an illustrative example of the se-

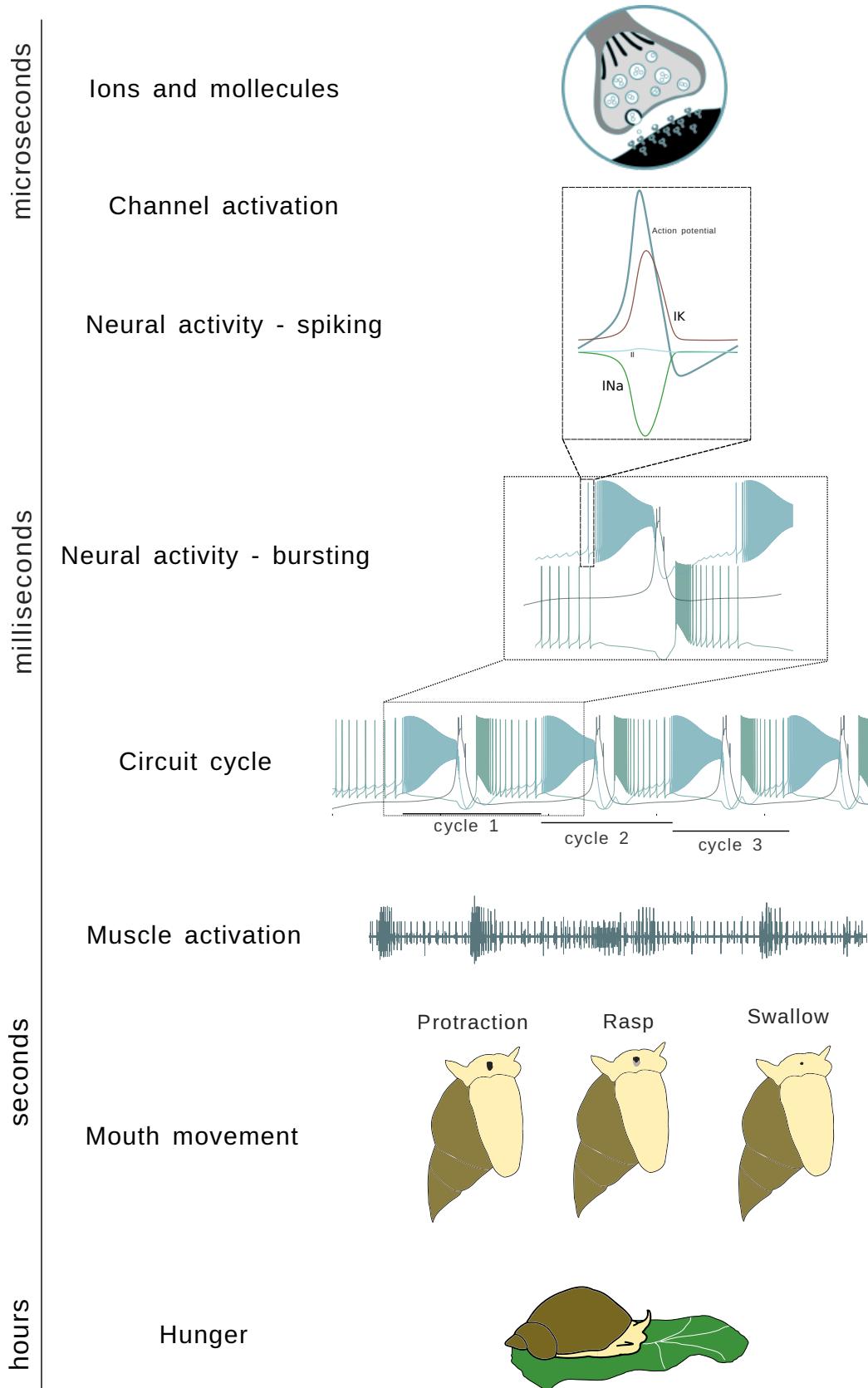


Figure 1.7: Illustration of the sequential feeding process at different time scales in *Lymnaea stagnalis*.

quential nature of neural activity at different scales in the generation of coordinated motor activity in the feeding of a snail. At the scale sub-milliseconds, there is a flow of ions that generate a sequence of ionic channel activation, that in the scale of milliseconds produce action potentials. The combination of them in form of rhythmic bursts, activate the corresponding muscles at the scale of seconds and generate the necessary sequential movement to eat: open the mouth, rasp food and swallow, that is repeated along the day.

The study of the action potential dynamics and the interaction between ionic channels and synapses is crucial, since it is a key part in any brain process, and it cannot be detached from the whole. The alteration of the dynamics of these channels at different levels can affect synaptic inputs/outputs, how the neurons communicate and the resulting process. Ionic channels are the starting point of the electrical signals underlying neuronal network activity, and their malfunction can contribute to neural disorders (Kecske et al., 2023). Thus, understanding brain activity not only at large scales but also from the stage of voltage generation dynamics can be crucial for a real and complete understanding of neural systems. Their study can also help distinguish between short- and long-term modulation, a key aspect in neural plasticity and the application of neuromodulatory techniques (Burke & Bender, 2019; Chambers & Kramer, 2008).

It is important to explore the mechanisms that allow to maintain a robust sequential activity despite changes in context and the variability underlying the neural dynamics. Action potentials and bursts can be classified depending on their waveform shape and grouped spiking activity. However, in those subgroups there is a high intra-variability, where for example bursting activity can differ in shape and duration, i.e., number of spikes in a bursts. Figure 1.8 shows an example of the variability in the burst waveform and duration for a sequence of several bursts.

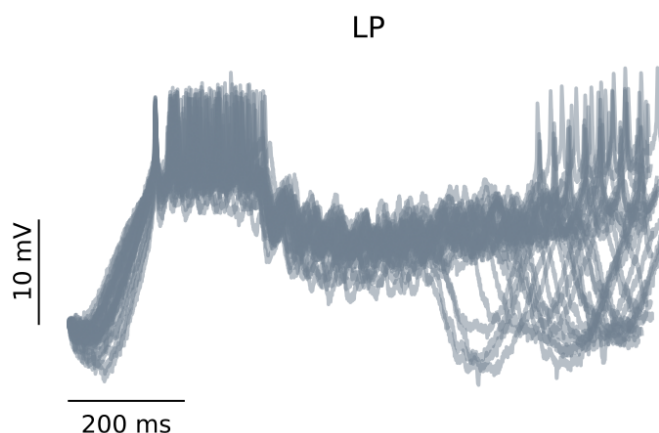


Figure 1.8: Superimposition of bursts at different time instants aligned by the first spike in the burst for intracellular recordings of an LP neuron in the sthomatogastric CPG.

The study of this variability unveils key factors in the sequentiality and how it is maintained despite different intrinsic or external modulations. This is the case for example of sequential dynamical invariants, i.e., robust relationships between time intervals that conform a neural sequence, when analyzing the activity cycle-by-cycle (Berbel et al., 2024; Elices et al., 2019; Garrido-Peña et al., 2021; Reyes et al., 2008). This sequential dynamical invariants might have a crucial role understanding the coordination of sequential activity and the balance between robustness and flexibility required for effective function in many brain processes (Dragoi, 2020; Tatsuno, 2015; Ullén et al., 2003; Zhou et al., 2020; Zimnik & Churchland, 2021). We will discuss in detail this phenomena in the feeding CPG of *Lymnaea stagnalis* in chapter 5.

1.3 Studying neural dynamics in computational models.

Computational Neuroscience is a subfield of neuroscience that uses theoretical and computational techniques to address the study of nervous system at multiple levels, from the molecular level all the way to the complex networks that shape behavior. It is thus a multi-disciplinary field. The basis of Computational Neuroscience lay on the understanding of brain dynamics from its electrical signals and the information they carry (Catterall et al., 2012; Dimitrov et al., 2011; Schwiening, 2012; Shannon, 1948). Computational Neuroscience has extended its scope, leading to new paths of research including complex networks, graph theory, single cell analysis and machine learning techniques (cns2023). In fields such as Artificial Intelligence there is even a symbiotic relationship between fields, where both inspire and help each other grow (Amunts et al., 2019; Gonçalves et al., 2020; Woźniak et al., 2020).

An important part of Computational Neuroscience is the description of neural systems with theoretical models and the reproduction of key phenomena by the model simulation. The simulation of neural activity is a powerful tool to explore neuronal dynamics, its biophysical sources, the possible mechanisms underlying the neural signaling, and the observed complex information processing. Its strength relies on the complete accessibility to the variables of the model, the typical extensive range of tunable parameters in the model which can be explored, and the ability to assess the role of distinct elements in the system or circuit by including or excluding them in the simulations. Although models cannot fully substitute research on living systems, they do lead us closer to the understanding of complex neural dynamics, being a fast, effective and a low cost alternative to advances in science. Also, models are an essential complement to experimental neuroscience reaching detailed descriptions where experimental approaches such as electrophysiology have limitations arising from the always present partial observability.

Models can be classified by their level of description, i.e. what level of simplification/abstraction is used, the detail of the structure/phenomenon being modeled and the size of the network, or their ability to reproduce the observed neural activity, e.g. chaotic dynamics. Figure 1.9 illustrates such kind of classification, with examples of models of large networks as Bezaire et al., 2016; Potjans and Diesmann, 2014, of single cell but still detailed as in Smith et al., 2013 and more abstract descriptions such as the one proposed in Izhikevich, 2003. Regarding the level of description, in the different biophysical models there is always a choice between detailed description of nonlinearities, channels and excitation properties, and efficiency in computation. In this line, researches can choose from conductance-based models Hodgkin and Huxley, 1952b, rich in the description of nonlinearities or simplified dynamical models FitzHugh, 1961; Hindmarsh and Rose, 1984, which typically represent nonlinearities with polynomial simplifications (see Torres and Varona, 2012 for a review of different levels of neuronal modeling).

1.3.1 Conductance-based models

In this thesis, all experimental recordings have been supported with simulations on conductance-based models. They are defined as mathematical descriptions of the ionic channels dynamics, based on their voltage-dependent conductance. The pioneer study by Hodgkin and Huxley, 1952b defined dynamical equations based on the equivalent electrical circuit of the electrical properties of neurons in the giant squid axon, see Fig. 1.10. This modeled circuit is also used to conform the intracellular recording configuration, where the pipette is included as an extra current compensated by the electrode in the bath (see Fig. 1.11).

In these models, the simulation of neural electrical activity is based on the mathematical description of different ionic channels in the circuit, whose dynamics are also well defined by activation gates. First, there is a mathematical description of the voltage dependency on time, as described by the equation 1.3.1:

$$C_m \frac{dV}{dt} = I - \sum I_x, : \quad (1.3.1)$$

where V is the membrane potential, I is an external current, e.g. an external stimulus or a synaptic current, I_x is the current description for each channel involved in the action potential generation, e.g., sodium, potassium, calcium (I_K , I_{Na} , I_{Ca}).

Second, each channel is also described voltage-dependent composed by activation-gates dynamics:

$$I_x = g_x m^n h^n (V - E_x), \quad (1.3.2)$$

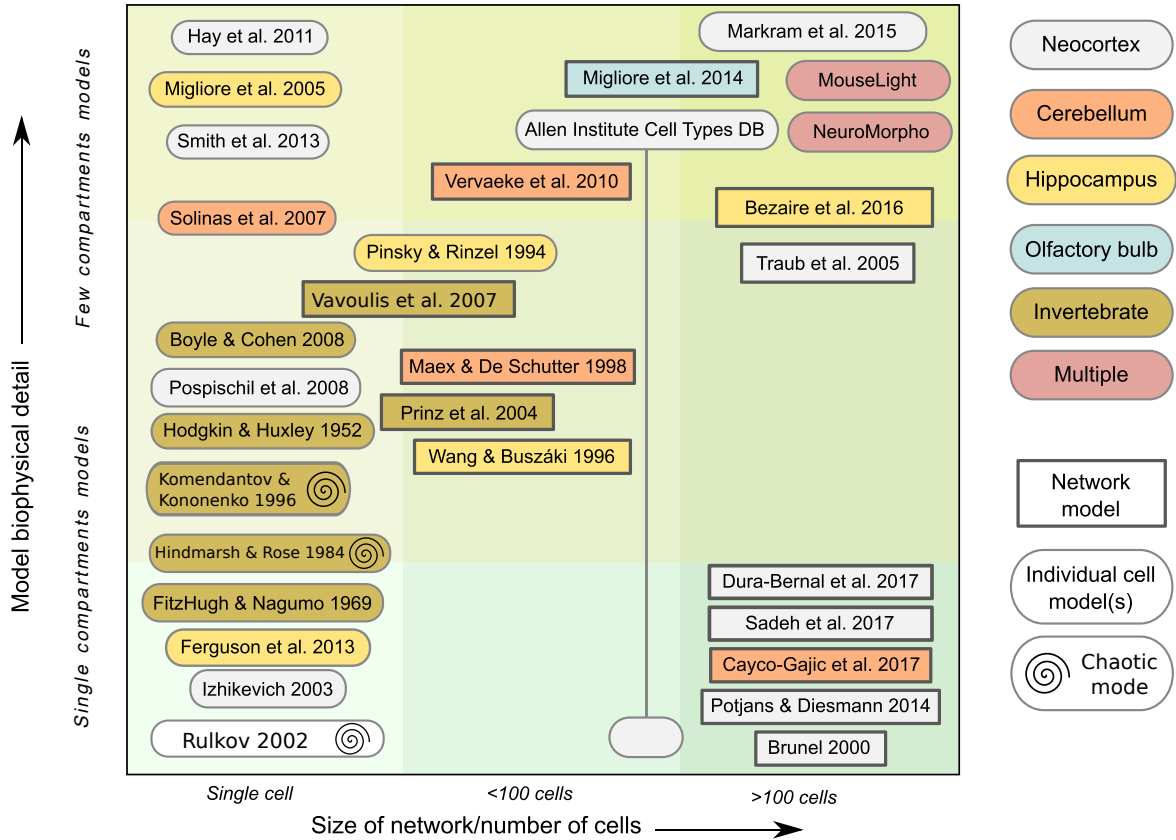


Figure 1.9: Neural and network models classified by biophysical detail, structure modeled and size of the network. Figure adapted from Fig. 2 Gleeson et al., 2019 under [Creative Commons CC-BY license](#). Models are classified by the biophysical detail, by y-axes being the models in the bottom the less specific ones; by the size of the network modeled, from left to right one cell to hundreds of cells; and by the brain-structure they model, represented in colored boxes. The shape of the box also classifies the model in network model or individual cell model. A third category was here included from the original work, representing by an spiral in the box the ability of the model to produce chaotic activity without external alterations, i.e, reproduce spontaneous variability. Although the figure does not contain all model approaches, it illustrates key milestones in neuronal modeling.

where g_x is the corresponding conductance of the channel, E_x is the reversal potential for that channel and m and h represent activation and inactivation variables, respectively. Activation gates usually have an exponential tendency, and are defined by activation and inactivation dynamics, also dependent on voltage and time. They follow the structure in equation 1.3.3

$$\frac{dm}{dt} = \frac{m_{\infty,i} - m_i}{\tau_{m,i}} \quad (1.3.3)$$

where $\tau_{m,i}$ are the relaxation time constants which are usually voltage-dependent and modeled using sigmoid or Gaussian functions. Note that m was used here but this formula corresponds also to

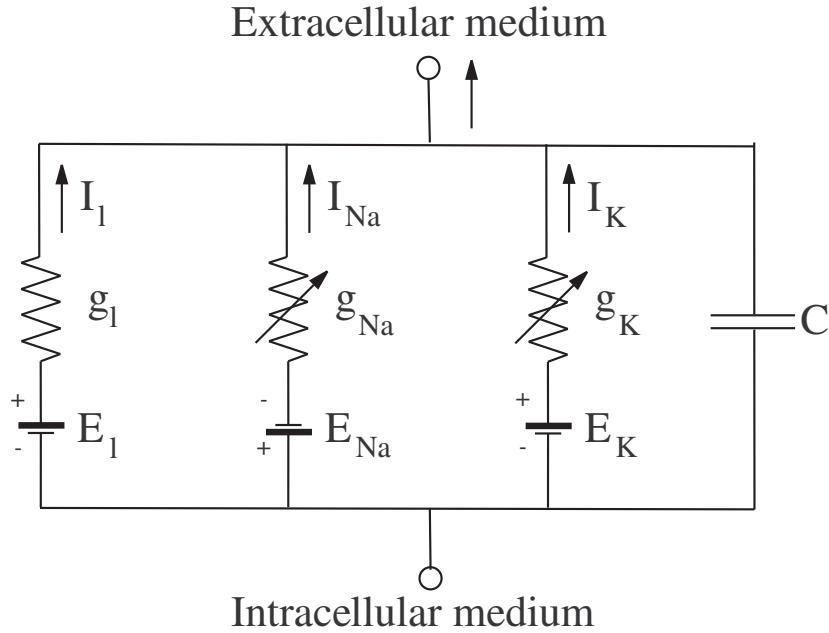


Figure 1.10: Electrical circuit describing the membrane voltage in a conductance based neuron model.

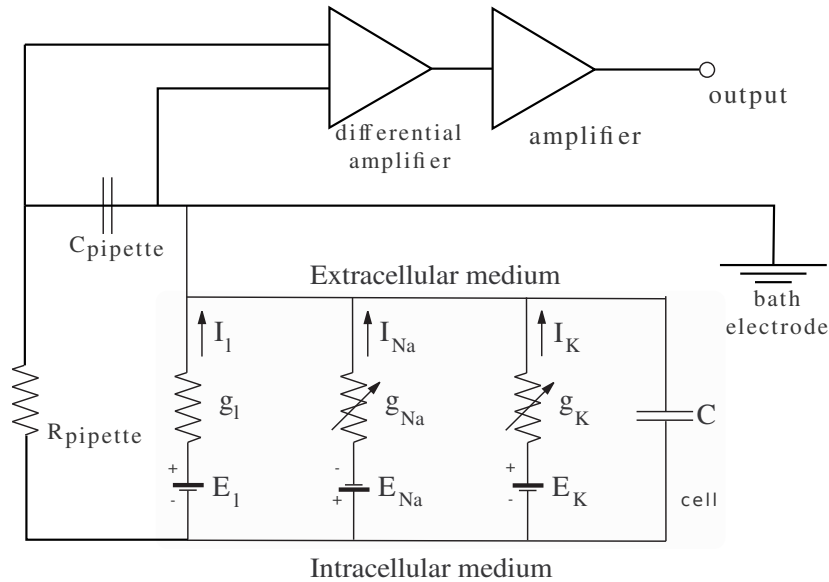


Figure 1.11: Electrical circuit representing the scheme for intracellular recordings.

inactivation variables.

Following the Hodgkin and Huxley formalism, the equations that describe the voltage dynamics and the conductance dynamics of the active channels (Na and K) in the circuit shown in Fig. 1.10 are:

This combination of channels generates the spike waveform shown in Fig. 1.12a) but, as in living systems, the combination of different channels leads to distinct outputs, e.g. shoulder and no-shoulder type neurons (see previous section, Fig. 1.3). This is the case of waveform in Fig. 1.12 b), where this shoulder shape could be reproduced in models by including calcium specific channels.

Voltage equation	$C \frac{dV}{dt} = I - g_K n^4 (V - E_K) - g_{Na} m^3 h (V - E_{Na}) - g_L (V - E_L)$		
Activation variables		Inactivation variable	
gating variables	$\frac{dm(t)}{dt} = \frac{m_\infty(V(t)) - m(t)}{\tau_m(V(t))}$	$\frac{dn(t)}{dt} = \frac{n_\infty(V(t)) - n(t)}{\tau_n(V(t))}$	$\frac{dh(t)}{dt} = \frac{h_\infty(V(t)) - h(t)}{\tau_h(V(t))}$

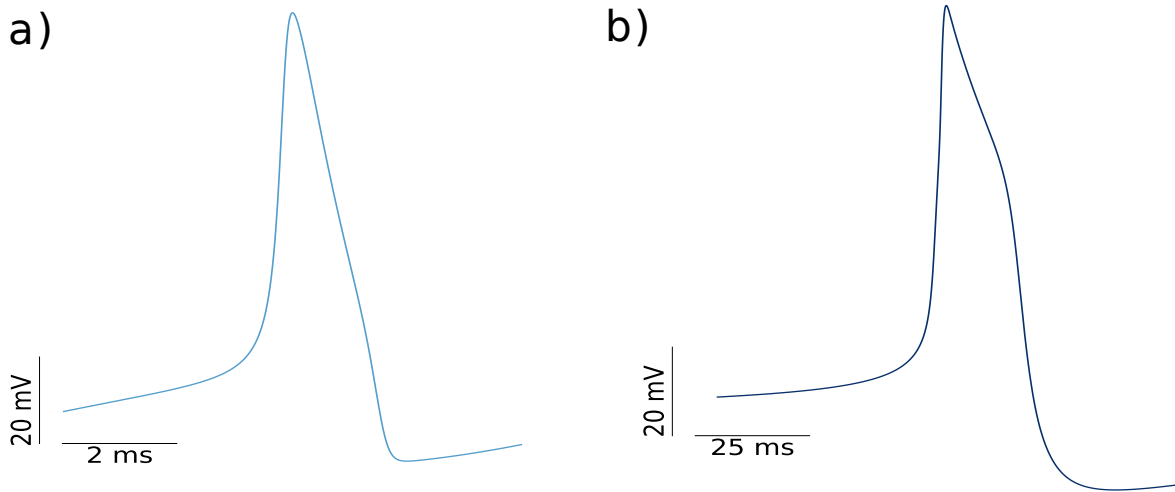


Figure 1.12: Simulation of two distinct spike types: no shoulder (a) and shoulder shaped (b), described by equations in Hodgkin and Huxley, 1952b and Vavoulis et al., 2010, respectively

Modeling networks

In addition to the modeling of the action potential generation, synapses can also be modeled with different mathematical representations depending on the type and the level of specificity. A combination of conductance-based models and synapses can modulate neural networks at different levels of complexity (Aguirre et al., 2007; Huerta et al., 2001; Latorre et al., 2013). Synapses are introduced in conductance-based models as an extra current that simulates the alteration in the neuron dynamics by chemical or electrical synapses. In conductance based models, electrical synapses or gap junctions are usually defined by the following equation:

$$I_{ij}(t) = \bar{G}_{ij}(V_i(t) - V_j(t)) \quad (1.3.4)$$

where i and j represent the two neurons conforming the electrical synapse and \bar{G}_{ij} is a constant representing the maximum value of synapse conductance in the connection. For symmetrical gap junctions, the other cells receives exactly the same current with inverse sign.

On the other hand, chemical synapses are by definition asymmetrical and can be described as in equation 1.3.5:

$$I_{ij}(t) = G_{ij}(t)(V_i - E_j^{syn}) \quad (1.3.5)$$

where E_j^{syn} is the voltage value at which the synaptic current cancels and G_{ij} can now have complex dynamics considering the trafficking of neurotransmitters as in equation 1.3.6 (Torres & Varona, 2012).

$$G_{ij}(t) = \bar{G}_{ij} \Theta(t - t_j^{\text{sp}}) \alpha(t - t_j^{\text{sp}}) \quad (1.3.6)$$

where \bar{G}_{ij} is the constant value for the conductance, t_j^{sp} is the time at which the presynaptic spike occurs. $\Theta(x)$ is the Heaviside step function and $\alpha(t)$ is a function to model an evoked postsynaptic responses that can be defined by exponential functions.

Depending on the selection of this level of specification, the neuron can be activated by a (i) binary cause: occurrence or absence of an action potential, or (ii) a dynamic model that is also dependent on the the postsynaptic voltage level (e.g. a graded synapse) or represents phenomena such as synaptic depression or facilitation. In that second case the level of specification is higher, with a richer description of the synapse dynamics. This is the case for example of Tsodyks and Markram, 1997, represented in equations 1.3.7, 1.3.8 or the gradual synapse in the CPG model by Vavoulis, Straub, et al., 2007a, discussed in methods chapter, section 4.4.1.

$$\frac{dU}{dt} = -\frac{U}{\tau_{\text{rec}}} + U_{\infty}(1-U)\delta(t - t_{\text{spike}}) \quad (1.3.7)$$

$$\frac{dX}{dt} = -\frac{X}{\tau_{\text{fac}}} + (1-X)\frac{U(t_{\text{spike}})}{U_{\infty}}\delta(t - t_{\text{spike}}) \quad (1.3.8)$$

where U is the fraction of resources available for release, X is the fraction of available neurotransmitter resources in the synaptic terminal. τ_{rec} is the time constant of synaptic resource recovery and τ_{fac} the time constant of synaptic facilitation. U_{∞} is the steady-state value of U and t_{spike} is the time of presynaptic spike. The delta function consider that a spike arrives to the synapse at a fixed time.

1.3.2 Variability in computational models

Most studies use deterministic models that produce regular neural activity, which are sufficient for many research questions when exploring input/output responses, studying the role of different biophysical elements or supporting experimental results on steady state dynamics. However, living systems are highly variable, often working in transient regimes, often displaying chaotic activity, and still able to produce sequential and robust patterned activity (Selverston et al., 2000). Variability in the activity of living neurons has been proven to play an important role in relevant information processing tasks(M. Ding & Glanzman, 2011; Hutt et al., 2023; Masquelier, 2013; Renart & Machens,

2014; Ribeiro et al., 2024). While this is a key aspect in neural dynamics, models usually exclude intrinsic variability from their description, particularly in membrane potential waveforms and in collective adaptive dynamics. To induce some level of stochasticity, models typically include Gaussian noise as external input (Linaro et al., 2011; Pezo et al., 2014; Zheng et al., 2020). However, this is a limited approach when exploring the role of variability intrinsically and dynamically generated by the neurons and the circuits for a specific computational tasks, e.g. for sequence coordination. There are several possibilities to include variability in neuronal intrinsic dynamics as it is the example of Hindmarsh and Rose, 1984 or Komendantov and Kononenko, 1996, where in both descriptions, there is a combination of parameters that lead both to a chaotic state, where the resulting activity is not regular. When the source of the variability in the system comes from its intrinsic properties, there is a possibility to study its dynamics and the role of this variability in the system without random sources, which in cycle-by-cycle dynamics can canceled out.

1.4 Vertebrate and invertebrate animal studies

The study of neural dynamics and behavior is carried out using many different animal models. Apart from the hegemonic rodents models, there have been invaluable findings using invertebrates, such as in genetics and developmental biology in *C. elegans* (Brenner, 1974), *Zebra fish* (Streisinger et al., 1981) and *Drosophila* (Nüsslein-Volhard & Wieschaus, 1980); neural dynamics in *Aplysia* (Wachtel & Kandel, 1967) or *Loligo* (Hodgkin & Huxley, 1952a), motor activity in *Panulirus* (Selverston et al., 1976) and *Carcinus maenas* (Eisen & Marder, 1982) or *Lymnaea stagnalis* (P. R. Benjamin & Rose, 1979), the main animal model in this thesis. Besides those examples, these animal models have been used for a wide variety of fields including behavioral studies, ecotoxicology, evolution, human disease modeling, etc. (Romanova & Sweedler, 2018)

Despite brain differences between invertebrates and mammals, there are many universal characteristics of nervous systems that can be extrapolated to humans. We should keep in mind that any animal model is still a research framework, with differences from the real focus of study –the human brain– and as a model, there are differences in the structure, even within mammal species (Preuss, 2000). So by using computational models or exploring more animal species there can be set a ground truth for the aspects that shape the neuronal and behavioral dynamics.

Findings in invertebrates are sometimes overlooked, often under the excuse that features in invertebrates cannot be extrapolated to humans. However, invertebrates models have proven their utility not only in basic science. We can find examples of this in human diseases, memory, motor activity and

neuromodulation. Particularly, in the study of neural processes, the ease of accessibility and finite number of large neurons in the system, have made invertebrates an interesting case of study.

Among the advantages in using invertebrates, it is worth mentioning the easy access to the nervous system and the duration of the spontaneous activity after the dissection for hours., the ease of breeding and reproduction or the simplicity of their biological features, that makes possible a full description of it, i.e. the genomic description of *C. elegans* or the nervous system in *Lymnaea stagnalis*. Also some selected species were a main field of study in the last decades, so there is plenty of literature for each one even in different fields. Furthermore, despite the simplicity of these systems, their nervous system is still capable of generating robust sequential neural activity, preset behavior and even learning processes.

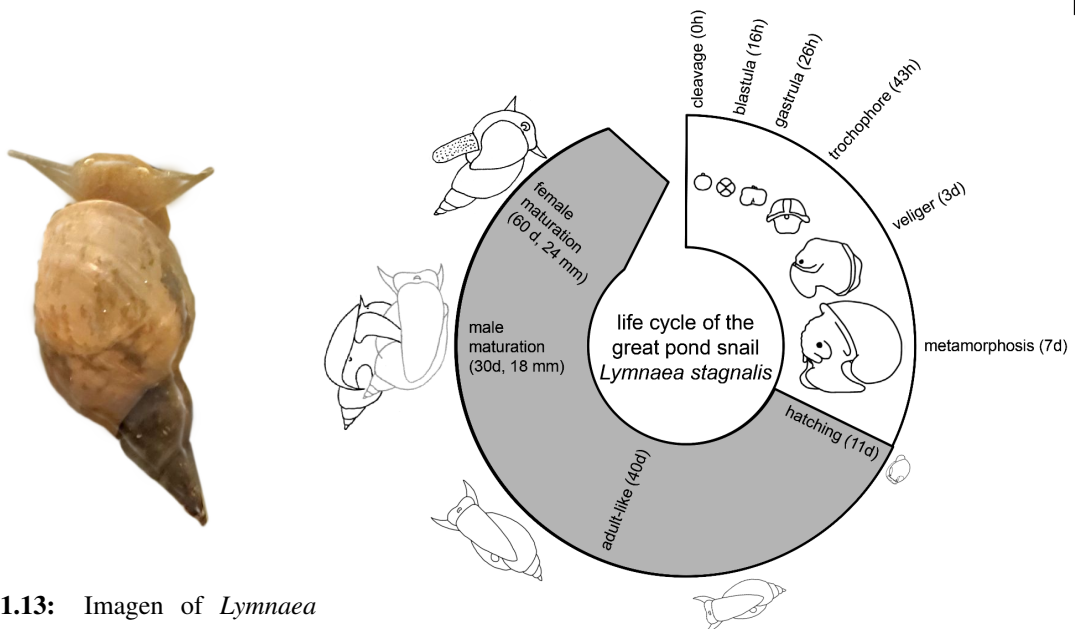
Apart from the possible advances in science from a productivist view, invertebrates models can also bridge the gap between resources and science, allowing low-income labs and countries to *do* science. This animal models are usually cheaper to obtain, maintain and there is usually a possibility of breeding own colonies. This makes their use extendable and breaks some economical barriers in science, where high-income countries usually centralize the science production with strong conventions (Castillo & de la Guardia, 2017; Stephan, 2015).

However, in any animal model, it is important to prioritize scientific advancement responsibly. Alternatives such as computational models should be considered alongside experimental studies, aiming to reduce the need for them and offering a less invasive path to extend our knowledge.

***Lymnaea stagnalis*, the great pond snail**

In this thesis, we explore the neural system of the great pond snail, *Lymnaea stagnalis* (see Fig. 1.13). This mollusk has been an important case of study since the late XX century, when it was used extensively to study neurobiological processes and nervous system functioning. This career-time effort lead to a detailed description of the buccal ganglia in its CPG, including the three main interneurons conforming it (B. Y. P. R. Benjamin et al., 1979; Benjamin et al., 1989; Brierley et al., 1997; Rose & Benjamin, 1979) and the modulatory neurons that influence the CPG activity such as SO and CGC neuron in the cerebral ganglia (Kemenes et al., 2001; McCrohan & Benjamin, 1980; Rose & Benjamin, 1981)). Besides the buccal ganglia, other neurons in different ganglia are also well identified, with specific characteristics such as electrical coupling or dopamine containing neurons as in the Right Parietal Ganglia(P. R. Benjamin & Pilkington, 1986; Winlow et al., 1981)).

From that point on, it has been key in other fields as host-parasite or genome editing. This last

**Figure 1.13:** Imagen of *Lymnaea**Stagnalis*

The unlimited potential of the great pond snail, *Lymnaea stagnalis*
 Fodor et al. eLife 2020;9:e56962 <https://doi.org/10.7554/eLife.56962>

Figure 1.14: Representation of *L. stagnalis* life cycle. Figure 2A from Fodor et al., 2020 (Creative Commons license).

field is thanks to the short and well studied life-cycle in *L. stagnalis* (see Fig. 1.14), as well as the easiness to lab-bread them, without losing its main characteristics through generations (Noland & Carriker, 1946). Recordings and analyses in this work are framed in the study of neural activity in its central nervous system (CNS). *L. stagnalis* CNS is composed by 11 ganglia that conform the system: symmetrical pairs of buccal, pedal, cerebral, pleural and parietal, and a single visceral ganglion (see Sec. 4.1). We will focus specially in its feeding CPG, that by a distributed combination of motor- and inter-neurons allocated mainly in buccal and cerebral ganglia, produce a rhythmic pattern movement that allows feeding in three phases (protraction, rasp and swallow). Beyond this study of the CPG, we will work on the giant neurons located in the right parietal ganglion (RPG), enhancing the high-voltage (up to 80mV) and slow activity (30 to 100 ms per spike) to analyze in detail the action potential dynamics.

1.5 Neural stimulation

1.5.1 Stimulation techniques

Neural stimulation have been an essential aspect in the study of neural dynamics, allowing the modulation of the neural system to explore, reproduce and alter its dynamics for their study. There are

several techniques to produce the stimulation, we could classify them in chemical –using chemical components to block/enhance neural mechanisms–, electrical –injecting current in the cell membrane or nerves– or optical –where neurons or circuits are stimulated through a illumination process. In this thesis, we focus in the last two. In the electrical techniques, since the firsts applications of electrophysiology by Neher and Sakmann, 1976 and the subsequent apparition of patch-clamp technique Hamill et al., 1981, many different techniques have been developed, for distinct systems. Voltage-clamp and patch clamping modified the paradigm in physiology and basic medicine in the study of the cell membrane dynamics with an exceptional detail that still today is heading ranges of precise recording and stimulation (Hamill et al., 1981). To Voltage-clamp followed variations such as dynamic-clamp, that enhances the electrophysiology possibilities by combining it with the possibilities of computing through a closed-loop protocol in real-time (Nowotny & Varona, 2022). This allows implementing specific algorithms to intervene the neural activity and test it to different approaches (Chamorro et al., 2012). Regarding optical stimulation, a novel and widespread technique is opto-genetics, that by genetically modifying the animals, neurons are reactive to light and have had great achievements in the last decades using for both stimulation and exploration (Chen et al., 2022). Other example still under study is near-infrared laser, a novel technique that will be explored in detail along this thesis. This technique have proven its potential for neuronal stimulation in different systems such as the hippocampus (Liang et al., 2009), spinal ganglia in the cochlea Barrett et al., 2018; Brown et al., 2020; Goyal et al., 2012 and other systems (Begeng et al., 2022; Cayce et al., 2014; Shapiro et al., 2012).

1.5.2 Neuromodulation and its need for clinical applications

Beyond the necessity for neural stimulation in basic research to understand and explore the brain signaling and dynamics, there is a direct social impact for neural stimulation in clinical applications. In this context, Neuromodulation is an area of medicine involving many specialities that can be defined as "the science of how electrical, chemical and mechanical interventions can modulate distinct models of the nervous system function [and it is] inherently non-destructive, reversible, and adjustable" (Krames et al., 2009). This field is so important due to its possibilities in brain disorder treatments, for functional stimulation but also by the long-term modulation through neuronal plasticity. Neuromodulation can be classified, depending on the technology used for it, as invasive or non-invasive. Invasive technologies are those that require a direct interaction with the living system, which causes harm, e.g. including surgery. A well-known example of this type is deep-brain stimulation (DBS), this technique has been effectively used to treat movement disorders by electrically stimulating the

CHAPTER 1: INTRODUCTION AND STATE OF THE ART

brain at certain brain areas after implanting a device (Hariz & Blomstedt, 2022; Limousin & Foltynie, 2019). In the case of non-invasive neuromodulation, we can find transcranial magnetic stimulation (TCM), that by electric fields stimulates certain areas of the brain, successful for example in the treatment of depression or obsessive compulsive disorder (Clarke et al., 2018; Valero-Cabré et al., 2017). Each type of technique has its own advantages, invasive techniques are usually more precise in space and time, whereas non-invasive techniques provide more flexibility and adaptability to different patients and the spreadness of the technique. In this context, the optical techniques discussed for stimulation in basic research have been rising in popularity also for clinical applications.

CHAPTER 2

Introducción y Estado del Arte

2.1 Neurociencia, neuronas y su dinámica

La neurociencia es un campo de la ciencia amplio y desafiante. Afronta preguntas cruciales, tales como el estudio de los mecanismos neuronales subyacentes a la actividad cerebral, cómo pueden esos mecanismos resultar en la cognición o el comportamiento humano, cómo se procesa y transfiere la información a través de la actividad neuronal, cómo se generan las enfermedades neuronales y cómo podemos detectarlas y tratarlas. Estas preguntas y muchas más han sido problemas abiertos que han intrigado a la comunidad científica desde los primeros pasos en el campo. La neurociencia nació como una disciplina a partir de la anatomía, la fisiología, la bioquímica y la biofísica. Debido a la amplitud del campo, se suele abordar desde distintas perspectivas y comúnmente se le hace referencia por sus subcampos, por ejemplo, Neurobiología, Neurofarmacología, Neurociencia Clínica, Neurociencia del Desarrollo, Neurociencia de Sistemas, Neurociencia Cognitiva, Neurociencia Computacional, Neurotecnología, etc. Todos estos campos tienen como objetivo explicar o reparar la función cerebral, ya sea en su totalidad o en partes. Utilizan diferentes técnicas y enfoques, algunos de los cuales dan lugar a campos completamente nuevos, como la Neuroimagen.

No podemos pensar o discutir sobre neurociencia sin destacar el trabajo de Santiago Ramón y Cajal, crucial en los primeros pasos para comprender el cerebro (De Carlos & Borrell, 2007; de Castro, 2019; de Castro & Merchán, 2016; Delgado-García, 2015; Ramón y Cajal, 1899). La idea de la "doctrina de la neurona" fue un impulso en el estudio del cerebro, explicando y describiendo la estructura de células individuales llamadas *neuronas* que son capaces de conectarse y, por lo tanto, comunicarse mediante *sinapsis*. La Figura 2.1 muestra uno de los dibujos de Cajal que ilustra la retina de la abeja y una primera aproximación al posible curso de las corrientes en ella.

El cerebro es un sistema complejo que podemos estudiar desde diferentes prismas. En esta tesis,

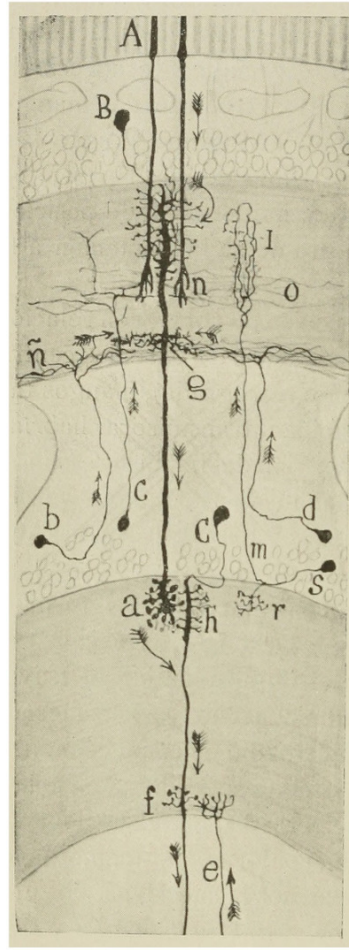


Figure 2.1: Ilustración de Ramón y Cajal que muestra el probable curso de las corrientes en la retina de la abeja. (A) bastones; (B) segunda neurona visual (monopolar gigante); (C) corpúsculo ganglionar (tercera neurona visual); (B,C) centrífugas cortas; (M,S) célula T o célula de conexión interzonal; (F,G) dendritas basales destinadas a articularse con fibras centrífugas (Ramón y Cajal y Sánchez, 1915). Copyright Serrano-Herrera y Espinosa-Sánchez [serrano-herrera_domingo_2024](#) (CC BY-SA 4.0)

seguimos un enfoque *bottom-up* (de abajo hacia arriba), en el que analizamos de forma experimental y teórica la actividad neuronal en canales iónicos y en pequeños circuitos (con pocas sinapsis). Además, seguimos una perspectiva neurocomputacional basada en el procesamiento secuencial jerárquico de la información, que se definirá en detalle en la subsección ???. En las siguientes líneas abordaremos las bases de la activación neuronal desde una perspectiva computacional necesaria para la comprensión de este documento. Nos centraremos no en sus propiedades moleculares sino en el cambio de voltaje que son capaces de producir y cómo eso interopera para dar lugar a la actividad neuronal.

2.1.1 Dinámica neuronal

Las neuronas son células morfológicamente compuestas por dendritas, donde se reciben las conexiones de otras neuronas a través de sinapsis, un soma o cuerpo celular (donde típicamente se integra la información) y un axón (donde la información se transmite como salida). Dado que las neuronas son las células que presentan la mayor diversidad en morfología. Aunque esta descripción no se aplica a todos los tipos neuronales, nos sirve para comenzar a resaltar la importancia de las escalas espaciales en el sistema nervioso.

La actividad eléctrica neuronal a menudo se describe en términos de la evolución del voltaje de la membrana causada por el flujo de canales iónicos entre el interior y el exterior de la célula (Kandel et al., 2012). El cambio rápido característico en el voltaje de la membrana cuando una neurona emite una señal de salida se llama potencial de acción o *spike*. Estas suelen considerarse unidades mínimas de información para la recepción, procesamiento y transmisión llevadas a cabo por las neuronas. Una definición más concreta de *spike* podría ser "un cambio abrupto y transitorio del voltaje de la membrana que se propaga a otras neuronas a través de una larga protusión llamada axón" (Izhikevich, 2007). Así, cuando no se reciben entradas, el potencial de la membrana de una neurona es negativo y se llama potencial de reposo. Cuando este potencial se altera por una entrada que hace que el voltaje aumente, se conoce como despolarización. Después de alcanzar un pico de voltaje, típicamente un valor positivo de alrededor de 40mV, el potencial comienza a disminuir nuevamente. Cuando el potencial es más negativo que el potencial de reposo, se conoce como hiperpolarización. La Figura 2.2 ilustra las fases secuenciales de la generación del potencial de acción.

La actividad neuronal se genera por el flujo de diferentes canales iónicos que contrarrestan el valor del voltaje generando el potencial de acción (Koch, 1999). La membrana puede estar compuesta por diferentes canales iónicos, y su dinámica está condicionada por esa combinación y las posibles conexiones sinápticas. Estos cambios en la dinámica pueden manifestarse de diferentes maneras, pero las más notorias son la forma y la evolución temporal del potencial de acción. Por ejemplo, en la Fig. 2.3 hay un ejemplo de dos potenciales de acción distintos con diferencias visibles en su forma, uno de ellos presenta una forma simétrica, donde las pendientes de despolarización y repolarización son similares, mientras que en la forma de onda de la derecha, hay un notable hombro en la repolarización y su escala temporal es casi el doble en comparación con el ejemplo mostrado en (a).

Si los picos se consideran las piezas mínimas de información al codificar la actividad neuronal, la combinación de estas piezas mínimas de información lleva a nuevas formas de información, también conocidas como ráfagas. Aunque no hay una descripción fija de una ráfaga, y dependiendo del animal

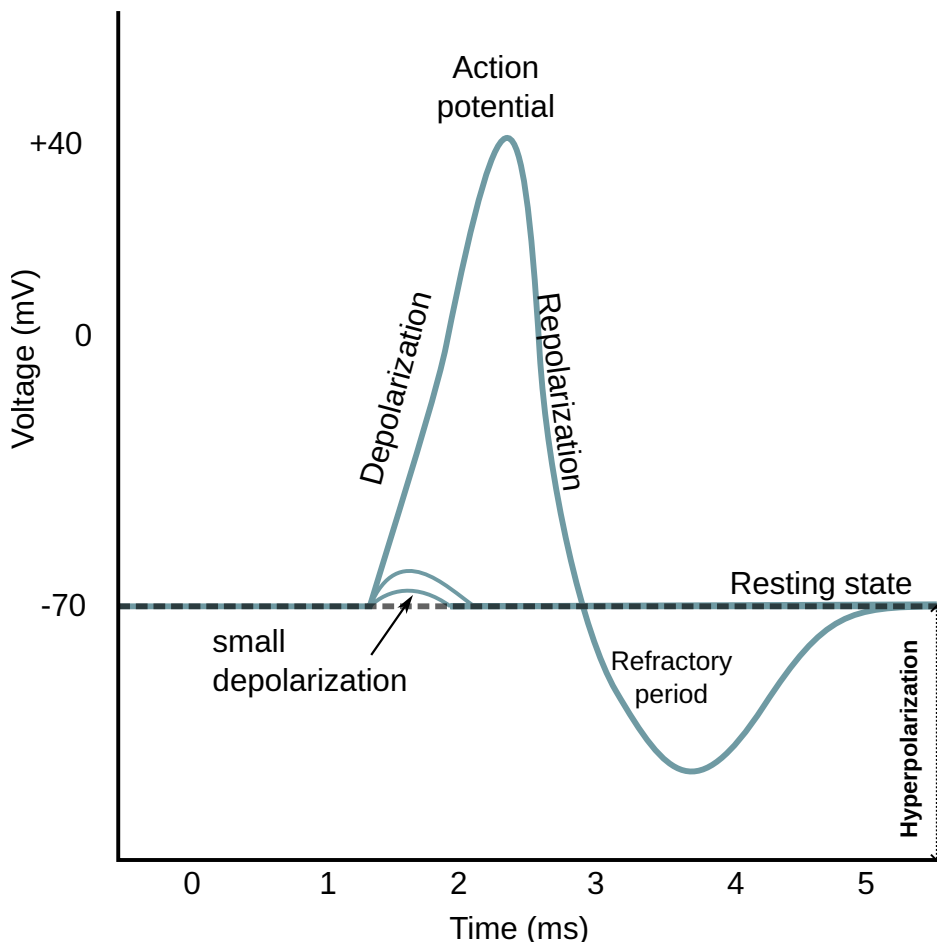


Figure 2.2: Representación de las fases secuenciales y terminología de un potencial de acción. (Adaptado de Chris73, Wikimedia Commons, CC BY-SA 3.0). En cada una de estas fases de la generación del potencial de acción, se activan secuencialmente diferentes canales iónicos, por ejemplo, el canal de sodio está involucrado durante la fase de despolarización y su actividad disminuye a medida que el canal de potasio se activa principalmente en la fase de repolarización.

y el sistema una ráfaga puede verse diferente (Lundqvist et al., 2016; Palmu et al., 2010; Russell & Hartline, 1978), hay algunas características comunes en las ráfagas: típicamente consisten en un grupo de *spikes* (más de dos) sobre una despolarización sostenida, y estos grupos están separados por un período de quiescencia de hiperpolarización llamado intervalo entre ráfagas (IBI). La Figura 2.4 muestra varios ejemplos de distintas actividades neuronales observadas en grabaciones intracelulares. Dependiendo de la neurona específica y el circuito, las neuronas pueden presentar disparo tónico (primera columna), a diferentes velocidades, o actividad en ráfagas (segunda columna).

Tradicionalmente, los códigos neuronales se han estudiado centrándose en la activación de *spikes* individuales, por ejemplo, mediante la binarización de la actividad (la neurona genera un pico o no). Las ráfagas también pueden ser informativas en términos de la actividad neuronal, ya sea como una

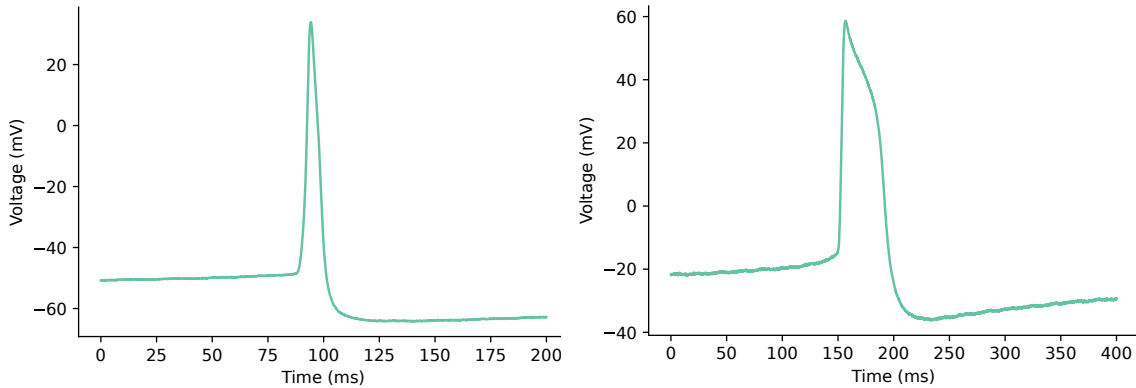


Figure 2.3: Ejemplos de diferentes formas de picos. Representación de dos grabaciones de dos células diferentes en el ganglio parietal derecho de *Lymnaea stagnalis*. Izquierda: pico simétrico; derecha: pico con forma de hombro.

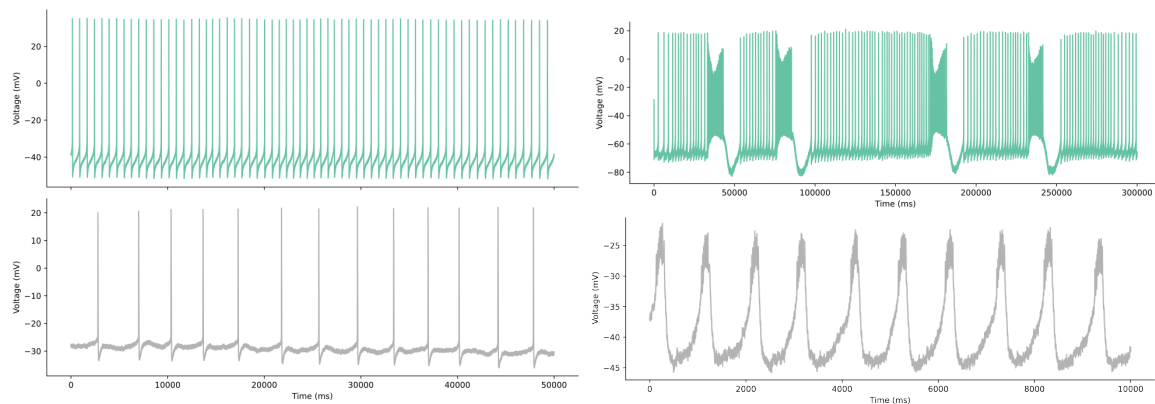


Figure 2.4: Representación de dos ejemplos de diferentes actividades neuronales de disparo. Izquierdo: dos grabaciones intracelulares simultáneas en *Lymnaea stagnalis* mostrando disparo tónico a dos frecuencias diferentes. Derecho: Dos ejemplos de actividad en ráfagas, de registros intracelulares en *Lymnaea stagnalis* (panel superior) y en *Carcinus maenas* (panel inferior).

pieza completa de información o como una caja de datos compleja en sí misma: "las ráfagas son una familia de patrones de disparo que desencadenan mecanismos fisiológicos que no se activan con el mismo número de *spikes* en relativo aislamiento" (Friedenberger et al., 2023). Las ráfagas pueden originarse por activación interna, principalmente por canales de calcio o por la dinámica sináptica que involucra a la célula correspondiente (inhibición/excitación) (para una revisión extendida ver (Friedenberger et al., 2023)). Este es el caso en muchos Generadores Centrales de Patrones (CPGs) (Katz, 2016; Steuer & Guertin, 2018), que se discutirán en detalle a continuación y en el Capítulo 5.

2.1.2 Dinámicas de redes

Aunque el análisis de la actividad de una sola neurona es importante para caracterizar su dinámica, cuando se habla de procesamiento de información y comportamiento, también es crucial estudiar la dinámica general del circuito. Un circuito de neuronas se define por células nerviosas interconectadas por sinapsis. Existen dos tipos principales de sinapsis en el sistema nervioso: conexiones eléctricas y químicas, como se muestra en la Fig. 2.5. La principal diferencia entre ellas radica en cómo se lleva a cabo la comunicación. Las sinapsis químicas ocurren mediante la mediación de *neurotransmisores*, donde una neurona presináptica libera estas moléculas que se unen a los neuroreceptores para producir una alteración en la neurona postsináptica. Por lo tanto, esta conexión es asimétrica y unidireccional, mientras que en las sinapsis eléctricas encontramos una conexión simétrica y bidireccional. En estas sinapsis, las neuronas están casi unidas por una estructura llamada *unión gap* (*gap junction* en inglés), que conecta ambas neuronas en una estructura tisular que limita la fuga al espacio extracelular. Esta comunicación permite que la carga eléctrica fluya de una neurona a otra y es más rápida que las sinapsis químicas, que, en comparación, no tienen retraso. La actividad de las neuronas acopladas eléctricamente suele ser sincrónica (Levitin & Kaczmarek, 2002).

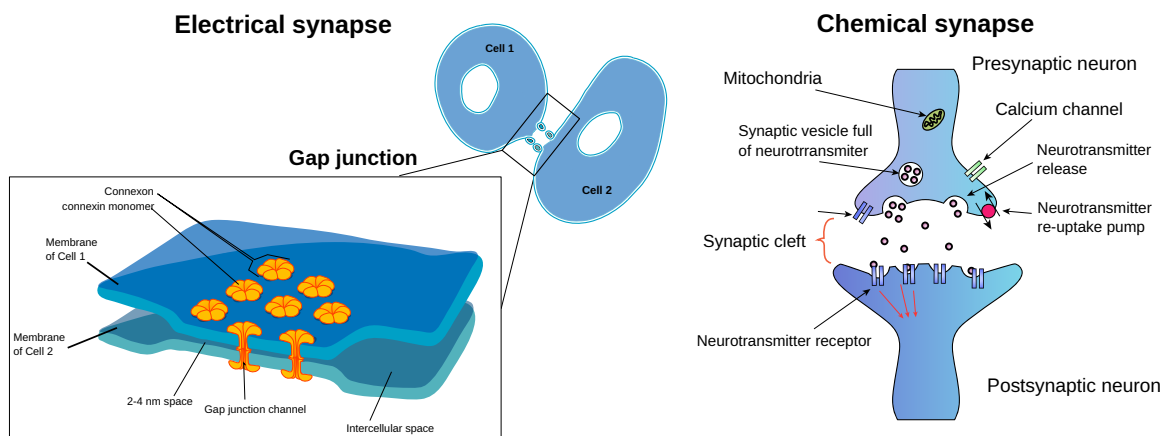


Figure 2.5: Representación de tipos de sinapsis. Izquierda: Ejemplo de sinapsis eléctrica entre dos células y diagrama de unión estrecha (Adaptado de [Wikimedia Commons](#)). Derecha: Ejemplo de estructura de sinapsis química (Adaptado de [Wikimedia Commons](#))

En los circuitos neuronales, las células pueden estar conectadas por uno o ambos tipos de sinapsis químicas y eléctricas, y generalmente también están conectadas a otros circuitos o neuronas moduladoras. La Figura 2.6 ilustra dos ejemplos de circuitos a nivel celular y macroscópico. En este contexto, se forman sistemas complejos de redes de red, que pueden funcionar a diferentes escalas temporales y pueden participar en una o varias funcionalidades. Esta interconexión de redes y, a un nivel más bajo, de células, conduce a activaciones secuenciales y transferencias de acciones en

secuencias de secuencias.

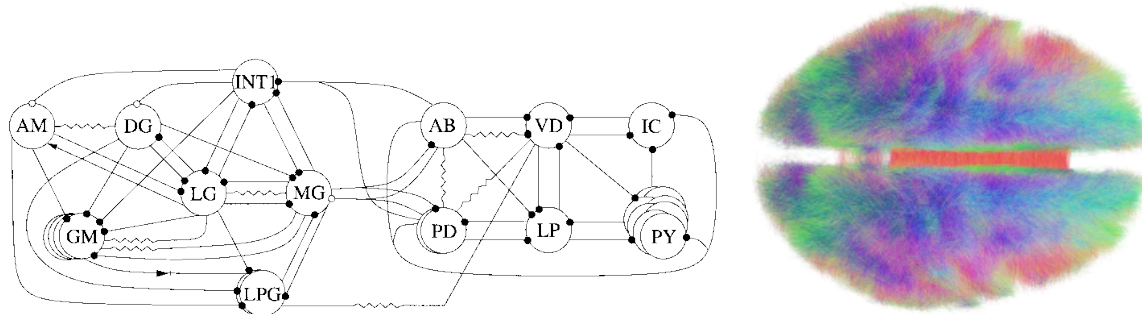


Figure 2.6: Izquierda: Esquema del circuito gástrico y pilórico de *Carcinus Maenas* (Huerta et al., 2001). Derecha: Conectoma en el cerebro humano renderizado a partir de 20 sujetos (Por Andreashorn - Trabajo propio, CC BY-SA 4.0)

2.2 La naturaleza secuencial de la dinámica neuronal

Las dinámicas cerebrales pueden describirse como secuencias de interacciones, desde moléculas, hasta neuronas, movimientos motores y comportamiento, dentro de una jerarquía coordinada de escalas temporales y espaciales (Kiebel et al., 2008; Rabinovich et al., 2023; Rabinovich & Varona, 2018; Yuste et al., 2005), desde activaciones de canales iónicos hasta codificación sensorial, procesamiento y toma de decisiones. Su estudio revela aspectos fundamentales de la función cerebral y la cognición, por ejemplo, la transmisión de impulsos, la función ejecutiva, el procesamiento espacial o la memoria.

Un ejemplo común de procesamiento secuencial es el habla, donde los patrones secuenciales están presentes en la estructura de las frases, como secuencias de secuencias de sílabas, palabras y silencios (Kiebel et al., 2009). En esta línea, un caso de estudio extendido es el canto de los pájaros, que tiene similitud con el habla humana, ya que involucran secuencias de sonidos coordinados (Fishbein et al., 2019; Prather et al., 2017). Aparte de en el habla, el procesamiento secuencial también está presente en el movimiento motor, desde la activación muscular hasta acciones coordinadas repetitivas como el golpeteo rítmico o la interpretación musical (N. Ding et al., 2017). Además, hay muchos procesos cognitivos importantes que dependen de mecanismos secuenciales como la percepción, la memoria, la toma de decisiones, la atención y la emoción (He, 2018; Rabinovich et al., 2020; Varona & Rabinovich, 2016).

Sin embargo, no está claro cómo procesa exactamente el cerebro el tiempo. En contraste con la teoría de un reloj central que gestiona el tiempo para cada tarea conductual, la teoría de un proce-

samiento temporal distribuido (Buonomano & Merzenich, 1995; Ivry, 1996) es bien aceptada. En este marco, especialmente en la coordinación del movimiento, existe la necesidad de circuitos que gestionen la actividad rítmica secuencial. Este es el caso de los Generadores Centrales de Patrones (CPGs), circuitos de neuronas con topología cerrada que activan secuencialmente neuronas y generan actividad motora coordinada (Selverston et al., 2000). Están presentes en muchos sistemas, desde insectos hasta humanos (MacKay-Lyons, 2002; Marder & Bucher, 2001; Minassian et al., 2017; Pearson, 1972). Hay varios aspectos clave que hacen de estos circuitos un caso de estudio interesante. Primero, sus neuronas están organizadas en topologías cerradas recibiendo retroalimentación de células compañeras (Huerta et al., 2001). Estos circuitos pueden mantener una actividad rítmica de manera autónoma, típicamente mediante interacciones inhibitorias mutuas (Katz, n.d.). Segundo, su actividad es lo suficientemente flexible como para adaptarse a cambios en el contexto, por ejemplo, variaciones en el terreno al caminar. Finalmente, están presentes en muchos sistemas y en algunos de ellos hay una relación directa entre la actividad de las neuronas en el circuito y el movimiento motor que producen. Por ejemplo, en el CPG estomatogástrico en el cangrejo *C. maenas*, encargado del movimiento del píloro, las neuronas PD (dilatador pilórico), LP (pilórico lateral) y PY (PYlórico) corresponden a la dilatación del píloro, el cierre del píloro y la contracción del constrictor rostral para mover los alimentos en el sistema digestivo (Moulins & Selverston, 1987; Selverston & Ayers, 2006).

La actividad secuencial en el cerebro va desde la escala de sub-milisegundos hasta días (la escala temporal de los ritmos circadianos (Mauk & Buonomano, 2004)). La Figura 2.7 muestra un ejemplo ilustrativo de la naturaleza secuencial de la actividad neuronal en diferentes escalas en la generación de actividad motora coordinada en la alimentación de un caracol. A la escala de sub-milisegundos, hay un flujo de iones que genera una secuencia de activación de canales iónicos, que en la escala de milisegundos produce potenciales de acción. La combinación de ellos en forma de ráfagas rítmicas, activa los músculos correspondientes en la escala de segundos y genera el movimiento secuencial necesario para alimentarse: abrir la boca, raspar el alimento y tragarse, que se repite a lo largo del día.

El estudio de la dinámica de los potenciales de acción y la interacción entre los canales iónicos y las sinapsis es crucial, ya que es una parte clave en cualquier proceso cerebral, y no puede separarse del estudio de la actividad en su conjunto. La alteración de la dinámica de estos canales a diferentes niveles, puede afectar las entradas/salidas sinápticas, cómo se comunican las neuronas y el proceso resultante. Los canales iónicos son el punto de partida de las señales eléctricas subyacentes a la actividad de la red neuronal, y su mal funcionamiento puede contribuir a trastornos neuronales (Kecske et al., 2023). Por lo tanto, comprender la actividad cerebral no solo a gran escala sino

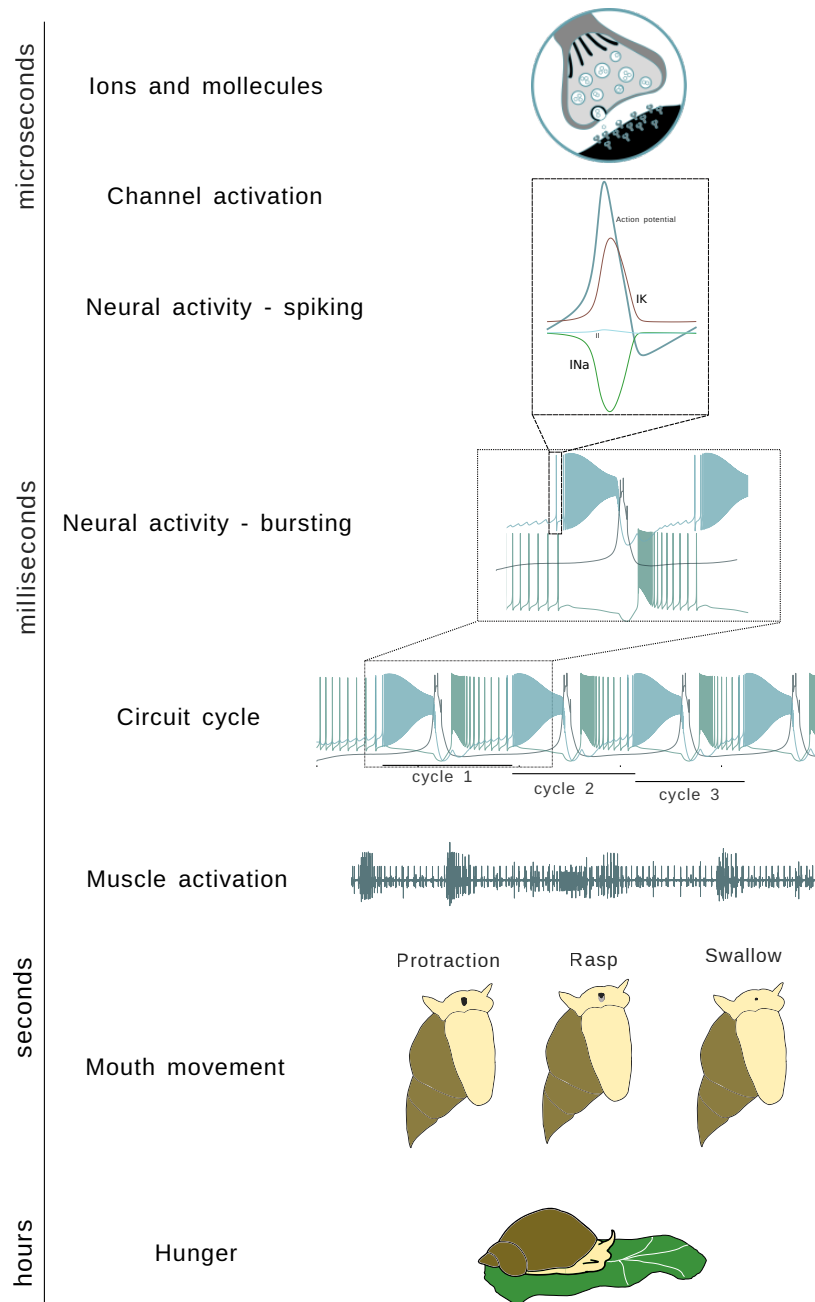


Figure 2.7: Ilustración del proceso de alimentación secuencial en diferentes escalas de tiempo en *Lymnaea stagnalis*.

también desde la etapa de generación de dinámicas de voltaje puede ser clave para una comprensión realmente completa de los sistemas neuronales. Su estudio también puede ayudar a distinguir entre la modulación a corto y largo plazo, un aspecto clave en la plasticidad neuronal y la aplicación de técnicas neuromoduladoras (Burke & Bender, 2019; Chambers & Kramer, 2008).

Es importante explorar los mecanismos que permiten mantener una actividad secuencial robusta a pesar de los cambios en el contexto y la variabilidad subyacente en la dinámica neuronal. Los poten-

ciales de acción y las ráfagas pueden clasificarse según su forma de onda y la actividad de disparo agrupada. Sin embargo, en esos subgrupos hay una alta intra-variabilidad, donde, por ejemplo, la actividad de ráfagas puede diferir en forma y duración, es decir, en el número de picos en una ráfaga. La Figura 2.8 muestra un ejemplo de la variabilidad en la forma de onda y la duración de la ráfaga para una secuencia de varias ráfagas.

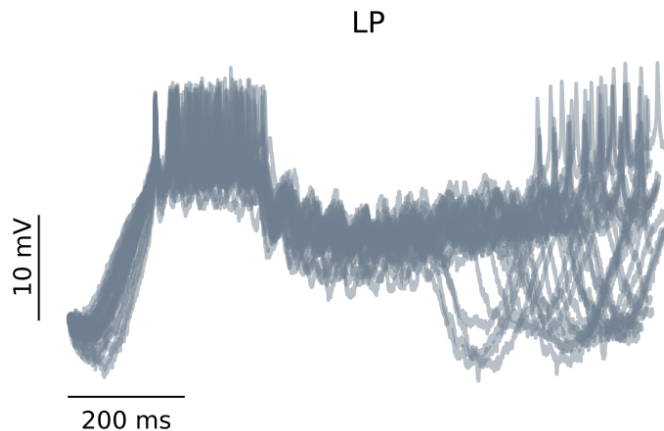


Figure 2.8: Superposición de ráfagas en diferentes instantes de tiempo alineadas por el primer *spike* en la ráfaga para grabaciones intracelulares de una neurona LP en el CPG estomatogástrico.

El estudio de esta variabilidad revela factores clave en la secuencialidad y cómo se mantiene a pesar de diferentes modulaciones intrínsecas o externas. Este es el caso, por ejemplo, de los invariantes dinámicos secuenciales, es decir, relaciones robustas entre intervalos de tiempo que conforman una secuencia neuronal, al analizar la actividad ciclo a ciclo (Berbel et al., 2024; Elices et al., 2019; Garrido-Peña et al., 2021; Reyes et al., 2008). Estos invariantes dinámicos secuenciales pueden tener un papel crucial para entender la coordinación de la actividad secuencial y el equilibrio entre la robustez y la flexibilidad requerida para una función efectiva en muchos procesos cerebrales (Dragoi, 2020; Tatsuno, 2015; Ullén et al., 2003; Zhou et al., 2020; Zimnik & Churchland, 2021). Discutiremos en detalle este fenómeno en el CPG alimentario de *Lymnaea stagnalis* en el capítulo 5.

2.3 Estudiando la dinámica neuronal en modelos computacionales.

La Neurociencia Computacional es un subcampo de la neurociencia que utiliza técnicas teóricas y computacionales para abordar el estudio del sistema nervioso en múltiples niveles, desde el nivel molecular hasta las complejas redes que dan forma al comportamiento. Es, por lo tanto, un campo multidisciplinario. La base de la Neurociencia Computacional radica en la comprensión de la dinámica

cerebral a partir de sus señales eléctricas y la información que transportan (Catterall et al., 2012; Dimitrov et al., 2011; Schwiening, 2012; Shannon, 1948). La Neurociencia Computacional ha ampliado su alcance, llevando a nuevos caminos de investigación que incluyen redes complejas, teoría de grafos, análisis de células individuales y técnicas de aprendizaje automático ([cns2023](#)). En campos como la Inteligencia Artificial incluso existe una relación simbiótica entre ambos, en la que se inspiran y se ayudan mutuamente a crecer (Amunts et al., 2019; Gonçalves et al., 2020; Woźniak et al., 2020).

Una parte importante de la Neurociencia Computacional es la descripción de sistemas neuronales con modelos teóricos y la reproducción de fenómenos clave mediante la simulación del modelo. La simulación de la actividad neuronal es una herramienta de gran potencial para explorar la dinámica neuronal, sus fuentes biofísicas, los posibles mecanismos subyacentes en la señal neuronal y el complejo procesamiento de la información observada. Su fuerza radica en la completa accesibilidad a las variables del modelo, el rango típicamente extenso de parámetros ajustables en el modelo que se pueden explorar y la capacidad para evaluar el papel de elementos distintos en el sistema o circuito incluyéndolos o excluyéndolos de las simulaciones. Aunque los modelos no pueden sustituir completamente la investigación en sistemas vivos, sí nos acercan a la comprensión de la dinámica neuronal compleja, siendo una alternativa rápida, eficaz y de bajo costo para los avances científicos. Además, los modelos son un complemento esencial para la neurociencia experimental, alcanzando descripciones detalladas donde los enfoques experimentales como la electrofisiología tienen limitaciones debido a la observabilidad parcial subyacente.

Los modelos pueden clasificarse según su nivel de descripción, es decir, qué nivel de simplificación/abstracción se utiliza, el detalle de la estructura/fenómeno que se modela y el tamaño de la red, o su capacidad para reproducir la actividad neuronal observada, por ejemplo, dinámicas caóticas. La Figura 2.9 ilustra este tipo de clasificación, con ejemplos de modelos de grandes redes como Bezaire et al., 2016; Potjans and Diesmann, 2014, de células individuales pero aún detallados como en Smith et al., 2013, y descripciones más abstractas como la propuesta en Izhikevich, 2003. En cuanto al nivel de descripción, en los diferentes modelos biofísicos siempre hay una elección entre la descripción detallada de las no linealidades, canales y propiedades de excitación, y la eficiencia en la computación. En esta línea, los investigadores pueden elegir entre modelos basados en conductancia Hodgkin and Huxley, 1952b, ricos en la descripción de no linealidades, o modelos dinámicos simplificados FitzHugh, 1961; Hindmarsh and Rose, 1984, que típicamente representan no linealidades con simplificaciones polinomiales (ver Torres and Varona, 2012 para una revisión de diferentes niveles de modelado neuronal).

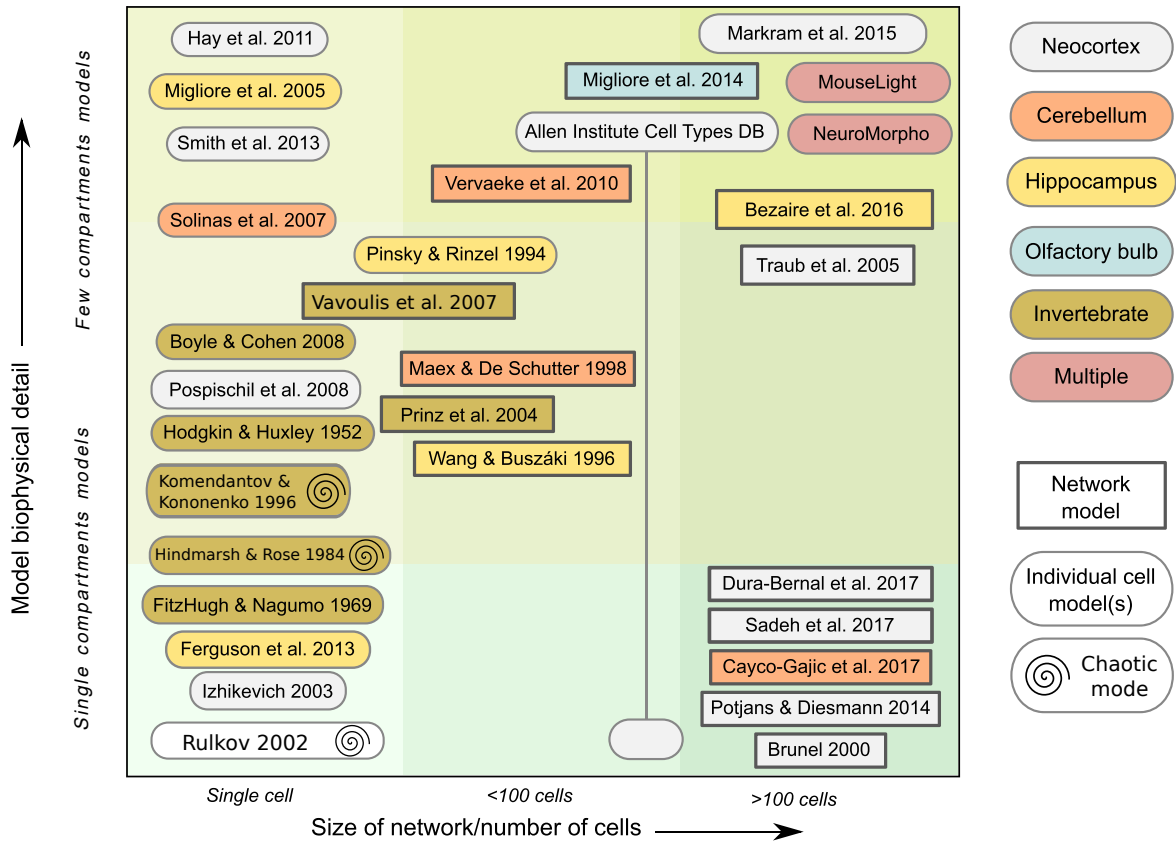


Figure 2.9: Modelos neuronales y de red clasificados por detalle biofísico, estructura modelada y tamaño de la red. Figura adaptada de la Fig. 2 Gleeson et al., 2019 bajo licencia Creative Commons CC-BY. Los modelos están clasificados por el detalle biofísico, siendo los modelos en la parte inferior los menos específicos; por el tamaño de la red modelada, de izquierda a derecha, una célula a cientos de células; y por la estructura cerebral que modelan, representada en cajas de colores. La forma de la caja también clasifica en modelo de red o célula individual. Se incluyó una tercera categoría a partir del trabajo original, representada por una espiral en la caja, que indica la capacidad del modelo para producir actividad caótica sin alteraciones externas, es decir, reproducir variabilidad intrínseca espontánea. Aunque la figura no contiene todos los enfoques de modelos, ilustra hitos clave en el modelado neuronal.

2.3.1 Modelos basados en conductancia

En esta tesis, todos los registros experimentales se han apoyado en simulaciones con modelos basados en conductancia. Se definen como descripciones matemáticas de la dinámica de los canales iónicos, basadas en su conductancia dependiente del voltaje. El estudio pionero de Hodgkin and Huxley, 1952b definió ecuaciones dinámicas basadas en el circuito eléctrico equivalente de las propiedades eléctricas de las neuronas en el axón gigante del calamar, ver Fig. 2.10. Este circuito modelado también se utiliza para conformar la configuración de registro intracelular, donde la pipeta se incluye como una corriente adicional compensada por el electrodo en la solución (ver Fig. 2.11).

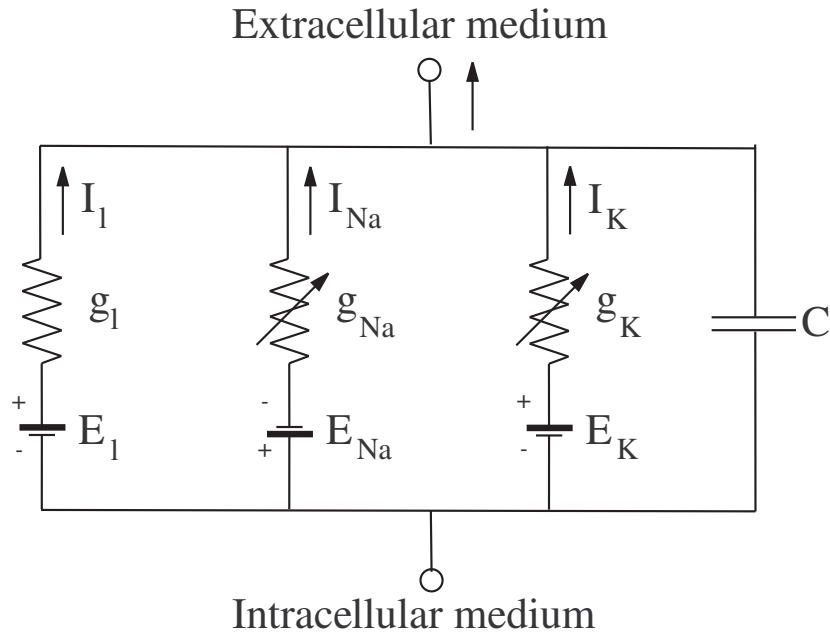


Figure 2.10: Circuito eléctrico que describe el potencial de membrana en un modelo de neurona basado en conductancia.

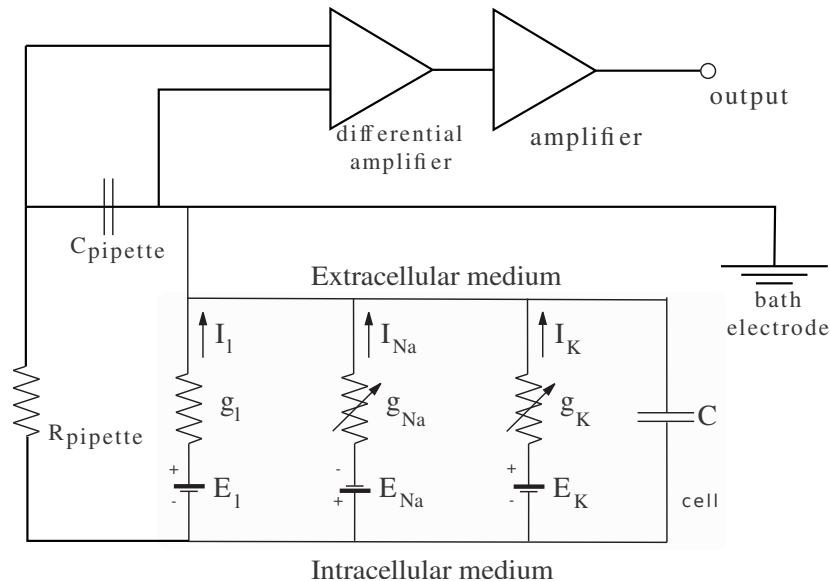


Figure 2.11: Circuito eléctrico que representa el esquema para registros intracelulares.

En estos modelos, la simulación de la actividad eléctrica neuronal se basa en la descripción matemática de diferentes canales iónicos en el circuito, cuya dinámica también está bien definida por compuertas de activación. Primero, hay una descripción matemática de la dependencia del voltaje en el tiempo, como se describe en la ecuación 2.3.1:

$$C_m \frac{dV}{dt} = I - \sum I_x, : \quad (2.3.1)$$

donde V es el potencial de membrana, I es una corriente externa, por ejemplo, un estímulo externo o una corriente sináptica, I_x es la descripción de la corriente para cada canal involucrado en la generación del potencial de acción, por ejemplo, sodio, potasio, calcio (I_K, I_{Na}, I_{Ca}).

En segundo lugar, cada canal también se describe dependiente del voltaje compuesto por dinámicas de compuertas de activación:

$$I_x = g_x m^n h^n (V - E_x), \quad (2.3.2)$$

donde g_x es la conductancia correspondiente del canal, E_x es el potencial de reversión para ese canal y m y h representan las variables de activación e inactivación, respectivamente. Las compuertas de activación suelen tener una tendencia exponencial y están definidas por dinámicas de activación e inactivación, también dependientes del voltaje y el tiempo. Siguen la estructura en la ecuación 2.3.3:

$$\frac{dm}{dt} = \frac{m_\infty - m}{\tau_m} \quad (2.3.3)$$

2.4 Estudios de animales vertebrados e invertebrados

El estudio de la dinámica neuronal y el comportamiento se lleva a cabo utilizando muchos modelos animales diferentes. Aparte de los modelos dominantes de roedores, ha habido hallazgos de valor incalculable utilizando invertebrados, como en genética y biología del desarrollo en *C. elegans* (Brenner, 1974), *pececillos* (Streisinger et al., 1981) y *Drosophila* (Nüsslein-Volhard & Wieschaus, 1980); dinámica neuronal en *Aplysia* (Wachtel & Kandel, 1967) o *Loligo* (Hodgkin & Huxley, 1952a), actividad motora en *Panulirus* (Selverston et al., 1976) y *Carcinus maenas* (Eisen & Marder, 1982) o *Lymnaea stagnalis* (P. R. Benjamin & Rose, 1979), el principal modelo animal en esta tesis. Además de estos ejemplos, estos modelos animales se han utilizado en una amplia variedad de campos, incluidos estudios conductuales, ecotoxicología, evolución, modelado de enfermedades humanas, etc. (Romanova & Sweeney, 2018).

A pesar de las diferencias cerebrales entre invertebrados y mamíferos, existen muchas características universales de los sistemas nerviosos que pueden extrapolarse a los humanos. Debemos tener en cuenta que cualquier modelo animal sigue siendo un marco de investigación, con diferencias respecto al enfoque real de estudio –el cerebro humano– y como modelo, existen diferencias en la estructura, incluso dentro de las especies de mamíferos (Preuss, 2000). Por lo tanto, mediante el uso de modelos computacionales o explorando más especies animales, se puede establecer una verdad fundamental

para los aspectos que conforman la dinámica neuronal y del comportamiento.

Los hallazgos en invertebrados no alcanzan la misma relevancia en muchas ocasiones, a menudo bajo la excusa de que las características en los invertebrados no pueden extrapolarse a los humanos. Sin embargo, los modelos de invertebrados han demostrado su utilidad no solo en la ciencia básica. Podemos encontrar ejemplos de esto en enfermedades humanas, memoria, actividad motora y neuromodulación. Particularmente, en el estudio de procesos neuronales, la facilidad de accesibilidad y el número finito de grandes neuronas en el sistema han hecho de los invertebrados un caso de estudio interesante.

Entre las ventajas de usar invertebrados, vale la pena mencionar el fácil acceso al sistema nervioso y la duración de la actividad espontánea después de la disección durante horas, la facilidad de cría y reproducción o la simplicidad de sus características biológicas, que hacen posible una descripción completa de ellas, como la descripción genómica de *C. elegans* o el sistema nervioso en *Lymnaea stagnalis*. Además, algunas especies seleccionadas fueron un campo principal de estudio en las últimas décadas, por lo que hay una gran cantidad de literatura para cada una, incluso en diferentes campos. Además, a pesar de la simplicidad de estos sistemas, su sistema nervioso sigue siendo capaz de generar actividad neuronal secuencial robusta, comportamiento automático e incluso procesos de aprendizaje.

Aparte de los posibles avances en la ciencia desde un punto de vista productivista, los modelos de invertebrados también pueden cerrar la brecha entre recursos y ciencia, permitiendo que los laboratorios y países de bajos ingresos *hagan* ciencia. Estos modelos animales suelen ser más baratos de obtener y mantener, y generalmente hay posibilidad de criar colonias propias. Esto hace que su uso sea ampliable y rompe algunas barreras económicas en la ciencia, donde los países de altos ingresos suelen centralizar la producción científica con fuertes convenciones (Castillo & de la Guardia, 2017; Stephan, 2015).

***Lymnaea stagnalis*, el gran caracol de estanque**

En esta tesis, exploramos el sistema nervioso del gran caracol de estanque, *Lymnaea stagnalis* (ver Fig. 2.12). Este molusco ha sido un caso importante de estudio desde finales del siglo XX, cuando se utilizó ampliamente para estudiar procesos neurobiológicos y el funcionamiento del sistema nervioso. Este esfuerzo de su estudio durante de años ha resultado en una descripción detallada de los ganglios bucales, incluyendo las tres principales interneuronas que lo conforman (B. Y. P. R. Benjamin et al., 1979; Benjamin et al., 1989; Brierley et al., 1997; Rose & Benjamin, 1979) y las neuronas modulatorias que influyen en la actividad de la CPG como las neuronas SO y CGC en la ganglia

cerebral (Kemenes et al., 2001; McCrohan & Benjamin, 1980; Rose & Benjamin, 1981). Además de los ganglios bucales, otras neuronas en diferentes ganglios también están bien identificadas, con características específicas como el acoplamiento eléctrico o neuronas que contienen dopamina como el ganglio parietal derecho (P. R. Benjamin & Pilkington, 1986; Winlow et al., 1981).

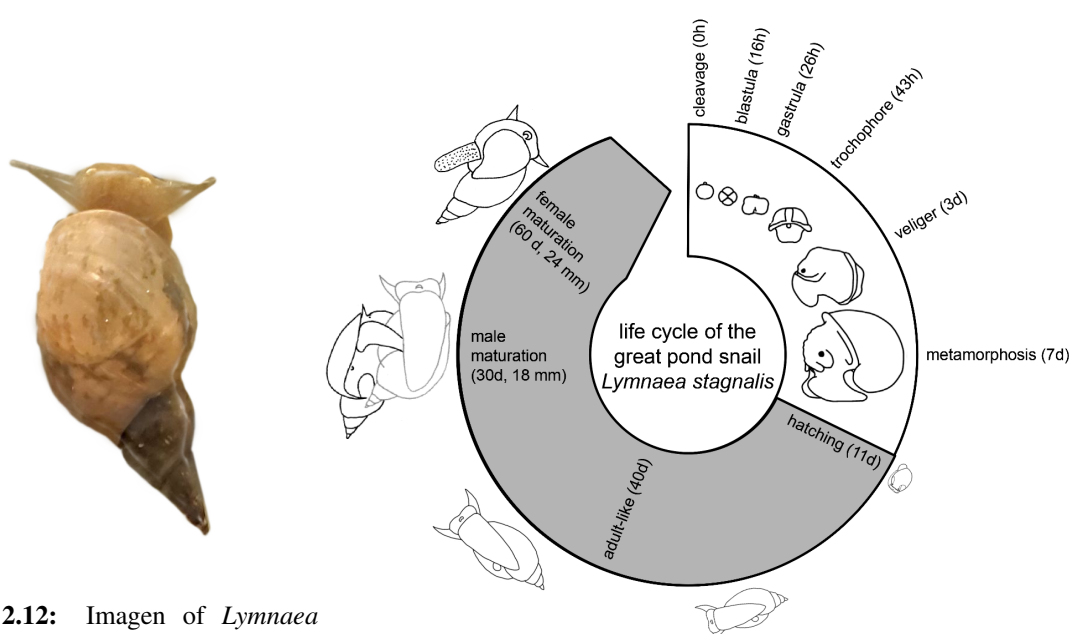


Figure 2.12: Imagen de *Lymnaea*

Stagnalis

The unlimited potential of the great pond snail, *Lymnaea stagnalis*
Fodor et al. eLife 2020;9:e56962 <https://doi.org/10.7554/eLife.56962>

Figure 2.13: Represnetación del ciclo de vida de *L. stagnalis*. Figura 2A de Fodor et al., 2020 (Creative Commons license).

Además de estos estudios, ha sido clave en otros campos como el huésped-parásito o la edición del genoma. Este último campo se debe al ciclo de vida corto y bien estudiado en *L. stagnalis* (ver Fig. 2.13), así como a la facilidad para criarlos en laboratorio, sin perder sus principales características a lo largo de las generaciones (Noland & Carriker, 1946). Las grabaciones y análisis en este trabajo están enmarcados en el estudio de la actividad neuronal en su sistema nervioso central (SNC). El SNC de *L. stagnalis* está compuesto por 11 ganglios que conforman el sistema: pares simétricos de ganglios bucal, pedal, cerebral, pleural y parietal, y un solo ganglio visceral (ver Sec. 4.1). Nos centraremos especialmente en su circuito CPG alimentario, que mediante una combinación distribuida de neuronas motoras e interneuronas ubicadas principalmente en los ganglios bucales y cerebrales, produce un patrón rítmico de movimiento que permite la alimentación en tres fases (protracción, raspado y deglución). Además de este estudio del CPG, trabajaremos en las neuronas gigantes ubicadas en el ganglio parietal derecho (RPG), mejorando la actividad de alto voltaje (hasta 80mV) y lenta (30 a 100 ms por pico) para analizar en detalle la dinámica del potencial de acción.

2.5 Estimulación neuronal

2.5.1 Técnicas de estimulación

La estimulación neuronal ha sido un aspecto esencial en el estudio de la dinámica neuronal, permitiendo la modulación del sistema nervioso para explorar, reproducir y alterar su dinámica para su estudio. Hay varias técnicas para producir la estimulación, que podríamos clasificar en químicas –utilizando componentes químicos para bloquear/mejorar los mecanismos neuronales–, eléctricas –inyectando corriente en la membrana celular o los nervios– u ópticas –donde se estimulan neuronas o circuitos a través de un proceso de iluminación. En esta tesis, nos centraremos en las dos últimas. En las técnicas eléctricas, desde las primeras aplicaciones de electrofisiología por Neher and Sakmann, 1976 y la posterior aparición de la técnica de *patch-clamp* Hamill et al., 1981, se han desarrollado numerosas técnicas diferentes para distintos sistemas. El *voltage-clamp* y el *patch-clamp* modificaron el paradigma en la fisiología y la medicina básica en el estudio de la dinámica de la membrana celular con un detalle excepcional que todavía hoy dirige rangos de grabación y estimulación precisos (Hamill et al., 1981). A la técnica de *voltage-clamp* le siguieron variaciones como el *dynamic-clamp*, que mejora las posibilidades de electrofisiología combinándolo con las posibilidades de computación a través de un protocolo de bucle cerrado en tiempo real (Nowotny & Varona, 2022). Esto permite implementar algoritmos específicos para intervenir en la actividad neuronal y probar diferentes enfoques (Chamorro et al., 2012). En cuanto a la estimulación óptica, una técnica novedosa y ampliamente utilizada es la optogenética, que mediante la modificación genética de los animales, hace que las neuronas sean reactivas a la luz y ha tenido grandes logros en las últimas décadas utilizando tanto para la estimulación como para la exploración y visualización de la actividad (Chen et al., 2022). Otro ejemplo aún en estudio es el láser infrarrojo cercano, una técnica novedosa que se explorará en detalle a lo largo de esta tesis. Esta técnica ha demostrado su potencial para la estimulación neuronal en diferentes sistemas como el hipocampo (Liang et al., 2009), ganglios espinales en la cóclea (Barrett et al., 2018; Brown et al., 2020; Goyal et al., 2012) y otros sistemas (Begeng et al., 2022; Cayce et al., 2014; Shapiro et al., 2012).

2.5.2 Neuromodulación y su necesidad para aplicaciones clínicas

Más allá de la necesidad de la estimulación neuronal en la investigación básica para comprender y explorar la señalización y dinámica del cerebro, hay un impacto social directo para la estimulación neuronal en aplicaciones clínicas. En este contexto, la neuromodulación es un área de la medicina que involucra muchas especialidades y que puede definirse como "la ciencia de cómo las interven-

ciones eléctricas, químicas y mecánicas pueden modular las distintas funciones del sistema nervioso [y es] inherentemente no destructiva, reversible y ajustable" (Krames et al., 2009). Este campo es tan importante debido a sus posibilidades en el tratamiento de trastornos cerebrales, tanto por estimulación funcional como por la modulación a largo plazo a través de la plasticidad neuronal. La neuromodulación puede clasificarse, según la tecnología utilizada, como invasiva o no invasiva. Las tecnologías invasivas son aquellas que requieren una interacción directa con el sistema vivo, lo que causa daño, por ejemplo, incluyendo la cirugía. Un ejemplo conocido de este tipo es la estimulación cerebral profunda (DBS), esta técnica se ha utilizado de manera efectiva para tratar trastornos del movimiento al estimular eléctricamente el cerebro en ciertas áreas cerebrales después de implantar un dispositivo (Hariz & Blomstedt, 2022; Limousin & Foltynie, 2019). En el caso de la neuromodulación no invasiva, podemos encontrar la estimulación magnética transcraneal (TMS), que mediante campos eléctricos estimula ciertas áreas del cerebro, exitosa, por ejemplo, en el tratamiento de la depresión o el trastorno obsesivo compulsivo (Clarke et al., 2018; Valero-Cabré et al., 2017). Cada tipo de técnica tiene sus propias ventajas, las técnicas invasivas suelen ser más precisas en espacio y tiempo, mientras que las técnicas no invasivas ofrecen más flexibilidad y adaptabilidad a diferentes pacientes y la difusión de la técnica. En este contexto, las técnicas ópticas discutidas para la estimulación en la investigación básica también han aumentado en popularidad para aplicaciones clínicas.

CHAPTER 3

Motivation and Objectives

During this work, we will analyze and explore the neuronal dynamics with a bottom-up approach, focusing on their dynamics. We saw in the state of art the importance of sequential dynamics, and how we can describe this sequentiality at different scales, from milliseconds (ionic channels) to hours or days in terms of behavior or cycles. It is important to study neuronal dynamics at different levels to understand the mechanisms behind information processing and the subsequent outputs. To explore sequential activation at cell levels we will use intracellular recordings of single neurons and CPG circuits of *Lymnaea stagnalis* combined with bursting conductance-based models. In the case of the CPGs we will explore the possible restrictions in the intervals contained cycle-by-cycle. Although this approach has not always been typical in these kinds of studies [nadim_inter-animal_2022](#), the study of the variability and time-intervals cycle-by-cycle can unveil important characteristics of their restrictions (Elices et al., [2019](#)). Bursting activity is a good case of study for this, since it is easier to define the first and last event to conform the time-intervals. In this work, we will discuss the universality of sequential dynamical invariants, showed in the pyloric CPG (Elices et al., [2019](#)), exploring it in the feeding CPG of *Lymnaea stagnalis* in a computational model and experimental recordings. We will explore the restrictions underlying the CPG but also the possible functional role of these restrictions under different cases of activation of the CPG, e.g., feeding initiated by the presence of food or feeding activity initiated even in the absence of food.

On the other hand, we also reviewed in the previous chapter the importance of stimulation techniques to explore the neural dynamics and behavior but also for possible clinical applications. In the second part of this work, we will explore a novel technique for neuronal dynamics modulation: the infrared laser. This optical stimulation has potential for effective modulation of neuronal dynamics, but its exact mode of action is not known yet. There are different candidates proposed to be altered in the process of the signal modulation, such as calcium channels, capacitance or long-term process as mi-

CHAPTER 3: MOTIVATION AND OBJECTIVES

tochondria modulation, as well as different sources for the effect, as photo-thermal or photo-chemical effect. During this work we will characterize its effect in single neurons combining experimental and theoretical approaches to narrow down the possible candidates and the source of the effect. We will also design a novel stimulation technique for closed-loop stimulation by designing and testing a new activity-dependent protocol to predict spikes and stimulate at different stage of the action potential generation.

In summary the objectives of this thesis are:

1. Explore the sequential nature of neuronal dynamics
2. Analyze the feeding CPG of *Lymnaea stagnalis* to test the universality of sequential dynamical invariants.
 - (a) Characterize the invariants cycle-by-cycle in the bursting model.
 - (b) Analyze intracellular recordings with spontaneous activity and with different rhythm initiation stimulations.
3. Study the restrictions of variability in the reproduction of neural models and circuits.
4. Discuss the possible functionallity of sequential dynamical invariants in robotics.
5. Test the capability of Near-infrared laser stimulation to modify neural activity.
 - (a) Characterization of the effect in the spike waveform dynamics.
 - (b) Analysis of its stimulatory action.
6. Study the possible candidates underlying the effect in model simulation.
7. Design and implementation of a new technique for the stimulation in closed-loop.

The sequential dynamics explored in the first part of this thesis provide foundational insights into the intrinsic timing mechanisms that govern neural processes. Understanding these sequential patterns at the level of CPGs and single neurons allows us to identify universal principles that can be applied to broader neural circuits and behaviors. By exploring novel modulator techniques, as near-infrared laser stimulation, we bridge the gap between neural dynamics and the necessary modulation techniques. Also, will allow the precise dissection of sequential activation at ionic-channels by the activity-dependent delivery.

CHAPTER 4

Materials and Methods

This chapter will cover the common ground of the materials and methods applied in this thesis and in the results exposed for chapters 5 and 6. The methods here presented will be complemented with a specific version of the methods in those two chapters.

4.1 The neural system of *Lymnaea stagnalis*

The neural system of *Lymnaea Stangalis* (the great pond snail) is shown in Fig. 4.2. As in some other mollusks, e.g. *Clione*, the neural system is conformed by several ganglia, each of them controlling (mainly, but not exclusively) some specific function of the snail. Figure 4.2 shows a labeled image of the different ganglia in this system. All ganglia in the neural system are paired and distributed symmetrically, except from the visceral ganglion (unique) and the parietal, that although symmetrical, the right parietal is larger than left parietal ganglion (see 4.2). All ganglia are interconnected by nerves (grey stripes in the image). As mentioned before, each ganglion has an associated behavioral task in the snail. From top to bottom: we find the buccal ganglia (upper pair), which control the buccal muscle involved in the processes of open-rasp-swallow, known as the feeding cycle, initiated by a CPG circuit contained in these ganglia. The two cerebral ganglia (right below) are involved in the activation and modulation of many circuits and processes, including the modulation from specific neurons in all ganglia. Located on the sides of the diagram, the pedal ganglia control the snail pedal movements as crawling or swimming, and they are originally joined. The pleural ganglia, which contain sensory neurons, are connected to the mantle. And finally, at the bottom of the diagram, we find the parietal ganglion, involved in the control of the gill (respiratory organ) and the olfactory organ, and the visceral ganglion, connected to organs such as the intestine, the heart, and part of the genital system.

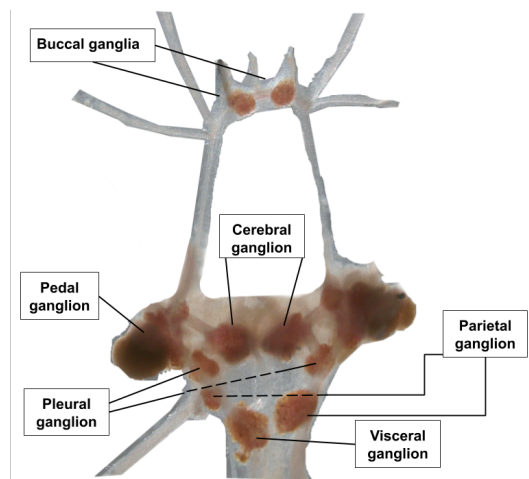
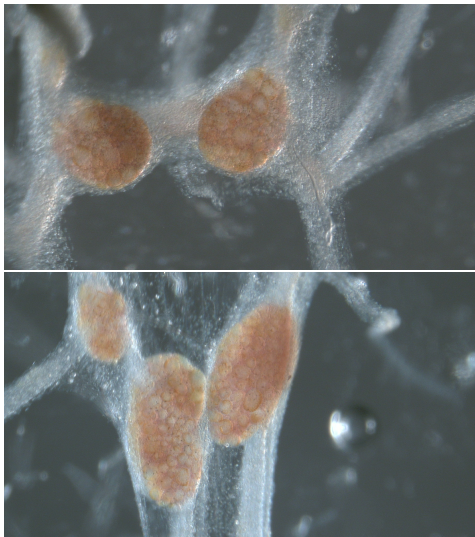


Figure 4.2: *L. stagnalis* nervous system diagram

Figure 4.1: *L. stagnalis* buccal ganglia (top) and representing all ganglia.
parietal ganglia and visceral ganglion (bottom).

Neuronal recordings showed in this work are from the CPG in the buccal ganglia in chapter 5) and right parietal ganglia, containing large neurons with tonic firing and a giant electrical couple cell to the visceral ganglia in chapter 6). Both ganglia are showed in detail in figures 4.1.

4.2 Feeding CPG in *L. stagnalis*

Lymnaea feeding rhythm

The feeding activity of the *Lymnaea*, concerning the buccal mass, is classified in three main steps: Rest, protraction, rasp and swallow. This sequence of buccal movements in the snail is generated by the motor neurons distributed in the ganglia. Each of these phases is leaded by one interneuron from the CPG: N1M, N2v, N3t, and followed by the motoneurons associated to them. This is a complex distributed system where motoneurons do not exclusively follow the interneurons but are also implied in the feeding cycle activation Staras et al., 1998. In this circuit there are also some modulatory neurons implied such as SO neuron (in the same buccal ganglia) or CGC (in the cerebral ganglia).

Hence, an initial resting state, where the CPG as well as the moto-neurons have no activity, may change due to a sensory input. This input, received in the presence of food or during hunger, is handled in the cerebral ganglia generating activity and changing the SO tonic spiking during resting (which was inhibiting the CPG) to a bursting mode, meaning the start of the feeding cycle.

This CPG circuit can be studied in a dissected preparation, since snail's neurons are active for a long time after the isolation of the system. Specially, the CPG rhythm is maintained after its activation and it is generated in an autonomous way by the neurons in the circuit. However, due to the slow dynamics of the system and the nature of the experimental setting there are different ways to initiate the rhythm. In *Lymnaea* literature, several options are proposed to solve this issue. The first solution is stimulating the neurons responsible for the initiation of the feeding rhythm, such as the SO modulator neuron on the buccal ganglia or also the CBC, CVs neurons, located on brain ganglia. Stimulating these cells usually activates the target circuits P. R. Benjamin, 2012. However, the access to these neurons is not always easy and it might be necessary to keep them in constant stimulation. Another option for activation discussed in the literature is applying octopamine. Some neurons in the buccal ganglia are sensitive to octopamine and, as a result, this procedure activates the rhythm Vehovszky et al., 2004. Alternatively, in a semi-intact preparation, it can be applied sucrose to activate the rhythm Straub et al., 2002; Vavoulis, Nikitin, et al., 2007; Vehovszky et al., 2004. Similar to this approach but performing the complete dissection it is the stimulation of the Medium Lip Nerve (MLN), that simulates the lip stimulation. The recordings analyzed in chapter 5 are either spontaneous activity or electrical stimulation in CV1a or SO neuron, or the Medium Lip Nerve (MLN).

4.3 Electrophysiology in *Lymnaea Stagnalis*

In this thesis, intracellular neuronal recordings have been carried out in the mollusk *Lymnaea Stagnalis*. Beyond the advantages of invertebrates discussed in section 1.4 – its easy accessible neural system, the size and resistance of its neurons to electrode impaling, the great pond snail's neural system is detailed described and so it is the feeding CPG which has been the model of study for chapter 5 in this work. Also its slow dynamics, are convenient when studying the sequential evolution of the modulation, as in the case of the laser stimulation described along chapter 6.

The technique followed for the neural activity acquisition was intracellular recordings with filled with 3 M KCl sharp electrodes, In this technique, a glass micropipette penetrates the cell to record its activity, with a minimal damage on the cell, and the membrane potential is then recorded using a DC amplifier (ELC-03M, NPI Electronic, Hauptstrasse, Tamm, Germany). Glass micropipettes were pulled using a Sutter Instruments puller (Model P-97) (see Figure 4.3). Membrane potential was recorded and recordings were acquired at 10 KHz using an A/D board (PCI-625 with a BNC-2090A DAQ device, National Instruments).

To facilitate the access to the cell, the sheath above it was reduced using protease (Sigma XVII)

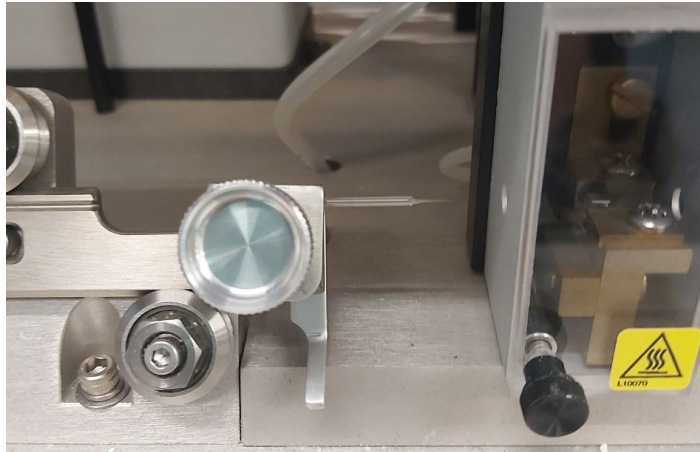


Figure 4.3: Example of a sharp micro-electrode glass in the SUTTER puller.

over the ganglion for ~ 1 min and then washed with fresh saline. In order to record cell signals extra- and intracellularly, it is necessary to have full access to the neural system (see Garrido-Peña, 2022 for more details). The preparation was immersed in a saline solution (in mM: 51.3 $NaCl$, 1.7 KCl , 1.5 $MgCl_2 \cdot 6H_2O$, 4.1 $CaCl_2 \cdot 2H_2O$, 5 $HEPES$, corrected to pH 7.8 with 4 M $NaOH$). All procedures followed the European Commission and Universidad Autónoma de Madrid animal treatment guidelines.

The recordings analyzed in 5.4 were carried out in a equivalent procedure by Michael Crossley in the University of Sussex.

4.4 Conductance based models

For the theoretical analyses in this work, there have been used simulations of conductance-based models. As discussed in section 1.3, these models are based on a specific combination of ionic channels with a dynamic dependent on time that reproduces the Voltage value in the membrane at each time instant. There are many types of models and descriptions, depending on the specific combination of channels. Models used in this work, for both chapters 5 and 6, are description of neurons in *Lymnaea stagnalis* for the neurons in the feeding CPG in the buccal ganglia –SO, N1M, N2v, N3t, (Vavoulis, Nikitin, et al., 2007) and for a neuron in cerebral ganglia, CGC (Vavoulis et al., 2010). The first one is a detailed description of the CPG circuit with a combination of two-compartment neurons and a gradual synapse, that allows sufficient flexibility in the circuit to induce variability in the model –this will be discussed in detail in section 5.3. The second model simulates a tonic firing and shoulder shape spike waveform, similar to the activity in some neurons in the right parietal ganglion characterized in chapter 6.

4.4.1 Feeding CPG model

The Vavoulis et al. description of the individual neurons considers a two-compartment model to represent the soma and the axon as differentiated structures coupled by an axial resistance Vavoulis, Straub, et al., 2007b. This separation of the soma and the axon is used to regulate the interaction between the fast and slow dynamics in the model. The slow dynamics are located the soma, whereas the fast dynamics are included in the axon compartment. This distributed formalism is represented in Fig. 4.4a., where each circle represents either soma or axon, containing the different ionic currents for each one. The description of the voltage dynamics is provided by equations (4.4.1) and (4.4.2) for soma and axon compartments, respectively:

$$\tau_m \frac{dV_S}{dt} = i_{inj} - i_{L,S} - i_X - i_{ec,S} - i_{syn}, \quad \text{with} \quad i_X = [i_{ACh}, i_{NaL}, i_T] \quad (4.4.1)$$

$$\tau_m \frac{dV_A}{dt} = -i_{L,A} - i_{NaT} - i_K - i_{ec,A} \quad (4.4.2)$$

Here we follow the notation of Vavoulis, Straub, et al., 2007b where τ_m represents the time constant of the membrane (in ms) given by the ratio of the membrane capacitance (in nF) and the leakage conductance (in μ S). In equations 4.4.1 and 4.4.2, i variables (given in mV) are the product of the corresponding currents (in nA) times the passive input resistance given in $M\Omega$.

The soma compartment contains a slow current I_X whose ionic nature depends on the specific CPG neuron described (see Fig. 4.4a.). Thus, I_X represents one channel, either I_{ACh} , I_{NaL} or I_T , responsible of the specific slow dynamics associated with neurons N1M, N2v and N3t, respectively. Along with the slow ionic channel and the leakage channel $I_{L,S}$, the soma compartment also receives the synaptic current I_{syn} and the injection current I_{inj} . All currents are explained in detail below.

On the other hand, fast channels are part of the axon compartment: a fast inactivating sodium current I_{NaT} and a delayed rectifier potassium current I_K . These channels, along with the axon leakage channel $I_{L,A}$ follow the definition in Hodgkin and Huxley, 1952a model.

The model cells as described above are not endogenously bursters so to achieve bursting activity, a distinct constant value of i_{inj} is applied to the cells.

The CPG topology scheme is shown in Fig. 4.4, where the connections between neurons are represented by dashed or solid lines, depending on whether the connection is slow or fast, respectively, and filled or empty circles at their end denoting the direction and the effect on the postsynaptic neuron: excitation (empty circles) or inhibition (filled circles). Individual neurons following the previous de-

CHAPTER 4: MATERIALS AND METHODS

scription are connected by graded synapses, defined by equations 4.4.3-4.4.6 (Vavoulis, Straub, et al., 2007b). The differential point of a graded synapse is that it is dependent on voltage values and time, many synapses models used are just dependent on a trigger voltage value, that activates the synapse (see chapter 1.3.1 for details). This model of synapse allows dynamical adaptation of neurons in the circuit to maintain the rhythm despite the variability.

$$i_{syn} = \sum_j \gamma_{syn,j} s_j (V_S - E_{syn,j}) \quad (4.4.3)$$

$$\frac{ds_j}{dt} = \frac{r_j - s_j}{\tau_{syn,j}} \quad (4.4.4)$$

$$\frac{dr_j}{dt} = \frac{r_{\infty,j} - r_j}{\tau_{syn,j}} \quad (4.4.5)$$

$$r_{\infty,j} = \frac{1}{1 + e^{(-40 - V_{prev_S})/2.5}} \quad (4.4.6)$$

where index j runs over all presynaptic neurons and $\gamma_{syn,j}, E_{syn,j}, \tau_{syn}, V_{prev_S}$ are the product of input resistance and maximal synaptic conductance, the synaptic reversal potential, the synaptic time constant and the presynaptic potential, respectively.

The 3 inter-neurons described in this circuit have different waveform shapes, determined by their corresponding ionic channel and the axon connectivity, in Fig. 4.5 there is an example of a simulation with all neurons in the circuit. First, N1M voltage characteristics are provided by an acetylcholine sensitive channel ($i_{ACh} = 200 * p^3 * (V_S + 30)$), which causes the gradual spiking frequency increase as well as the visible plateau, i.e., the slow wave is sustained before hyperpolarization. On the other hand, N2v has a slowly inactivating sodium channel ($i_{NaL} = 2 * p^3 * q^3 * (V_S - 55)$), which causes the slow depolarization in this neuron. N2v neuron has a lower spiking frequency caused by the conductance value given for the axial g_{ec} linking the two compartments, which is much lower in this cell. Finally, the N3t neuron has the particularity of a post inhibitory rebound, which generates an initial fast spiking followed by a decrease in the firing rate as the burst evolves. This latter property is caused by a low-threshold calcium channel ($i_T = 3.27 * p^3 * q * (V_S - 80)$). SO neuron has no I_X channel (in contrast to N1M, N2v and N3t neurons) so its activity is the result of the combination of the common ionic channels in the axon and the soma.

CHAPTER 4: MATERIALS AND METHODS

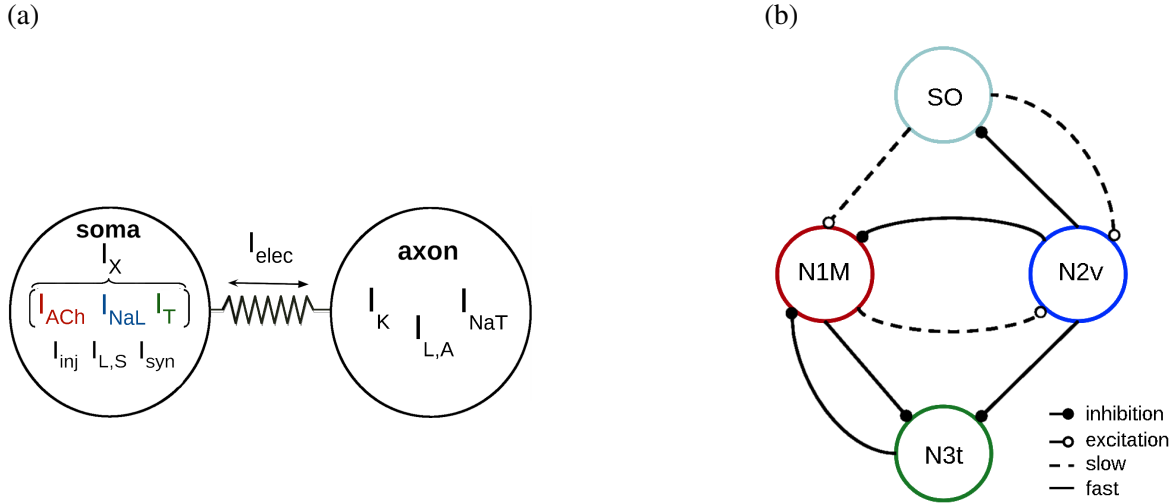


Figure 4.4: **Panel (a).** Ionic channel distribution in the two-compartment description for the individual neurons in the Vavoulis et al. model used in this study. At the soma: I_{ACh} , acetylcholine ionic channel; I_{NaL} , slowly inactivating sodium ionic channel; I_T , low-threshold calcium current; I_{inj} , injected current; $I_{L,S}$, leakage current in the soma; I_{syn} , synaptic current. At the axon: I_{NaT} , fast inactivating sodium current; I_K , delayed rectifier potassium current; $I_{L,A}$, leakage current in the axon. The color for each I_X current represents the CPG neuron that includes it at the soma, N1M, N2v and N3t, respectively. **Panel (b).** Connection scheme for the *Lymnaea* feeding CPG circuit model. The colors indicating each neuron in the circuit match those in the representation of their corresponding somatic membrane potential traces in section 4.4.1.

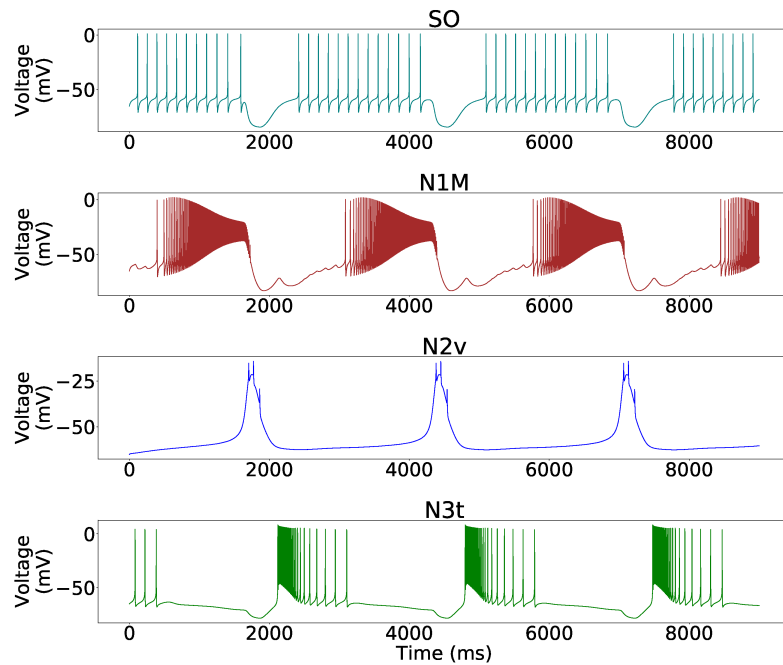


Figure 4.5: Triphasic feeding rhythm as produced by the circuit CPG model described in Fig. 4.4. In this simulation, i_{inj} values applied to each neuron are 8.5, 6, 2 and 0 mV, respectively.

4.4.2 CGC neuron model

This model is described by six different ionic channels: Persistent and transient sodium currents (I_{NaP} , I_{NaT}), that primarily drive depolarization and action potential initiation; transient and delayed rectifier potassium currents (I_A , I_D), key for repolarization and contribute to the shoulder shape waveform in this neuron (specially I_D); and a low-voltage-activated and high-voltage-activated calcium currents (I_{LVA} , I_{HVA}), which are crucial for both immediate excitability and long-term plasticity. These channels are described by Eqs. 4.4.7 to 4.4.13.

$$C_m \frac{dV}{dt} = I_{inj} - I_{NaT} - I_{NaP} - I_A - I_D - I_{LVA} - I_{HVA}, \quad (4.4.7)$$

$$I_{NaT} = g_{NaT} m_\infty^3 h (V - E_{Na}), \quad (4.4.8)$$

$$I_{NaP} = g_{NaP} r^3 (V - E_{Na}), \quad (4.4.9)$$

$$I_A = g_A a^4 b (V - E_K), \quad (4.4.10)$$

$$I_D = g_D n^4 (V - E_K), \quad (4.4.11)$$

$$I_{LVA} = g_{LVA} c_\infty^3 d_\infty (V - E_{Ca}), \quad (4.4.12)$$

$$I_{HVA} = g_{HVA} e^3 f (V - E_{Ca}). \quad (4.4.13)$$

Inactivation and activation dynamic variables r, a, n, e and h, b, f are defined by:

$$\frac{dx}{dt} = \frac{x_\infty - x}{\tau_x}, \quad (4.4.14)$$

where $x = h, r, a, b, n, e$ or f and x_∞ and τ_{x_∞} are defined by:

$$x_\infty = \left(1 + \exp\left(\frac{V_H^x - V}{V_S^x}\right)\right)^{-1} \quad (4.4.15)$$

See Supplementary Material in Vavoulis et al., 2010 for more details.

The implementation of this model is available at Neuron library github.com/GNB-UAM/neun (Vavoulis-CGCModel).

Temperature dependence description in the model

To simulate the temperature dependency in the neuronal activity, a Q_{10} factor was incorporated to every dynamical equation in the model (i.e., conductances and activation gates). Q_{10} represents temperature sensitivity in each channel and it was included as a new factor as shown in Eqs. 4.4.16 and

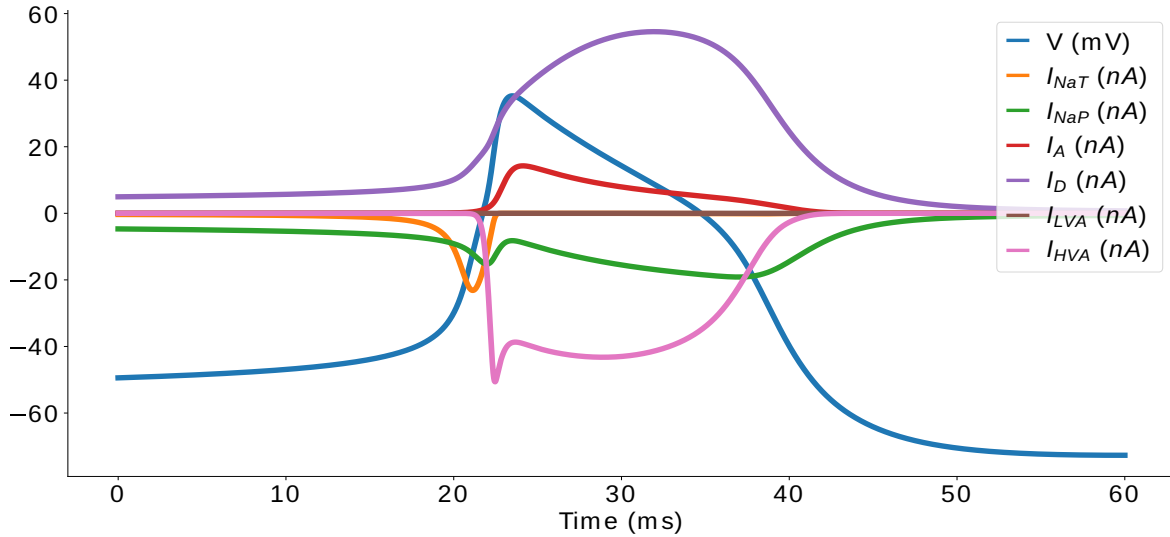


Figure 4.6: Simulation of the CGC-model representing the voltage dynamics during an action potential and the corresponding ionic currents defined in the model ($I_{NaP}, I_{NaT}, I_A, I_D, I_{LVA}, I_{HVA}$). The units in the y-axis are specified in the legend.

4.4.17, with $i = Na_T, Na_P, A, D, LVA, HVA$ for Eq. 4.4.16 and $i = h, r, a, b, n, d, e, f$ for Eq. 4.4.17. The capacitance was also defined as temperature dependent (C_T) with a linear relation to the difference of temperature:

$$g_i(T) = \bar{g}_i Q_{10}^{\frac{T-T_0}{10}}, \quad (4.4.16)$$

$$\phi_i(T) = \bar{\phi}_i Q_{10}^{\frac{T-T_0}{10}}, \quad (4.4.17)$$

$$C_T = c_0 + c_0 \gamma (T - T_0). \quad (4.4.18)$$

where $\bar{g}_i, \bar{\phi}_i, c_0$ are the original values used in the model and $\gamma = 0.05$.

4.5 Neural data analysis

To analyze the recordings of intracellular signals and the outputs of the models simulations, we relied on the detection of single events, mainly spikes and then we either defined time-intervals for the CPG rhythm or analyze each single spike based on metrics as in chapter 6. The detection of these references allowed us to study the sequentiality of neural dynamics at different time-scales. Also, we focused on each event and cycle, avoiding the averaging of the results, since we consider this hinders information in the activity, such as the sequential activation cycle-by-cycle.

For the study of the time-intervals variability and the presence of sequential dynamical invariants, the spikes of the recordings and model simulation of the bursting activity were detected using the

CHAPTER 4: MATERIALS AND METHODS

change in the derivative along with a voltage threshold condition, i.e., all peaks over a voltage value were considered action potential peaks. Then, bursts were identified from the temporal structure of the spikes, and intervals were characterized by the timing of the first and last spike in each burst. In some recordings this temporal reference was adjusted to the needs of the data available, this will be specified in the corresponding section 5.4.

All intervals defined in section 5.2.1 were defined by the events in the ini and end of the burst, the time-intervals described were characterized as follows:

```

1 ##### SINGLE INTERVALS
2 # on = 0; off = 1
3
4 # off1 - on1
5 def get_burst_duration(data):
6     return np.array([b - a for a, b in zip(data[:, 0], data[:, 1])])
7
8 # on2 - off1
9 def get_burst_interval(data):
10    return np.array([a - b for a, b in zip(data[1:, 0], data[:, 1])])
11
12 # on2 - on1
13 def get_burst_period(data):
14    return np.array([a - b for a, b in zip(data[1:, 0], data[:, 0])])
15
16 ##### PAIRED INTERVALS
17 def get_intervals(d1,d2):
18     if d1.size == 0 or d2.size == 0:
19         return [],[]
20
21     d1d2_interval = np.array([b-a for a,b in zip(d1[:,0],d2[:,0])])
22     d1d2_delay = np.array([b-a for a,b in zip(d1[:,1],d2[:,0])])
23     d2d1_interval = np.array([a-b for a,b in zip(d1[1:,0],d2[:-1,0])])
24     d2d1_delay = np.array([a-b for a,b in zip(d1[1:,0],d2[:-1,1])])
25
26     return [d1d2_interval,d1d2_delay],[d2d1_interval,d2d1_delay]
```

On the other hand, in the recordings and model simulations of the tonic firing activity of large cells in the right parietal ganglia, regarding the stereotyped spike waveform it was enough with a voltage threshold to detect the events in the sequence, and to analyze the waveform after the detection of the events, each one was extended N milliseconds left and right, defining segments of signal that capture the shape of the waveform. The characterization of that waveform was carried by defining

CHAPTER 4: MATERIALS AND METHODS

four metrics: the duration, amplitude and depolarization and repolarization slopes, implemented as follows:

```
1 def get_spike_duration(spike ,dt ,tol=2, thres_val=0.5, max_dur = 5, v_scale=1):
2     spike = spike[~np.isnan(spike)]
3
4     peaks , properties = find_peaks(spike , prominence=1*v_scale , width=20)
5
6     #Warning: this may fail for not centered waveforms
7     if len(peaks)>1: # in case spike has several peaks , gets mid one.
8         mid_peak = np.isclose(len(spike)//2, peaks , atol=10)
9         peaks = peaks[mid_peak]
10    results_half = peak_widths(spike , peaks , rel_height=thres_val)
11
12    try :
13        duration_vals = np.array([ results_half [2][0] , results_half [3][0]])
14        th = results_half [1]
15    except Exception as e:
16        duration_vals = np.array([])
17        th = 0
18
19    if duration_vals.size == 0: #Safety comprobation
20        return (0,0),th
21    else:
22        return (duration_vals [0]*dt ,duration_vals [-1]*dt ),th
23
24 def get_spike_duration_value(waveform , dt , plot=False , v_scale=1):
25     dur_refs,th = get_spike_duration(waveform , dt , plot=plot , v_scale=v_scale)
26     duration = dur_refs [1]-dur_refs [0]
27     return duration
28
29 # Description:
30 #   Receives spike values and return the amplitude value measured as the distance
31 #   between
32 #   maximum and minimum voltage value.
33 # Parameters:
34 #   spike voltage values
35 #   dt time rate
36 # Return:
37 #   amplitude
38 def get_spike_amplitude(spike ,dt , v_scale=1):
39     spike = spike[~np.isnan(spike)]
```

CHAPTER 4: MATERIALS AND METHODS

```

39 mx_value = np.max(spike) #maximum V value (spike)
40 mn_value = np.min(spike) #minimum V value (spike)
41
42 return mx_value-mn_value
43
44 # Description:
45 #   Receives spike values and return the increasing and decreasing slope values at
46 #   the
47 # two points matching a threshold in "the middle" of the spike maximum and
48 #   minimum voltage value.
49 # Parameters:
50 #   spike voltage values
51 #   dt time rate
52 #   n_points: number of points around position to calculate slope
53 #   slope_position: where to calculate slope: defalut value, mid of spike.
54 # Return:
55 # depolarization slope, repolarization slope
56
57 def get_slope(spike ,dt ,n_points=10, slope_position=0.5, plot=False , v_scale=1):
58     spike = spike[~np.isnan(spike)]
59     mid_ps ,th = get_spike_duration(spike ,dt ,thres_val=slope_position , v_scale=
60                                         v_scale)
61     indx1 = int(mid_ps[0]/dt) #From ms to point ref
62     indx2 = int(mid_ps[1]/dt) #From ms to point ref
63
64     scale = int(0.1/dt)
65     n_points *= scale
66
67     n_ms = n_points*dt
68
69     slope1 = (spike[indx1+n_points]-spike[indx1-n_points])/(n_ms*2)
70     slope2 = (spike[indx2+n_points]-spike[indx2-n_points])/(n_ms*2)
71
72     return (slope1 ,slope2)

```

Finally, model were implemented in C++ taking advantage of its computational speed and most analysis where performed in Python3, since it is a frequently used tool and libraries such as Pandas are very effective for data analysis. Scripts used in this work are available at github.com/agarpe/neural-dynamics-utils and all conductance-based models are included in Neun github.com/agarpe/neural-dynamics-utils

4.6 CW-NIR laser

The experimental results presented here were obtained using a continuous-wave (CW) NIR diode laser in single TEM00 operation and 830nm wavelength output (Integrated Optics 0830L-13A-NI-PT-NF).

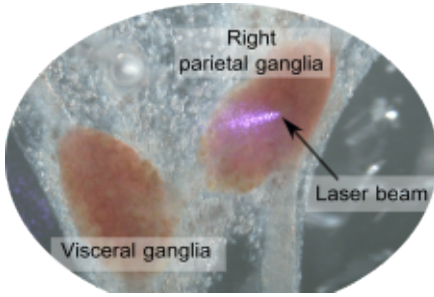


Figure 4.7: Illustration of the laser beam focused on a neuron in the right parietal ganglia.

In Figure 4.8 shows the experimental setup. The diode laser output was coupled to a single-mode optical fiber to efficiently guide the laser beam to the sample. To adapt the divergence of the laser beam to the fiber optic output, an aspherical lenses-collimator (Thorlabs, F280FC-850) was installed. An achromatic doublet with focal length $f=50\text{mm}$ was used to focus the laser beam on the sample (Thorlabs AC127-050-B-ML). The experiments were performed with a laser output power of $\sim 90\text{ mW}$ and a power density over the sample of 146 W/cm^2 . The grazing incidence of the laser beam on the sample created a quasi-elliptical spot, with a minor axis of approximately $34\mu\text{m}$, as shown in Fig. 4.7.

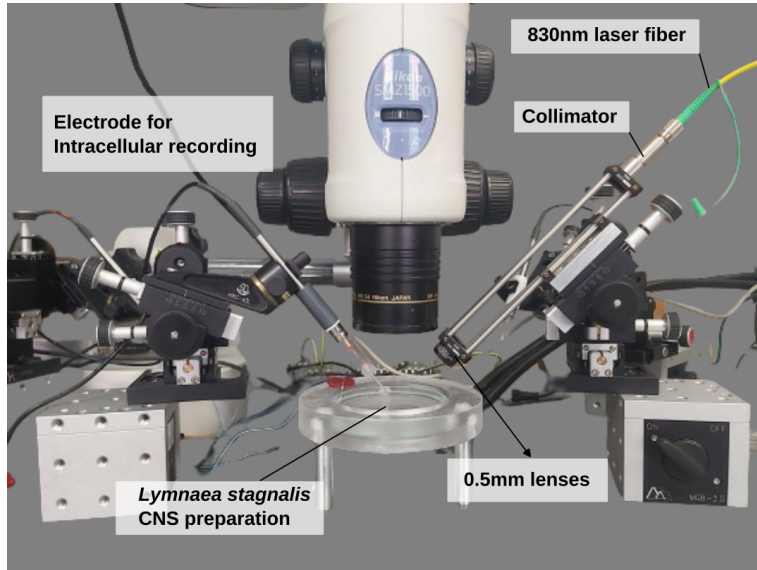


Figure 4.8: Image of the NIR-laser stimulation setup. On the left there is the micromanipulator with the electrode and the glass micropipette for the intracellular recording. In the center of the image in the base there is the preparation of the CNS of *Lymnaea stagnalis*. On the right side the laser fiber is attached to the collimator and at the end of the holder there is the lenses to focus the laser beam. This is also attached to another micromanipulator for a precise focusing.

The laser was attached to a micro-manipulator (Siskiyou MX160), allowing micrometer precision of

CHAPTER 4: MATERIALS AND METHODS

the beam placement over the neuron and optimization of the beam focus. The focusing was performed using a binocular microscope (Nikon SMZ-1500) coupled to a CCD camera (XCAM1080PHA, ToupTek Photonics, Zhejiang, China).

CHAPTER 5

Sequential constrains in CPG circuits: Dynamical invariants

In this chapter we will analyze and discuss the temporal constraints in the feeding CPG circuit of *Lymnaea stagnalis* previously reported in the pyloric CPG of *Carcinus maenas*. We will address this research by computational models and experimental recordings to analyze the phenomena of sequential dynamical invariants from spontaneous activity and different stimulation scenarios. We will also discuss the need of models able to simulate the intrinsic variability of neural activity without stochastic inputs and the possibility to explore the functional role of sequential dynamical invariants into effective robotic locomotion.

5.1 Introduction

Although often disregarded in many experimental and theoretical studies, neural sequences are key elements of brain activity which, in many cases, have a direct relationship to behavior (Buzsáki & Tingley, 2018; Elices et al., 2019; Hahnloser et al., 2002; Paton & Buonomano, 2018; Rabinovich & Varona, 2018; Venaille et al., 2005). The study of neural sequences involves the assessment of time references, time intervals and the associated temporal structure of individual neurons, groups of neurons or large neural ensembles, which typically hinder their characterization due to experimental limitations. In this context, Central Pattern Generators (CPGs) are adequate neural circuits to study the generation and coordination of neural sequences.

CPGs are neural structures capable of generating rhythmic activity that involves robust motor sequences in a highly autonomous manner (Hartline & Maynard, 1976; Marder & Bucher, 2001; Selverston et al., 2000). This kind of circuits are found in many different organisms including humans

(Arichi et al., 2017; Dimitrijevic et al., 1998; Pavlidis et al., 2016). CPG neurons have rich intrinsic dynamics and their connections form non-open circuit topologies in which all members of the circuit receive information from at least another member in the ensemble Huerta et al., 2001; Selverston et al., 2000. This favors rhythm coordination through closed-loop computation and endows CPGs with the ability to produce robust yet flexible rhythms where intervals building the sequences can be adapted in different behavioral contexts (Elices et al., 2019). In Fig. 5.1 there is an example of the robust sequential generation of bursts in a CPG.

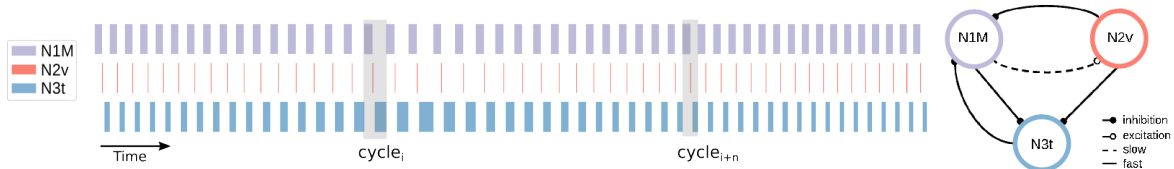


Figure 5.1: Example of robust sequential bursting dynamics in CPGs. Representation of burst duration in 3 neurons in a CPG model, the sequential activation of the three neurons conform cycles (transparent grey boxes in the sequence). The connections between the three neurons are represented in the diagram on the right side of the panel.

The sequence of intervals underlying CPG rhythms present variability in the duration of each cell activation/inactivation, which has been identified in different nervous systems, e.g. see Elliott and Andrew, 1991; Martinez et al., 2019; Reyes et al., 2008. Consequently to the study of variability in cycle-by-cycle sequences, we have recently found sequential dynamical invariants in the form of robust linear relationships between specific sequence intervals and the period in the pyloric CPG of shore crabs (*Carcinus maenas*) (Elices et al., 2019). Dynamical invariants represent constraints of particular sequence intervals in relation to different intervals in the same cycle as the instantaneous duration of the period and build rules for the overall flexibility of the rhythm. It is important to note that not all intervals composing the sequence display such constraints. The presence of invariants in the crustacean pyloric CPG are observed in all control conditions as well as in experiments under the effect of ethanol, which induces irregular rhythms (Elices et al., 2019).

While the existence of phase maintenance and linear relationships between rhythm intervals and the period have been discussed before in convenient animal models, e.g. Grillner and Kashin, 1976; Hooper, 1997; Vavoulis, Straub, et al., 2007a, detailed characterization of cycle-by-cycle variability to understand the existence of these relationships and the corresponding analysis of the universality of robust dynamical invariants are pending in both computational models and living recordings. The observation of this restriction in other animal models, can also support the association of these temporal restrictions to a functional, biological meaning.

During this chapter we will characterize the sequence interval variability in a model of the *L. stagnalis* feeding CPG inducing variability with a ramp current injection, we will also address the issue of variability in models to study this kind of phenomena, and explore and discuss the presence of sequential dynamical invariants in living intracellular recordings as well as their possible functional role by inducing the activity from different methods but also from a practical approach in robotics.

5.2 Methods

5.2.1 Time references, intervals and CPG sequence

The variability study addressed in this chapter is based on the characterization of cycle-by-cycle intervals in the rhythm produced by the model CPG. In our analysis of variability, we assess the presence of linear relationships between the intervals that build the sequence and the cycle-by-cycle period to characterize and unveil similar dynamical invariants as those found in the stomatogastric CPG Elices et al., 2019. The intervals here analyzed can be measured for any three neurons following a robust triphasic rhythm. In this paper N1, N2 and N3 represent the feeding CPG phases, represented in the model by interneurons N1M, N2v and N3t, respectively and in the experimental data by different combinations of moto- and interneurons.

This is illustrated in Fig. 5.2, where single neuron intervals and intervals defined between neurons are depicted and the definition of each interval is as follows:

1. **Burst Duration (BD)**, measured as the time interval between the first and the last spike of the burst (start to end in the trace of a given neuron).
2. **Inter Burst Interval (IBI)**, characterized as the difference between the last spike of a burst and the first one of the next one (end to start in the trace of a given neuron).
3. **Period**, which envelops the bursts from the three neurons, measured as the distance between the first spike of one burst in a neuron and the first spike of the next one on that neuron (start to start).
4. **NeuronX-NeuronY interval**, this interval is measured from the start of the burst of neuron X to the start of the burst of neuron Y (start X to start Y).
5. **NeuronX-NeuronY delay**, being the time lapse between the burst end of a neuron X and the burst beginning of neuron Y. (end X to start Y).

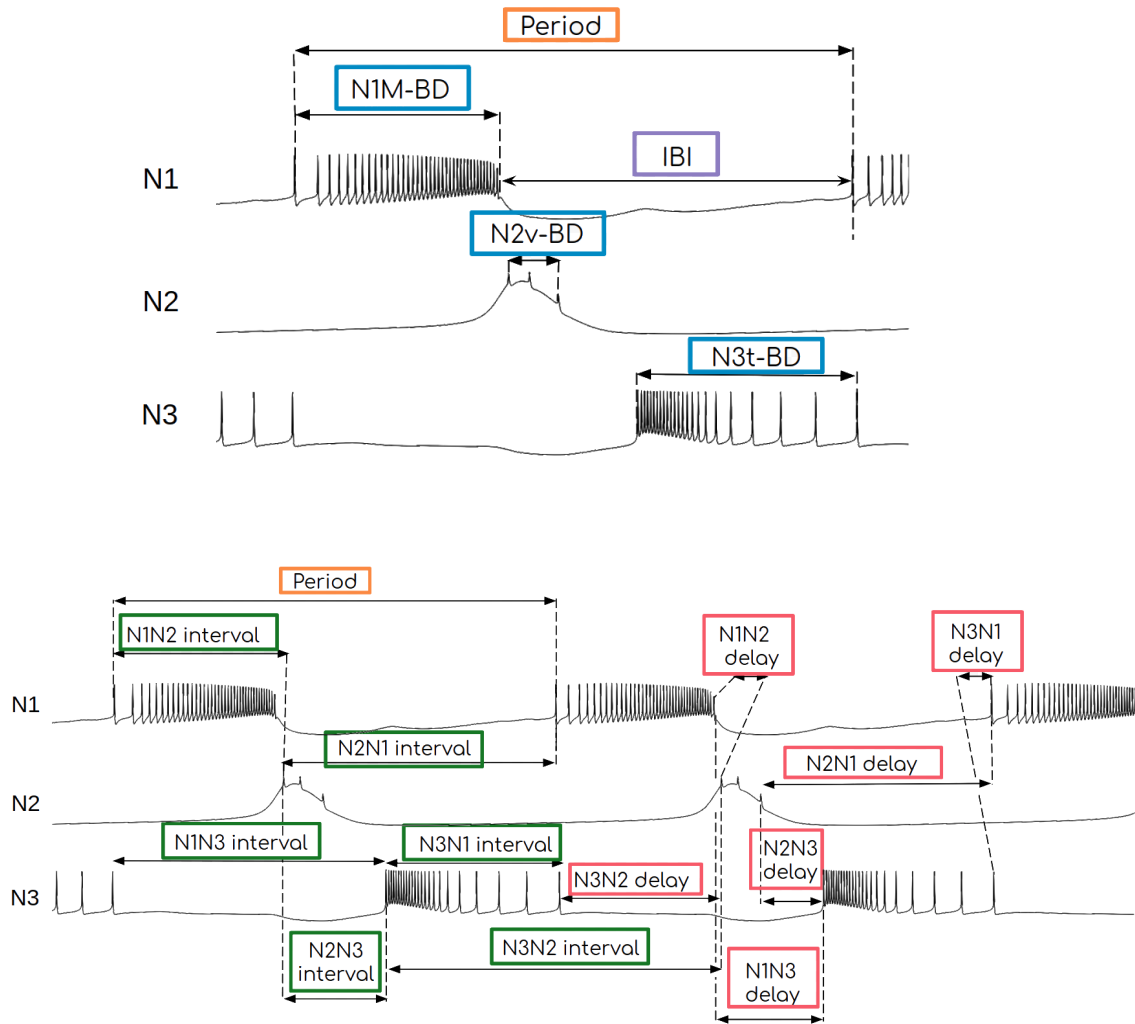


Figure 5.2: Panel A. Individual neuron sequence interval definitions. Each BD label represents the burst duration, defined as the time interval from the first spike to the last spike in the neuron's burst. Period was measured as the interval from the first spike of N1 burst to the first spike of the next N1 burst, covering three phases in relation to the activity of the other neurons. IBI represents the interburst interval, defined as the time from the last spike of a neuron's burst to the first one of the next burst in the same neuron. **Panel B.** Definition of intervals involving pairs of neurons. NXNY interval represents interval from NX start to NY start. NXNY delay represents interval from NX end to NY start. Period was measured from N1 start to N1 start, covering the three phases of the CPG rhythm.

Note that it is also possible to define those intervals only with the references from two neurons. For example, the intervals conformed based on N1 and N3 intervals would be: N1N3 and N3N1 intervals and N1N3 and N3N1 delay. Note that the intervals corresponding to the third neuron are enclosed in the others defined, e.g., in this example N2 burst and N2N1 delay would be contained in N1N3 delay. This consideration allows the characterization of the variability cycle-by-cycle in cases where

it is not possible to define time references for the three neurons in the circuit.

5.2.2 Inducing variability in the model by current injection

The spiking-bursting activity of the model CPG neurons can be modulated by using an additional current injection on each cell, implemented in the i_{inj} term of equation (4.4.1), as performed in many experimental protocols. Depending on the current value applied, the corresponding neuron dynamics changes. While for N2v a change in this injection corresponds to a change in burst frequency (i.e. the number of bursts increases/decreases), for the rest of the neurons in the model a change in i_{inj} affects burst duration for N3t and SO, and the length of the depolarization phase in N1M.

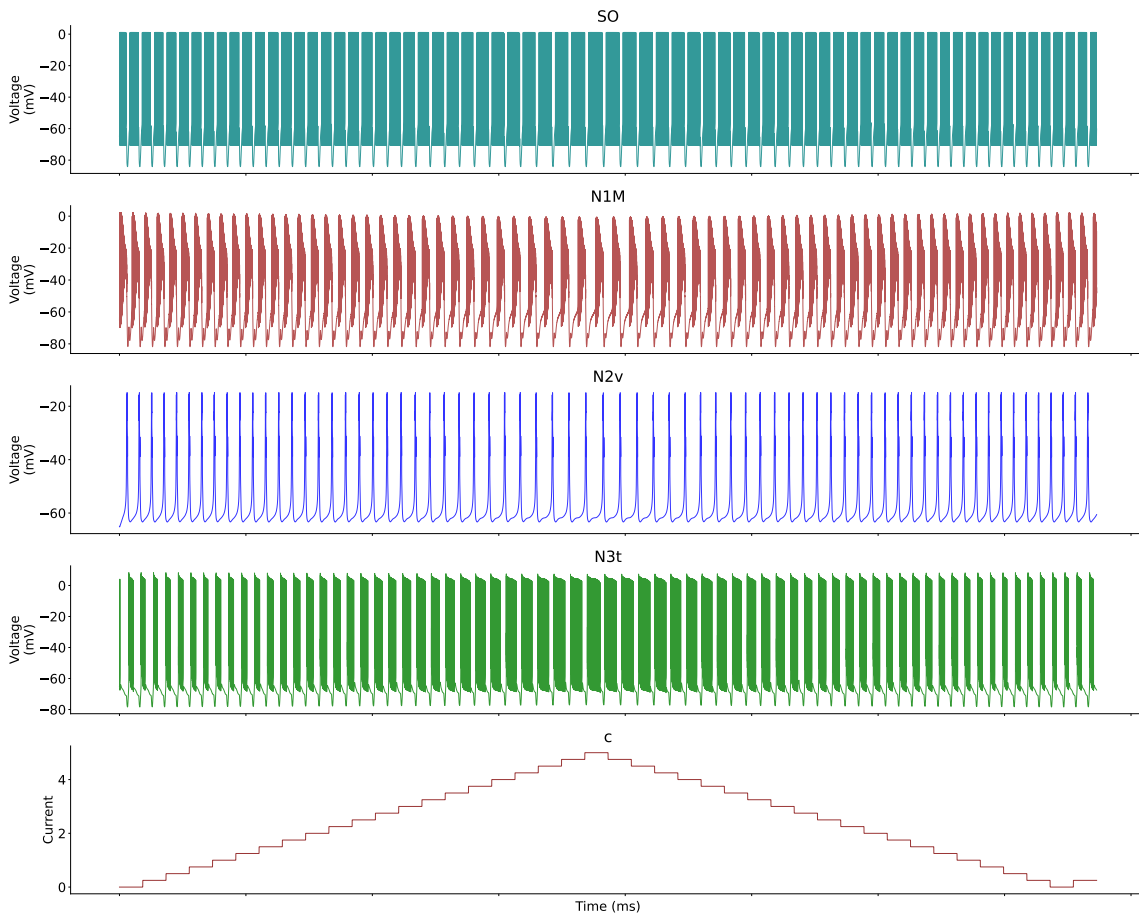


Figure 5.3: Illustration of the CPG activity when a current ramp i_{inj} is applied to N3t. Variability in the sequence intervals was induced by applying two consecutive ramps as the one shown in this figure into different cells.

Whilst the single neuron model descriptions have no intrinsic variability, the effect produced by the modulation of the injected current in each neuron induces variability into the circuit, which allows characterizing the sequence intervals and the period, the associated robustness of the rhythm and the

presence of dynamical invariants. Such stimulation has been used previously in the living circuit, as reported by Elliott and Andrew, 1991. The authors of this work showed that it is possible to activate the feeding CPG with variability caused by current injection into individual cells in the circuit. CPG rhythms obtained under this type of stimulation differ depending on which neuron is being stimulated. To induce variability in the model we used a ramp protocol resulting in circuit time-interval variations as in Fig. 5.3.

By varying the current injected into N1M, its burst duration is kept nearly constant, but its depolarization phase before the spiking activity begins becomes longer. Since N3t is the neuron fitting in the sequence in that phase (see Fig. 4.5), it also increases its burst duration, being the most variable one in the CPG rhythm.

When value i_{inj} is increased on neuron SO, its burst duration becomes longer. Since SO has a modulator effect over N3t and N1M, it also alters the burst duration of these two neurons.

Neuron N3t also shows variable burst duration when an evolving current is injected. When i_{inj} value on N3t is larger, its burst duration increases, elongating the N1M depolarization phase.

Finally, when current is applied to N2v the effect on its burst duration or the burst duration of the rest of the neurons is rather small. However, i_{inj} modulates N2v burst frequency through the hyperpolarization phase.

Therefore, we used a current ramp protocol to induce variability in the CPG model defined as follows: a ramp variable c , which controlled the current injection value ($i_{inj} = c$) on the neuron being stimulated, was increased from a minimum to a maximum value, and then decreased back to the initial value. This was repeated twice in each simulation. The ramp variable was modified with a fixed step value every 4.6 seconds (the approximate duration of two N3t bursts). The minimum and maximum c values were different in each cell and were tuned to generate realistic spiking-bursting behavior. All parameters used for the simulation analyses reported in this paper are summarized in Table 5.1.

Simulations of Vavoulis, Nikitin, et al., 2007 model were implemented in C++. The code of the feeding CPG model implementation is available at <https://github.com/GNB-UAM/CPG-feeding-Lymnaea>. This model was also included in Neun library in a Github repository <https://github.com/GNB-UAM/Neun>. Each simulation had the duration of two consecutive cycles of up and down ramps as the one shown in Fig. 5.3 using the parameters described in Table 5.1. The number of bursts in each simulation was approximately 140 (this number slightly depends on the neuron stimulated). Parameter values such as reversal potentials and synaptic conductances were the same ones specified in Vavoulis, Straub,

Neuron stimulated	<i>i_{inj}</i> value				Ramp values (c)		
	SO	N1M	N2v	N3t			
N1M	8.5	<i>c</i>	2	0	0	10.5	0.5
N3t	9	10	1	<i>c</i>	0	5	0.25
SO	<i>c</i>	10	1	4	8.2	13	0.25

Table 5.1: List of i_{inj} values that yield realistic bursting rhythms for each neuron in the model CPG used in the stimulation protocols reported in this paper. The left section of the table displays the i_{inj} values applied to each neuron (columns) during each simulation condition (rows). Ramp values on the right section refer to the minimum and maximum values of the ramp variable c in each simulation, increasing i_{inj} in the specified step every 4.6 seconds (the approximate duration of two N3t burst) to induce variability.

et al., 2007b.

5.2.3 Experimental recordings and stimulation

The experimental recordings analyzed in section 5.4 were performed by Michael Crossley, University of Sussex, and kindly provided for this work.

Each recording had at least 5 microelectrodes, which allowed to characterize the rhythm based on combinations of different neuron's activity. There are cases of experiments in that section:

- Spontaneous activity: After the isolation of the CNS, the electrodes impaled in the neuron recorded the spontaneous activity in the CPG, with no further stimulation.
- Nerve electrical stimulation: For the activation of the rhythm it is possible to stimulate the median lip nerve (MLN). The data analyzed there was stimulated by a 4V stimulus at 1Hz.
- Neuron electrical stimulation: To modulate the CPG rhythm, SO and CV1a neurons were stimulated (in different experiments) by injecting a constant depolarizing current.

To define each phase, we used different neurons and bursting references, depending on the ones available on the circuit, following intervals definition in table 5.2.

For each recording each phase was defined as follows:

Spontaneous Activity Example 1 N1 phase was analyzed from B1 activity (bursting and depolarization); N2 phase was analyzed from B5 hyperpolarization, which has a strong inhibition from N2v; N3 phase was analyzed from the bursting activity of B8, that replicates the N3t duration.

Spontaneous Activity Example 2 N1 phase was analyzed from B1 activity (bursting and depolarization); N2 phase was analyzed from B1 hyperpolarization, which has a strong inhibition from N2v; N3 phase was analyzed from the bursting activity of B8, that replicates the N3t duration. Since the reference for N2 here coincides with N1 reference, we display here only the intervals corresponding to N1 and N3 phases, since the intervals that correspond to 3 phases, such as N1-N2 delay or N2-N3 delay, either are already represented in the defined intervals or have a duration close to 0 ms.

Spontaneous Activity Example 3 N1 phase was analyzed from B1 activity (bursting and depolarization); N2 phase was analyzed from B5 hyperpolarization, which has a strong inhibition from N2v; N3 phase was analyzed from the bursting activity of B8, that replicates the N3t duration.

Spontaneous Activity SO modulation N1 phase was analyzed from B1 activity (bursting and depolarization); N2 phase was analyzed from B5 hyperpolarization, which has a strong inhibition from N2v; N3 phase was analyzed from the bursting activity of B8, that replicates the N3t duration.

5.2.4 Models with chaotic activity

As we presented in the introduction there are some models that are able to reproduce variability without the introduction of gaussian noise. These models reproduce a deterministic chaos which is usefull to reproduce the biological stochasticity. In this subsection we find the equations of the models used in [5.5](#) to represent variable and non-variable activity.

LP model by Nowotny et al., [2008](#)

The membrane potential of axon and soma compartment, V_{axon} and V_{soma} respectively, are described by

$$\frac{dV_{\text{axon}}}{dt} = \frac{1}{C_a} (-I_{\text{Na}} - I_{\text{Kd}} - I_M - I_{\text{leak,a}} + I_{VV}) \quad (5.2.1)$$

$$\frac{dV_{\text{soma}}}{dt} = \frac{1}{C_s} (-I_{\text{Ca}} - I_{\text{KCa}} - I_A - I_h - I_{\text{leak,s}} - I_{VV} + I_{\text{scale}}(I_{\text{DC}} - I_{\text{offset}} + I_{\text{syn}})) \quad (5.2.2)$$

$I_{\text{offset}} = 2 \text{ nA}$ stems from the residual coupling at the end of the parameter estimation procedure which introduces a current bias due to differences in baseline voltage of data and model (on top of V_{shift}). I_{syn} denotes the total incoming synaptic current. All ionic currents except for the ones mentioned explicitly below are given by

$$I_x = g_x m^p h^q (V - V_x) \quad (5.2.3)$$

where g_x is the maximal conductance of the current, V is the membrane potential of either the axon compartment (I_{Na} , I_{Kd} , and I_M) or the soma compartment (all other currents), and V_x is the reversal potential of the current. The activation and inactivation variables are governed by

Non chaotic model Ghigliazza and Holmes, 2004

The Ghigliazza and Holmes model for motoneurons is described by the following equations:

1. The membrane potential dynamics of a neuron is given by:

$$C_m \frac{dV}{dt} = - \sum I_x + I_{\text{syn}} \quad (5.2.4)$$

where C_m is the membrane capacitance, V is the membrane potential, I_x are the various ionic currents, and I_{syn} is the synaptic current.

2. The ionic currents I_x are typically given by:

$$I_x = g_x m^p h^q (V - V_x) \quad (5.2.5)$$

where g_x is the maximal conductance, m and h are the activation and inactivation variables, p and q are the respective powers, and V_x is the reversal potential of the current.

3. The gating variables m and h are governed by first-order kinetics:

$$\frac{dm}{dt} = \alpha_m(1-m) - \beta_m m \quad (5.2.6)$$

$$\frac{dh}{dt} = \alpha_h(1-h) - \beta_h h \quad (5.2.7)$$

where α_m , β_m , α_h , and β_h are voltage-dependent rate constants.

4. For a central pattern generator (CPG), the model includes a set of coupled differential equations to describe the rhythmic activity:

$$\frac{d\phi_i}{dt} = \omega_i + \sum_j K_{ij} \sin(\phi_j - \phi_i - \psi_{ij}) \quad (5.2.8)$$

where ϕ_i is the phase of the i -th oscillator, ω_i is the intrinsic frequency, K_{ij} is the coupling strength between oscillators i and j , and ψ_{ij} is the phase shift.

5.2.5 Hybrot structure

The experimental paradigm designed in order to test the correct behavior and locomotion of the FLC-Hybrot –FLC stands for Functional Living Circuit– established a real-time closed-loop interaction between the robot and a living pyloric CPG of *Carcinus maenas* Elices et al., 2019. During the experiment, the FLC-Hybrot had to walk through a straight and flat lane, with no obstacles, along which there were interspersed sections with lights and shadows. Neural activity was recorded online from the living circuit and used to modulate the robot movement. At the same time, feedback current was injected into the living circuit when the robot's light-sensor detected a shadow.

Top panel of Figure 5.4 shows an illustration of the experimental setup for the FLC-Hybrot implementation with all its main components. A computer was employed to serve as nexus between both the robot and the biological elements and was in charge of executing a periodic real-time loop (Figure 5.4A), inside of which the following tasks were performed:

1. First, it read the CPG neurons electrophysiological signals from the DAQ device, that at the same came through the amplifiers (Figure 5.4B) after being recorded online from the living preparation (Figure 5.4C).
2. From this acquired data it extracted, online, the duration of the temporal intervals of the cycle-by-cycle CPG activity, which were then sent to the robot's controller via Bluetooth.
3. In the opposite direction, it received the robot's light-sensor data through the same Bluetooth connection.
4. If this data indicated that the robot was located under a shadow at that moment, then it sent feedback to the DAQ device in the form of electric current. This current was injected into the neurons, delivered by the amplifier, altering their behavior.

All these operations were repeated while the robot traversed the trial track (Figure 5.4D). Robot's locomotion was determined by its legs oscillation, so we utilized video tracking tools to capture their movement during the experiment (Figure 5.4E). Two electrodes were used in order to measure the pyloric CPG activity. First, an extracellular electrode picked up all the surrounding neurons' activity. In this signal, the spikes and bursts of the LP neuron were clearly recognizable due to their larger amplitude. One of the PD neurons' membrane potential was recorded using an intracellular

electrode. A second intracellular electrode was used to inject the feedback current into a PD neuron to implement the robotic sensory feedback (Figure 5.4F).

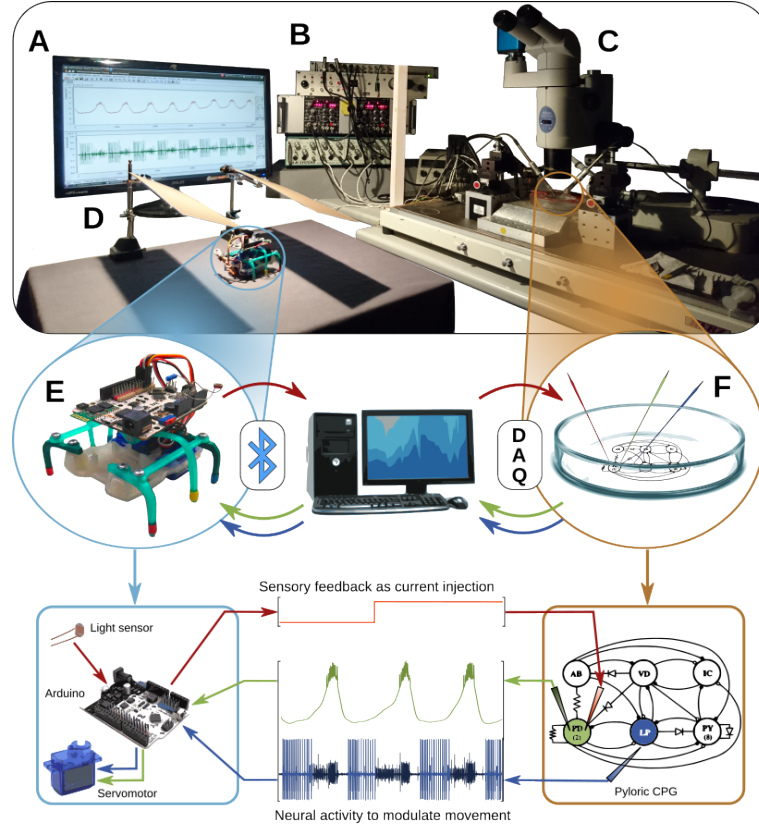


Figure 5.4: Top panel: illustration of the experimental setup for the FLC-Hybot implementation: A) Computer that controls the closed-loop interaction between the living CPG and the robot. B) DAQ and signal amplifiers; C) Microscope; D) Testing track with light and shadows regions. **Middle panel:** detail of the elements of the setup: E) Hexapod robot, receives the neural information from the computer and sends back the sensory feedback through a Bluetooth connection; F) *In vitro* pyloric CPG preparation with three electrodes, one to record extracellular activity from the nerve which includes the activity from the LP neuron (blue), one to record intracellular activity from the PD neuron (green) and another to introduce the feedback current into a PD neuron (red). Electrodes and computer are connected through the DAQ device. **Bottom panel:** detail of the elements of the robot and the preparation. PD neuron (intracellular recording, green trace) and LP neuron (extracted from the extracellular recording, blue trace) behavior is analyzed online by the computer and used to modulate the movement of the robot. Meanwhile, robot's light sensor detects the presence of light or shadow over it and the Arduino board sends that information to the computer, which injects feedback current into the PD neuron (red trace).

5.3 Sequential dynamical invariants in computational models

In this section we will investigate the cycle-by-cycle sequential restrictions found in Elices et al., 2019 in a computational model, the detailed reproduction of the activity allows to study in detail the mechanisms associated to the circuit and the time-intervals relations. We used the feeding CPG model description of Vavoulis, Straub, et al., 2007a, which even though it does not have a chaotic mode, the model is flexible enough to adapt the variability of one of the neurons. Following the current injection protocol defined in section 5.2.2, N1M, N3t and SO neurons in the model were stimulated for our analysis of the sequence interval variability. Using this induced variability we were able to explore the presence of sequential dynamical invariants under different scenarios. The effect on injecting a current ramp on N2v is not reported here since it leads to lower variability than the other cases. In all simulations, we could test the robustness of the rhythm while inducing the external perturbation that evoked variability in the search for dynamical invariants. The results summarized and adapted for this section were published in Garrido-Peña et al., 2021.

First we saw in the simulations is that the model of the feeding CPG faithfully reproduces the activity of the main neurons involved in the generation of its triphasic rhythm (Vavoulis, Straub, et al., 2007b). This includes their waveforms and the relationships between the cycle period and the duration of several intervals reported in (Elliott & Andrew, 1991). Note that, since there was not a description of a chaotic mode, all the rhythms explored here were analyzed from induced stimulation, not by simulating spontaneous activity. This was a restriction when exploring spontaneous activity, since the circuit needed to be altered by one of the neurons, simulating a extended experimental protocol, but still altering the circuit in a predefined way. Also, other phenomena reported in the pyloric CPG experimental work, were there was a "reset" in the inter-cycle dynamics of the dynamical invariants, could not be explored in this model, since the ramp value was progressive (see Appendix Fig. B.1 for a representation of this non-reset output). All this will be illustrated in the following Section 5.4 with experimental recordings and other options to reproduce the functional variability will be discussed in Sec. 5.5

5.3.1 N1M driven variability

N1M neuron is frequently stimulated using ramp protocols in living preparations (Elliott & Andrew, 1991) as it plays an important role in initiating the CPG rhythm. In our case, after applying the current injection protocol into N1M and detecting the spike and burst events for each neuron in the CPG model, all intervals represented in Fig. 5.2 were quantified. We show in Fig. 5.5 the variability

and the correlation between the period and each interval.

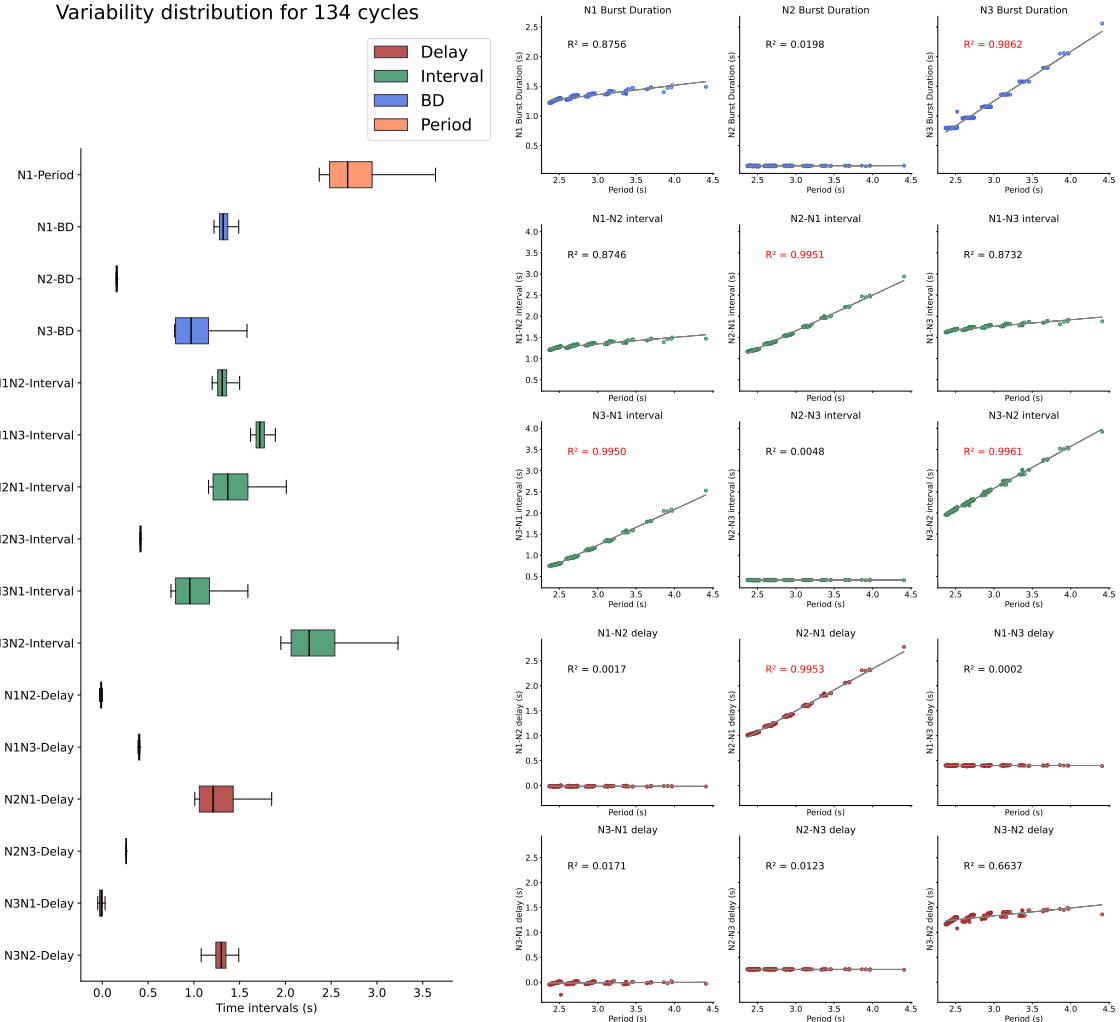


Figure 5.5: N1M stimulation: a) Box-plots of the sequence intervals under N1M neuron stimulation. b) Interval correlations to period for N1M-driven simulation. First row: Burst duration. Second and third row: Two-neuron intervals. Forth and fifth row: Two-neuron delays. Linear relationships are quantified by the R^2 values of the linear regression.

Figure 5.5.a) displays the boxplots of the duration of all sequence intervals defined above. Regarding burst duration of the neurons (N1M-BD, N2v-BD, N3t-BD), we can observe in this figure that the most variable one corresponds to N3t neuron. Furthermore, the derived intervals which cover N3 burst duration are also the ones presenting larger variability (i.e., N2-N1, N3-N1 and N3-N2 intervals and N2-N1 delay). On the other hand, the least variable intervals correspond to the ones related to N2v and N1M burst duration, i.e., N1-N2, N1-N3, N2-N3 intervals and N1-N2, N1-N3, N3-N1, N2-N3, N3-N2 delays. They show a nearly a constant duration during each period.

Figure 5.5.b) plots the cycle-by-cycle measurements of the intervals defined in 5.2 against the period.

The first row displays burst duration intervals, which are the intervals analyzed in Elliott et al. (Elliott & Andrew, 1991) from data obtained in electrophysiological recordings of living neurons, and in Vavoulis et al. from data obtained in model simulations (Vavoulis, Nikitin, et al., 2007). The results shown in this row match those results, being N3t-BD the most correlated to the period, which can be noted by the R^2 value close to one in the linear regression. The other two intervals (N1M-BD and N2v-BD), which were also the least variable, are not strongly correlated to the period.

Likewise, the most variable intervals derived from other time references of the sequence also show a high correlation with the period, i.e., they present dynamical invariants, in this case N2-N1, N3-N1, N3-N2 intervals and N2-N1 delay. The cycle-by-cycle period variability is a consequence of the variability in these specific intervals.

On the other hand, intervals related to neuron N2v and N1M are the least variable. N2v is the one least affected by the global activity of the circuit, in terms of its burst duration. Moreover, some of the intervals are very short, or even negative, since the end of a given neuron's burst overlaps the next one's beginning (N1-N2 and N3-N1 delay). This is the case for N1-N2 and N3-N1 delay (4th row, 1st column and 5th row, 1st column, respectively in Fig. 5.5.b).

5.3.2 N3t driven variability

The stimulation protocol was also applied to N3t neuron. In spite that no previous analysis on injecting a current ramp into this neuron has been reported neither experimentally nor in the feeding CPG computational model, due to the connectivity in the circuit, it can be expected that stimulation of N3t will induce variability in the rhythm. The characterization of the sequence intervals in this case are shown in Fig. 5.6.a) and the correlation analysis is displayed in Fig. 5.6.b).

Results shown in Fig. 5.6.a) indicate that the larger variability is present in the same intervals related to N3t burst duration, as when the stimulation was delivered to N1M. However, in this simulation we observe that N1M had a lower variability while N3t had a higher variability with respect to the previous condition. In contrast, N2v-BD maintained its variability, as well as all the derived intervals containing this burst duration.

Note that N3-N1 delay, which is the interval from the end of the N3t burst to the beginning of N1M burst, shows negative values. This means that neuron N1M started earlier than the end of N3t in every cycle. Whilst this was also present in N1M-driven activity, here the variability of this interval is much higher, leading to a larger overlapping.

Figure 5.6.b) plots each interval duration against the period. As in the previous condition, the dynam-

ical invariants (i.e. intervals presenting a strong correlation to the period) show up in the intervals related to N3t, which were the ones presenting also the highest variability, whereas those intervals that do not participate in dynamical invariants, are the ones related to N1M and mostly N2v (the least variable ones).

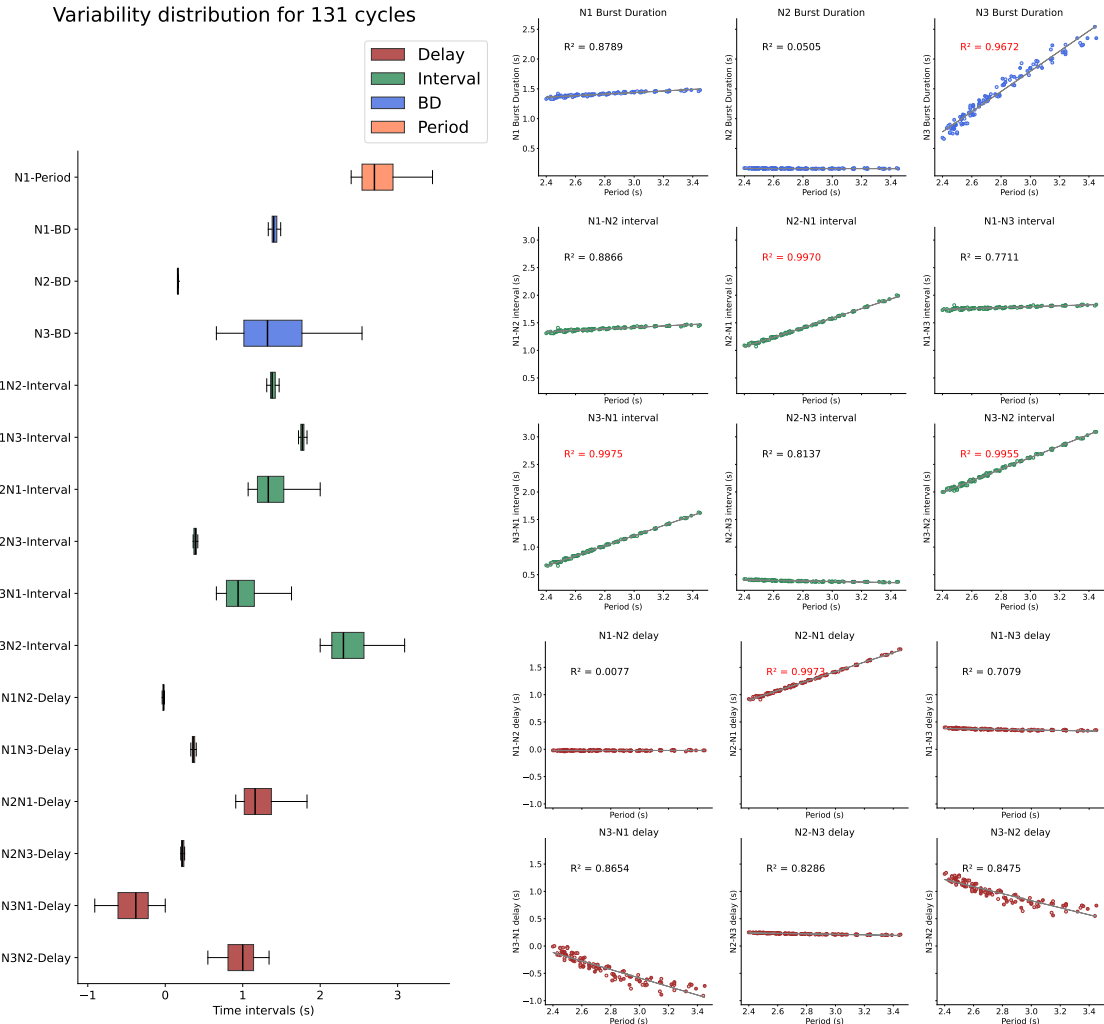


Figure 5.6: N3t stimulation: a) Box-plots of the sequence intervals under N3t neuron stimulation. b) Interval correlations to Period for N3t-driven simulation. First row: Burst duration. Second and third row: Two-neuron intervals. Forth and fifth row: Two-neuron delays.

5.3.3 SO driven variability

The same protocol was implemented with a ramp stimulation applied to SO to induce variability, using the injected current values shown in Table 5.1 for each neuron. Events were detected and all intervals were measured (Fig. 5.2) and their variability was characterized.

Figure 5.7.a) displays the box-plot representing the distinct interval variability. In this case, we found

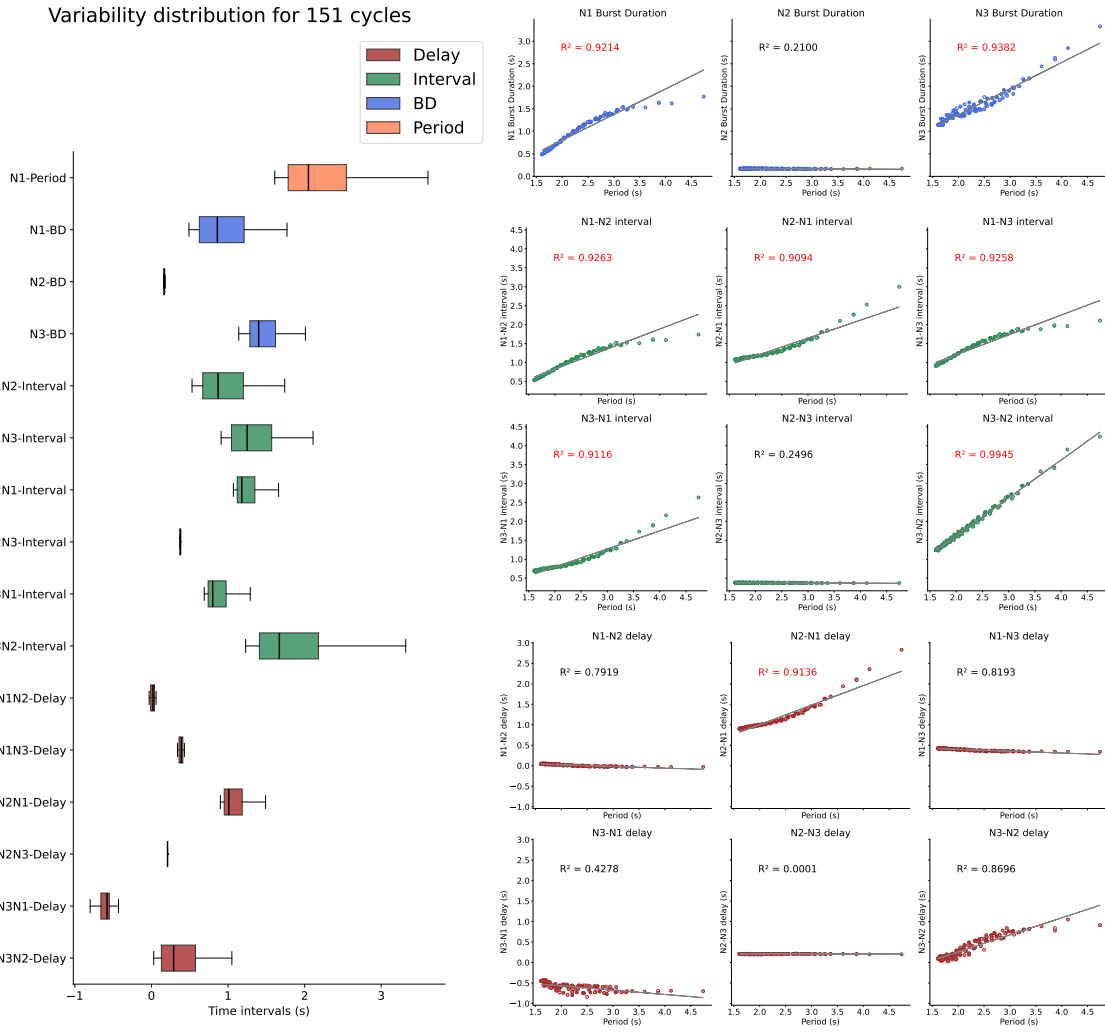


Figure 5.7: SO stimulation: a) Box-plots of the sequence intervals under SO neuron stimulation. b) Interval correlations to Period for SO-driven simulation. First row: Burst duration. Second and third row: Two-neuron intervals. Forth and fifth row: Two-neuron delays.

more intervals showing large variability than in the previous cases. N2v intervals, as it happened in the previous results, show low variability. N1M and N3t neurons show high variability in their burst duration intervals, being N1M even more variable than N3t, as opposed to the previous results when the stimulation was introduced in other cells. All intervals derived from these two neurons have high variability and a similar structure.

Figure 5.7.b) displays the corresponding correlation analysis between all intervals and the period. In this case, we found correlations in the same intervals as before: N2-N1, N3-N1, N3-N2 intervals and N2-N1 delay; which are the intervals related to N3t burst duration. However, under SO stimulation, N1-N2, N1-N3 intervals were also highly correlated to the period. Even the correlation for N3-N2 delay considerably increased in relation to the other stimulation conditions. These intervals are the

ones related to N1M neuron activity, and were also the most variable ones. These results reproduce the experimentally analyzed effects set out in (Elliott & Andrew, 1991), when rhythm and variability was induced by injecting current into a living SO neuron.

Compared to the N1M and N3t stimulation results, there is another difference when driving the rhythm with SO: burst duration is much shorter, so the period and the rest of intervals are consequently smaller. Therefore, when driving the rhythm by SO, the period variability seems to arise from both N3t as well as by N1M.

5.3.4 Time intervals relations cycle-by-cycle beyond period

We saw so far the sequential dynamical invariants in terms of strong linear relationships between the distinct intervals in a cycle and the period, however, studying the relations between all possible combinations between intervals can also show interesting information about the temporal variability distribution in the ongoing activity. In Figs 5.8 to 5.10 there is a representation of all these combinations of the defined intervals for the three scenarios of induced variability (current in N1M, N3t or SO) showed in this section. In this extended representation of the relations cycle-by-cycle we can see that there are more intervals presenting strong linear relations, besides of the periods. Some of them are intervals that are contained in others, as the case of N1-BD and N1-N2 interval and have similar durations, and so they are more likely to have a strong linear relation between them. However, there are other intervals that, as it is the case of the period, although they share part of the time-interval, they are not correlated, since they are not the variable part, as it is the case of N2-BD with N1-N2. This distinction can help dissect the source of variability and its distribution when an interval is related to the period. Also, the further study of linear relation between some intervals (as N1-BD and N3-BD) that do not share time-interval, can show significant information about the ongoing activity cycle-by-cycle. This representation can also show non-linear relation between the intervals as we can see in some plots in the case of SO (Fig. 5.10), observed in the pyloric CPG in modeling and experimental scenarios (Berbel et al., 2024).

5.3.5 Comparison with two-phase intervals

During this section we analyzed the sequential dynamical invariants in for three phases, but we can also define the intervals for two phases of the neurons, taking as reference for example, N1 and N3. This is the case in the work by Elices et al., 2019, and in the following section we will also use two phases for some of the recordings were the N2 phase was not possible to characterize out of

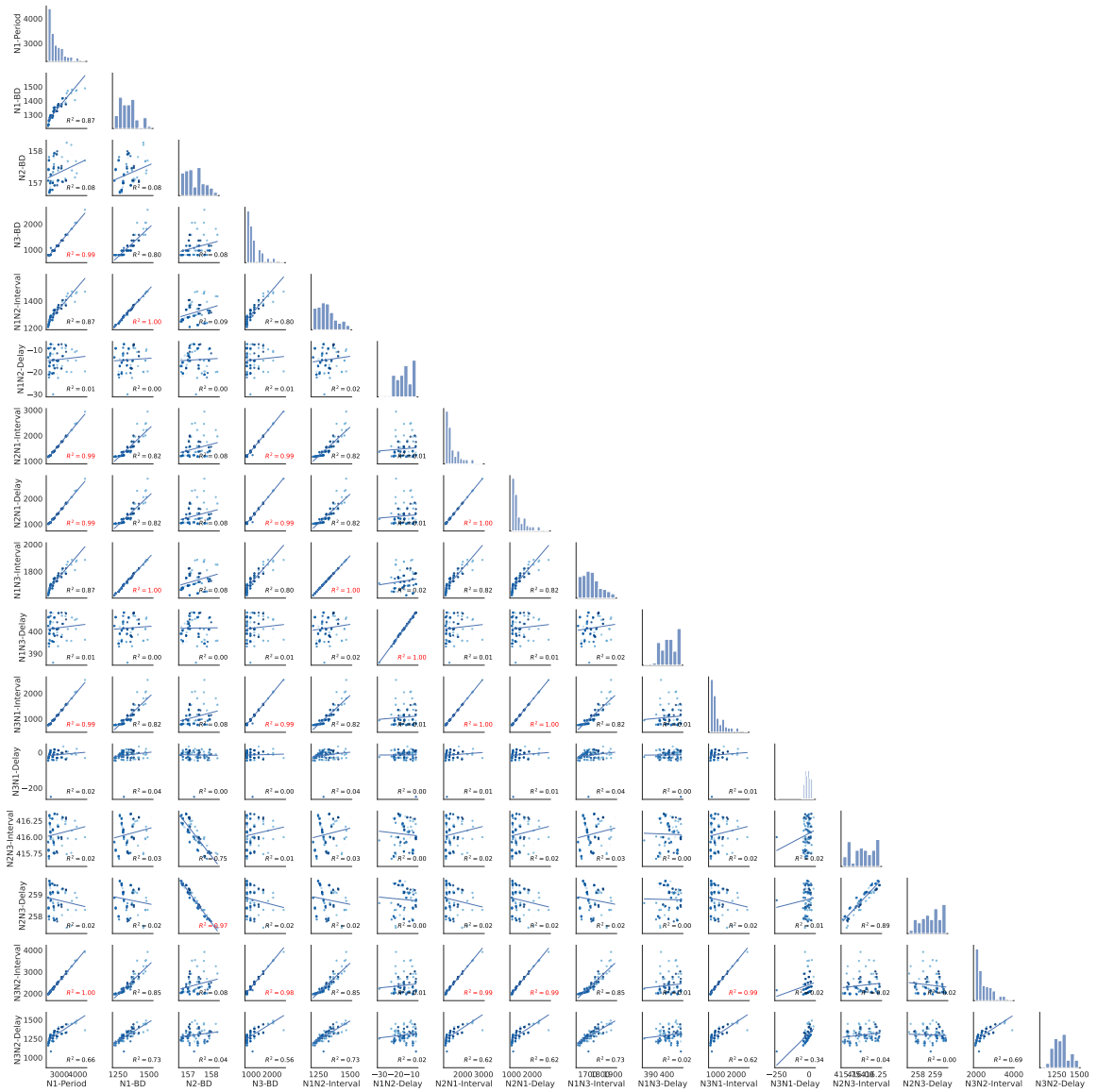


Figure 5.8: N1M stimulation: Pairplot with all possible combination between time intervals within a cycle.

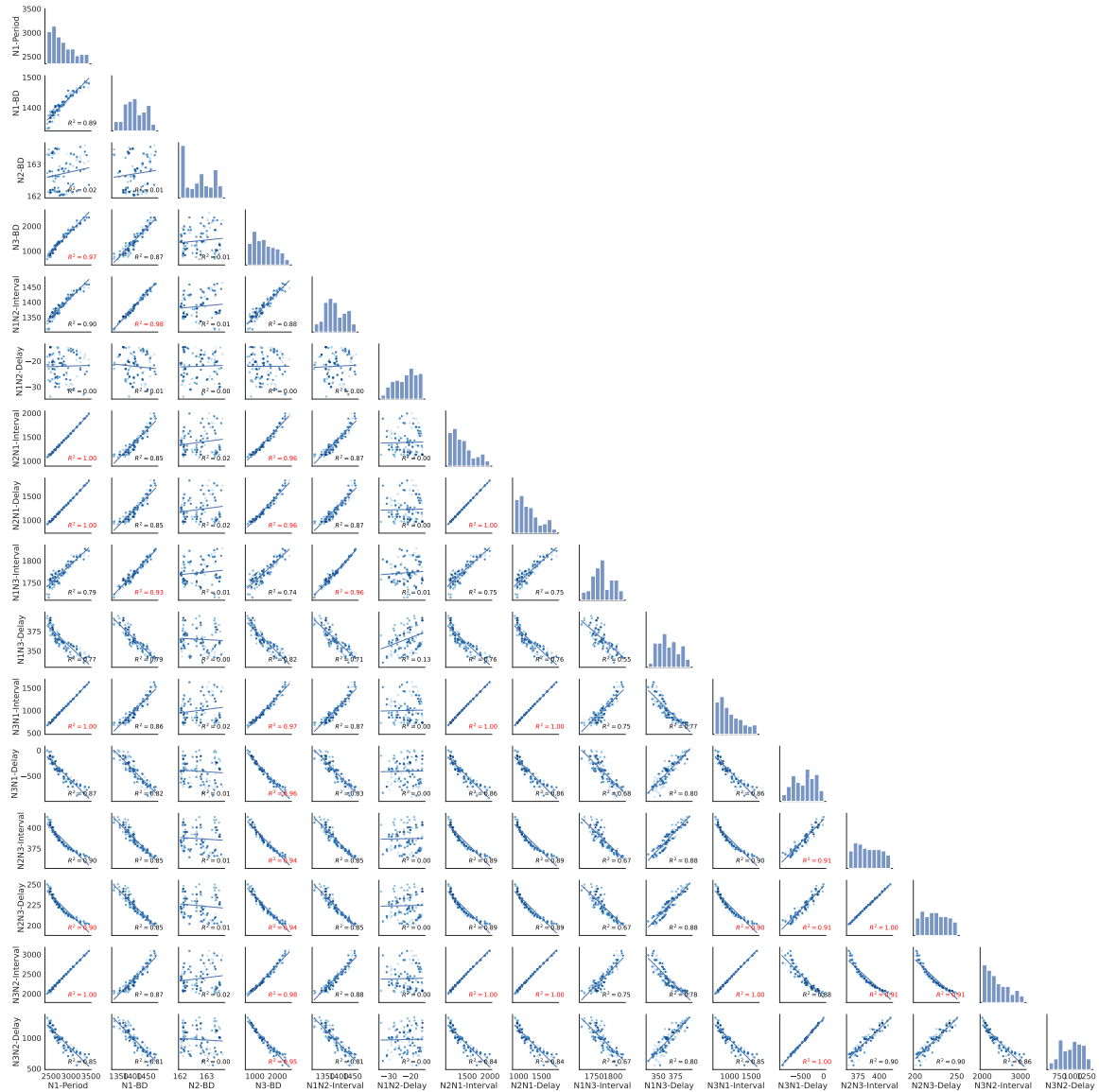


Figure 5.9: N3t stimulation: Pairplot with all possible combination between time intervals within a cycle.

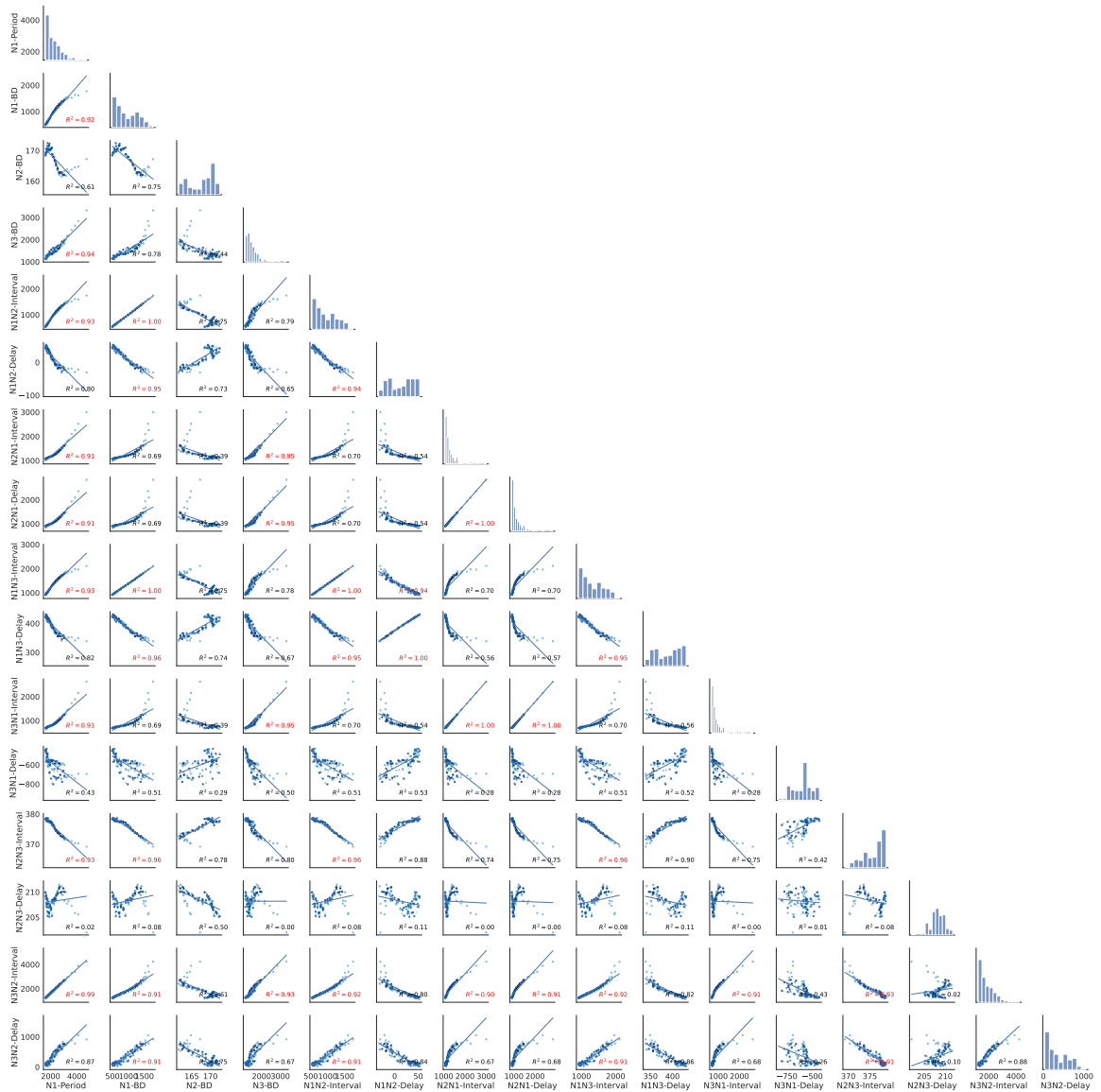


Figure 5.10: SO stimulation: Pairplot with all possible combination between time intervals within a cycle.

the intracellular recordings. In Figure 5.11 there is a comparison of the linear relations and different intervals conforming the sequence when the references are in N1, N2 and N3 (as we have shown so far) or only for N1 and N3.

When we only consider two phases, we have less possible combinations and the time-intervals that would correspond to the third neuron are contained in the resulting ones. For example as we can see in Fig. 5.11a), N2N3 delay would be represented by N1N3 delay; N2 burst duration is included in the N2N3 interval. So when analyzing dynamical invariants in two-phase intervals each interval is more informative of the variability constrains cycle-by-cycle.

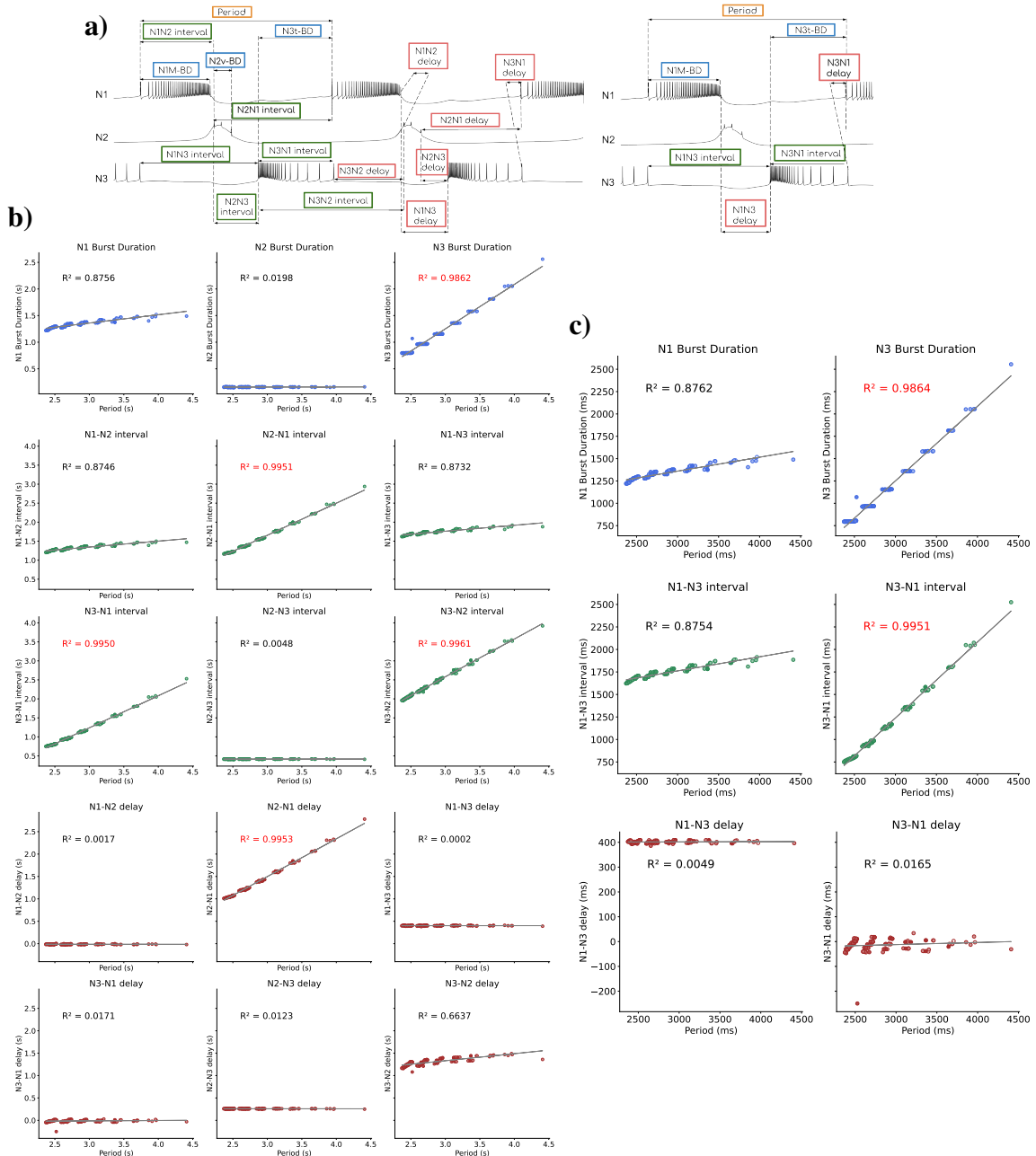


Figure 5.11: a) Representation of the intervals for each cycle when considering three or two phases (left and right, respectively). b) Interval correlations to period for SO-driven simulation for 3 phases. First row: Burst duration. Second and third row: Two-neuron intervals. Forth and fifth row: Two-neuron delays (Data shown in Fig. 5.5). c) Interval correlations to period for N1M-driven simulation for 2 phases. First row: Burst duration. Second row: Two-neuron intervals. Third row: Two-neuron delays. For b) and c) the linear relationships are quantified by the R^2 values of the regression.

5.4 Experimental results in *Lymnaea Stagnalis*

In the previous section we analyzed the presence of sequential dynamical invariants in a CPG model, showing that strong correlations can be formed when stimulating certain neurons in the circuit and only when the circuit modeled has enough flexibility to adapt to the changes in the rhythm. In this section we will explore this phenomena in intracellular recordings of the living activity of *Lymnaea stagnalis* feeding CPG. The aim here is to search for sequential dynamical invariants as those reported in Elices et al., 2019 in another animal model, and also explore their functional meaning by analyzing different sources of stimulation of the rhythm. The data here characterized was kindly provided for this work by Michael Crossley 5.2.3, University of Sussex.

When studying temporal structures in neural dynamics, the definition of time references is a key first point. In the computational analysis described in the previous section, the time references to define cycle-by-cycle sequence intervals were the first and last spikes of each burst. In that case, as in the case of the pyloric neurons in *C. maenas* the CPG phases are directly related to the bursting activity of these motoneurons and the burst can be consistently identified by the first and last spike. However, in the case of the feeding CPG in *Lymnaea stagnalis*, the activity is usually characterized with recordings from both interneurons and motoneurons (P. R. Benjamin, 2012; Elliott & Benjamin, 1985; Staras et al., 1998). This requires a more complex combination of burst references to characterize the phases of the CPG based on cycle-by-cycle time intervals. Thus, for this analysis, we will consider the three phases of the CPG: protraction, rasp and swallow, which are associated mainly to the N1M, N2v and N3t neurons. Since it is not always possible to record these neurons at the same time (specially N2v that is located in the ventral side), we will establish the time references for the sequence analysis by a combination of interneuron and motoneuron events following their activity at each phase.

For example, in Figure 5.12 the three phases in the CPG are marked by a colored background over the recording. Note that they can be delimited by the neurons in the circuit but some of the motoneurons cover several phases, as it is the case of B4 in panel a) or B3 in panel b). Phases can also be defined by the first and last spike, as it is the case for phase N3 and neuron B8, but in other cases as the phase N2, the relevant reference is the hyperpolarization of specific neurons, such as the strong inhibition visible in neuron B5 in panel b). Also, the depolarization of some neurons carries relevant information, since, for example in the case of B1 in Fig. 5.12.b), the visible depolarizations that did not generate action potentials, represent the N1 phase, through the connection between N1M and B1. Therefore, to characterize the time sequences in the feeding CPG, we need compound references from several neural recordings, which are summarized in Table 5.2. Note that, different

time references must be taken into account to reach conclusions about the time-interval constraints in the cycle-by-cycle analysis. All possible intervals conforming each cycle between the neurons are taken into account in this analysis (see [5.2.1](#)). The events and neural recordings to define each time-interval for each are described in section [5.2.3](#) for each experiment.

	N1-Protraction	N2-Rasp	N3-Swallow
Start	Last spike of N3t/B3 Depolarization or first spike in B1 First spike in B6	Inhibition of B5	First spike of B8
End	Last spike of B5 Hyperpolarization in B1 or B6	First spike of B8	Last spike of N3t/B3

Table 5.2: Time reference boundaries for the three phases in the feeding CPG

Another key point in the study of the feeding CPG of *L. stagnalis* is that the generation of the rhythm is a combined action of different cells (P. R. Benjamin, [2012](#)), not only interneurons but also motoneurons have a role in the activation (Staras et al., [1998](#)), and modulatory neurons in the buccal and cerebral ganglia are involved in the rhythm. All these factors affect the rhythm and thus the neuronal sequential activation and how variability is distributed among the different intervals cycle by cycle. Also, not all the neurons are involved every time the rhythm is active, and that gives also information about the different contexts in which the rhythm evolves. For example, the rhythm can be activated by the presence of food or sucrose stimulation, in which case the animal needs to initiate the activity and ingest food. Then the rhythm is started by the stimulation of the lip nerve that also stimulates N1M. Also, even at the absence of food, when the animal is hungry, the CPG can be activated, in this case with a strong role of N3t as modulator. The modulation of the rhythm is also a key aspect, and modulatory neurons such as SO or CV1a control the rhythm after its initiation, and they have shown to have distinct alternative roles in the activity (Kemenes et al., [2001](#)).

In this section we will analyze and describe different examples of experiments for the isolated ganglia with intracellular recordings under different conditions: spontaneous activity, SO-driven activity, medium lip nerve stimulation driven activity and CV1a-driven induced activity.

5.4.1 Invariants in spontaneous activity

The spontaneous activity here refers to intracellular recordings of the buccal ganglia after the isolation of the CNS with no chemical or electrical induced stimulation. In that case, since the CPG is able to maintain the activity in an autonomous manner, it keeps the motor activity as if the CNS was

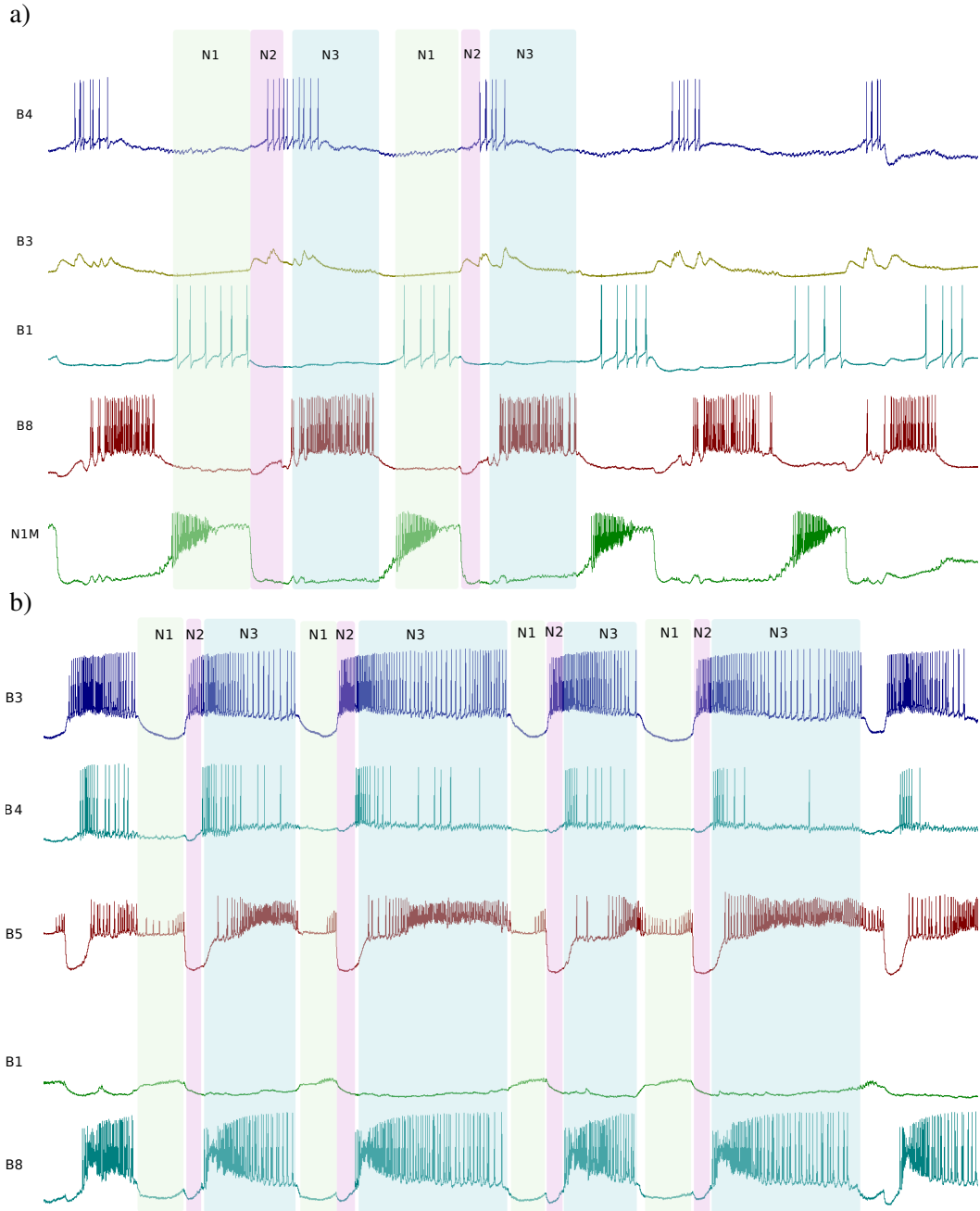


Figure 5.12: Delimitation of phases in the feeding CPG of *Lymnaea stagnalis* based on different recordings. Panel a) intracellular recordings for motoneurons B4,B3,B1 and B8 and the interneuron N1M. Phases are delimited by N1M and B1, that have the same activation time for phase N1, the inhibition of N1M and the start of the depolarization in B8 for phase N2 and the first and last spike of burst B8 for phase N3. Panel b) intracellular recordings for motoneurons B3,B4,B5, B1 and B8. Phases are delimited by B1 depolarization for phase N1, the strong inhibition of B5 for phase N2 and the first and last spike of burst B8 for phase N3.

not isolated. In this condition, although the characterization of the sequential dynamical invariants can be done, their possible functionality association is more complicated, since the context of the

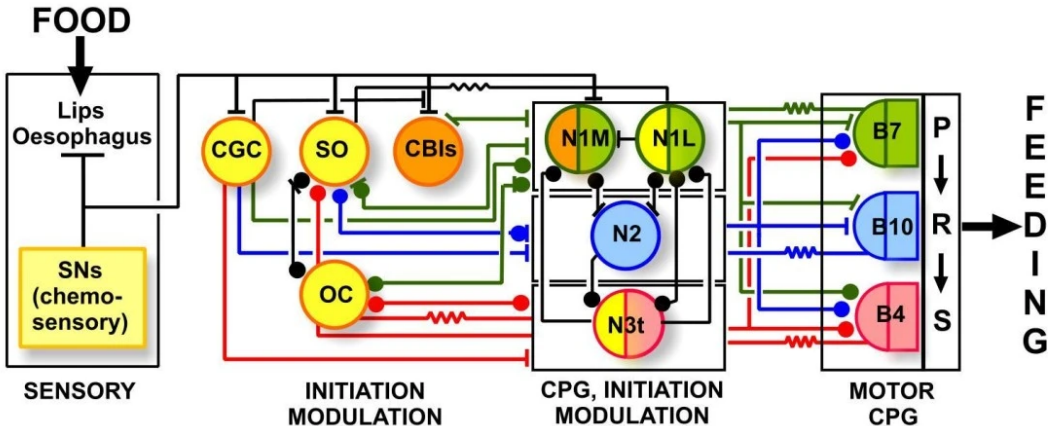


Figure 5.13: Representation of the distributed system of the feeding CPG. Dots indicate inhibitory chemical synapses, bars excitatory chemical synapses and resistor symbols electrotonic (electrical) synapses. Colors indicate the function of the neuron classified in modulatory or initiator (yellow and orange, respectively) and the three phases protraction, rasp and swallow (green, blue and red, respectively). From left to right food detection represented by Lips that stimulate CGC, SO CBIs and N1M neurons and initiate the rhythm. The ongoing activity is then modulated by those neurons but also by OC neurons and N1 and N3t neuron. Some examples of motor neurons are represented on the right side of the panel, associated to each feeding phase. This figure was adapted from Panel C from Figure 1 in P. R. Benjamin, 2012 (work under license [Creative Commons Attribution](#))

movement origin is lost. The study of these sequential restriction in artificial stimulation contexts can help classify this spontaneous activity, even when the rest of the system is not available.

Here we analyze three examples of spontaneous activity. We do not know what was the source or context for the feeding activation, but there are differences between the three experiments regarding their dynamical invariants. The case with the strongest linear correlation is the first example showed in Fig. 5.14, where the N3 burst duration and the associated intervals covering N3 phase (N2N1 interval, N3N1 interval, N3N2 interval and N2N1 delay) had a strong linear correlation with the period ($R^2 > 0.9$). This is also clear in the variability boxplot, where the variability distribution of the period is really similar to N3 burst duration, N2N1 interval, N3N1 interval, N3N2 interval and N2N1 delay, and the rest of the intervals are not similar to the period. This difference in variability is also important, since while there are intervals with a strong linear correlations illustrating cycle-by-cycle dynamical restrictions, some other intervals have no relation, all have $R^2 < 0.1$, i.e. are free to display unrelated variability. Observing the recording of this example (first row in Fig. 5.14), we can see that the N3 neuron had long periods of tonic firing (that were excluded from the time-interval relations), and that the spontaneous activity was lead by N3 neuron, associated in the literature with spontaneous activity in sated animals. The N3t was tonically firing producing long periods of

silence interrupted by short rasps (P. R. Benjamin, 2012; Staras et al., 2003).

However, in the following examples in Figs. 5.15 and 5.16 the variability distribution is different. In the example shown in Fig. 5.15, we can see the distribution of the variability between N1 and N3 phases illustrated in the boxplot and also the linear regressions, in which, although they have low R^2 values, we can observe some linear tendencies between the intervals and the period, specially in combined intervals such as the N3-N2 interval. What is a common characteristic with the previous example is the presence of unrelated intervals to the period, since N2 burst durations and other time-intervals associated to the N2 phase (N2N3 delay, N1N2 delay) have a $R^2 < 0.1$. These intervals also remain unrelated to the period in the third example, showed in 5.16, where N2 and N2N3 delay have similar R^2 values. In that last case, however, the variability is mostly in the N1 phase. Again, the linear correlations with the period are in combined periods, usually the ones involving N1 and N3 phases: N3N1 interval, N2N1 delay, N3N1 delay; this points to the distribution of variability between those two phases. Also, the fact that the combined intervals have much stronger linear correlations is affected by the time references in these intervals.

Figure 5.17 contains the pairplots for each of these three experiments, with all possible combinations between intervals. Note that, for a better representation, there are only two phases taken here into account: N1 and N3. Most part of the time-intervals involved in the N2 phase are contained in the N1N3 delay, which goes from the end of N1 to the start of N3 (see 5.2.1). The intervals' relations with the period correspond to the first column, the rest are combinations between all possible intervals, including the period defined from N3 start to N3 end. We see again that each recording has a different variability distribution: In the first panel, we can observe several robust dynamical invariants. This is also the case for the second panel, where we can observe that, in relation to N1 and N3, it is interesting to see that the N1-BD has a really strong linear relation with the N1N3 interval, which suggests that all variability in that phase comes from the burst duration, and the N2 phase remains mostly constant. In the last panel we can appreciate this increase in the correlation between N1-BD and the period and the decrease in the correlation with the N3-BD. This is shown in the linear correlation unveiled in this pairplot by the N3N1-Interval and the N3N1-Delay, representing the constancy in the time duration of the burst.

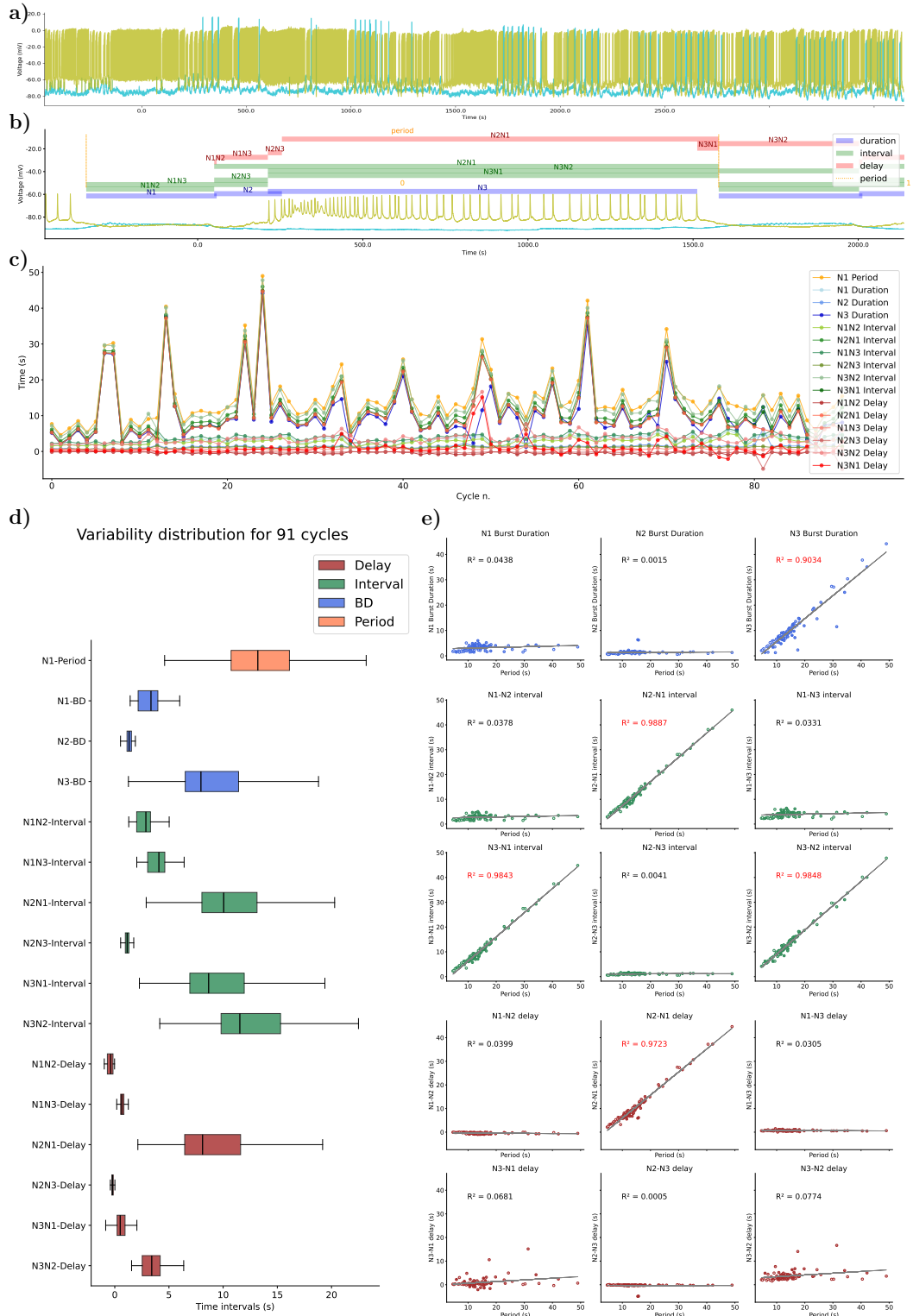


Figure 5.14: Spontaneous case 1: Panel of intervals distribution and dynamical invariants for the three phases in the CPG for spontaneous activity. a) Voltage traces for the intracellular recording analyzed for this panel. b) Representation of the time-intervals described. c) Duration of each time interval (y-axis) at each cycle. d) Box-plot with the variability distribution of the duration of each time-interval. e) Time-intervals duration against the period for NX-duration (blue), NXNY-Interval (green) and NXNY-Delay (red)

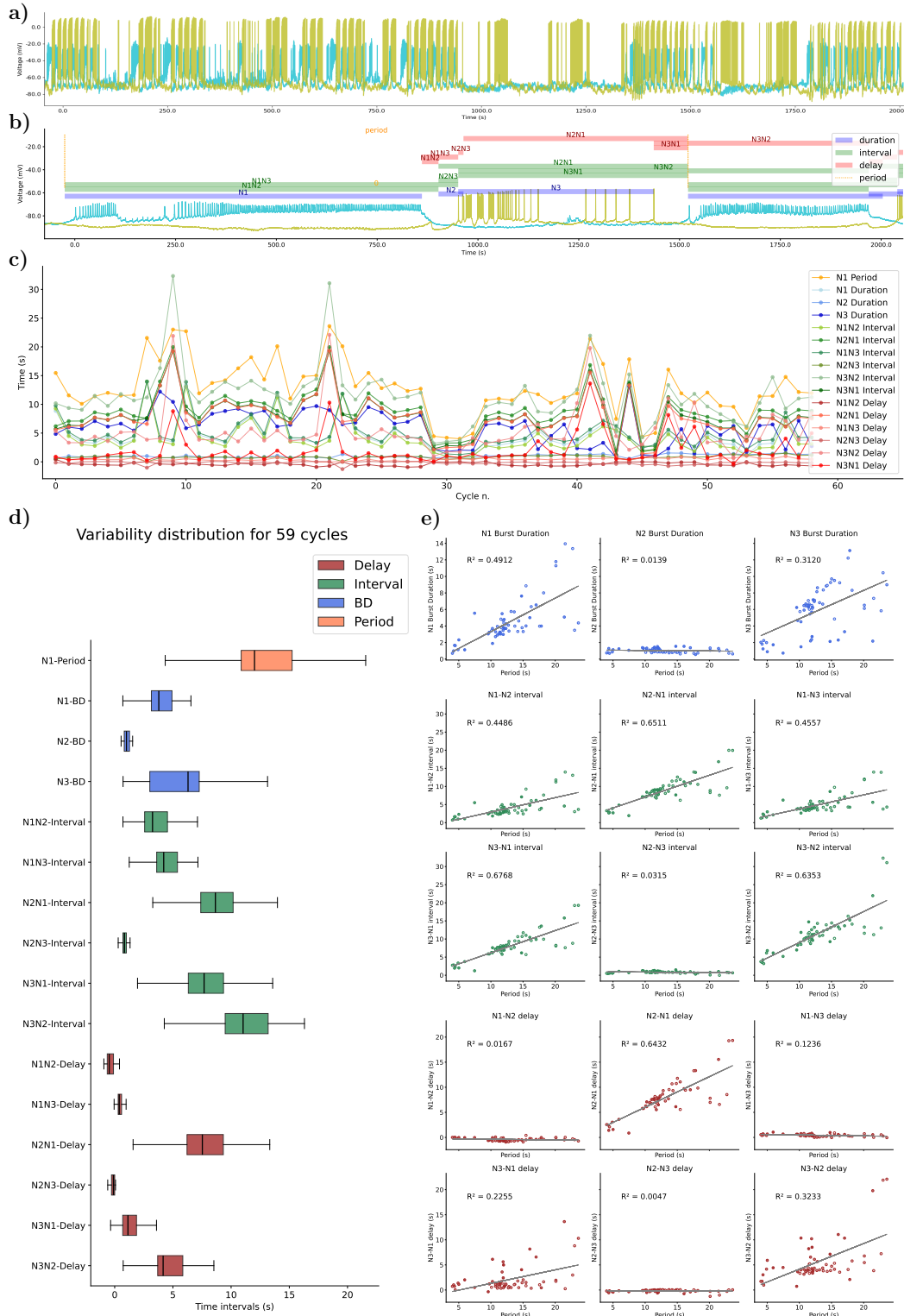


Figure 5.15: Spontaneous case 2: Panel of intervals distribution and dynamical invariants for the three phases in the CPG for spontaneous activity. a) Voltage traces for the intracellular recording analyzed for this panel. b) Representation of the time-intervals described. c) Duration of each time interval (*y* – axis) at each cycle. d) Box-plot with the variability distribution of the duration of each time-interval. e) Time-intervals duration against the period for NX-duration (blue), NXNY-Interval (green) and NXNY-Delay (red)

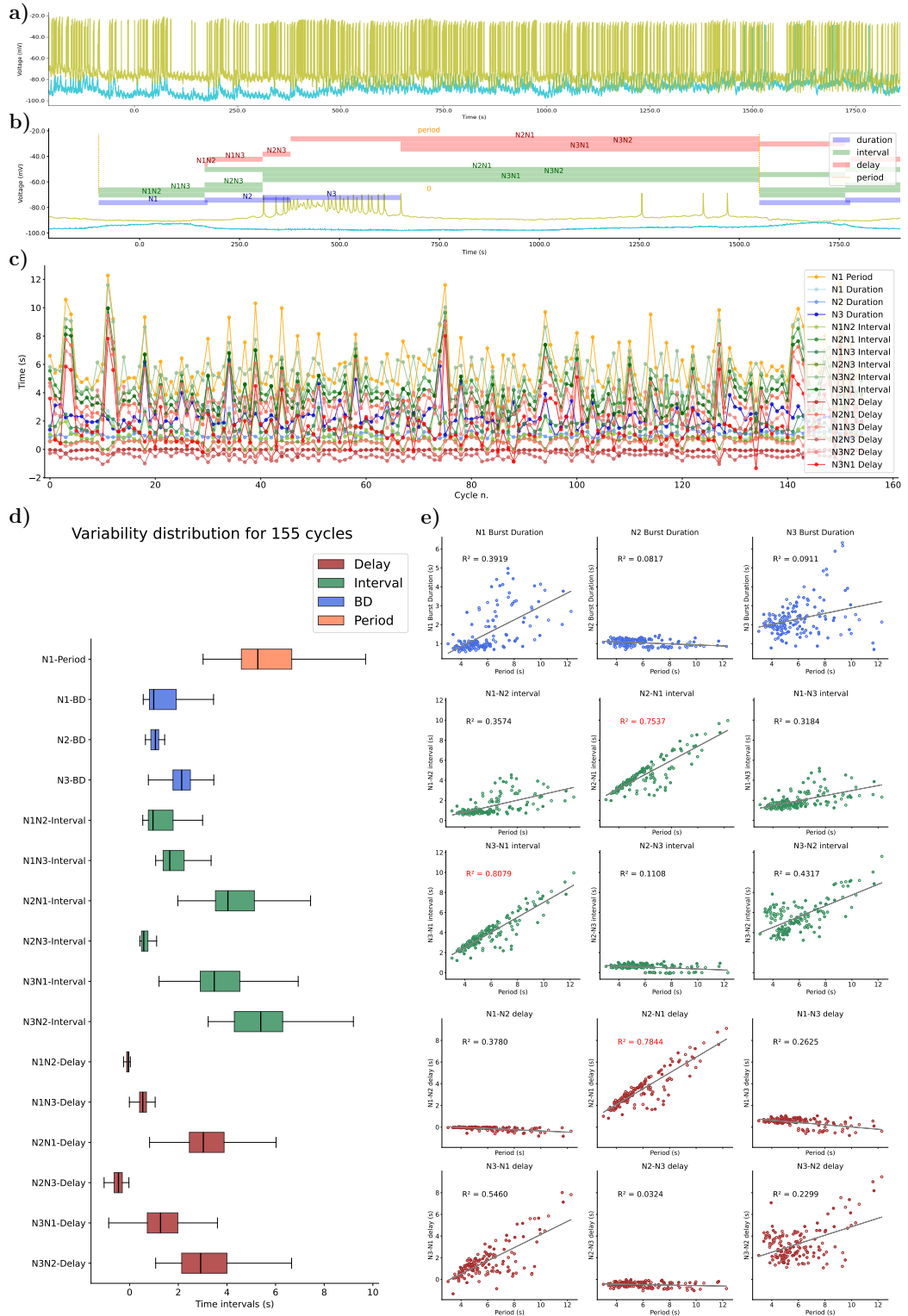


Figure 5.16: Spontaneous case 3: Panel of intervals distribution and dynamical invariants for the three phases in the CPG for spontaneous activity. a) Voltage traces for the intracellular recording analyzed for this panel. b) Representation of the time-intervals described. c) Duration of each time interval (y-axis) at each cycle. d) Box-plot with the variability distribution of the duration of each time-interval. e) Time-intervals duration against the period for NX-duration (blue), NXNY-Interval (green) and NXNY-Delay (red)

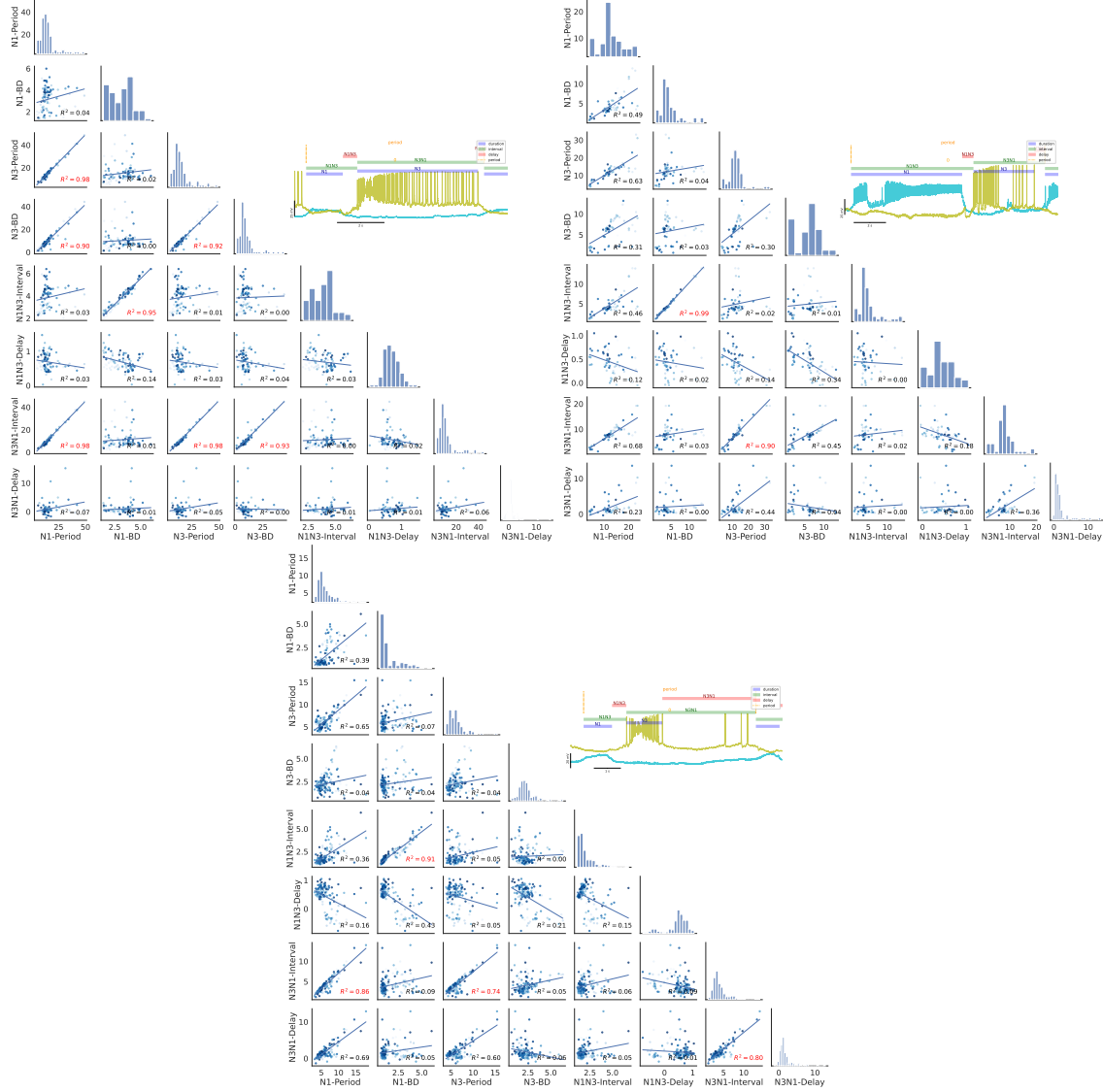


Figure 5.17: Panel of the pairplots for all possible combinations between the time intervals for two phases (N1 and N3) in the CPG recordings for the three examples of spontaneous activity recordings.

5.4.2 Invariants in SO driven activity

As we saw before, the SO role in the feeding CPG is modulatory, which means, that it modifies the rhythm once it is activated. In the model analysis, in section 5.3.3, we showed that when the variability in the simulations was induced by adding a ramp current to the SO neuron, the time-interval variability was distributed between the N1 and N3 phases, having both a strong correlation with the period, which increased the R^2 values. Therefore, in the living recordings we can expect that the variability cycle-by-cycle is distributed during the modulation of SO, which is connected to N1M and N3t (see Fig. 5.13).

In this subsection, we will see an example from a spontaneous activity where the SO neuron was modulating for two lapses of time during the recording. This can be identified by the inhibition of B4 and activation of B3, as illustrated in Fig. 5.18. We can also see in this figure how, during the SO modulation, the rhythm was "stabilized" with less variability in the intervals' duration. The characterization of the variability of the time intervals and their relation to the cycle period for this trace is depicted in Figs. 5.21, 5.20 and 5.19, when SO was modulating, when it ceased its modulation and when it then restarted it, respectively.

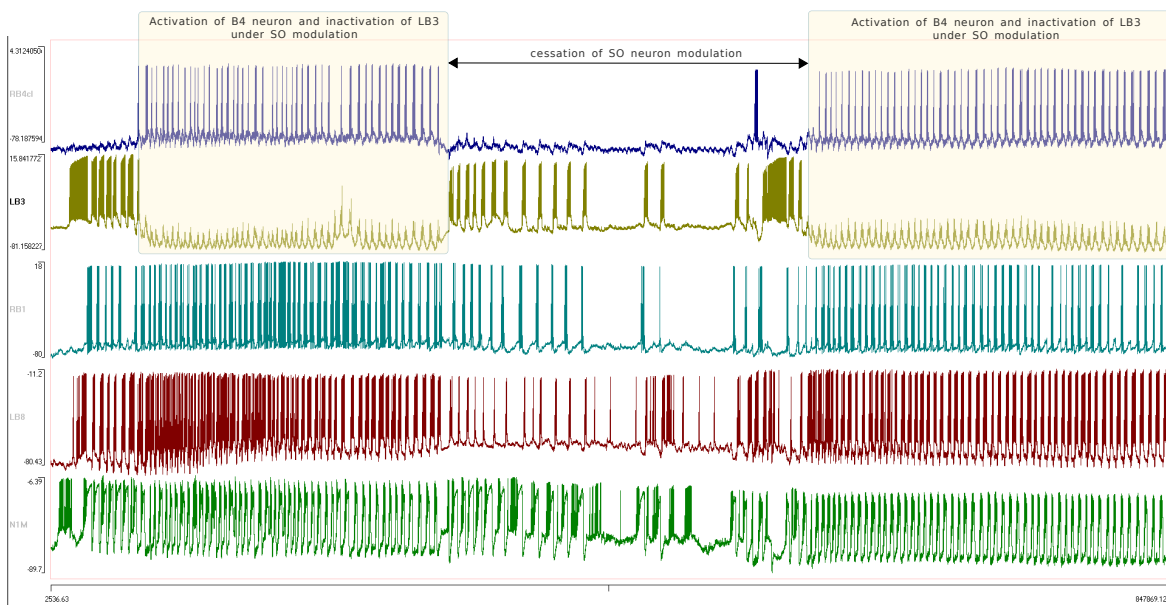


Figure 5.18: Representation of the spontaneous recording with lapses of SO modulation. The parts of the recording with yellow background highlight were the activity was modulated by the SO neuron. From top to bottom, intracellular recording of a neuron from the B4 cluster, B3 motoneuron, B1 motoneuron, B8 motoneuron, and N1M interneuron.

When the rhythm was driven in SO, we can see how the variability for N1-BD and N3-BD was constrained reflected in the low variability observed in the boxplots of Figs. 5.21 and 5.19, and also

in the third panel representing the duration of each interval per cycle in both figures. In the correlation of the intervals with the period, although R^2 value is not significantly high, N1-BD and N3-BD have around 0.7 and 0.3 in both cases, pointing to this redistribution of the variability. When the SO stops its modulation, the major source of variability concentrates in the N1 phase (see N1-BD, period correlation with $R^2 = 0.9$). In Fig. 5.20 the R^2 value of N1-BD is in the order of 0.9, while the N3-BD is close to 0. Although this example had only a few cycles, this suggest that the variability in that lapse of time was all carried by the N1 phase. Regarding the rest of the time-intervals in the cycle, the one with the largest variability is N3N1 interval, since it contains N1-BD. Also, when activity ceases, the N3N1 delay variability rises, which is notable compared to the rest of the experiments and the model, and might be caused by the burst shape and how the intervals were defined (see Fig. 5.20, first panel). This result, also matches the experimental work by Elliott and Andrew, 1991, which showed this distribution between N1-BD and N3-BD. In that work, the SO modulation was induced by stimulating SO neuron. Figure 5.22 shows an example inducing the SO modulation by electrical stimulation. Again, we can see the same variability distribution between N1 and N3 phases, having N1 a strongest correlation with the period, reaching $R^2 = 0.8$ this time. It is also important to highlight that the intervals associated to N2 phase (N1N3 delay and N3N1 delay) do not have any relation with the period, and their variability is minimal. To further compare this two panels, the pairplots for one example of spontaneous activity and the SO induced modulation are in Fig. 5.23. In the pairplot, we see the same interval relations and also another strong relation between N1N3 Interval and N1-BD, which appears in both cases and supports the N1 variability and the constancy of N2phase, since in the N1N3 interval, all the variability is associated with N1-BD.

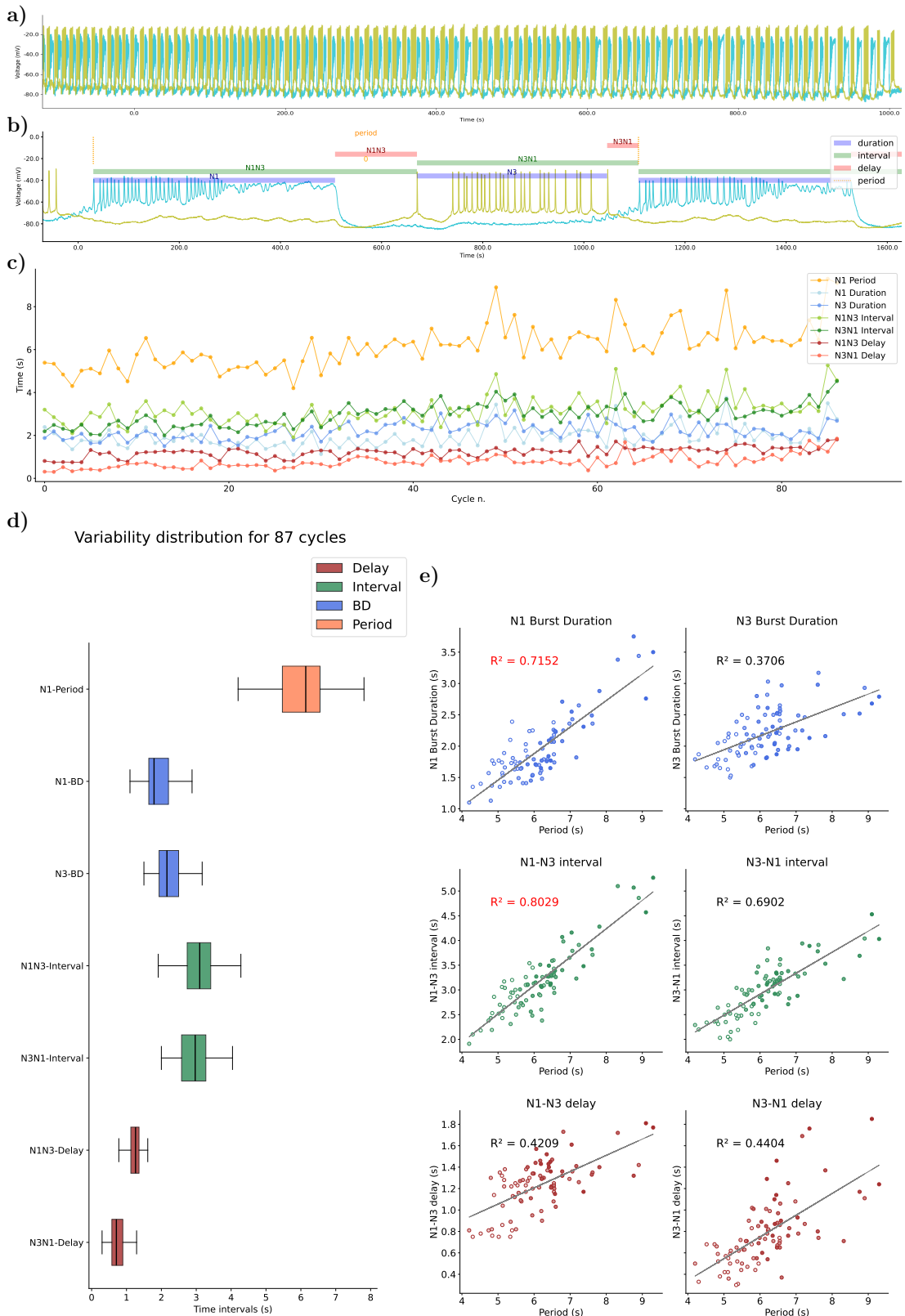


Figure 5.19: Spontaneous SO neuron driven: Panel of intervals distribution and dynamical invariants for the two phases in the CPG for spontaneous activity driven by SO neuron. a) Voltage traces for the intracellular recording analyzed for this panel. b) Representation of the time-intervals described. c) Duration of each time interval (y – axis) at each cycle. d) Box-plot with the variability distribution of the duration of each time-interval. e) Time-intervals duration against the period for NX-duration (blue), NXNY-Interval (green) and NXNY-Delay (red)

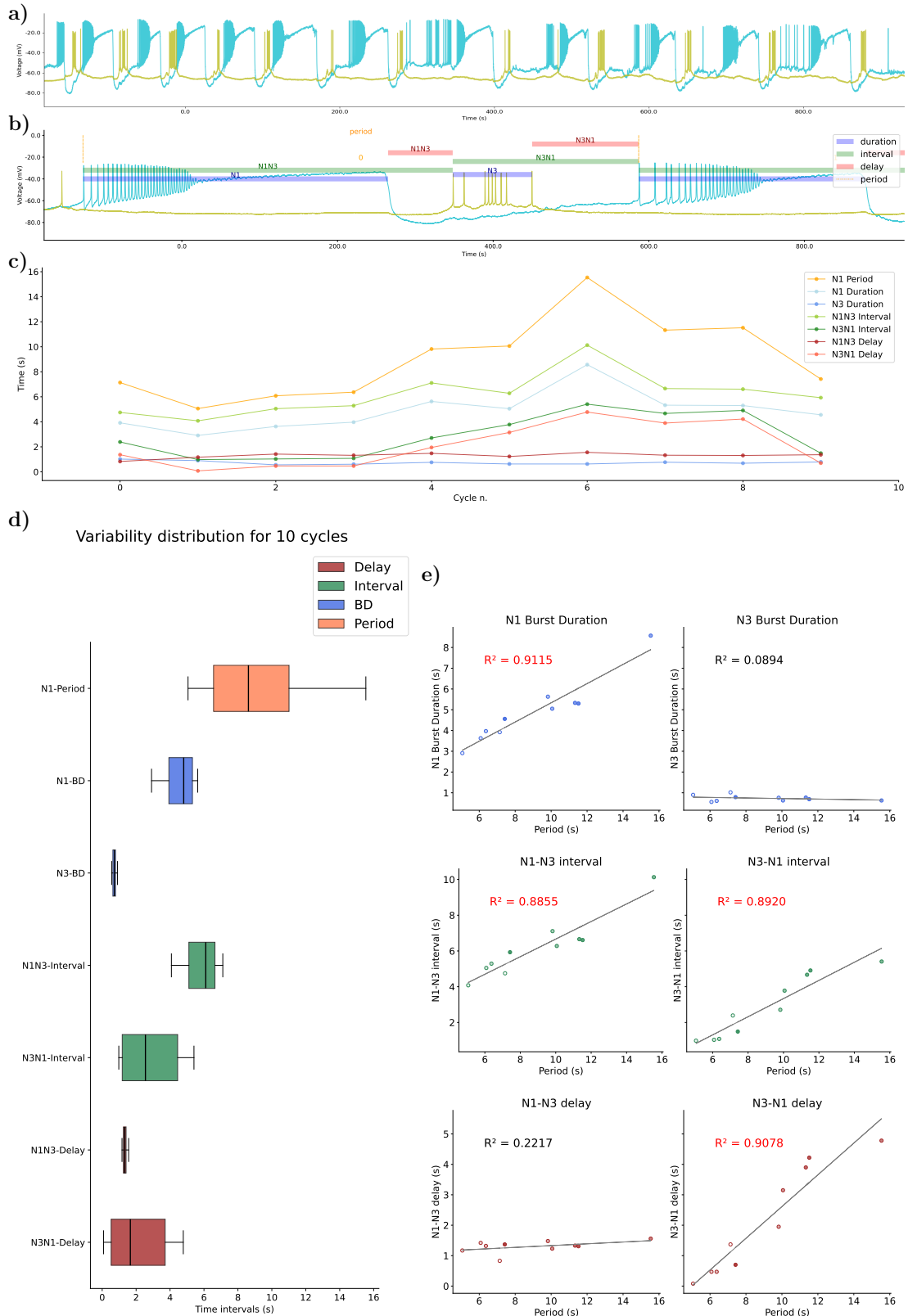


Figure 5.20: Spontaneous activity when the SO-driven modulation ceases: Panels illustrate the interval distribution and dynamical invariants for the three phases in the CPG during spontaneous activity. a) Voltage traces for the intracellular recording analyzed for this panel. b) Representation of the time-intervals described. c) Duration of each time interval (*y* – axis) at each cycle. d) Box-plot with the variability distribution of the duration of each time-interval. e) Time-intervals duration against the period for NX-duration (blue), NXNY-Interval (green) and NXNY-Delay (red)

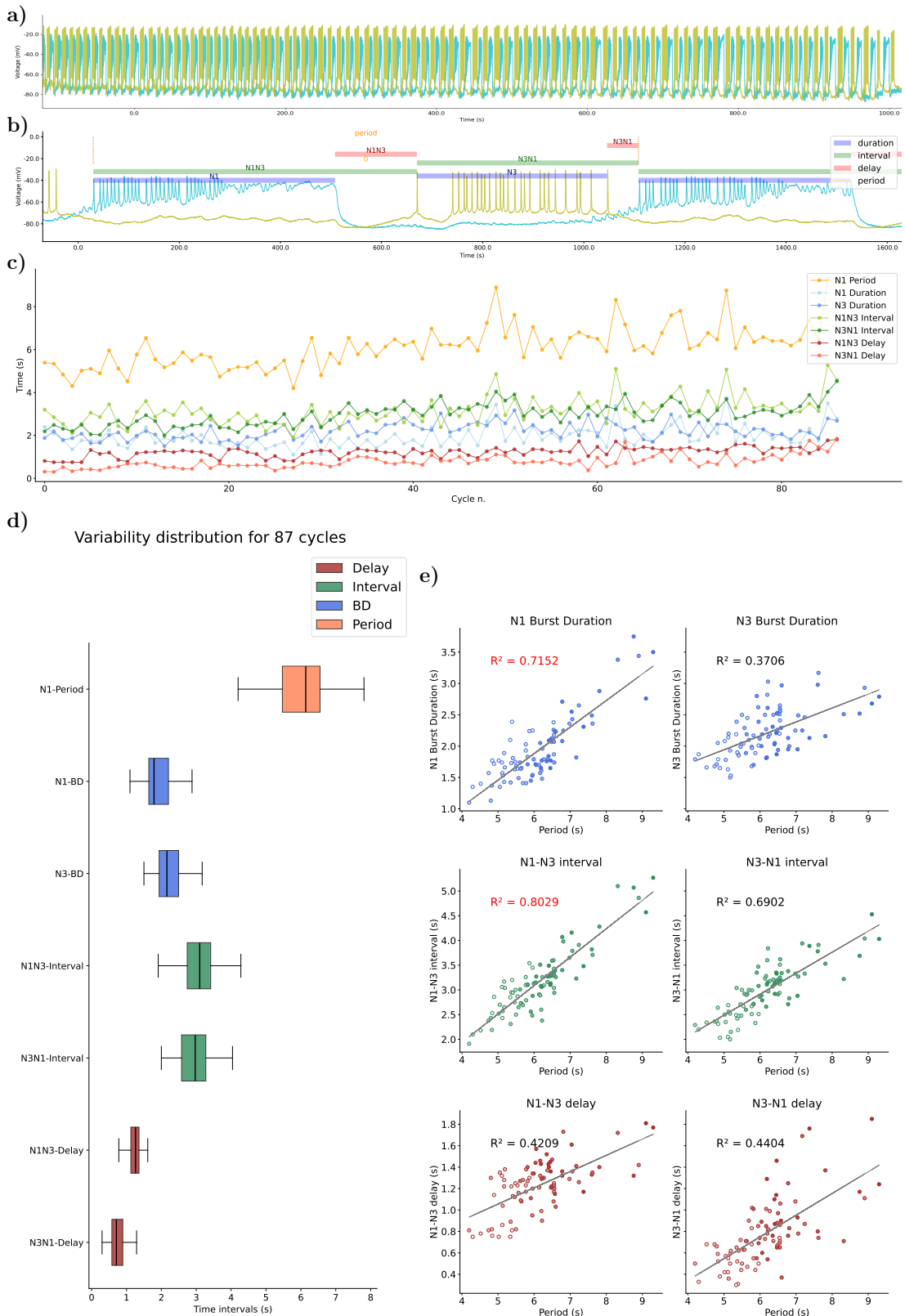


Figure 5.21: Spontaneous SO neuron modulation restarts: Panel of intervals distribution and dynamical invariants for the two phases in the CPG for spontaneous activity driven by SO neuron. a) Voltage traces for the intracellular recording analyzed for this panel. b) Representation of the time-intervals described. c) Duration of each time interval (y – axis) at each cycle. d) Box-plot with the variability distribution of the duration of each time-interval. e) Time-intervals duration against the period for NX-duration (blue), NXNY-Interval (green) and NXNY-Delay (red)

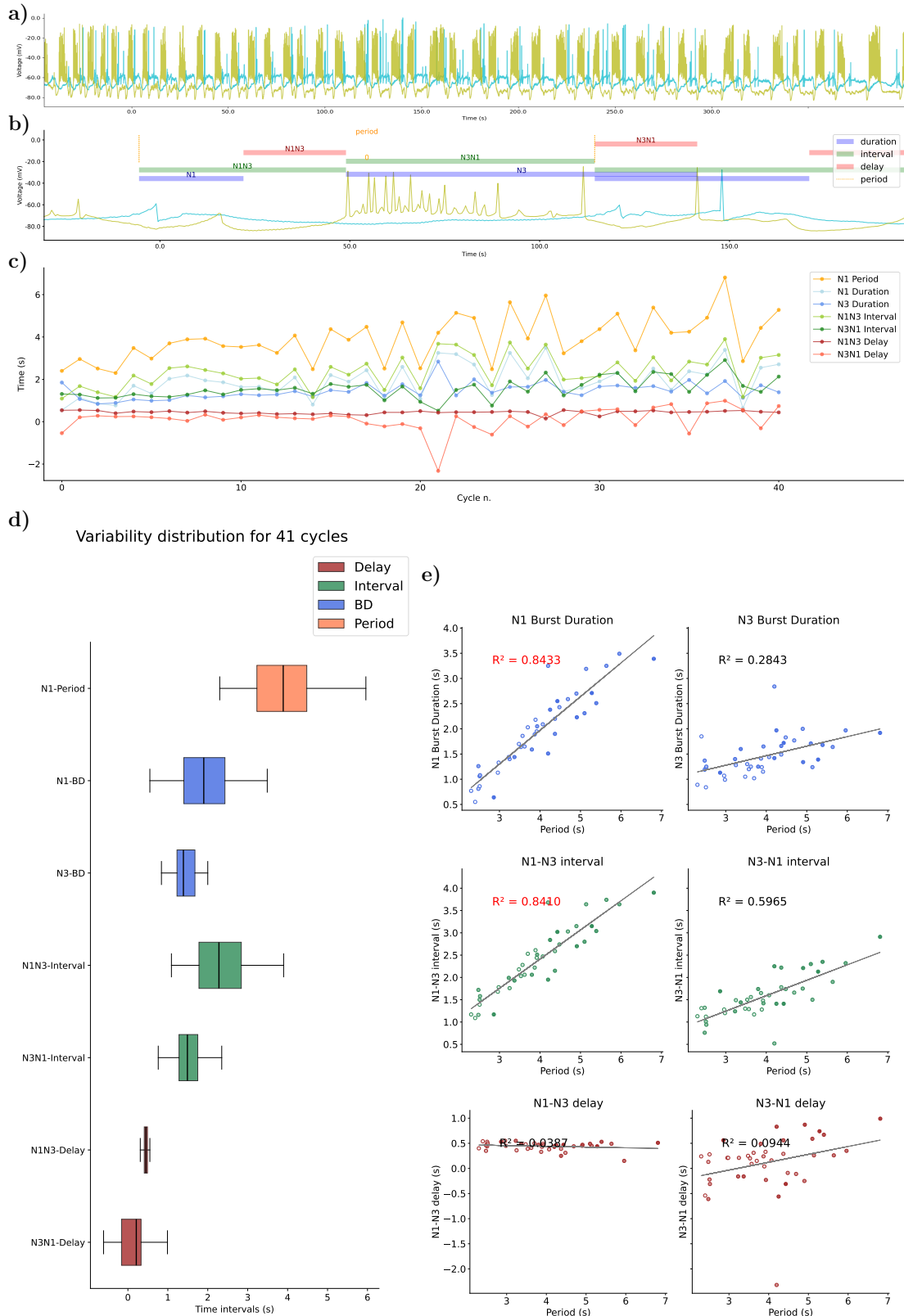


Figure 5.22: Induced SO neuron modulation: Panel of intervals distribution and dynamical invariants for the two phases in the CPG for activity driven by SO neuron induced by its electrical stimulation. a) Voltage traces for the intracellular recording analyzed for this panel. b) Representation of the time-intervals described. c) Duration of each time interval (*y* – axis) at each cycle. d) Box-plot with the variability distribution of the duration of each time-interval. e) Time-intervals duration against the period for NX-duration (blue), NXNY-Interval (green) and NXNY-Delay (red)

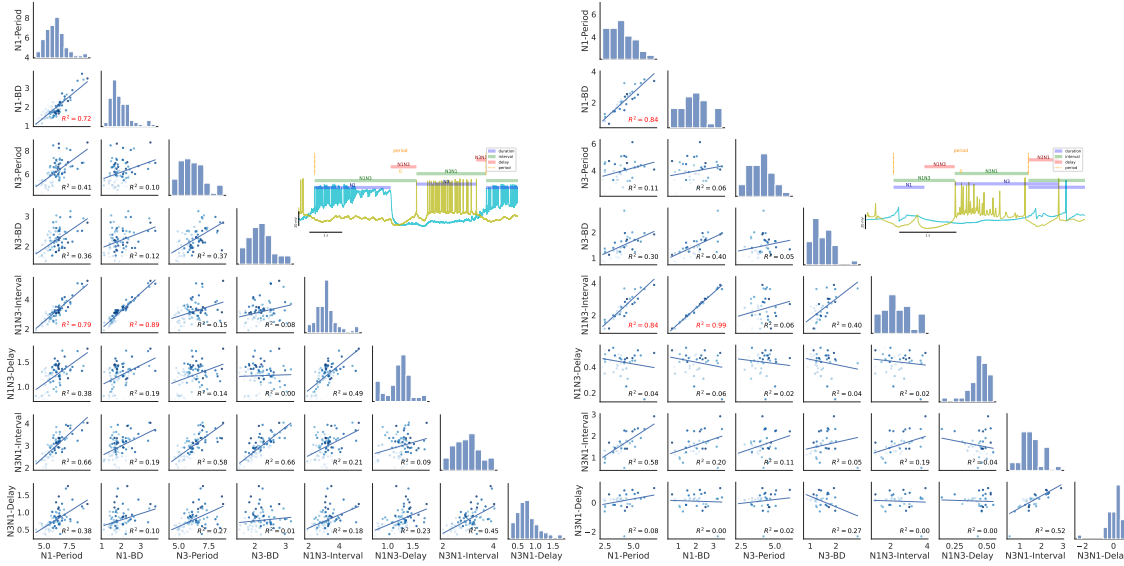


Figure 5.23: Panel of the pairplots for all possible combinations between the time intervals for two phases in the CPG recordings for (left) spontaneous SO rhythm modulation and (right) the induced SO rhythm modulation

5.4.3 Invariants in MLN stimulation driven activity

The snail's lips are connected to the cerebral ganglia by the MLN (median lip nerves). It is possible to activate CPG activity by its stimulation, simulating the initiation of the rhythm in food presence (Staras et al., 1999). This nerve directly stimulates the N1M interneuron, in charge of the initiation of the rhythm, associated to protraction phase. In Fig. 5.24 the variability and time-intervals correlations are characterized for a recording of this induced stimulation. We can see in that figure that there is a strong linear correlation in the panel, leading the rhythm completely by N1 phase. This is visible in the robust dynamical invariant between N1 burst duration and the period and by N1N3 Interval and the period. It is also important that no other intervals have relation with the period, so both N2 and N3 phases remain constant. Note that the N1 burst duration takes a wide range of values for its duration, even at really low ranges, shorter than N3 burst for example. This is also clearly represented in the figure in the third row, where N1 burst duration and N1N3 Interval robustly follow the period. In Fig. 5.25 all possible combination of time-intervals for two phases are represented. We can see there another strongly related intervals N1N3 interval with N1 burst duration, that again highlights the steadiness of N2 phase. This results suggest that during the MLP stimulation, the feeding rhythm variability is lead by N1 phase, activating the rhythm and stabilizing the activity.

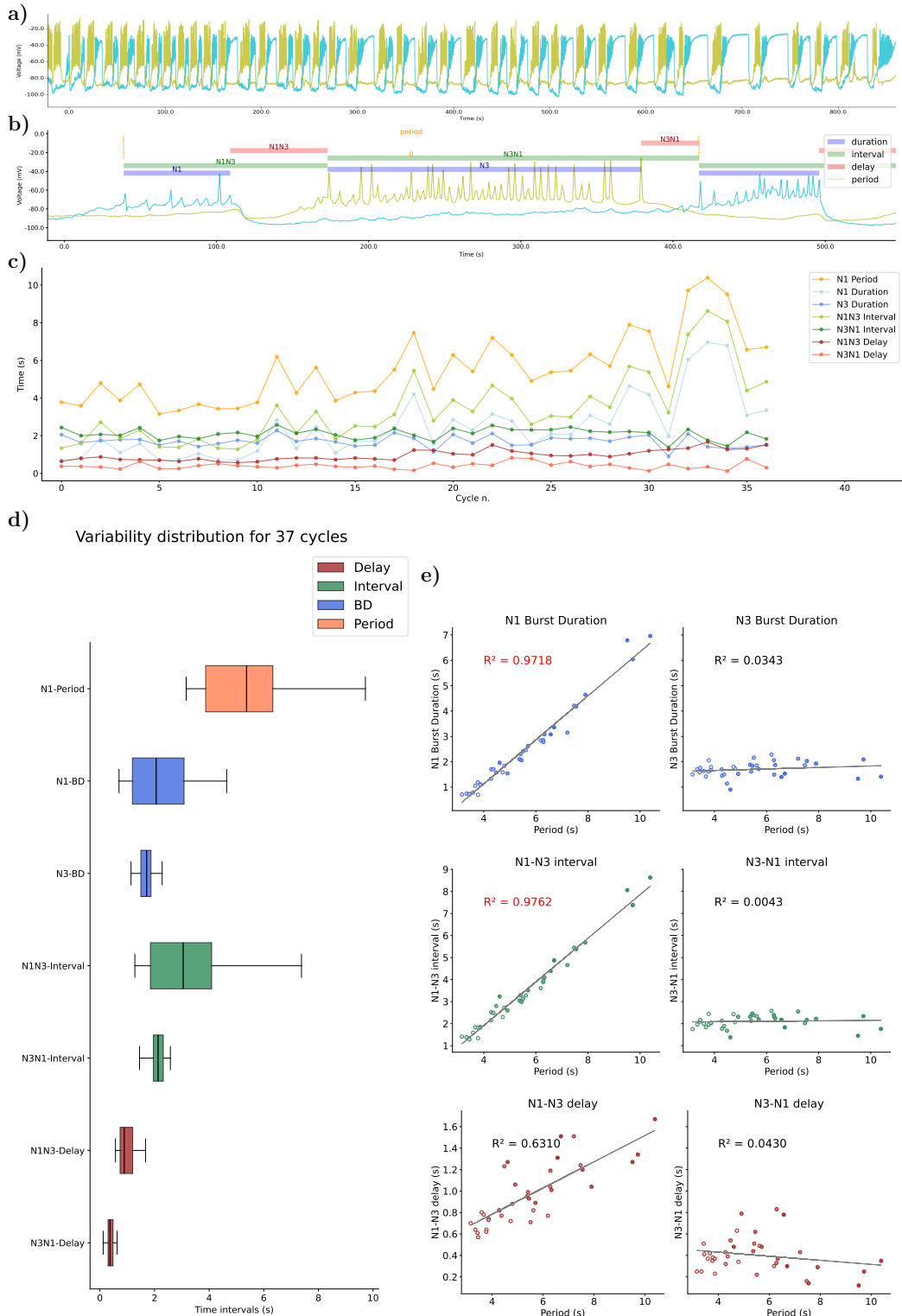


Figure 5.24: MLN stimulation: Panel of intervals distribution and dynamical invariants for the three phases in the CPG under MLN Medium Lip Nerve (MLN) stimulation. a) Voltage traces for the intracellular recording analyzed for this panel. b) Representation of the time-intervals described. c) Duration of each time interval ($y - axis$) at each cycle. d) Box-plot with the variability distribution of the duration of each time-interval. e) Time-intervals duration against the period for NX-duration (blue), NXNY-Interval (green) and NXNY-Delay (red)

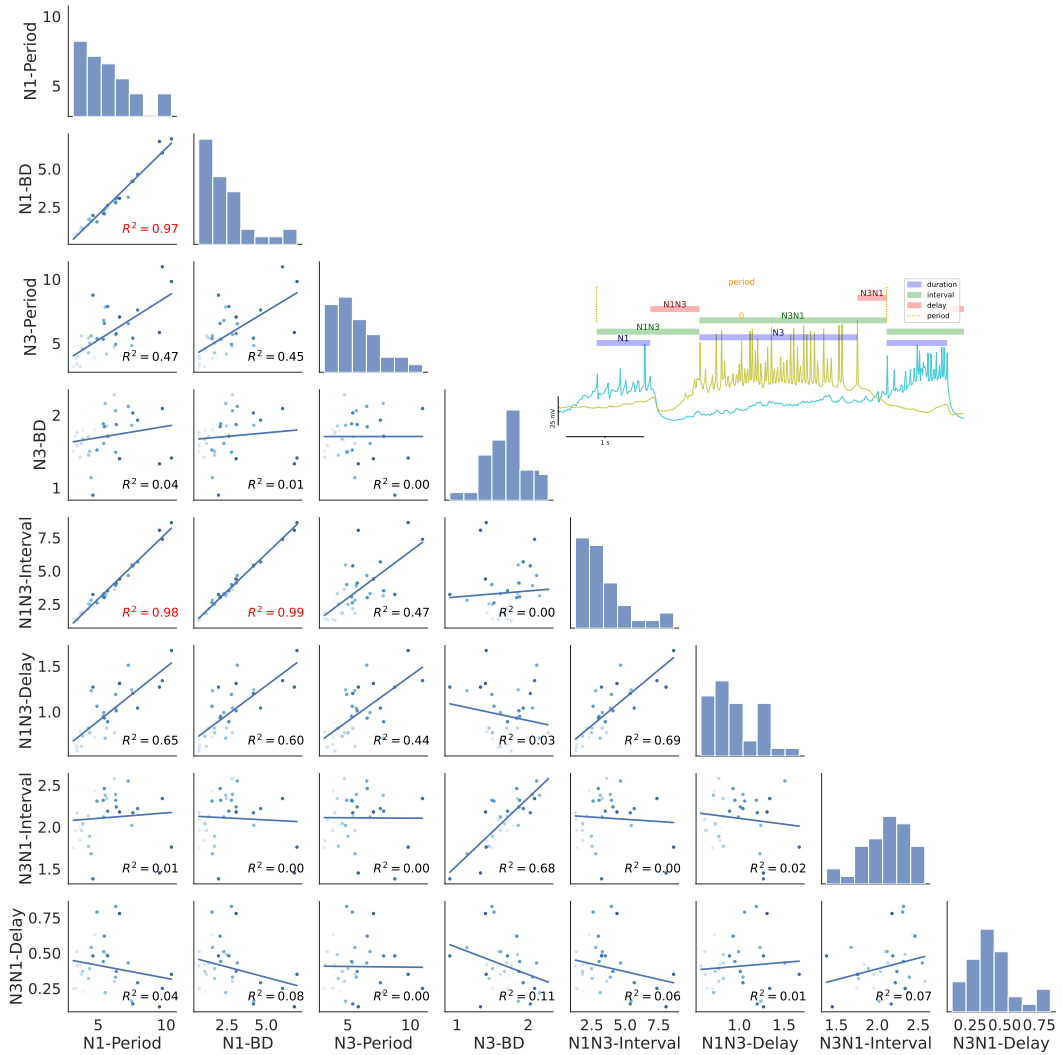


Figure 5.25: MLN stimulation: Pairplot of the invariants reset within cycles.

5.4.4 Invariants in CVa1 driven activity induced by electrical stimulation

CV1a neuron is part of a larger population of CBIs that is influenced by sucrose, which can drive the rhythmic activity in that group of neurons. CBIs are connected by mutual excitation to interneuron N1M, involved in the rhythm initiation (see Fig. 5.13). Therefore, it can be expected to observe in this case a stronger role of N1 phase in the variability distribution. For this case there are 4 examples of different recordings, represented from figures 5.26 to 5.29. In the first three panels we can see that the stronger relation is in N1 burst duration, specially in the first case where there is a strong sequential dynamical invariant with $R^2 > 0.9$. The rest of the intervals conforming that sequence were not strongly related, being N3 phase more variable than the N2 phase, barely presenting variability and with no linear correlation with the period. It is interesting to highlight that not all of the cases where the variability was larger, the correlation to the period was also larger, as it is the case in example 3 in Figs. 5.27 and 5.28. In those examples, the variability in N3 neuron is large but it is not related to the period. Seeing the third figure in each of those panels, we can explain it by the opposite direction of the changes in N3 (dark blue) and N1 (light blue) and the period (orange), pointing that the N3 burst is adapting to the N1 strongest variability. This distribution is maintained for the three first cases, however, in the last case this is shifted. In the example characterized in Fig. 5.29, the N3 burst duration has a stronger linear relation with the period than N1, presenting also a larger variability. During that period the electrode stimulating CV1a slipped away and the stimulation was not as effective as it was in the rest of the examples. We can appreciate in the correlation between N1 and the period that there are some points white-colored that correspond to the beginning of the trace, that might look as outliers but present a tendency to a linear regression. Although this was not a methodic study, we decided to include this case since it represents the sensitivity to the circuit to changes in the context, redistributing in a flexible way the activity between the different phases, in this case from N1 to N3.

Finally, in Fig. 5.30 the plots for 2 phases for each panel are depicted. For some of the recordings when the N2 phase could be well identified, the pairplots for three phases are in the Appendix ??,B.5. In the pariplot, again we see a similar distribution in all figures except of the last one, where there are new correlations, present in the N3 burst duration with the N3N1 interval. Also there is a correlation of a negative slope in the first case, in case N3-BD and N3N1 Delay, representing a regular overlapping of N1 and N3 phases.

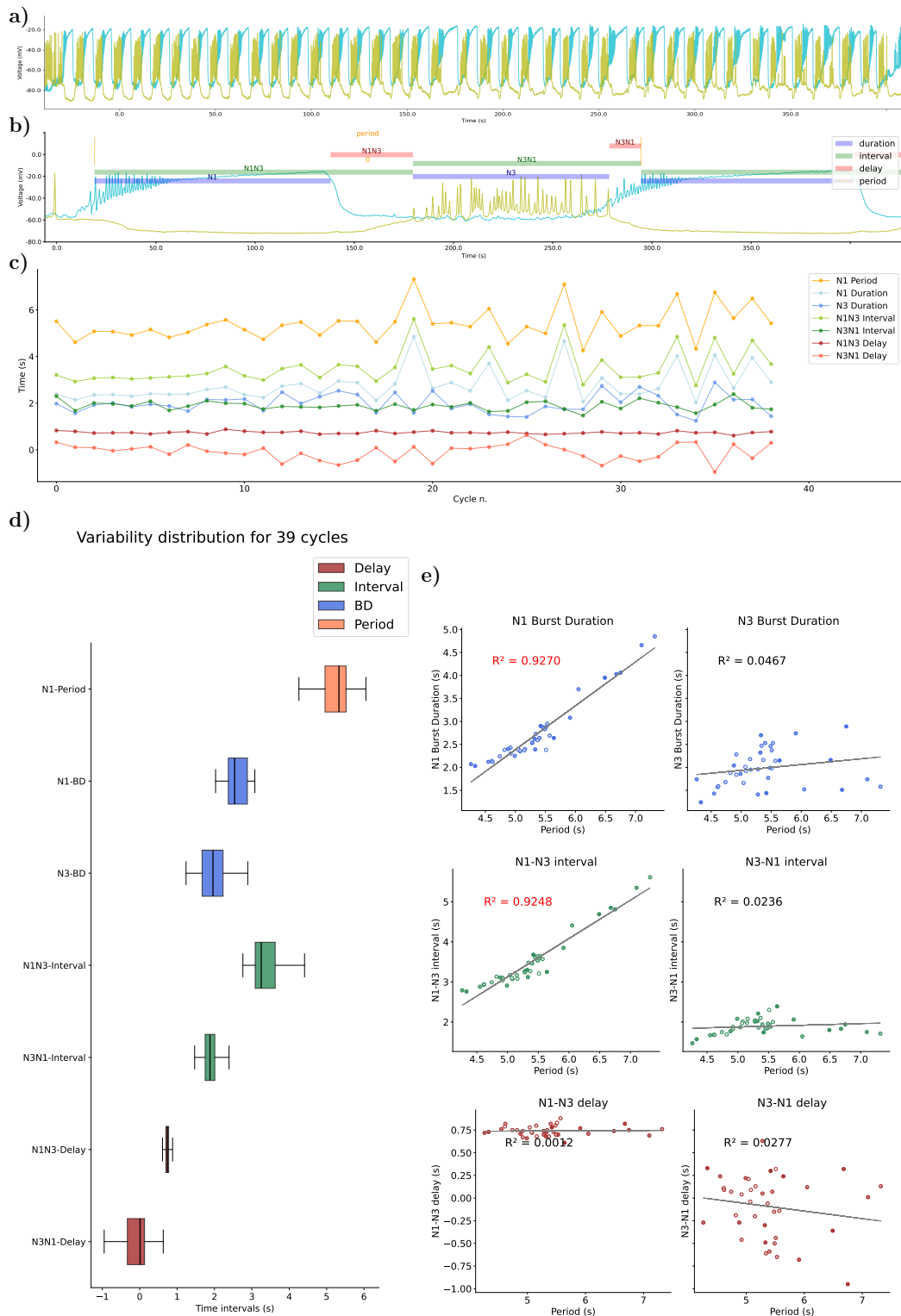


Figure 5.26: CV1a driven case 1: Panel of intervals distribution and dynamical invariants for the two phases in the CPG under CV1a stimulation. a) Voltage traces for the intracellular recording analyzed for this panel. b) Representation of the time-intervals described. c) Duration of each time interval (*y* – axis) at each cycle. d) Box-plot with the variability distribution of the duration of each time-interval. e) Time-intervals duration against the period for NX-duration (blue), NXNY-Interval (green) and NXNY-Delay (red)

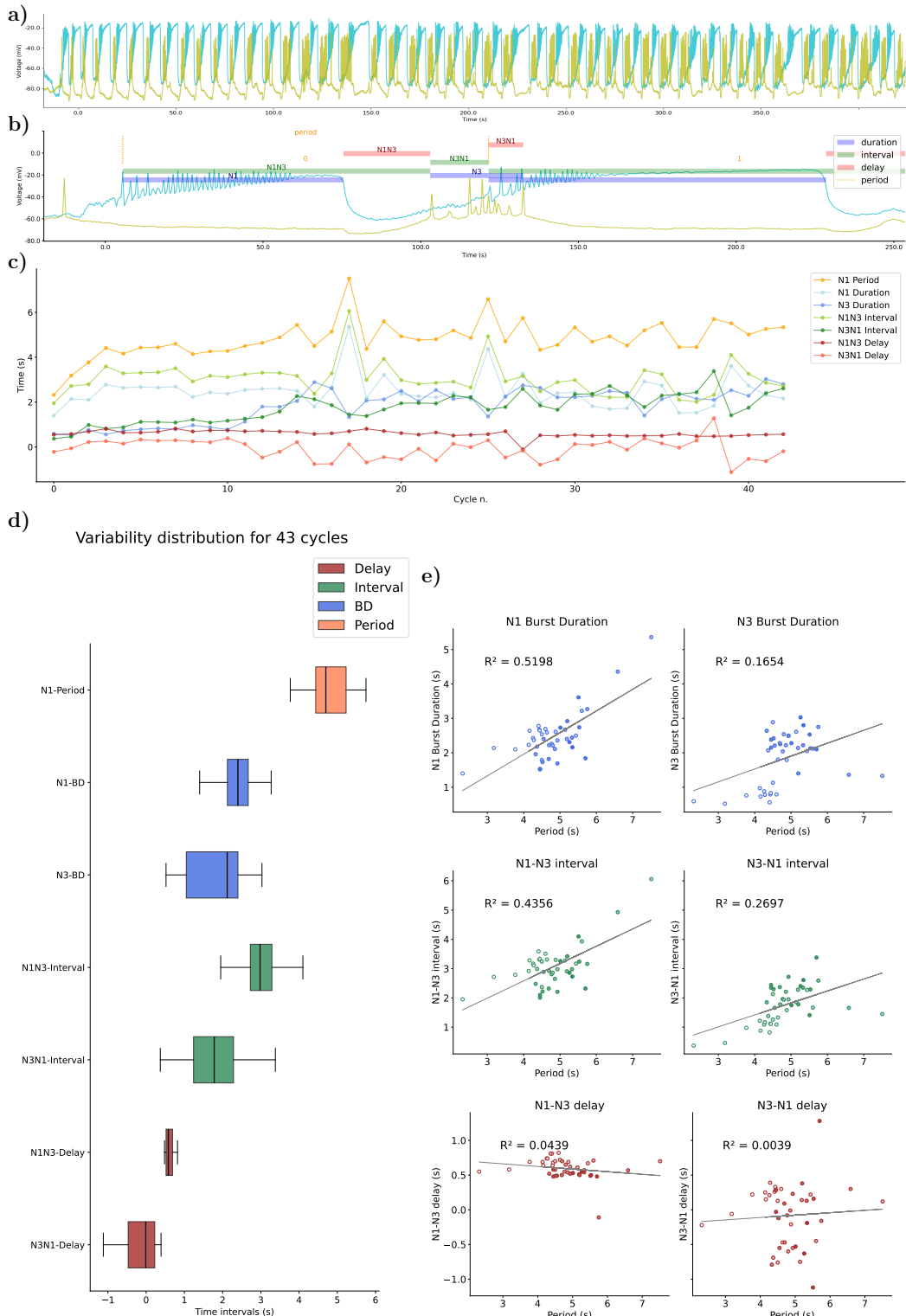


Figure 5.27: CV1a driven case 2: Panel of intervals distribution and dynamical invariants for the two phases in the CPG under CV1a stimulation. a) Voltage traces for the intracellular recording analyzed for this panel. b) Representation of the time-intervals described. c) Duration of each time interval (*y* – axis) at each cycle. d) Box-plot with the variability distribution of the duration of each time-interval. e) Time-intervals duration against the period for NX-duration (blue), NXNY-Interval (green) and NXNY-Delay (red)

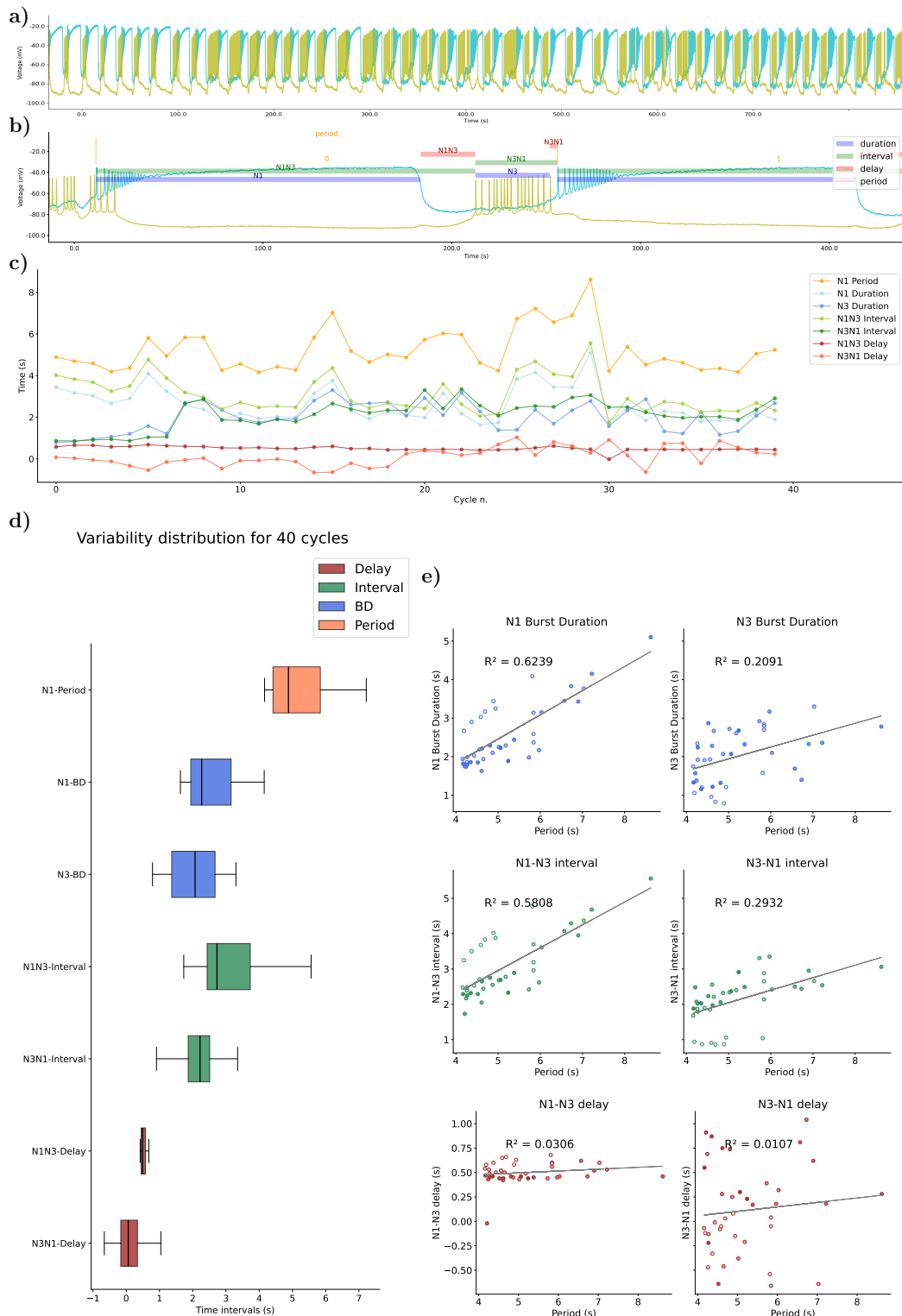


Figure 5.28: CV1a driven case 3: Panel of intervals distribution and dynamical invariants for the two phases in the CPG under CV1a stimulation. a) Voltage traces for the intracellular recording analyzed for this panel. b) Representation of the time-intervals described. c) Duration of each time interval (y-axis) at each cycle. d) Box-plot with the variability distribution of the duration of each time-interval. e) Time-intervals duration against the period for NX-duration (blue), NXNY-Interval (green) and NXNY-Delay (red)

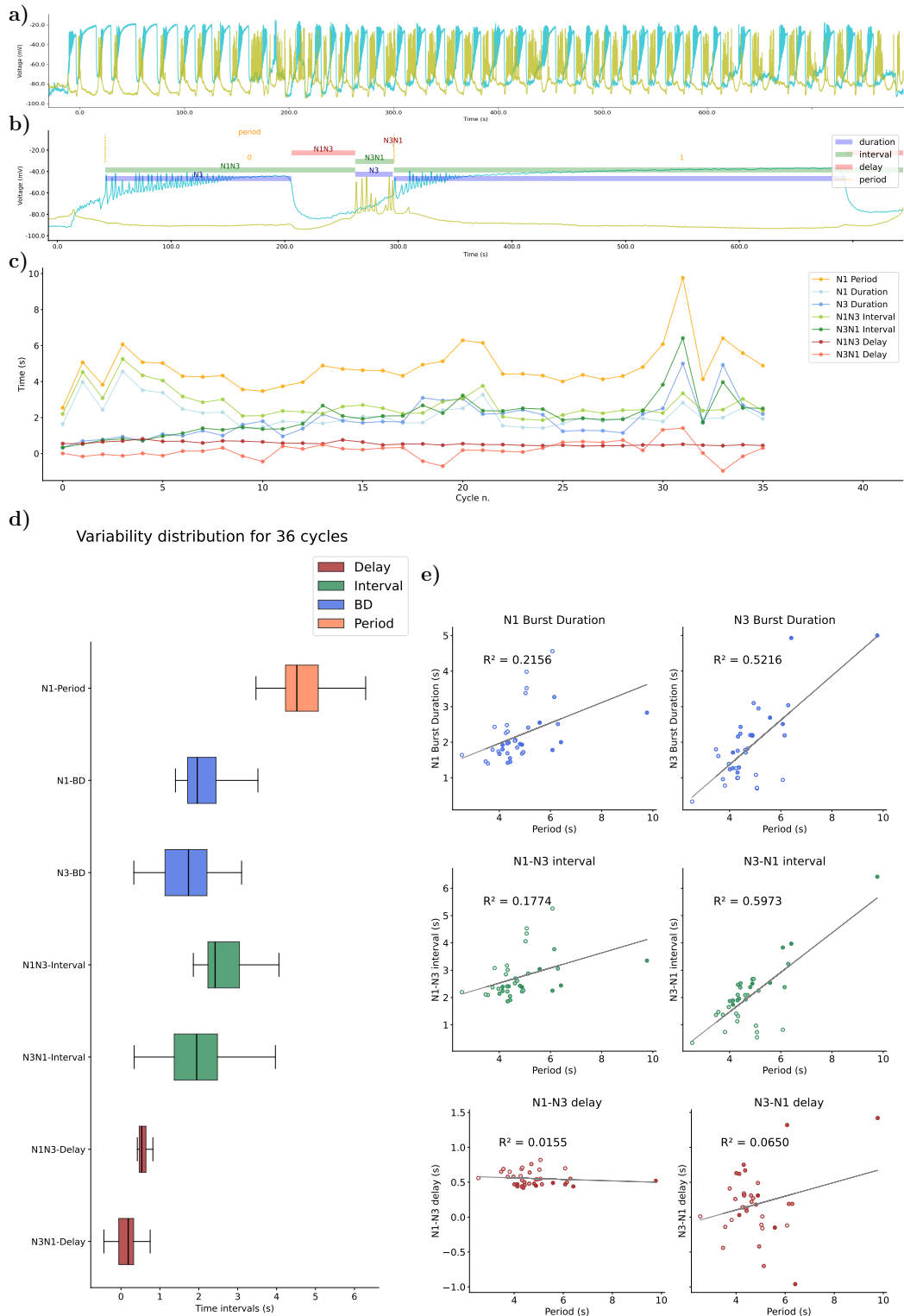


Figure 5.29: CV1a driven case 4: Panel of intervals distribution and dynamical invariants for the two phases in the CPG under CV1a stimulation. a) Voltage traces for the intracellular recording analyzed for this panel. b) Representation of the time-intervals described. c) Duration of each time interval (y – axis) at each cycle. d) Box-plot with the variability distribution of the duration of each time-interval. e) Time-intervals duration against the period for NX-duration (blue), NXNY-Interval (green) and NXNY-Delay (red)

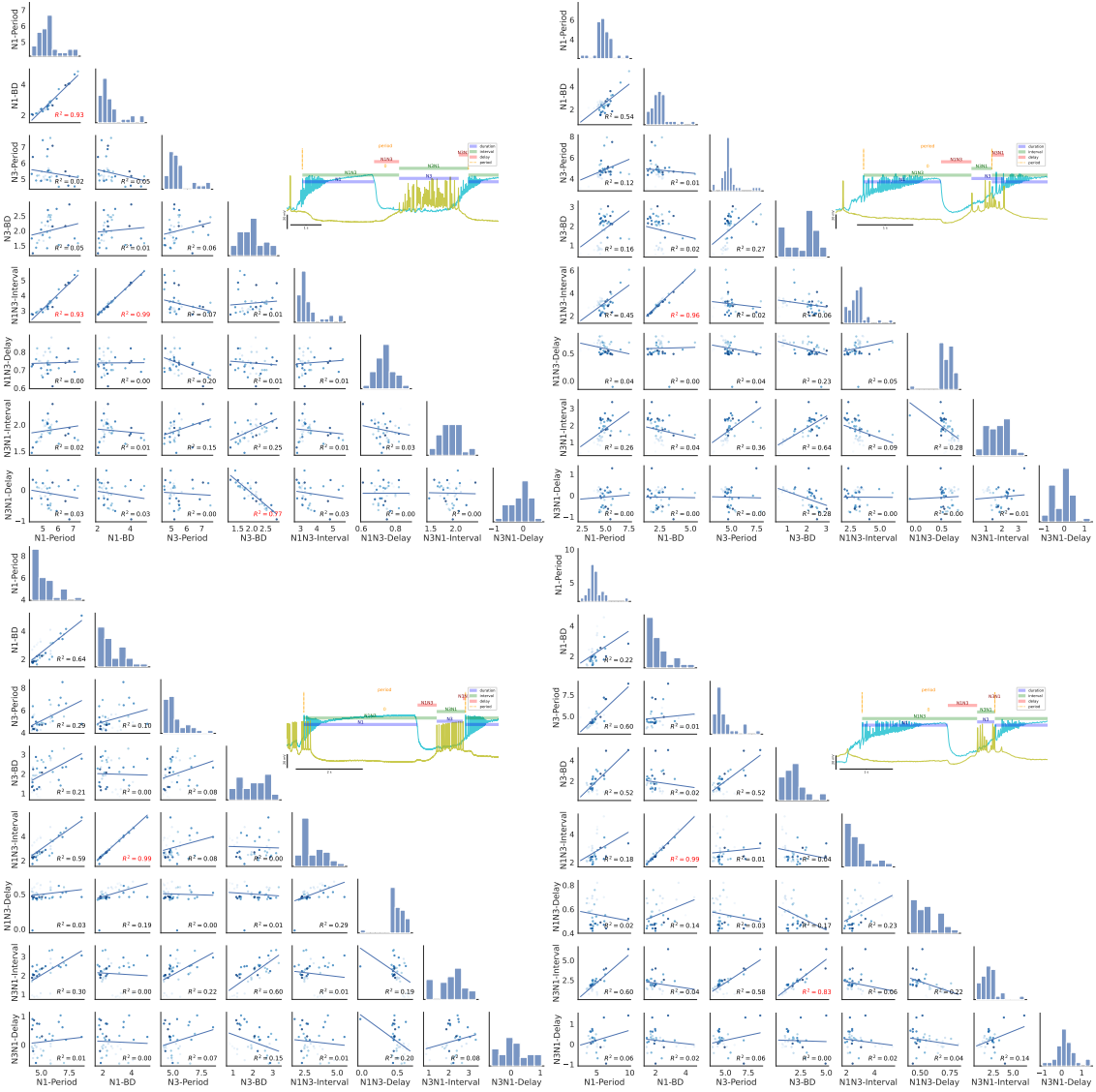


Figure 5.30: Panel of the pairplots for all possible combinations between the time intervals for two phases (N1 and N3) in the CPG recordings for the four examples of induced CV1a neuron modulation recordings.

5.4.5 Invariant resetting

There is another feature of the sequential dynamical invariants reported in Elices et al., 2019, that there is no relation of the time intervals cycle-by-cycle, which means there is no gradual modification of the rhythm but a stochastic relation. We saw that in panels of this section, where most cases represented an time-interval duration with no linear relation when represented against the number of the cycle. In the model the study of this phenomena was not possible since the current ramp provided a gradual change of the time-intervals duration and so forcing all intervals correlated in a period to be also correlated in the next one (see Appendix Fig. B.1).

In this subsection, we include several experimental examples of this relation in the examples presenting robust sequential dynamical invariants. We represent this "reset" with a pairplot gathering a cycle in the bottom triangle, and the relations of each interval with the next cycle represented in the upper triangle (Fig. 5.31). There it can be appreciated that when comparing the intervals of one cycle to the next one, the correlations disappear, the most clear example for this is the first figure, for the spontaneous activity, being all relations with a R^2 close to 0. In the two examples in the second row, the MLN stimulation and CV1a stimulation recordings, there are some strong correlations, but note that they are not in within the same intervals, e.g., the robust dynamical invariant in N1 burst duration with the period, disappear when comparing to the next cycle in both cases. The strong correlations are present between N1 and N3 periods and between N1 burst duration and N3 period. Both periods overlap, which can explain the relation. Therefore, cycle-by-cycle the variability is reset, there is not a restriction in the variability where the duration of a interval pre-defines the next one, but a stochastic distribution of the activity that is compensated cycle-by-cycle.

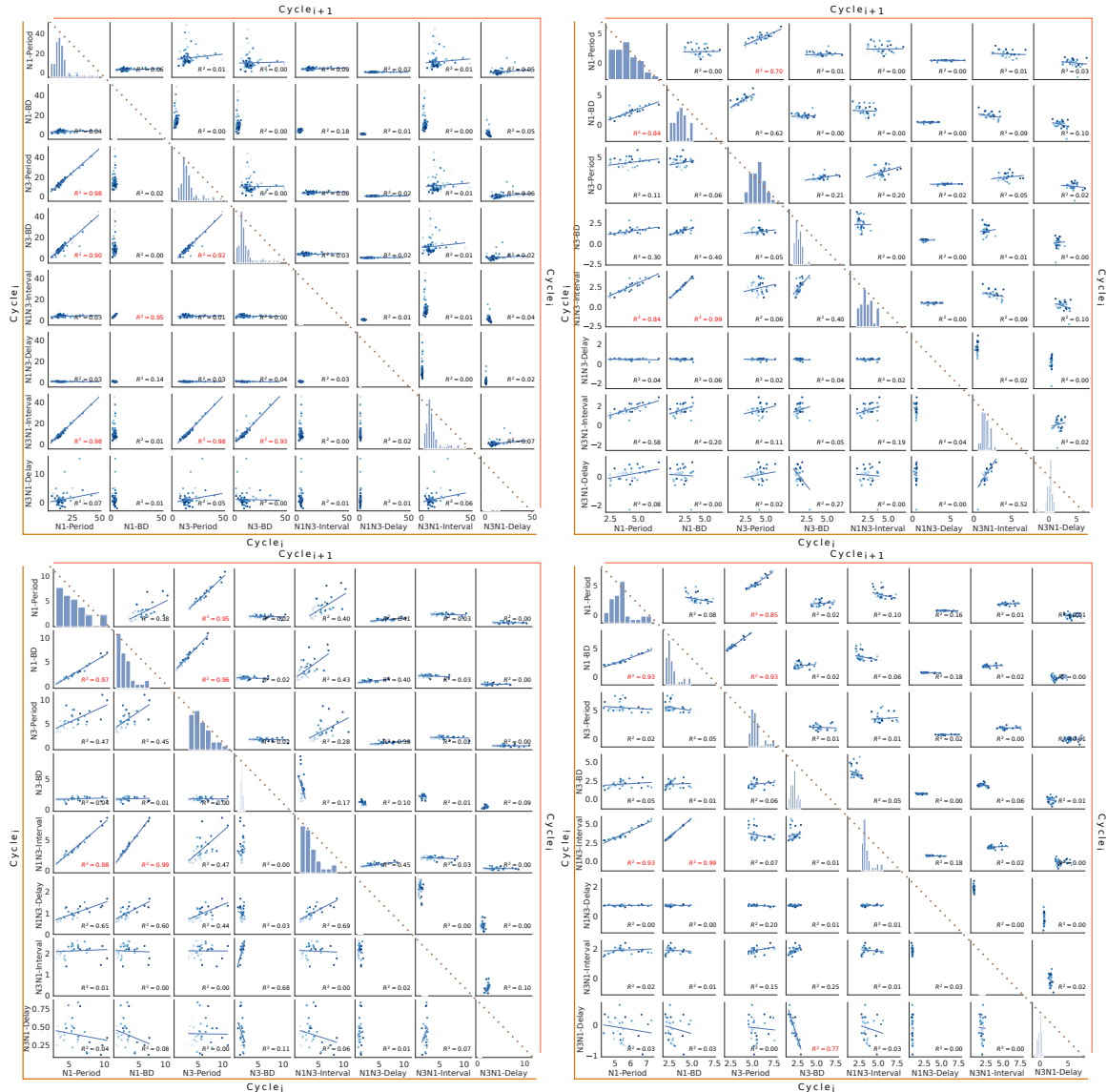


Figure 5.31: Panel representing the reset cycle-by-cycle of dynamical invariants. For each pairplot the lower triangle represent a cycle and the upper triangle represents the intervals of that cycle against the intervals of next cycle. The examples showed here are from top left to right: Spontaneous activity example 1 (Fig. 5.14), SO induced modulation (Fig. 5.22), MLN stimulation (Fig. 5.24) and Cva1 stimulation (Fig. 5.26)

5.5 Characterization of variability in bursting models and its functionality

Bursting dynamics has been extensively studied in a wide variety of neural systems, as it is instrumental for many brain functions, including motor coordination and cognitive performance, and can be related to both healthy and pathological states. Neuronal models in computational neuroscience often reproduce key functional features of their biological counterparts. However, they also present limitations such as their poor ability to mimic the observed intrinsic variability of living neurons, particularly in membrane potential waveforms and in collective adaptive dynamics. Biophysical models typically produce stereotyped fixed membrane potential depolarization and repolarization waveforms, and restricted dynamical flexibility as compared to those observed in experimental recordings. Variability in the activity of living neurons has been proven to play an important role in relevant information processing tasks. We have seen in this chapter, the importance of variability in the presence of sequential dynamical invariants in the bursting activity and the limitations of studying them in a model when the variability is induced by a current ramp stimulation. The variability in models has usually been induced by gaussian noise, but this ignores the importance of the functional variability in the neurons, the observed variability is not only a cause of stochastic alterations but a functional outcome.

In this line, in this section we will describe this variability characteristics in the living recordings, not only in their time-intervals but also in their waveforms and compare it with classical models and models able to reproduce chaotic activity. First, in Figs. 5.32 there is an example of the bursting and waveform variability in the intracellular recordings of LP and PD neurons in the pyloric CPG of *Carcinus maenas*. In both neurons we can appreciate a wide variability in the burst shape and duration, including the variability in the hyperpolarization.

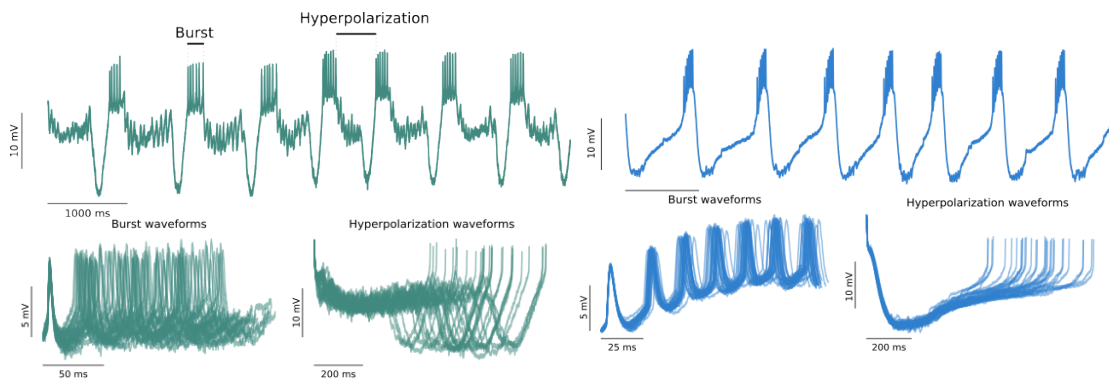


Figure 5.32: Example of variability in waveforms from intracellular recordings of the LP and PD neurons in the pyloric CPG

Although models can faithfully reproduce the activity and shape of neural models, they usually fail on reproducing the intrinsic and collective variability that we observe in electrophysiological recordings, this is the case for example of Hodgkin and Huxley, 1952b or Vavoulis, Straub, et al., 2007a, represented in Fig. 5.33. In that reproduction, although the waveform shape is accurate, the functional variability is hindered, reproducing a tonic and steady bursting activity.

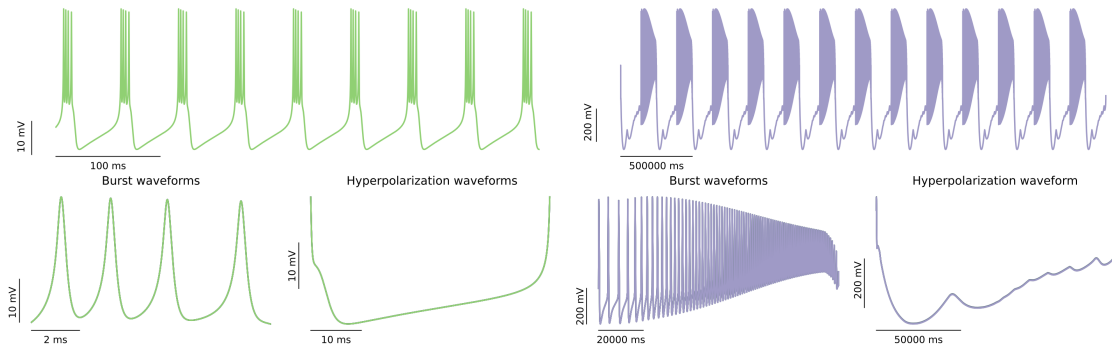


Figure 5.33: Example of bursts with no variability in waveforms from model simulation of neuron from Ghigliazza and Holmes, 2004 model in chaotic mode and N1M neuron from Vavoulis, Straub, et al., 2007a with no ramp stimulation in the CPG circuit. The equations for both models can be found in Secs. 5.2.4 and 4.4.1, respectively.

In section 4.4.1 we saw that variability can be induced by including a current ramp, although it can reproduce the variability, when studying the activity cycle-by-cycle it hinders the functional variability of the spontaneous activity.

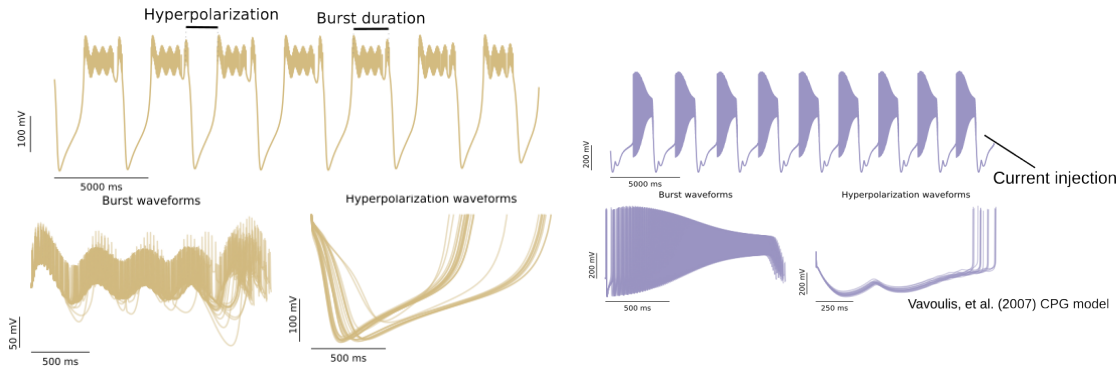


Figure 5.34: Example of variability in waveforms from model simulation of neuron from Nowotny et al., 2008 model in chaotic mode and N1M neuron from Vavoulis, Straub, et al., 2007a under current stimulation in the CPG circuit. The equations for both models can be found in Secs. 5.2.4 and 4.4.1, respectively.

Modern experimental techniques involving activity-dependent electrical, optical and chemical stimulation can further unveil and explain functional variability of bursting sequences in a wide variety of nervous systems, it is important to rely on models able to reproduce the intrinsic variability. It will also be relevant for designing associated applications in the context of neurotechnology, artificial

intelligence and robotics (Garrido-Peña et al., 2024).

5.6 Transformation of sequential intervals into effective robot movement

To validate the importance of the balance between robustness and flexibility in the CPG circuits, as provided by cycle-by-cycle dynamical invariants present in its dynamics discussed in this chapter, we include in this section a first approach of the translation of dynamical invariants into an effective motor locomotion in a Functional-Living-Circuit-Hybrot (FLC-Hybrot). This work was published in Amaducci et al., 2020, 2021. The combination of models, novel tools and experimental approaches has proven its effectiveness revealing and exploring features of neural dynamics (Chamorro et al., 2012; Reyes-Sánchez et al., 2023; Szücs et al., 2000). In this first step into the applications in robotics of the variability time constrains found in CPGs, we built an hexapod robot whose legs performed oscillatory motions to move forward. The period and amplitude of these oscillations were determined by the sequential cycle-by-cycle activity of the CPG neurons recorded from the living preparation and sent online to the robot. At the same time, the hybrot included a light sensor and sent feedback information regarding the light conditions around it back to the neural circuit in the form of an electrical current. These stimuli modified the behavior of the cells, resulting in a change of the hybrot locomotion, preserving always the required motor coordination, and therefore forming a real-time closed-loop interaction among living and electronic components (Figure 5.35 shows a summary of these interactions). The goal of the FLC-Hybrot is to demonstrate that a dynamical principle of the functional living circuit can be used to coordinate the locomotion with sensory feedback from the robot. In our case, we use the presence of dynamical invariants in the form of robust relationships between the time intervals that build the cycle-by-cycle activity of the CPG in the neurons of the pyloric CPG in *Carcinus maenas*, which are sustained under any circumstances even when there are external inputs to the circuit, to modulate the behavior of the robot. There is a detailed description of the experimental setup of the robot in section 5.2.5

To validate the adequate locomotion of the FLC-Hybrot when modulated by the pyloric CPG online behavior, as well as the living circuit real-time adaptation to the injected feedback, we performed a set of experiments employing a 1.5 meters long trial track. Along this surface there were interspersed segments of lights and shadows. This configuration caused the FLC-Hybrot to alter its behavior several times during the experiment due to the injection of current into the PD neuron when it walked under a shadow. The current injected in the cell in a shadow section varied from one experiment

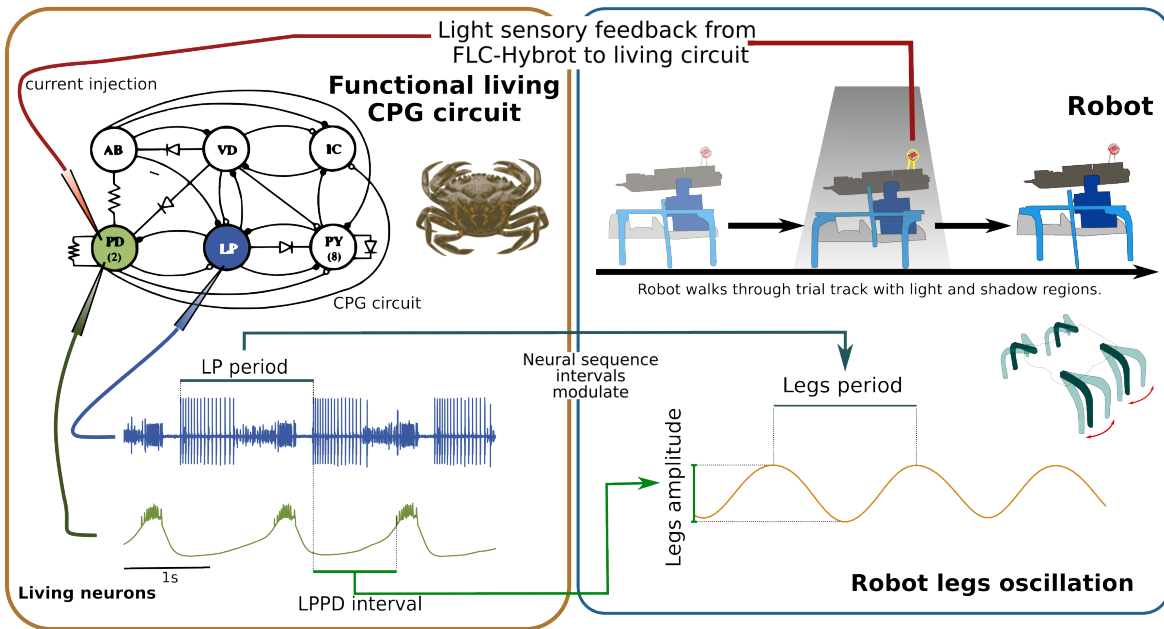


Figure 5.35: Representation of the FLC-Hybrot paradigm design. Neural dynamics from a functional living CPG circuit are recorded online and used to coordinate the robot movement in real-time. Activity from the PD neuron is recorded intracellularly (green trace), while the LP bursts are extracted from the nerve's extracellular signal (blue trace). This robot walks through a trial track with interspersed light and shadow regions. When the robot's light sensor detects that it is located under a shadow, it sends feedback current to the living circuit. CPG dynamics change as a reaction to the injected current, thus modifying the robotic locomotion. The following video shows an example of this experiment <https://youtu.be/ny2dJGbG8lo>.

to another, according to the neurons response to the stimuli. No current was injected when the robot was located on a luminous area. The following video illustrates one of such experiments <https://youtu.be/Dltec7TeGso>.

Figure 5.36 shows the results for one of these tests. We observe an alteration of the neural when -0.6nA current is inserted into the circuit, causing its rhythm to slow down while also modifying the PD neuron membrane's potential amplitude. This change is immediately reversed as soon as the current goes back to zero, restoring its previous behavior. Concerning the robot's locomotion, a variation in the legs' oscillation is observed just after the neurons alter their functioning. Despite the successive changes in the amplitude and period of its legs' oscillation, the FLC-Hybrot maintained a coordinated and effective locomotion during the whole experiment.

We know that in the pyloric CPG there is a sequential dynamical invariant, in the form of a linear relation between the LP neuron period and the LPPD interval. These are the intervals used to modulate the amplitude and period of the legs oscillation in the robot. This constrain was effectively transferred to the robot locomotion. Figure 5.37 shows a comparison between the living CPG and the robot

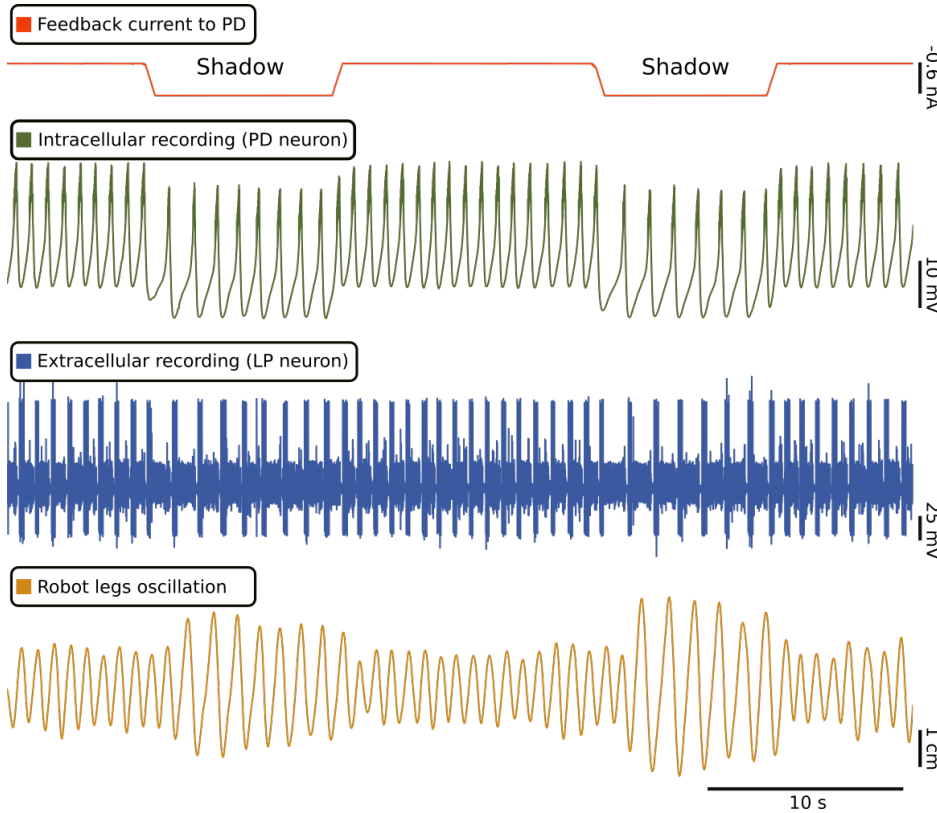


Figure 5.36: Flexible hybot adaptation to environmental changes when noticed by the robot sensors and associated coordinated locomotion. When the robot entered a shadow section, it sent sensory feedback to the living CPG in the form of positive electrical current (red trace). Blue and green traces are recordings of the extracellular and intracellular (PD neuron) activity of the circuit and display the change caused by the feedback current injection in the PD neuron, slowing down the CPG rhythm. The oscillatory movement of the robot legs is represented in the brown trace and it can be observed that a variation in the CPG rhythm leads to a change in the robotic locomotion, modifying both the period and the amplitude of the oscillation.

dynamical invariant, with the later reaching an R^2 correlation of 0.87 despite the lack of precision of its servomotors. It displayed the same correlation between its legs oscillation period and amplitude, which were modulated by the two previous temporal intervals.

This tested scenario, can help simulate context change situations in which the CPG rhythm is altered and there is a change of variability reflected in the relations between the intervals cycle-by-cycle. The reproduction of biological dynamics with its time constraints can have strong implications in robotics locomotion but also in neurorehabilitation processes. It can also help explain and associated the observed phenomena of sequential dynamical invariants to its living functionality.

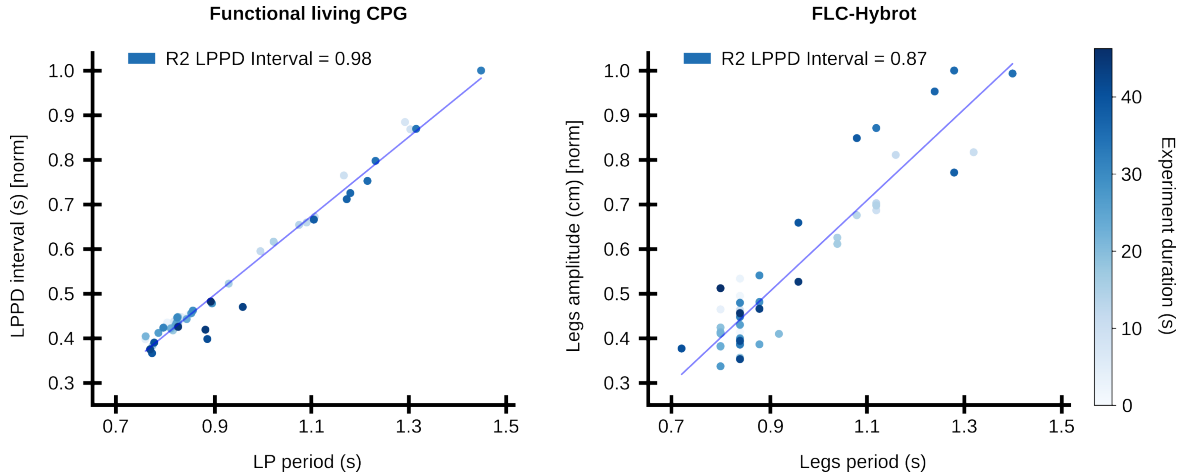


Figure 5.37: **Left:** dynamical invariant present in the living CPG activity during the validation test, represented as a linear relation between the LP neuron bursting period and the LPPD interval cycle-by-cycle. **Right:** dynamical invariant present in the FLC-Hybot locomotion during the validation test, represented as a linear relation between its legs oscillation period and amplitude cycle-by-cycle. The dynamical invariant property is effectively translated from the living CPG to the robot locomotion, codified as: Robot period = LP period, Robot amplitude = LPPD interval * factor.

5.7 Discussion

In this chapter, we studied the sequentially analyzing the bursting activity of the feeding CPG in *L. stagnalis*. As discussed before, this CPG is ideal for this kind of study due to their ability to maintain a robust sequential activation and still present a high flexibility to adapt to changes in the context. Also, the bursting activity provides clearer references than in other more complex circuits.

In this system addressed the characterization of the intervals building up the rhythmic sequence in this system with model simulations and also in experimental intracellular recordings. We tested the presence of sequential dynamical invariants in the form of linear relationships between the sequence intervals and the cycle period of the rhythm following the experimental results that we reported in Elices et al., 2019 for the crustacean pyloric CPG. Most extended studies usually study the averaged variability, masking the information in the relations taking place at each cycle of sequential activations. Taking that into account, here we characterize the variability cycle-by-cycle.

In the model, we extended the analysis of the reported relations by Elliott and Andrew, 1991 by characterizing each and every interval building the sequence and relating the strong linear relationships found in specific intervals to the concept of robust sequential dynamical invariants proposed in Elices et al., 2019 for the coordination of robust yet flexible CPG rhythms. In the simulations, three main cases have been addressed in the analysis: N1M-driven, SO-driven and N3t-driven stimulation.

This was based on the two different possibilities of inducing variability in the model according to the results reported in Vavoulis, Straub, et al., 2007a, as well as with a third neuron stimulation (N3t) which is easily addressable in the model circuit. When variability arises by the stimulation of N1M, the results are rather similar to the ones obtained stimulating N3t. Strong linear correlations to the period, i.e., dynamical invariants, are present mainly in all intervals related to N3 phase, since these are the ones with cycle-by-cycle variability related to the period variability.

We also show the redistribution of variability that takes place when the stimulation is applied on SO. In this scenario more intervals presenting large variability than in the other stimulation protocols are found. This is due to the specific variability of N1M and N3t burst duration, since in this case the largest influence on the period seems to come not only from N3t but also from N1M. Hence, consequently to the variability analysis, different linear relationships are found involving all intervals related to N3 and N1 phases. The intervals unrelated to the period are the ones associated with N2 phase, which is also the least variable entity in the circuit.

These results reproduce and extend the ones discussed in Vavoulis, Straub, et al., 2007a and Elliott and Andrew, 1991. It is interesting to highlight the differences in the results when the period is driven by N1M/N3t or SO. When the variability is induced in N1M/N3t, N3t is still able to inhibit the N1M neuron carrying the main variability, while SO is adapting to both. However, when SO is the neuron being stimulated, since it is connected to N1M by mutual excitation, they are both boosting each other's activity, leading to the higher variability of N1M. Here, N3t must adapt to N1M, which is harder due to the SO constant excitation. For this reason, it was necessary to inject some additional current in N3t in the simulations, which would usually be an input received from the cerebral ganglia.

Each of the three phases of the rhythm corresponds to a specific motor action: N1 protraction, N2 rasp and N3 swallow. As it is pointed out in Elliott and Andrew, 1991, the motor sequence consists of a two-stroke relaxation: protraction and rasp (N1,N2), in charge of moving the radula, and swallowing (N3). In these kind of systems, it is common to find one of them fixed and the other one variable, which in our case is the swallow phase. In this context, SO stimulation can be related to sucrose stimulation P. R. Benjamin, 2012; Kemenes and Elliott, 1994, this could be related with the increase in N1M variability, since in presence of food, protraction phase may become crucial for an effective food reaching. Thus, there might be now two phases showing more variability in their intervals duration. The discussed invariants can participate in the coordination of these mechanisms by imposing variability constraints in only specific intervals of the motor sequence. The results shown in this paper also indicate that distinct constraints in the form of dynamical invariants can emerge in the same network under different behavioral contexts.

The flexibility of this model to adapt the induced variability into the system is not an easy feature to achieve. Some characteristics in the description of this model such as the gradual synapse and the separation between fast and slow dynamics for each neuron, might be key achieving this. Although this realistic definition of the interrelations between the neurons in the CPG in this model, allowed the study of dynamical invariants, inducing the variability by a current ramp injection hinders the functional variability generated by the neurons and the spontaneous activity of the neurons. We saw this limitation when study the experimental intracellular recordings, where spontaneous activity and induced modulation recordings, showed the variability cycle-by-cycle, and the stochastic sequence of time-interval durations.

In the experimental study, even under those scenarios of high stochasticity, we showed that there were strong linear relationships in the form of sequential robust dynamical invariants in some of the intervals. Also, as we observed in the model, depending on the source of the activation, the distribution of variability and the intervals presenting this strong relationships changed. In the case of spontaneous activity, we found a different situation for each, the most robust example was a strong linear correlation for N3 phase, in a recording where the N3 seemed to be inducing periods of silence. In the other two cases, the variability was shifted, having N1 a larger relation to the period cycle-by-cycle and with a distribution of variability between both. What we saw in this case, and in the rest of the experiments in that section, was the absence of relation between N2 phase and the period, which means, the variability in each cycle is not carried by the rasp phase, which has a constant and low variable activation. Apart from the spontaneous recording, we analyzed three cases of CPG activity modulation: SO neuron driven, MLN stimulation and CV1a neuron driven. Each case is associated to a different source or modulation of the activity, with functional processes related and for each one we observed a different distribution of the variability between the time-intervals. During the SO modulation, in spontaneous and induced scenarios we saw, as in the model, that variability was carried by N1 and N3 phases, having both relation to the period cycle-by-cycle, being stronger in the case of N1. When stimulating the middle lip nerve (MLP), directly connected to the N1M to activate the rhythm, there was a robust sequential dynamical invariant in N1, showing that during this activation (in the simulated presence of food) the role of protraction phase was key, carrying all variability. Finally in the CV1a neuron stimulation, the N1 phase was again the one with a larger relation to the period, showing also that a small change in that stimulation, altered the distribution of variability shifting to N3 phase and the related intervals.

With these results, we saw the potential of dynamical invariants as functional variability indicators, since they reflect a balance between the robustness of the sequence and the flexibility to accommodate

longer or shorter intervals from the network interaction. The distinct sources of feeding activation changed the classification of variability, adjusting the importance from one phase to another. Also, in the model we saw that this phenomena is highly dependent on the intrinsic dynamics, network topology and synaptic dynamics that contribute to the generation of the dynamical invariants. Their observation in the model simulations where only possible when other neurons in the circuit adapted their activity to the neuron with the induced variability.

The study of cycle-by-cycle invariant relationships, found not only in experimental recordings but also in computational models as we report here, highlights the presence of organized variability in a motor rhythm. This points to the universality of this phenomena, and the functional associations to it show its potential as time indicator. The applications to this indicator can be key for future clinical applications, specially for novel neurotechnology tools. In this line, we showed a first approach of the extrapolation of this restrictions into an effective locomotion in the FLC-Hybrot. The hexapod robot showed that it is possible to translate the dynamical invariants into the relation between the oscillation amplitude and period, showing the possible future applications of locomotion based on the CPG features. This study paves the way for further exploration of dynamical invariants in more complex neural systems and their practical applications.

CHAPTER 6

CW-NIR laser as an effective neuromodulation technique

We saw in the previous chapter the importance of effective stimulation techniques to alter and explore the sequential neural dynamics in single neurons and circuits. In this chapter we will explore a novel neurotechnology to stimulate and alter neural activity in a potentially noninvasive manner: Continuous-wave Near-Infrared (CW-NIR) Laser. We will address its effect in single neurons dynamics in sustained and activity-dependent protocols, discussing the main biophysical candidates generating the experimental observed effect by the joint analysis of experimental and computational data. With the novel closed-loop protocol we will also assess the neural dynamics in in the sequential activation of ionic-channels in the action potential generation.

6.1 Introduction

Effective neural stimulation is an essential tool to study brain dynamics. Many techniques have risen since the first use of electrical, chemical and mechanical stimulation, e.g., see Refs. (Bickle, 2016; Carter & Shieh, 2015; Chamorro et al., 2012; Cogan, 2008). Optical methods are also widely spread, as they allow visualization (Lecoq et al., 2019) and stimulation in a less invasive manner. One example is optogenetics (Bansal et al., 2022; Boyden et al., 2005; Tye & Deisseroth, 2012; Yizhar et al., 2011), which is effective in modifying neural activity with high spatio-temporal resolution. Another example of non-invasive stimulation is Transcranial Magnetic Stimulation (Valero-Cabré et al., 2017), which is succeeding in clinical applications. However, they both present limitations such as the need to genetically modify the living system or restricted spatial precision, respectively. In this context, infrared laser stimulation is an optical technique that has risen in popularity in the last

decade. From its first applications (Izzo et al., 2007; J. D. Wells, M.D., et al., 2005a), studies have shown its ability for modulating action potentials in different systems (Barrett et al., 2018; Begeng et al., 2022; Brown et al., 2020; Cayce et al., 2014; Goyal et al., 2012; Liang et al., 2009; Shapiro et al., 2012). Beyond its potential as a research stimulation technique, it has also been tested for clinical use, e.g., in Parkinson's disease, reversing brain age-related effects or depression treatment (Disner et al., 2016; Konstantinović et al., 2013; Pan et al., 2023; Saucedo et al., 2021; Wang et al., 2017). This neural stimulation method is so attractive because of the wide range of possibilities that can provide for non-invasive neuromodulation offering high temporal and spatial precision.

The identification of the biophysical source of infrared neuromodulation is still under discussion as it has strong implications for applications in multiple contexts. It is difficult to associate this modulation to a single specific cause, since neural systems have distinct biophysical components reactive to the irradiation. However, most of the results point to a photo-thermal effect where the excitation driven by the laser stimulation might be caused by temperature gradient (J. Wells et al., 2007). In addition, different candidates to explain the change in neural activity have been suggested, such as capacitance (Plaksin et al., 2018; Shapiro et al., 2012), specific modulation of channels sensitive to temperature as TRPV4 (Albert et al., 2012), acceleration of ionic channels (Liang et al., 2009), or altering the Ca^{2+} cycle possibly mediated by modulation of mitochondrial activity (Dittami et al., 2011; Lumbrales et al., 2014; Saucedo et al., 2021).

Distinct types of infrared laser and action modes, in terms of the power, duration, frequency of stimulation and wavelength have been used in previous studies, see Refs. Izzo et al., 2007; Ping et al., 2023; J. D. Wells, M.D., et al., 2005a. The effect is highly dependent on the stimulation configuration. Most works have focused on pulsed lasers to induce spiking activity due to their stronger temperature gradient production. However, some clinical studies have successfully applied continuous-wave (CW) laser for brain stimulation (Saucedo et al., 2021).

The use of closed-loop techniques has a large potential in neuroscience, for both physiological and clinical research studies (Chamorro et al., 2012; Couto et al., 2015; Lareo et al., 2016; Linaro et al., 2015; Potter et al., 2014; Reyes-Sanchez et al., 2023; Varona et al., 2016; Zrenner et al., 2016), since they allow adjusting the stimulation to the context of the ongoing neural dynamics and the specific condition of the targeted system/subject. Some of these tools have been developed with open-source approaches, including optical techniques, e.g. Refs. (Amaducci et al., 2019; Dagnew et al., 2017; Robbins et al., 2021; Siegle et al., 2015; Štih et al., 2019), promoting the accessibility, reproducibility and standardization of the studies and methods. However, near-infrared (NIR) lasers have been used with fixed/periodic stimulus and, to the best of our knowledge, they have not been

exploited in activity-dependent protocols.

Here we explore the effect of CW-NIR laser on the dynamics of individual neurons in sustained and activity-dependent stimulation protocols. We employ a laser with constant optical power density on the sample for these two modalities. In the first case, the laser stimulation is sustained –the duration of the illumination is constant for more than 1 minute–, and in the second case it is driven in an activity-dependent manner implemented by the open-source RTXI(Patel et al., 2017) Linux software –the onset of the stimulation is determined by ongoing neural events and delivered transiently through software control–. We studied the effect of CW-NIR illumination focused on neurons with spontaneous tonic firing. Combining experimental results with modeling analysis allowed exploring the candidates that can explain the observed neuromodulation. We present a novel procedure for NIR laser stimulation to dissect and intervene in the waveform dynamics through activity-dependent stimulation. By interlacing results from theoretical simulations and sustained and activity-dependent stimulation, we identify the dynamical elements behind action potential dynamics under CW-NIR modulation. We discard any single candidate of the biophysical effect as the joint experimental and model analyses indicate that laser illumination affects multiple membrane factors simultaneously.

6.2 Methods

6.2.1 Sustained CW-NIR stimulation protocol

After the isolation of the *Lymnaea stagnalis* neural system, we searched for suitable neurons in the right parietal ganglion, i.e., cells with spontaneous activity preferably with fast activity and shoulder or symmetrical type in the spike waveform. Once the target neuron was identified, the laser was set-up. A lens with focal distance of $f=50\text{mm}$ was used and no polarizer was installed on the optical path. Guided with the microscope camera, the laser spot was located and then placed first over the ganglion and subsequently over the specific neuron where the electrode was recording the activity. At this point, the laser was focused with the micro-manipulator adjusting the focal distance. Finally, the laser power was increased to the above mentioned value for the experiments.

Once the laser spot was over the neuron while the membrane voltage was simultaneously recorded at the soma with the intracellular electrode, we followed the protocol described below to measure the effect of the CW-NIR laser on the activity of the neuron:

1. First control. The spontaneous activity in the neuron was recorded for 1-3 minutes, depending on the spiking frequency of the cell. During this control, there was no external modulation of

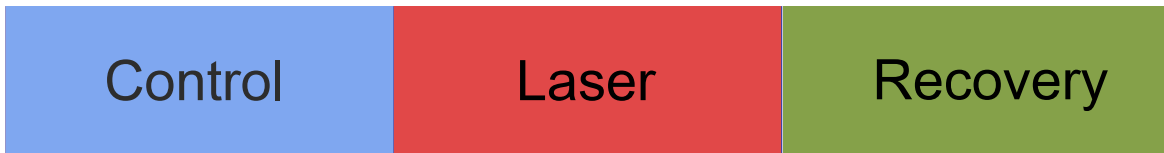


Figure 6.1: CW-NIR laser stimulation protocol sequence: Control, laser stimulation and recovery.

the neuron apart from the possible alteration by the intracellular procedure.

2. Laser stimulation. The laser was on during the same lapse of time than in the first control, stimulating the neuron with a constant optical power density. There was no modification in laser parameters during this time.
3. Recovery. After the illumination was off, a second control was performed, under the same conditions as the first one. During this recovery control, the activity in the neuron after the effect of the laser was recorded.

The sequence involving control, laser and recovery trials was replayed in each experiment (day and individual) for five times. Between each trial, the laser illumination was supervised to ensure that the spot was still over the neuron, guaranteeing that the procedure had as low variation as possible. Also, the laser was only turned off during the controls, it was not set aside, since that would have forced to redo the set-up for every trial altering the reproducibility between trials. The effect for each trial of a given day was very similar. For the analysis in Figure 6.6, the trial with the strongest effect in the day was selected.

6.2.2 Activity-dependent laser stimulation protocol

For stimulating the neurons depending on their ongoing activity, a closed-loop protocol was designed in the RTXI real-time software (Patel et al., 2017). This hard real-time tool allows an easy integration of new modules to read ongoing activity, process it online and send feedback in the form of analog signals. The real-time module designed for this experiment followed the scheme illustrated in Fig. 6.2. After processing the signal in RTXI, a TTL pulse was sent to the controller opening the laser shutter for the desired time, and thus stimulating the neuron during that time interval. Simultaneously, the neural activity was recorded, along with the TTL and the shutter feedback (recording the shutter delay with respect to the on signal).

The CW-NIR laser light was blocked with a mechanical shutter (Thorlabs SH05, Newton NJ). The shutter utilized in this work had a ~ 8 ms delay from the trigger signal, which might be a limitation for

neural stimulation in fast spiking cells. The slow spike dynamics in the neurons used for this research are compatible with this restriction and the protocol was developed considering this limitation.

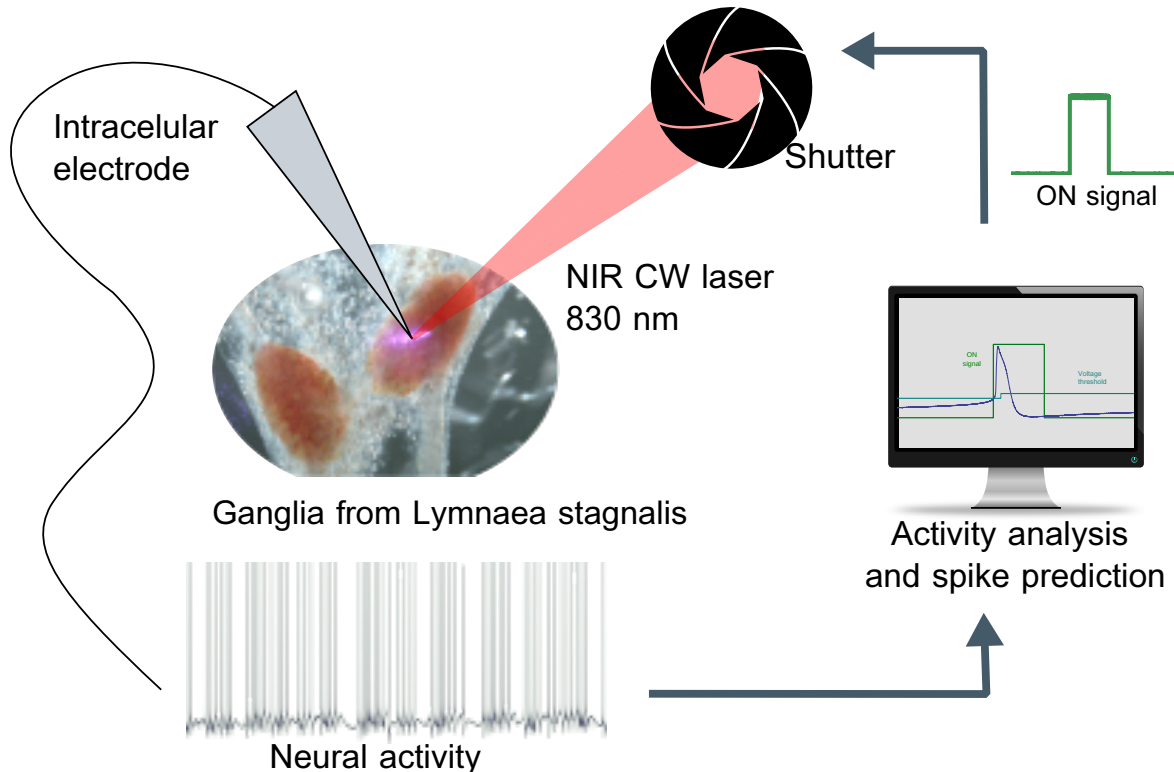


Figure 6.2: Activity-dependent protocol scheme. Neurons were recorded intracellularly and their voltage signals were processed in real-time with the RTXI software. Using the spike prediction algorithms, the shutter was triggered at the desired action potential phase illuminating the neurons.

The main challenge in this protocol is the identification of the specific phase of the spike waveform to deliver the stimulus, i.e., predicting the spike, since spontaneous neural activity has intrinsic variability that requires the online adaptation of specific thresholds instead of a hand-tuned preset value. For this purpose, the protocol relied on the reference values from the previous spike at a specific time interval from the peak. The voltage threshold was calculated based on the voltage value measured in the previous spike, and recalculated at each action potential. Thus, after each spike, the threshold for the spike prediction was updated using the following equation:

$$V_{threshold} = V[t_{spike}[i - 1] - \tau], \quad (6.2.1)$$

with τ being the selected time for the prediction before the spike and t_{spike} the time instant of the spike peak.

This prediction is effective for stereotyped spikes when only low amplitude subthreshold oscillations occur, but it is limited in other scenarios. Therefore, for neurons or action modes of the same neuron

when it was necessary to stimulate before the depolarization rise, another reference was used: the area of the recorded voltage. In this other mode of the protocol defined in Eq. 6.2.2, the voltage was accumulated along the activity and the sum was reset after each spike.

$$V_{area} = \int_{V[spike_{i-1}]}^{V[spike_i]} V(t). \quad (6.2.2)$$

The stimulation was triggered when the area reached a specific threshold, which was predicted as in the voltage case, or hand-tuned. For the detection of the minimum point to reset the voltage area, we used a RTXI module based on RTHybrid, a real-time software that includes automatic adaptation algorithms to handle the ongoing variability of the recordings (Amaducci et al., 2019; Reyes-Sanchez et al., 2020; Reyes-Sanchez et al., 2023), github.com/GNB-UAM/RTHybrid-For-RTXI. The use of each mode of the protocol in the experiment was decided depending on the specific requirements of the recorded activity.

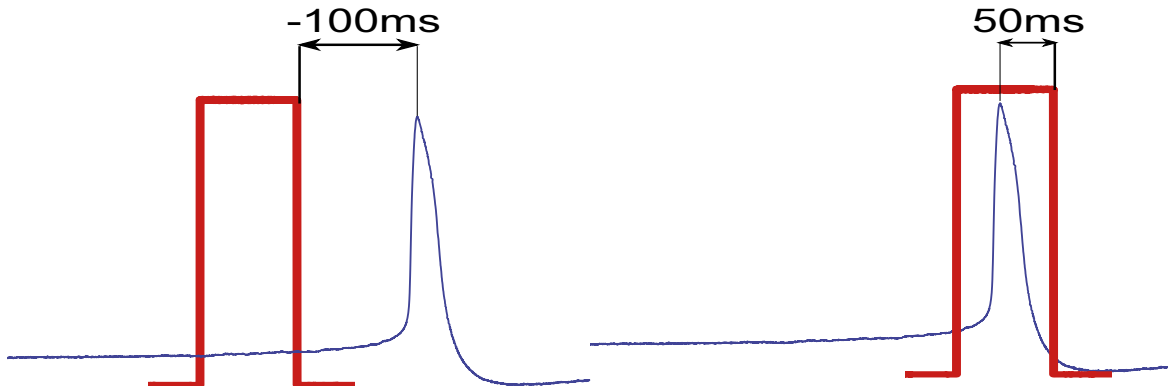


Figure 6.3: Examples of illumination offset, defined as the time interval from the end of the illumination to the peak of the spike.

Using this detection protocol, we assessed the effect of the illumination at different phases of the action potential in the range from 100 ms before the spike peak to 80 ms after the spike peak (see an example of the illumination offset in Fig. 6.3). The illumination interval was 58 ms, validated as the minimal duration for effective stimulation in the test trials. The RTXI module programmed for this study is available at github.com/GNB-UAM/spike_predictor.

6.2.3 Spike waveform characterization parameters

For both experimental recordings and model simulations, action potentials were detected as the maximum point over a threshold, and each waveform was segmented 100ms before and after the peak temporal reference. For the superposition of action potentials (Figs. 6.6, 6.13, 6.14) the waveforms

were aligned in the x -axis by the peak and in the y -axis by the first point of the waveform voltage values.

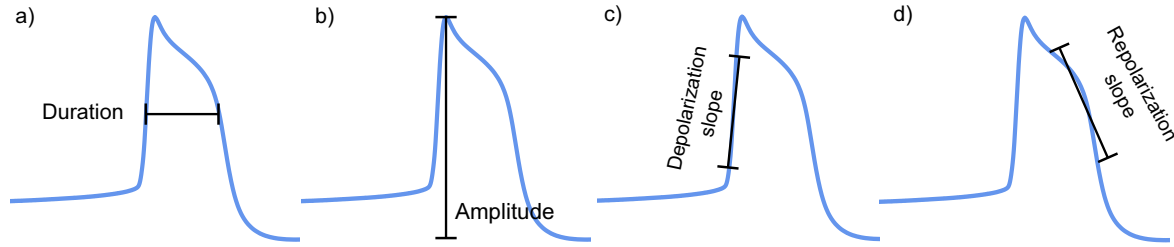


Figure 6.4: Representation of waveform shape's metrics: a) Spike duration at half width. b) Spike amplitude between the maximum and minimum voltage values. c) Depolarization slope at half width. d) Repolarization slope at half width.

For the waveform shape characterization, we used four metrics: duration, amplitude, depolarization and repolarization slopes. They are depicted in Fig. 6.4 and defined as follows:

- Duration: Time interval between the two points at half width of the action potential.
- Amplitude: Difference between minimum and maximum voltage values in the waveform in the analyzed segment.
- Depolarization slope: Slope in the depolarization phase (previous to the peak) measured 1 ms before and after the half width point reference.
- Repolarization slope: Slope in the repolarization phase (after the peak) measured 1 ms before and after the half width point reference.

These metrics were used for the quantitative analysis of the change in experimental recordings and model simulations. In Sec. 6.2.4 below we describe the quantification methodology for the waveform metric change as well as for the comparison between the experimental and model results.

6.2.4 Statistical Analysis

The statistical significance analysis in the data obtained from the sustained CW-NIR stimulation protocol in Figure 6.6 was performed applying a paired T-test to the four spike waveform metrics characterized here (see Fig. 6.4). Data from distinct experiments was gathered and paired by recordings of control-laser and control-recovery (see Fig. 6.6C). The null-hypothesis tested was that control group was equal to the laser group and that the control group was equal to the recovery group, respectively. Since we performed the test in the four waveform metrics –spike duration, depolarization

slope, repolarization slope and amplitude— we applied the Bonferroni correction, thus we considered high-significance when $p < 0.01/4$.

To compare recordings from different neurons, we normalized the change between the laser and the control conditions for each waveform metric using the following expressions for electrophysiological data:

$$\text{metric change}_{\text{experimental}} = \frac{|\mu(\text{metric}_{\text{laser}}) - \mu(\text{metric}_{\text{control}})|}{|\mu(\text{metric}_{\text{control}})|}, \quad (6.2.3)$$

where $\mu(\text{metric}_{\text{laser}/\text{control}})$ is the mean of the corresponding metric for all waveforms in a given laser stimulation or control trial.

Analogously, to compare the change between the distinct model simulations we normalized the change in the parameter-driven simulated variability range using the following expression:

$$\text{metric change}_{\text{model}} = \frac{|\text{metric}_{\text{min}} - \text{metric}_{\text{max}}|}{|\text{metric}_{\text{max}}|}, \quad (6.2.4)$$

where $\text{metric}_{\text{min/max}}$ refers to the minimum or maximum value of the corresponding waveform metric resulting from the model simulations in the considered parameter range.

For the comparison between experimental data and model simulations in Figure 6.13, we defined an experimental reference for each metric as the general mean and standard deviation for all experiments ($N = 23$). This allowed us to define a range of change due to the laser effect to which the model values could be compared. The mean of metric experimental change (MEC) was defined as:

$$\mu_{\text{MEC}} = \frac{1}{N} \sum_{i=1}^N \frac{|\mu(\text{metric})_{\text{laser}} - \mu(\text{metric})_{\text{control}}|_i}{|\mu(\text{metric})_{\text{control}}|_i}, \quad (6.2.5)$$

Here, $\mu(\text{metric})_{\text{laser}}$ and $\mu(\text{metric})_{\text{control}}$ represent the mean values for each experiment i in laser stimulation and control trials, respectively, where the index i ranges for all experiments, with N being the number of experiments.

Thus, the percentage change in waveform from the model simulations, as described in equation 6.2.4, was mapped to this reference range: $(\mu_{\text{MEC}} \pm 2\sigma_{\text{MEC}})$, with σ_{MEC} being the standard deviation of the MEC. To visually represent this range, we utilized a color gradient with the *background_gradient* option in *DataFrame* style in Python. The formula for mapping these values is:

$$\text{Gradient value} = \frac{\text{value} - \text{Vmin}}{\text{Vmax} - \text{Vmin}}$$

Here, *value* represents the percentage change in the model simulation for a specific metric, while

V_{min} and V_{max} represent $\mu_{MEC} - 2\sigma_{MEC}$ and $\mu_{MEC} + 2\sigma_{MEC}$ respectively, with μ_{MEC} and σ_{MEC} being the specific mean and standard deviation corresponding to the metric specified in *value*. Since all changes are in absolute value, the lower bound for V_{min} is 0.

All data analyses were performed in Python, the scripts are available in github.com/GNB-UAM/Garrido-Pena_Modulation-neural-dynamics-by-CW-NIR-stimulation.

6.3 Temperature estimation for analyzing laser neuromodulation

To estimate the CW-NIR laser induced temperature change, we used the open-pipette method employed in previous experimental studies to measure the temperature variation during the illumination (Brown et al., 2020, 2021; Li et al., 2013; Rabbitt et al., 2016). We calibrated the resistance and temperature relation using a thermistor (EPCOS, $10k\Omega$) to measure the temperature in the preparation solution in the range from 23°C to 29°C . We used two protocols: injecting a constant current to calculate the resistance change from the voltage recording, and injecting pulses of a specific current value. From the resulting recording slope of the linear regression, we computed the conversion from voltage to temperature. For the estimation of the temperature change during the laser stimulation, we measured the voltage change during short intervals of laser illumination and the temperature value at its saturation plateau. This estimation is represented in Fig. 6.5.

6.4 Sustained CW-NIR laser stimulation effect on single neuron dynamics

6.4.1 CW-NIR laser effect on spike waveform

In this paper we performed experimental triplets of control, sustained CW-NIR laser stimulation and recovery recordings (for details see Sec. 6.2.1). This protocol provided a reference for the characterization of the laser effect. The data analyzed in this section corresponds to the spontaneous activity of neurons from the right parietal ganglion (RPG) of *Lymnaea stagnalis*, under no stimulation other than the laser illumination when specified.

Left panels in Fig. 6.6A and B illustrate the stereotyped waveform of the action potential from two experiments in two distinct neuron types present in the RPG with symmetrical and shoulder spike shapes, respectively. Note that the two neuron types differ not only in spike waveform but also in duration. In the example shown in Fig. 6.6A, the duration of the spike was ~ 20 ms whereas the

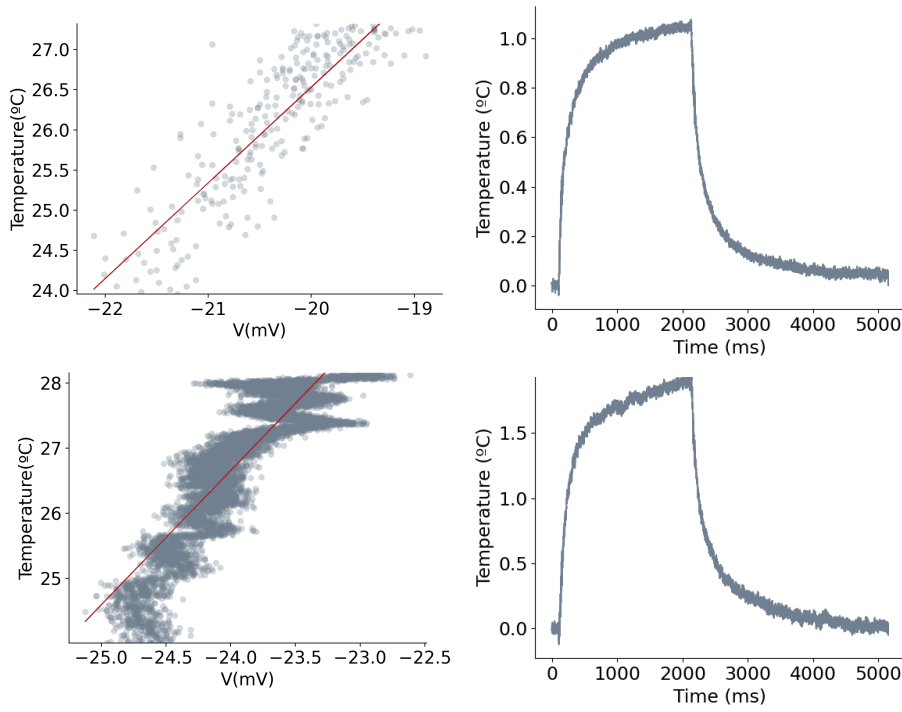


Figure 6.5: Open-pipette temperature estimation method. Each row in the panel represents pulsed and continuous current delivery for the estimation, respectively. For both examples: left column, temperature and voltage relation. Right column filtered mean of voltage recordings from short illumination intervals in the pipette.

one shown in Fig. 6.6B was \sim 40-50 ms. To characterize the sustained CW-NIR laser stimulation in terms of change and recovery, the three stages of the protocol –control, laser and recovery– are represented in all panels. The superimposition of the spike waveforms (\sim 40 and 110 spikes for each trial, panels A and B, respectively) for the same recording are aligned in the x axis by the spike peak and in the y axis by the voltage amplitude of the first point of the waveform, together with the trial mean spike represented with a wider line. Note how the control and recovery traces overlap for both neuron types, illustrating the resumption of the spike dynamics shortly after the laser stimulation ceases (see aligned spikes in Fig. 6.6 A and B).

Figures 6.6A and B illustrate that the variability was very small in amplitude, duration and in depolarization or repolarization slopes between the spikes within the same trial in both neuron types. However, during CW-NIR laser stimulation, the change in action potential waveform shape was notable with respect to the control and the recovery. This change was most clear in the spike duration, which was the result of changes in both depolarization and repolarization slopes.

The right panels ii) in Fig. 6.6A and B, show barcharts that quantify the change in terms of spike duration, amplitude, depolarization slope and repolarization slope. These metrics were used to characterize the action potential waveform and its possible change during the laser illumination (see also

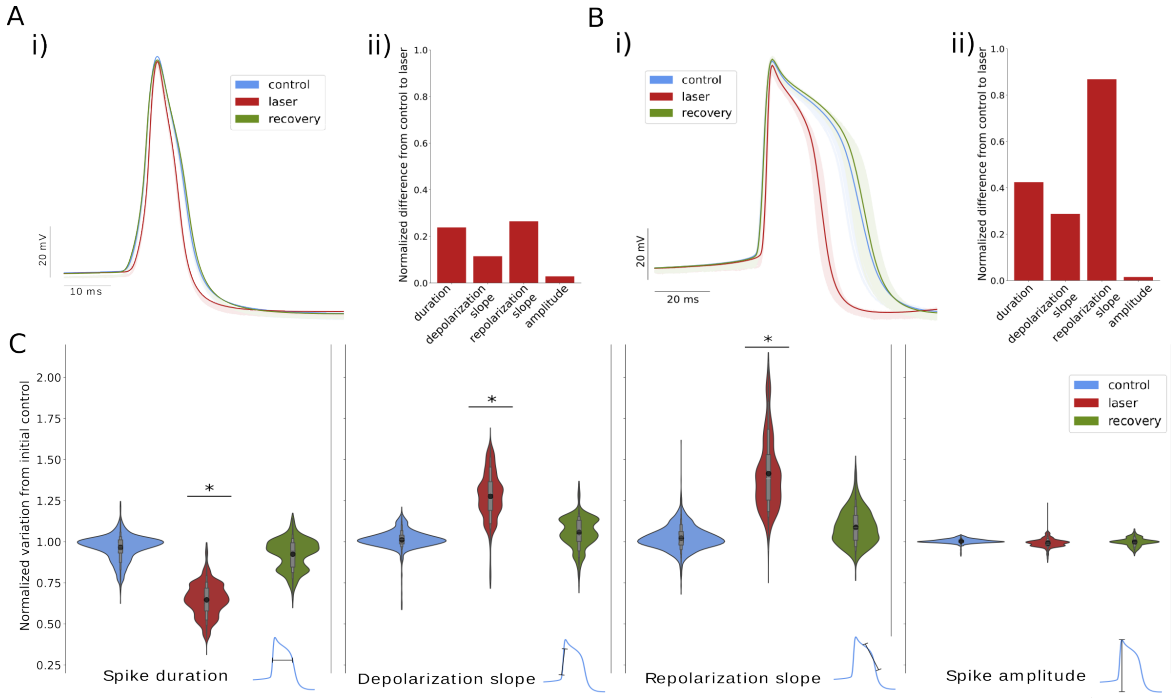


Figure 6.6: Effect of sustained CW-NIR laser stimulation on the spike waveform for two distinct neuron types. For all panels: control, laser and recovery are color coded in blue, red and green, respectively. Panel A. Characterization of no shoulder shape type neuron. Panel B. Characterization of shoulder shape type neuron. Ai) and Bi) Superimposition of spike waveforms in a single trial recording corresponding to a symmetrical and shoulder spike neuron, respectively. The spikes were aligned to the peak for the *x* axis and to the onset for the *y* axis, the mean is depicted in darker colors. Aii) and Bii) barcharts quantify the change using the difference from laser to control normalized by the mean control value for metrics: duration, depolarization and repolarization slopes, and amplitude. Panel C, violin plots representing the variation of the experiments with respect to the control ($N = 23$) for shoulder and symmetrical types together. For each metric of the waveform, the control, laser and recovery recordings are normalized to the first control. From left to right: duration, depolarization slope, repolarization slope and amplitude. Asterisks over the violins indicate that the metric change was highly significant (Bonferroni correction, $(\rho < 0.01/4)$, see Statistical Analysis Sec. 6.2.4 in Materials and Methods).

Fig. 6.4 and Sec. 6.2.3). Each one of these metrics is represented on the right panels as the absolute value of the difference of the laser stimulation to the control recording normalized by the mean control value (see Sec. 6.2.4). For both neuron types there was a change in duration and in the slopes, with the largest change being in the repolarization slope (around 26% for the symmetrical spike type neuron and 86% for the shoulder type). The alignment illustrated in the left panels shows that the change in amplitude was minimal in comparison to the rest of the metrics. Although both neuron types showed an effect of the sustained CW-NIR laser stimulation in the action potential waveform, the change in the shoulder neuron type was larger for duration and slopes. This may be due to specific

channels that generate the shoulder shape of the spike, which may allow for a wider range of change in the spike dynamics, especially in terms of the repolarization slope.

Panel C in Fig. 6.6 displays the results of multiple experiments following the same protocol described above, represented in violin plots as the normalization of each experiment with respect to the mean of the first control of the respective metric for each spike detected during control, laser and recovery. To avoid possible bias from the natural evolution of the intracellular recordings, in this figure we only included experiments where the activity was recovered within 10% change in firing rate with respect to the control. For each trial, only stereotyped waveforms were considered and large deviations (in the form of $z_{score} < -0.1$ in the normalized duration) were filtered out. The variability characterized in the control violins represents the variation within controls, which was also the most homogeneous in terms of density distribution. This is represented for each one of the selected spike waveform characterization metrics as in panels A and B –duration, depolarization slope, repolarization slope and spike amplitude (see Fig. 6.4).

The results shown in Fig. 6.6, panel C are consistent with the described change in the illustrative individual experiments shown in panels A and B in the same figure. On the one hand, the activity recovered its initial characteristics after the CW-NIR laser stimulation ceased for every metric, i.e., the recovery (green violin) returned to the same level as the control (blue violin). The differences in these distributions are mainly caused by the natural variability in the biological system. Also, as all values are normalized to the mean of the first control, it can be expected that the distributions may diverge more in laser and recovery violins than in control violins. A separate analysis for the two neuron types is available in Fig. 6.7

Regarding the change during the laser stimulation, for every waveform metric except amplitude, we can see in Fig. 6.6C how the overlapping of the distributions is minimal. The distribution for the duration was the most homogeneous, whereas the variation for depolarization and repolarization slopes had different density distributions, being the repolarization slope the one presenting a larger change in most cases. This can be explained by the variety of neurons in the collected data, the change in the slopes differed from one type of neuron to another. Thus, the distribution of variability was different. Some laser stimulation recordings presented a milder change than others. The slight change along neurons of the same type was likely due to the physical restrictions of the setup in each experiment: the angle of the laser, the laser focusing, the maximum power used and the overlaying tissue. Overall, considering these factors, we can see that stimulating with the sustained CW-NIR laser resulted in a significant change of the spike waveform. In the case of the amplitude, the change was very small.

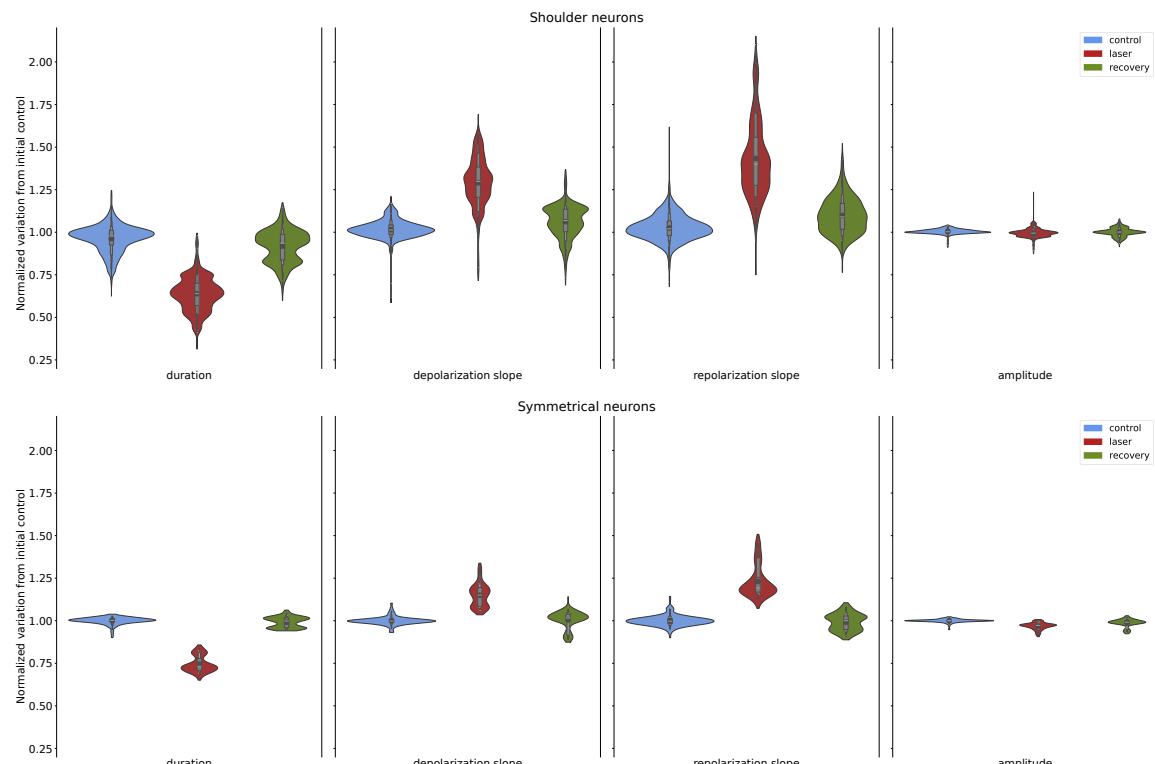


Figure 6.7: Segregation of data into shoulder and symmetrical neural types. Violin plots for the four metrics -duration, depolarization slope, repolarization slope and amplitude- grouped by control, laser and recovery trials. Spikes metrics are normalized to the first control, as in Fig. 6.6 panel C

We performed statistical tests on these data and confirmed that the changes in duration, depolarization and repolarization slopes were highly significant ($\rho < 0.01/4$) when comparing control and laser samples. The amplitude change was not highly significant, and so were not the changes in any metric comparing control and recovery samples (see Statistical Analysis Sec. 6.2.4).

This combination of changes points out to different biophysical candidates that might be involved in the modulation for the global change in both slopes or specific channels involved in the CW-NIR laser effect, since the depolarization and repolarization slopes were affected differently, while the amplitude did not change, and for distinct neuron types the characterized metrics had different variations (i.e., the repolarization slope in the shoulder shape neuron type was reduced to a greater extent than in the symmetrical type). In section 6.5 we assess these possible candidates using a computational model.

6.4.2 CW-NIR laser effect on spiking rate

During the identification of the biophysical effect at different phases of the action potential dynamics on single neurons, we identified a robust acceleration of the action potential (a shorter duration of the spike waveform). This could also point to an acceleration of the tonic activity of the neurons. Pulsed NIR laser stimulation has been proven effective as a stimulation technique, mainly eliciting action potentials (APs) in silent neurons at specific combinations of pulse duration and intensity (Cayce et al., 2014; Izzo et al., 2007; Shapiro et al., 2012; J. D. Wells, M.D., et al., 2005a). Thus, we also assessed the effect during sustained CW-NIR infrared laser stimulation on the spiking frequency in long stimulation recordings (1-3 min).

To avoid possible bias originated from intrinsic properties of the neuron and the circuit in which it was integrated, we only considered recordings where the neurons effectively recovered their control activity rate after the stimulation (i.e., absolute recovery change within 10% from the initial control). The activity frequency was characterized by the absolute firing rate (AFR) for control, laser and recovery, and by a histogram of Inter Spike Intervals (ISIs), i.e., the time interval from peak to peak.

In Fig. 6.8, the mean firing rates for control, laser and recovery are represented along with their standard error of the mean. Panel A depicts the general change in frequency for the neurons, showing the neural activity trend to excitation in the mean. In panels B and C, this set of triplets is divided into two groups depending on the difference between the laser and the control, classified as no change when the difference between control and laser was less than 10% (panel B), and as excitation for the opposite case (panel C). There is no representation of inhibition in this panel, since there was not any experiment that fulfilled the criteria of a 10% negative change during the laser stimulation

with respect to the control. Note how cases where the activity increases are the most consistent ones (12 out of 23) and that even in the set classified as unchanged, the mean of the AFR during laser stimulation is larger than the controls. These results support an excitatory tendency during CW-NIR sustained stimulation.

The absolute firing rate hinders some characteristics of the neural activity, such as the refractory pe-

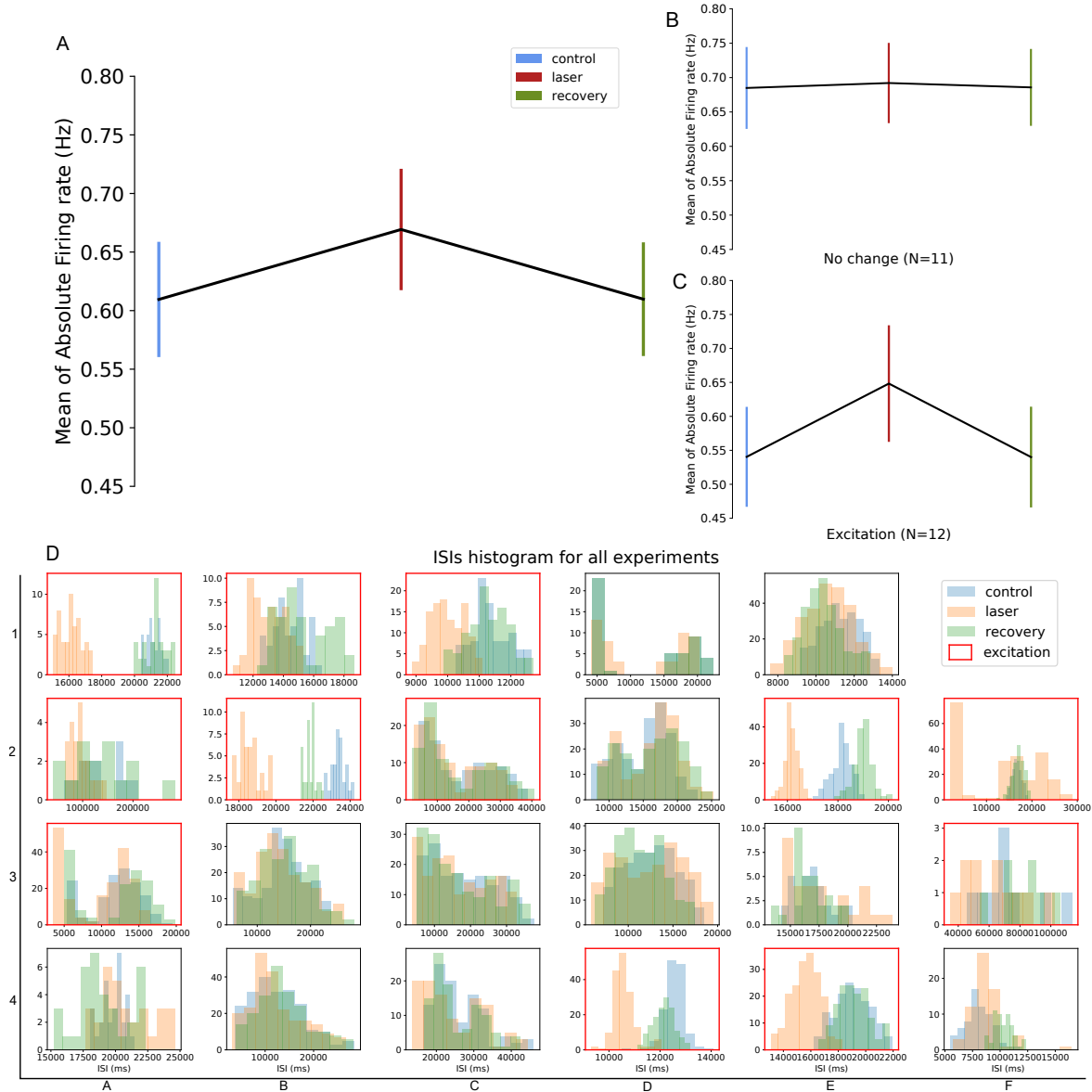


Figure 6.8: Firing rate and interspike interval (ISIs) analysis for the CW-NIR laser stimulation. A. Absolute firing rate in all experiments (N=23). B. Absolute firing rate for cases from the experiments in A with no change during laser illumination (N=11); C. Absolute firing rate for experiments from A showing an increase in the firing rate (N=12); D. ISI histograms for control, laser and recovery for each experiment. Cases showing increased excitation in their firing rate (sample in panel C) when illuminated by the CW-NIR laser are highlighted in a red square.

riod or the presence of bursting activity, which might also influence the firing frequency study. Thus, Fig. 6.8D displays the ISI histogram for each experiment showing again the triplets of control, laser and recovery, for each sample. Experiments showing excitation are highlighted in a red square. Note that for most cases classified as excitation, the ISIs tendency is to be reduced, which is observed in the laser histogram at the left of the control and the recovery. Note that there are some experiments where the laser ISI histogram seems to overlap with the controls and the recovery (see Fig. 6.8D, panels [2,A] [3,A] and [2,C]) but still the mean AFR of the laser recording was 10% higher than the control. In these situations, even though the activity was faster under stimulation, the time between spikes did not show a proportional change, which can be due to a modulation in the refractory period that compensated the spike acceleration. Under the laser modulation, we also found that some neurons would start firing in shorter ISIs, tuning the tonic spiking into pair spiking similar to small bursts, e.g. Fig. 6.8D, panel [2,F].

Overall, our results in this subsection show a larger tendency to a frequency increase in response to the NIR illumination indicating that it is possible to achieve neuronal excitation under sustained CW-NIR laser stimulation. It is also important to highlight that inhibition was not found in any of these experiments with sustained CW-NIR laser stimulation during tonic firing activity.

6.4.3 Effect of CW-NIR stimulation in a minimal circuit

Apart from the direct effect on the spike waveform and the firing rate, it is important to test the CW-NIR laser capability to modify the activity in a circuit. The aim is that a neuron affected by the laser illumination would also affect the circuit it is included in. As a first approach to test this, we illuminated two neurons electrically coupled in *Lymnaea stagnalis*, VD1 and RPD2 in the visceral and right parietal ganglion, respectively (Beekharry et al., 2015; P. R. Benjamin & Pilkington, 1986). In this experiment, we maintained the control, laser and recovery sequence of recordings, illuminating a neuron each time. In addition, we also tested the possible modulatory effect of the laser in the gap junction, by illuminating to areas where, based on the literature it should be for these two neurons. Note that the location of the gap junction and the two neurons is highly dependent on the position of the ganglia in the preparation, so this was an approximation. Figure ?? shows a image of the ganglia during the illumination of VD1 neuron in the visceral ganglion, RPD2 in the right parietal ganglion and the gap junction at its estimated position 6.9 Figure 6.10 shows the results for this experimental protocol in three different cases. In these preliminary results, we can see that in the recordings of the neuron being illuminated (VD1 recording during VD1 illumination and RPD2 recording during RPD2 illumination) we observe the same effect reported in section 6.4: the spike accelerates and

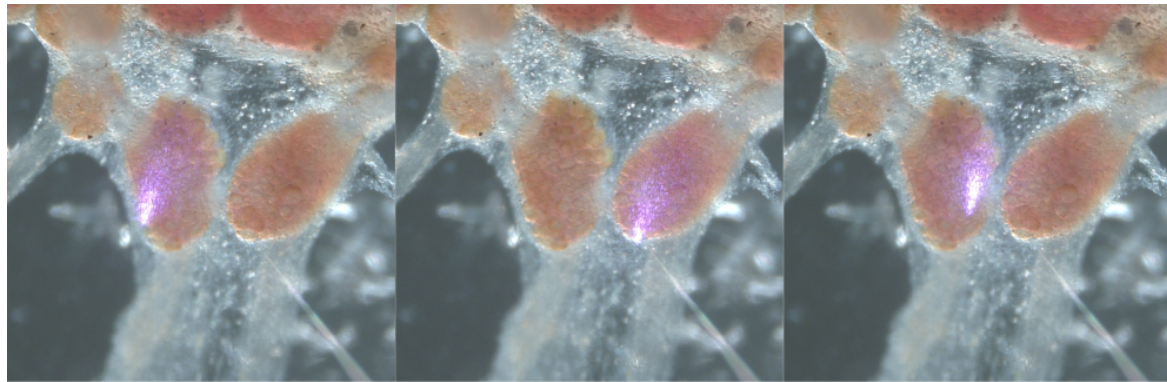


Figure 6.9: Microscope image of the three cases of illumination. From left to right illumination of VD1 neuron, RPD2 neuron and the gap junction of their electrical coupling. In the images it can be appreciated the electrode recording each cell, form the bottom right and from the top left.

its duration is shorter, affecting the slopes and without a equivalent change in the amplitude. In the recordings of the electrically coupled neuron, for all cases we can appreciate a mild change, specially clear in the example 3, were also the change is larger in the VD1 recording when the illumination was in RPD2, with respect of the change in RPD2 when the illumination was in VD1.

A methodical reproduction of these results would provide further information about the laser action and also pave the path to the application of this stimulation for the modification of activity in circuits such as the CPG.

6.4.4 Effect of CW-NIR stimulation at different wavelengths

To address one of the main questions in infrared laser stimulation, i.e., what is the source of the effect (photo-thermal, photo-electrical, etc.), it is necessary to characterize its effect in different configurations. It is proven that a specific configuration of wavelength, pulse duration and frequency, and intensity, is crucial for an effective neural stimulation (Izzo et al., 2007; J. Wells et al., 2007). However, the details on what is each parameter tuning or affecting have not been analyzed in detail. In this subsection we analyze the data from a preliminary study in collaboration with the laboratory of *Nanoparticles for Biomedical applications* in the department of Physics of Materials in UAM. Here we apply different wavelengths in CW-NIR lasers of 808nm, 830nm, 980nm and 1450nm. Following the hypothesis of the strong role of the temperature modification, the first difference between those wavelengths that we need to take into account is the water absorption at each one of them. In Fig. 6.11 there is a representation of the water absorption curve for different wavelengths. We can classify the wavelengths in this experiment regarding its water absorption in three groups: 808nm and 830nm in the lowest range; 980nm in the first peak and 1450nm with a significant increase of the extinction

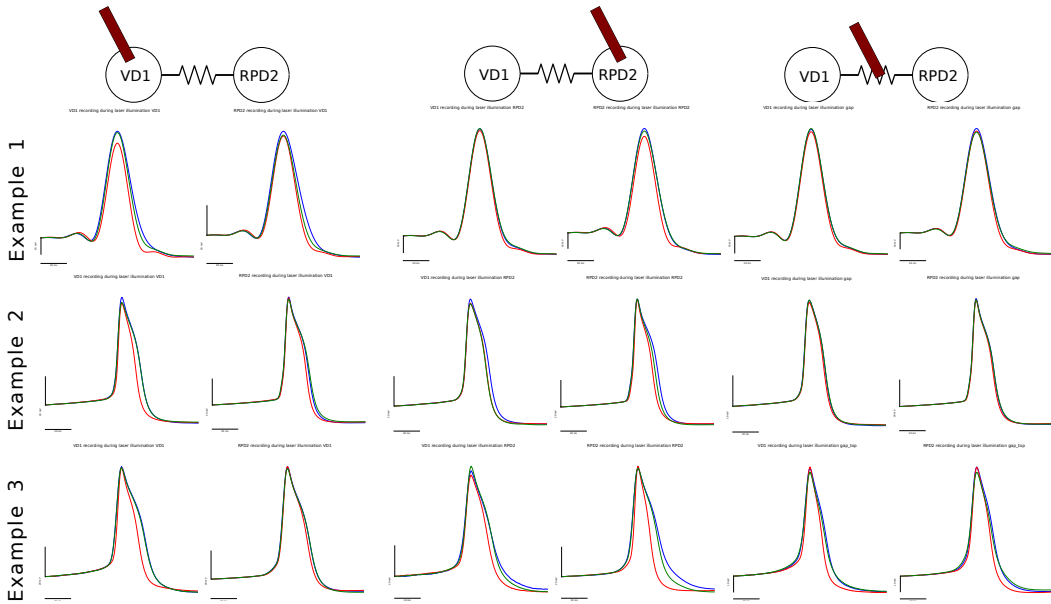
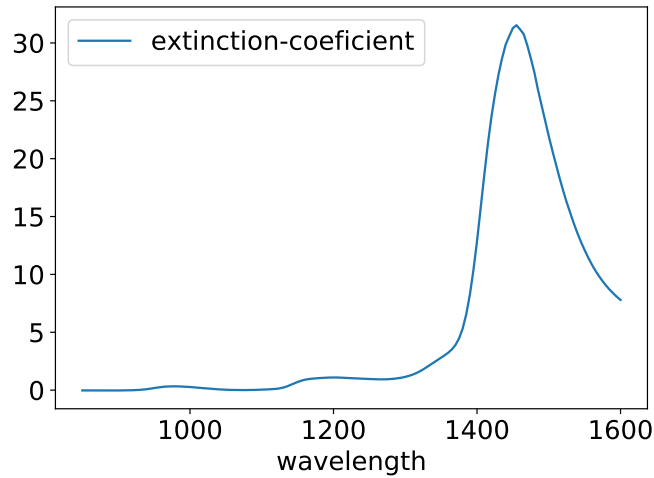
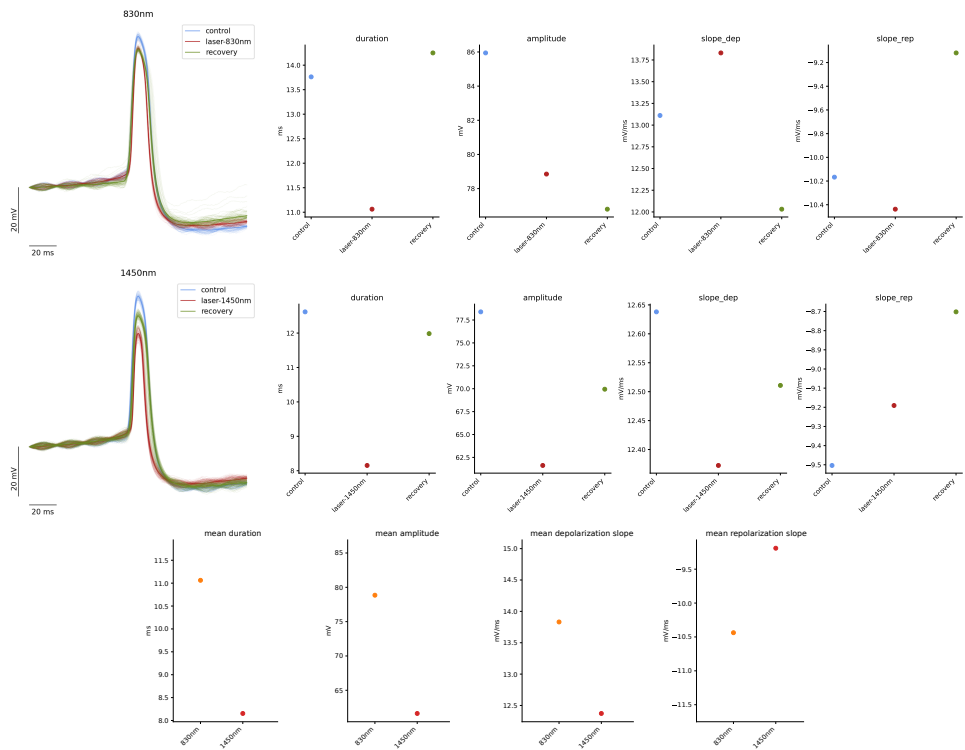


Figure 6.10: Electrically coupled neurons illumination, superimposition of the averaged waveform for control, laser and recovery in three different examples. For each case, it is the spike waveforms of VD1 and RPD2 illuminating first VD1; waveforms of VD1 and RPD2 illuminating then RPD2 and finally both waveforms illuminating the gap juntion. Each plot follows the previous color code for control, laser and recovery of blue, red and green, respectively).

coefficient. Therefore, the first thing to consider is the difference in the heating capacity of each laser in the surrounding water and the tissue.

As preliminary results, we present here the effect in the spike waveform for 830nm and 1450nm. We saw so far that the CW-NIR laser stimulation affects the spike waveform metrics in a reversible manner accelerating it, with a shorter duration, changing its depolarizartion and repolarization but with a minimal or negligible change in the amplitude. Those results, performed with a 830nm laser, correspond to the results depicted here for 830nm (see Fig 6.12 first row). In the case of 1450nm, the change is larger in every metric (specially regarding the comparison between the laser and the recovery) but particularly in the amplitude, which present a change that was not commonly visible in the 830nm stimulation. During this experiment there was a tendency in the recording to decrease the amplitude naturally, however relying on the recovery metrics, we can see that although there is a tendency in the recording to change the waveform, the effect during the aser stimulation is notable. In this last case it is remarkable, that after this large change in amplitude, the recovery value was not achieved at the same level, in fact, the spontaneous tonic spiking activity of this preparation was damaged after the illumination at this wavelength, which suggest the neuron was damaged after this stimulation.

**Figure 6.11:** Water absorption for different wavelengths values.**Figure 6.12:** Representation of the effect of sustained laser stimulation at 830nm at 90mW and 1450nm at 120mW. In terms of power density the corresponding values are: 194.88 W/cm² and 315.78 W/cm², respectively. The left panel in each row is the superimposition of the spike waveforms aligned to the first point, during a control recording with no stimulation, a laser recording during the illumination at the specific wavelength and a recovery control, again with no stimulation. The four panels in each row correspond to the mean value for each trial of control, laser and recovery for the spike waveform metrics: duration, amplitude, depolarization and repolarization slopes.

Based on this preliminary study we can observe a relation of the wavelength and the effect we observe in the waveform. Again, with a methodical repetition of this experiment, this relation could be set and the role of the wavelength and other factors beside the photo-thermal effect, could be explored.

6.5 Model analysis for constraining candidates to explain the effect of CW-NIR laser illumination in the spike dynamics

6.5.1 Parameter range modification for the biophysical candidates in the model.

Computational models are a powerful tool to assess the source of neural dynamics where all variables involved are accessible. By considering membrane potential recordings alone, it is difficult to understand the contribution of the biophysical candidates in the underlying dynamics shaping the action potential. While it is specially hard to carry out experiments using chemical and/or electrophysiological techniques to selectively block or compensate channels to mimic the observed CW-NIR laser effect, the simultaneous accessibility to all the variables in a model provides a unique tool to dissect the contribution of all biophysical candidates. Thus, to further explore the source of the experimentally observed CW-NIR effect, we analyzed the spike generation dynamics in three different conductance-based models assessing the change in the most likely candidates to be affected by the laser stimulation: modulation of membrane capacitance and ionic channels. More specifically, we modulated (i) the capacitance and the conductance of the active ionic channels $-I_{Na}$ and I_K- in the standard Hodgkin-Huxley (HH) model (Hodgkin & Huxley, 1952a); (ii) the conductance of ionic channels $-I_{NaP}$, I_{NaT} , I_D , I_A , I_{HVA} , I_{LVA} – and capacitance in a *Lymnaea stagnalis* CGC neuron model with a shoulder shape waveform (Vavoulis et al., 2010); and (iii) the capacitance in a two-compartment model –where the fast and slow dynamics are segregated– in a *Lymnaea stagnalis* buccal ganglion neuron (N3t) model (Vavoulis, Straub, et al., 2007b). The implementation of these models is available in the open-source model library Neun github.com/GNB-UAM/Neun and the code for the simulations can be accessed in github.com/GNB-UAM/Garrido-Pena_Modulation-neural-dynamics-by-CW-NIR-stimulation.

The model parameters were modulated to investigate and compare their effect to that of the CW-NIR laser stimulation on the neurons, and to evaluate the interrelationship between the observed changes. To identify changes in the spike dynamics similar to those observed under the CW-NIR laser illumination, in this section we covered a complete range of values in the parameter space of each biophysical candidate. The criteria for driving the parameter exploration were the preservation of tonic spiking in the activity and the assessment of a realistic range of values. As our initial

hypothesis did not assume that the CW-NIR laser effects were exclusively photo-thermal, model parameter changes were applied with no temperature description. Further down in Sec. 6.5.2 we present a detailed study considering the temperature dependency of the biophysical candidates.

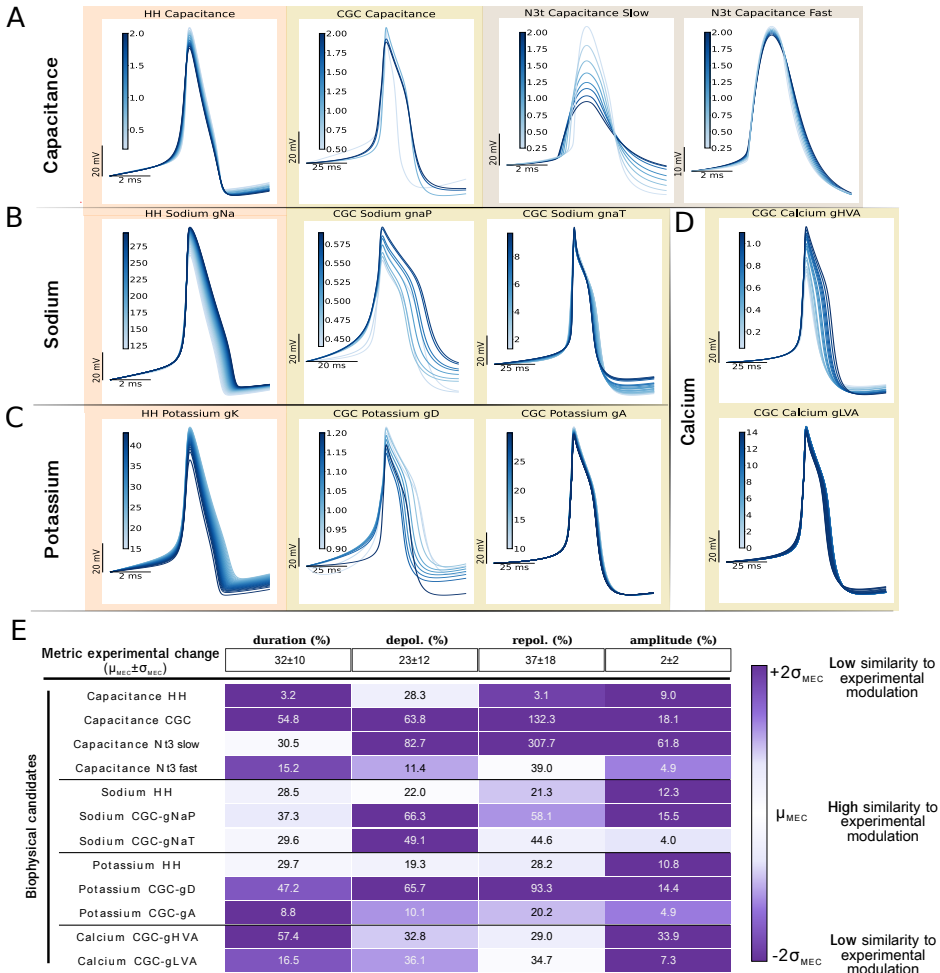


Figure 6.13: Modeling study of the CW-NIR laser stimulation effects due to isolated biophysical changes that alter the spike waveform. Panels A, B, C and D: Superposition of spike waveforms in each model by modulating a single biophysical candidate. The background colors correspond to each simulated model. In Panel A, the capacitance is changed for the HH and CGC neuron models, and in the two compartments for the N3t neuron model. Panel B shows the spike waveforms changing the conductances of I_{Na} channel currents: I_{Na} from the HH-model, I_{NaP} and I_{NaT} , from the CGC-model. Panel C, displays the modulation of K conductances in ionic currents: I_K in the HH-model and I_D and I_A for the CGC-model (from left to right). Panel D shows the modification of the calcium current conductances in the CGC-model (I_{HVA} and I_{LVA}). Table in panel E represents the quantification of the changes in the spike metrics when tuning each parameter for every model. Each cell contains the waveform change normalized to the maximum. The color gradient represents similarity based on the standard deviation of the normalized experimental change. Dark purple corresponds to low similarity ($2\sigma_{MEC}$ or larger) and white to high similarity. The quantified experimental reference (MEC) is annotated in the first row of the table.

The results of this study are shown in Fig. 6.13. The analysis for each model is sorted by the explored biophysical candidate –capacitance, sodium channels, potassium channels and calcium channels–. Thus, panels A, B, C and D show the superposition of all spike waveforms from the simulations for the range of explored model parameter values of each candidate. The table in Panel E represents how well the different model candidates reproduce the observed experimental effect. For each metric and biophysical candidate, there is a percentage of change in the model calculated as the change from minimum to maximum normalized with the maximum value (analogously to the quantification in Fig. 6.6, see also Sec. 6.2.4). The background color in each cell represents the ability of each model parameter modulation to produce results similar to the change in the experimental results. The color gradient (represented in the color bar) takes as reference the mean of the metric experimental change (MEC) quantification, considering the range of ($\mu_{\text{MEC}} \pm 2\sigma_{\text{MEC}}$) (see Sec. 6.2.4). The mean change and its standard deviation were computed as the normalized difference between mean values for each control and laser experimental pair for all experiments. These reference values are shown for each metric in the first row of the table in panel 6.13E to compare them with the model results. Thus, dark purple corresponds to values two times the STD of the mean over or under the mean, and white represents the mid point between those two values, i.e., high similarity to the experimental modulation. For example, in the case of Capacitance in the HH model, the change in duration was minimal 3.2%, while the mean change in the experimental observation was 32%, this color is then represented in dark purple, since 3.2% is not in the defined range (32±20). On the other hand, the change in depolarization slope for this model (28.3%) is depicted in light purple, since it is in the defined range and close to the mean metric experimental change (23±12).

Change in Capacitance

Capacitance has been one of the most discussed biophysical candidates to be affected by IR laser illumination (Cayce et al., 2014; Plaksin et al., 2018; Shapiro et al., 2012; Shapiro et al., 2017). A change in capacitance has a direct effect on the spiking frequency and exerts a global modulation on all ionic currents, so many studies have discussed this change both experimentally and theoretically. Here we explored the CW-NIR modulation of capacitance in three different conductance-based models: in the Hodgkin-Huxley model, used in other studies, in the CGC-Vavoulis model, which presents a variety of channels and in the N3t-model, which is the only one with more than one compartment and, thus, has two distinct capacitance values.

Figure 6.13A displays the waveforms of each simulation. In the case of the HH-model, there was a mild change in duration, mainly caused by the depolarization modulation, and a change in amplitude

larger than what was observed experimentally. The CGC-model exhibited a similar tendency to the HH-model but with an extreme case at a low value of capacitance $0.5\mu F/cm^2$, where moderated changes in depolarization and amplitude were combined with a large change in the repolarization, and consequently in the duration. This modulation made capacitance a better candidate for reproducing the experimental results in the case of the CGC neuron, preserving the metrics' change interrelations, i.e., the combination of a minimal change in amplitude and a large change in duration, together with a larger change in repolarization than in depolarization slope. In the N3t neuron, we can see contrasting results for the two different compartments. In the compartment containing slow currents, the change in amplitude was the most striking, seemingly conditioned by both slopes. In the case of the fast current compartment the main change was observed in repolarization rather than depolarization, which is more similar to the experimental outcome.

These results are quantified in the table in Fig. 6.13E. The HH-model showed a change comparable to the experimental one only for the depolarization slope. The CGC-model reached plausible values in terms of the interrelation between metrics (large change in duration generated by a larger change in repolarization than in depolarization slope), but it exceeded the experimental references. The change in amplitude was larger than seen in the experimental results for most parameters (dark purple). It is especially clear in the case of the two-compartment model (N3t neuron), in which the modulation of capacity in the slow compartment resulted in a large change in amplitude. In contrast, the small change in amplitude in the fast compartment was the most similar value with respect to the experimental results (light purple).

By changing the capacitance, we achieved some of the expected changes, but achieving the desired results for all four metrics simultaneously was not possible. Therefore, modulating capacitance alone does not reproduce the experimentally observed effects, especially regarding the combined change, e.g., large change in repolarization and small change in amplitude, larger change in repolarization than in the depolarization. It was only when the fast compartment of N3t was modified that relations between these four metrics matched the above relationships. But note that changing the capacitance in the slow compartment is equivalent to changing several ionic currents simultaneously, not just a single current property.

Ionic channels

The other mechanism to explain the laser modulation that we assessed here was a direct effect on the ionic channels involved in the generation of action potentials. These channels are activated in a sequential manner, and each of them is directly involved at distinct stages of the action potential

generation. They have been discussed in the laser stimulation literature (Li et al., 2013; Liang et al., 2009; Rabbitt et al., 2016) by a direct effect of maximal conductance, and channel opening and closing dynamics due to thermal effects, e.g., in calcium channels (Albert et al., 2012; Barrett et al., 2018). These candidates were assessed here in the two single compartment models, the HH-model due to its wide use in computational neuroscience and the Vavoulis-CGC model for its variety of channels (including calcium currents) and accurate reproduction of the observed neural waveform shape. Note that in the CGC-model analysis, all currents types are in pairs of high and low conductance as well as fast and slow dynamics, having two currents for sodium, potassium and calcium (see Fig. 4.6 in Materials and Methods).

In Fig. 6.13B the spikes from the simulations for each sodium current in the HH and CGC models – I_{Na} , and I_{NaP} and I_{NaT} , respectively– are superimposed. For the three currents, we observed modulation in both depolarization and repolarization slope, which resulted in a change in duration. Although the change in duration is close to the experimental outcome, the change in the depolarization is larger than in repolarization (see Fig. 6.13E), which is contrary to the experimental results, as it is also the change in amplitude for I_{Na} , and I_{NaP} . However, for channel I_{NaT} the change in amplitude was smaller, falling closer to the experimental range for amplitude and duration, but the change in depolarization exceeded the experimental range and the repolarization change was limited in the context of shoulder type neurons (the waveform type that reproduces CGC-model). Although the change of sodium channels alone generated a similar change in duration in relation to the experimental results, the rest of the metrics did not replicate those results.

Analogously, in Fig. 6.13C, simulations for potassium currents (I_K and I_D and I_A , respectively) are represented for HH and CGC models. For the three currents, the major change was in the repolarization slope followed by the depolarization (see quantification in Fig. 6.13E). This combination resulted in a modulation of the duration that lay in the range of similarity to the experimental results, with the exception of the amplitude, which does not correspond to the experimental results. It is especially applicable in the case of I_K in HH-model and in the conductance of the strong potassium current g_D of the CGC-model. Note that for the I_A current, although the combination of changes were comparable to the experimental change, their range was not, so a change in this current alone was not considered a plausible candidate. Thus, a change in potassium channels reproduced the experimental results for duration and the two slopes overall, but it was limited due to an excessive change in amplitude.

In order to inspect the CGC-model in detail, we also simulated the changes in the calcium currents – I_{HVA} and I_{LVA} – for this model. These currents have a key role in the generation of the shoulder shape

in the spike (Figure 6.13D). Both created a similar change in the repolarization slopes, as well as in the depolarization, which is also close to the experimentally observed modulation. For duration, I_{HVA} better matched the change, but this modulation was also accompanied by a large change in amplitude which was not observed in the experimental results. On the other hand, I_{LVA} had one of the minimum effects on amplitude but, contrary to experimental results, its effect on the duration was also minimal, although the depolarization and repolarization slopes had a comparable change to the experimental observations. Therefore, altering each calcium channel effectively reproduced the desired change in the slopes but the modulation in duration and amplitude occurred in the same proportion, which does not match the experimental results.

The results described in this section indicate that each candidate can be modulated to bring the waveform closer to the experimentally observed results, but when changed separately they account only for a partial set of metrics matching. The desired combination of changes for duration, slopes and amplitude was not achieved by tuning only one parameter at a time. However, some of the candidates came close to this combination. Considering the ionic current candidates, the one that was closer to the *in vivo* stimulation was potassium current, which reproduced a large range of change in the repolarization, depolarization and duration, though exceeding the change in the spike amplitude. This is relevant in terms of maintaining the observed interrelation of the metrics. Considering the range of change reached, the calcium channels where the best candidates for the reproduction of the experimental repolarization slope modulation, allowing a wide range of values and generating the shoulder shape waveform. We also saw how capacitance in single compartment models was not enough to reproduce the results. It was only when the capacitance was modified separately in two compartments, that the change reproduced the CW-NIR laser stimulation better. This points to a mechanism for explaining the CW-NIR laser effect with contribution from several candidates at the same time where specific factors might be of greater importance, such as the potassium channel in the case of shoulder shape neurons.

6.5.2 Change of spike dynamics considering temperature modulation in the model

Most studies in laser stimulation point out to a photo-thermal effect, e.g. see (Cury et al., 2021; Ganguly et al., 2016; Li et al., 2013; Pan et al., 2023; Rabbitt et al., 2016; Shapiro et al., 2012; J. Wells et al., 2007). Thus, in this section we include a model analysis with temperature modulation. We selected the CGC-model from Ref. (Vavoulis et al., 2010) since it is the richest model in terms of variety of channels and ability to mimic the spike waveform of shoulder type neurons. To study global temperature dependence in the model we added a Q_{10} coefficient, representing the temperature

sensitivity in the model parameters. The value for this parameter is usually applied to different channel properties and kinetics in a range from 1 to 4 (Alonso & Marder, 2020; Cosens et al., 1976; Schauf, 1973; Tang et al., 2010). Thus, we choose as a common value for Q_{10} 3, as an average general value used in the literature (Ganguly et al., 2019b; Heitler & Edwards, 1998; Hodgkin & Katz, 1949; Li et al., 2013; Rabbitt et al., 2016; Shapiro et al., 2012) and also proposed as a universal value for Q_{10} to characterize temperature dependency for biochemical processes (Elias et al., 2014). We estimated the temperature change under laser stimulation at maximum power following an open-pipette method, with a resulting temperature increase of 1–2°C (see Sec. 6.3 and Fig. 6.5). Note that our CW-NIR laser wavelength is at one of the lowest absorption bands of water, so the open-pipette method probably underestimates the change in temperature in the neuron, being the change in the temperature caused not only by water heating but also by heating the tissue. In addition, the reported temperature range of laser induced variation in the literature is wide, depending on the system, the estimation technique and whether it comes from a model or an *in vivo* estimation (Rabbitt et al., 2016; Shapiro et al., 2012; Thompson et al., 2012). Therefore, in our simulations we explored a wider range than our experimental estimation, considering 5°C as a reference and the quantification of the change up to 10°C.

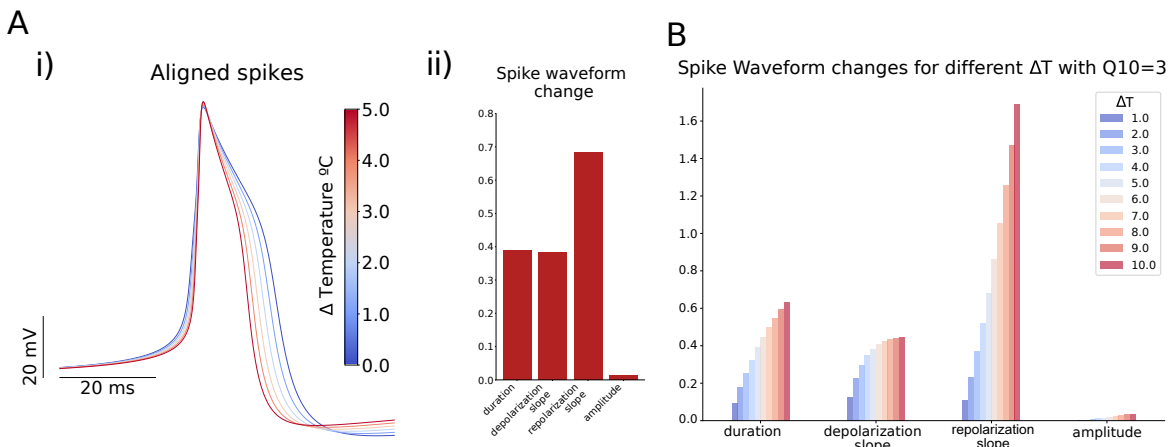


Figure 6.14: Waveform change in the CGC-model due to ΔT temperature variation. Panel A(i) shows the spike waveform superposition for distinct ΔT values. Spikes are aligned to the initial value of each waveform. In panel A(ii) the normalized change in the waveform is depicted for all metrics (duration, depolarization and repolarization slopes and amplitude). Panel B shows the change in response to temperature variation from 1 to 10°C ($Q_{10} = 3$) in the normalized metrics.

Figure 6.14 shows the change in the spike waveform caused by variations in temperature. The Q_{10} factor was added to every dynamical equation in the model (i.e., conductances, activation gates and capacitance, see Sec. 4.4.2). In panel A, we show the changes in the waveform for $\Delta T = 0 – 5^\circ\text{C}$, represented as superimposed waveforms in A(i), and its quantification in A(ii) normalized to the

maximum, which is analogous to the previous sections (see Figs. 6.13 and 6.6): $|max - min|/|max|$. Note how both the spike waveform shape and the quantification of the changes are similar to the experimental results. We can observe changes in duration, depolarization and repolarization slopes, with a very small change in amplitude. The modulation obtained by combining these parameters was not achieved by tuning them separately. It is important to highlight that as the temperature increased (red lines), the spike got narrower by the corresponding alteration in slopes and duration, which supports the hypothesis that the observed effect in single neurons of *Lymnaea stagnalis* might be, to a large extent, caused by temperature gradient. In panel 6.14B, there is a comparison of different temperature changes for the same Q_{10} value in the model. Note that the relation of each parameter to the change in temperature is different, being the repolarization slope the one with the strongest relation, increasing much more rapidly than the duration or the repolarization slope. This points to a main role in the change from some of the channels, especially those that have more tolerance to change. This relation in the repolarization is similar to the comparison of the two neuron types analyzed in the experimental results (Figure 6.6A), where the main difference was present in the repolarization.

Analogously to the simulations in the previous sections, we characterized the variations in the waveforms for each individual candidate, varying the temperature only for one ionic-channel at a time. To further explore these candidates and relations, we repeated the model simulation with temperature variations up to 5°C but also canceling the temperature dependency in one channel at a time. Note that overriding the temperature dependence of some of the channels at a time is only possible in a theoretical environment like this, which allows us to expose the role of each channel in relation to the temperature modulation. Figure 6.15 shows the result of these simulations. In panel A, there are depicted the waveforms of the model simulation with temperature variations up to 5°C but canceling the temperature dependency in one channel at a time (i) and describing the dependency of only one channel at a time (ii). In panel B there is a barchart with the metric characterization for each case (with and without temperature dependency) including also the experimental change reference in the dark bars. Panel A.i) shows how the general spike waveform shape was preserved in the range of the tested temperature variations when individually excluding low potassium and calcium currents $-I_A$ and I_{HVA} and I_{LVA} , respectively— we were able to simulate the same range as in Fig. 6.14 of $\Delta T = 0 - 5^\circ\text{C}$. However, when excluding the temperature dependency of I_{NaT} , the model could not generate action potentials when raising the temperature for the other channels above $\Delta T = 2^\circ\text{C}$, which suggests that I_{NaT} intervention during the temperature modulation is relevant for the action potential generation. This channel presented a non-linear relation between the amplitude and the temperature. It is important also to note that suppression of the temperature dependency in I_{HVA} in

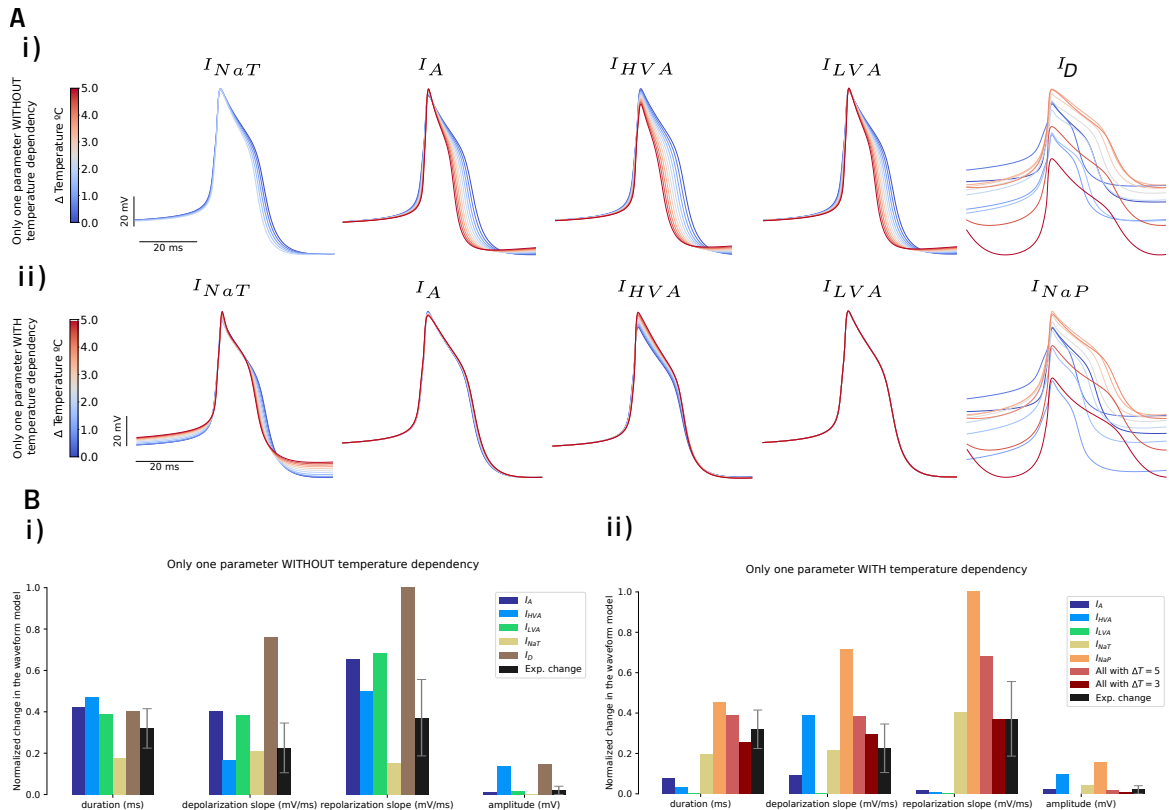


Figure 6.15: Simulation of the effect of individual channels on the spike waveform under temperature modulation. Panel A.i) Waveform modulation in the CGC-model excluding temperature dependency in one channel at a time, from left to right: I_{NaT} , I_A , I_{HVA} , I_{LVA} , I_D respectively. Panel A.ii) Waveform modulation in the CGC-model with temperature dependency only in one channel at a time, from left to right: I_{NaT} , I_A , I_{HVA} , I_{LVA} and I_{NaP} , respectively. Note that I_{NaP} is not in panel A.i) and neither is I_D in A.ii), as for these two particular simulations there was no spike generation. Panels B.i) and B.ii) show the quantification of the waveform change for $\Delta T = 5^\circ\text{C}$ in duration, depolarization slope, repolarization slope and amplitude for all channels in panel A. Both figures include, as reference, the experimental mean and STD (showed in black) and, for case B.ii) (only one channel at a time), the quantification when all channels have the same temperature dependency (all with $\Delta T = 5^\circ\text{C}/3^\circ\text{C}$, data used in Figure 5) is depicted in light and dark red bars.

Fig. 6.15Ai) resulted in a large change in the amplitude (20 mV decrease). This calcium current is needed to preserve the amplitude value while the slopes and duration values change during the temperature increase. The last waveform in that row, I_D , displayed a large change in the waveform shape, modifying the duration along with the depolarization currents and thus breaking down the spike. This change corresponds to a strong role in the generation of the action potential for this channel. In the contrary case, in Figure 6.15Aii) we observe that the channels with the strongest effect in the model are I_{NaT} , I_{HVA} and I_{NaP} , since their independent change of temperature produced a notable change in the waveform. Also in opposite to the previous case with temperature dependency, now it is I_D the channel that when it is the only one with temperature dependency, there was no spiking activity, and

now I_{NaP} displays a large change comparable to the one occurring before with I_D . In Panel B, we can observe for both cases that no candidate alone could reproduce the observed experimental laser modulation but some channels have a more direct relation to the temperature change such as I_{LVA} for the repolarization or I_D channel, crucial for the spike generation waveform.

Exploring the waveform change during temperature variation showed that the most similar change to the experimental laser modulation was reached in the models with the temperature dependency description in all parameters. We showed that, for most currents as the temperature increases, the experimentally observed modulation relations were maintained, changing in duration and repolarization slope, with a larger change in repolarization slope and a mild change in amplitude. This is also supported by excluding temperature dependency from isolated ion channels and proposing temperature dependency for one channel at a time. Furthermore, it is in agreement with the results of the modeling sweeping the parameter space for distinct candidates without a specific description of the temperature (see Sec. 6.5), which showed that no modulation of an individual candidate but a combination of them can explain the experimental quantification.

6.6 Activity-dependent stimulation to assess the laser effect at distinct stages of the spike dynamics

So far we have shown how sustained CW-NIR laser affects neural activity by modifying the dynamics of spike generation. In the previous section 6.5 we used a conductance-based model to theoretically assess the spike evolution and the different candidates involved in the modulation of the action potential generation (i.e., ionic channels and capacitance). To address this effect in an experimental setting is a complex task. Usually, it is accomplished using chemicals to block or open specific channels (Liang et al., 2009). This is not a generalizable method in different systems and individuals, and it restricts the channel study to a system with a detailed description of the specific neuron being recorded. We chose instead to assess the spike generation dynamics at different stages, which implies modifying the activity of several channels at a time in a precise timing relative to the spike generation dynamics. This task is only experimentally feasible with an activity-dependent stimulation protocol.

In infrared stimulation literature, the most spread technique has been pulsed illumination which stimulates at a fixed frequency. Although this approach has been effective in some tasks such as eliciting neural activity, it has limited possibilities in the context of precision and adaptability. Thus, with the activity-dependent protocol proposed here, we also provide an open-access alternative to the widely-used fixed-frequency pulsed laser stimulation protocols, which usually depend on a specific

combination of restrictions from manufacturers, controllers, and diode laser availability. In addition, a closed-loop approach provides further means to deal with the history-dependent nature of neural dynamics and its partial observability (Varona et al., 2016).

In this section we present a new protocol for closed-loop stimulation, we first validate the hypothesis in the CGC-model, by modifying some channels conductance only during depolarization or repolarization phase, and then test the protocol in a experimental environment, controlling the laser illumination by a mechanical shutter.

6.6.1 Model simulation of activity-dependent stimulation

To address in a computational approach the observed effect experimentally, we have simulated the effect on a CGC-model neuron modulating two of the channels where the effect on the neurons was larger. This way, only during a certain time interval, the conductance in channels g_D and g_{HVA} was modified to the value replicating the "maximum effect" (see Figure 6.16)

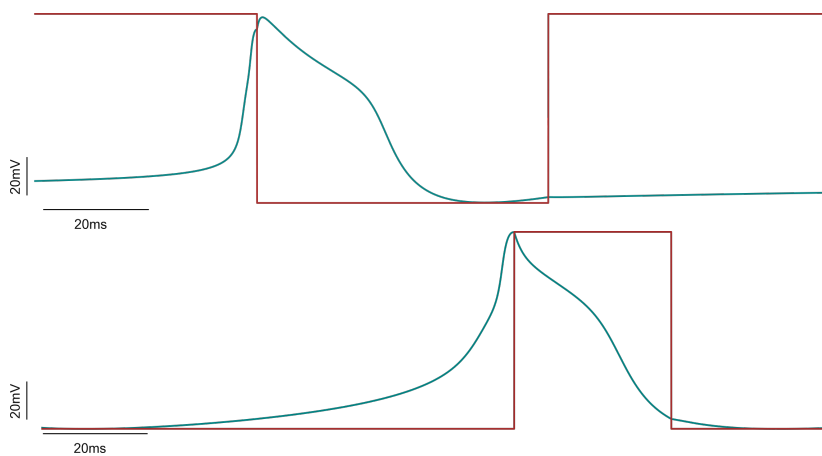


Figure 6.16: Simulation of the effect of CW-NIR laser in the CGC-model. Stimulating only during the depolarization or only during repolarization phases for first and second rows respectively.

With this simulation we obtained the results showed in Figure 6.17, where, as in the experimental results, the effect is larger when the stimulation is only in the repolarization slope, whereas while the effect is over the depolarization slope, the effect is only visible in the depolarization slope.

6.6.2 Experimental activity-dependent stimulation

Here we propose a closed-loop stimulation protocol where we can differentiate between the phases of the action potential and illuminate the neurons only at certain intervals of the spike generation dynamics. In this protocol, the laser illumination was controlled by a mechanical shutter triggered

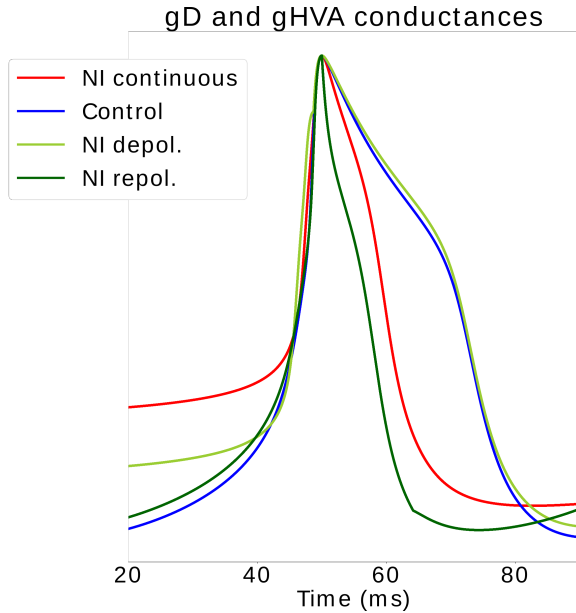


Figure 6.17: Results in the spike waveform for the simulation of the effect of CW-NIR laser in the CGC-model. Stimulating only during the depolarization or only during repolarization phases for first and second rows respectively.

by the prediction of events in the voltage signal. A real-time software system ran the prediction algorithm and triggered the illumination for short periods of time at different phases of the spike generation when distinct channels were active (see Sec. 6.2.2 and Fig. 6.2). The prediction of the events was computed by two algorithms, one based on a voltage threshold updated at each spike peak occurrence and a second one that calculated the voltage area from the hyperpolarization (minimum) to the next hyperpolarization. Based on this prediction the illumination was triggered at the specified time before the spike occurrence (see Sec. 6.2.2 for details in these algorithms). The implementation of these algorithms is available as a module for the real-time open-source system RTXI (Patel et al., 2017) in https://github.com/GNB-UAM/spike_predictor.

Figure 6.18 shows the outcome of the application of this closed-loop protocol, with a stimulation interval lasting 58 ms. The time line in the figure represents the offset of the illumination, i.e., the time that corresponds to the end of an illumination interval to the peak of the action potential (see an illustration exemplifying the illumination offset in Fig. 6.3). The offsets were in the range from 60 ms before the action potential peak up to 80 ms after its occurrence (this wide range is required because of the natural slow dynamics of *Lymnaea stagnalis*'s neurons). Each row in the figure represents the change in relation to the mean of the respective control trials for every illumination range. The change is represented for the three metrics in which we observed modulation during sustained illumination –duration, repolarization and depolarization slopes, respectively–. The different stimulation

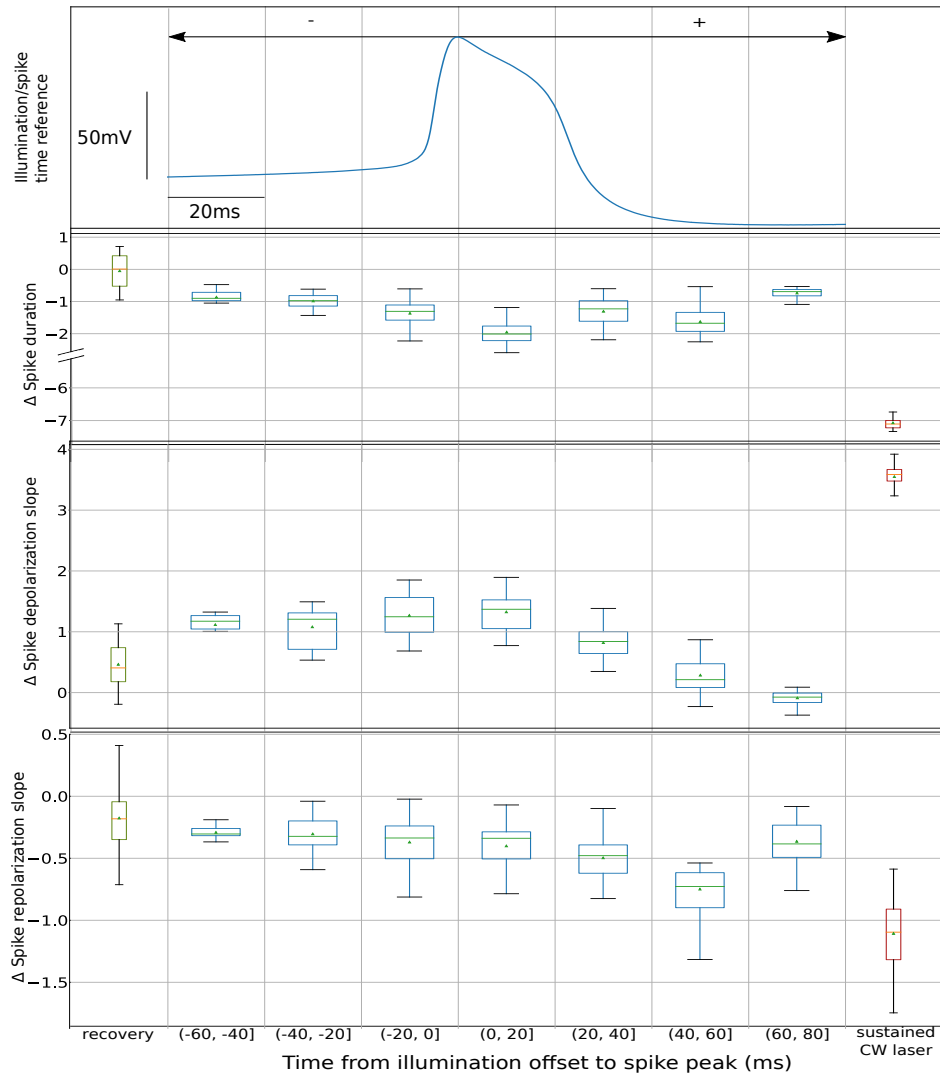


Figure 6.18: Study of the laser effect at different stages of the spike waveform with an activity-dependent stimulation protocol. The panels quantify the change induced by the laser stimulation at distinct illumination offsets, –time intervals from the end of the illumination to the peak of the spike–. Top panel shows a spike waveform from the experiment as a time reference for the offset –time 0 corresponds to the spike peak. Box-plots represent the difference of each metric with respect to the control. All illumination intervals, pictured in the blue boxes, had the same duration of 58 ms and spikes were grouped by the illumination offset. Recovery and continuous laser reference are also shown in green and red boxes at left and right in the figure, respectively. The spike metrics selected here were duration, depolarization and repolarization slopes, –second, third and fourth rows, respectively.

intervals are grouped by the time offset from the illumination to the peak of the action potential. The spike shown in the figure is plotted as a reference of the phase of the action potential in which the illumination finished. Recovery and sustained laser references are also represented at the left and right of each row, in green and red, respectively. For the three metrics here displayed, we can see how as the illumination offset got closer to the spike, the change was larger, and then recovered as the illum-

nation interval covered less the action potential, resulting in an arch shape trend. Although this trend is visible for the three parameters characterized, it is manifested to a different degree in each of them. Note also that there was a temporal shift of the laser effect depending on the instant of stimulation. The maximum change value and the initialization of the recovery was different for the depolarization and for the repolarization. The effect on each of these metrics directly depended on the spike phase when the laser was illuminating the neuron. Thus, this variation of the laser effect points to a distinct modulation on each channel. The magnitude of the change under the sustained laser stimulation was larger than that observed at any of the phases addressed with the activity-dependent protocol. This may be caused by a heating delay during the stimulation, although there was no difference between the first and last spike in the sustained laser, the opening time of the laser shutter might have been smaller than the heating time necessary for the neuron to reach the maximum effect.

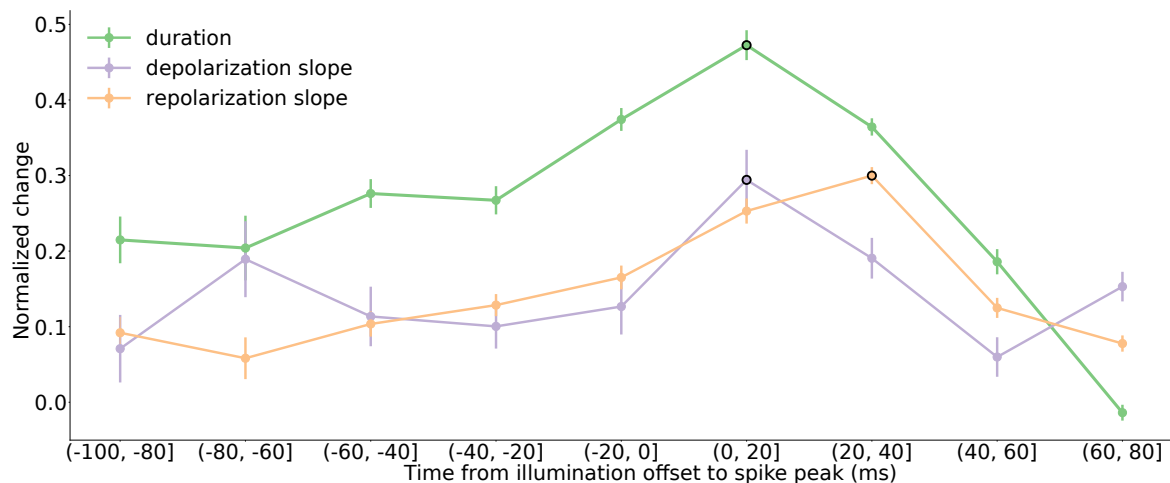


Figure 6.19: Normalized change for grouped values of spike duration, depolarization and repolarization slopes at distinct illumination offsets in the activity-dependent stimulation protocol. Each value in each group was normalized to the mean of its corresponding day controls as minimum value and the mean of the continuous laser recordings for each day as the maximum value. The maximum value for each metric is marked by a black circle.

Figure 6.19 agglutinates the results from 5 different closed-loop experiments, all of them normalized to the mean of the control and sustained laser references for each day, as minimum and maximum values, respectively. The arch trend is maintained. Again, note that the maximum effect for each spike metric occurs at a different stage. For the depolarization, the maximum change was found at the range of -20 to 0 ms, which corresponds to a stimulation during the whole depolarization. A fast rise when the illumination ceased right after the spike can be seen (i.e (0-20] range), since it corresponded to a stimulation during the depolarization and repolarization. In the repolarization, this trend was slightly delayed, reaching the maximum difference from the control at (20-40]. Such changes were

also reproduced in the duration. This points to a modulatory effect of the laser depending on the stimulation instant. Previous to -20 ms, the laser was illuminating the neuron while all ionic channels were starting to activate, specially those involved in the process of the depolarization. However, those channels involved in the repolarization and hyperpolarization were also active earlier than the peak. This is why we can see a difference in all three metrics even at the early ranges of the action potential generation (e.g. -80 ms).

Using the activity-dependent protocol we were able to assess the neural activity at different stages of its dynamics in a controlled way. The results from these experiments showed that it is possible to modify the action potential generation in a temporally precise manner and that the effect of the CW-NIR laser illumination is dependent on the instant of the stimulation. This sets the basis for assessing the biophysical sources of the effect impacting distinct channels without modifying the system condition. Also, it is a proof of concept demonstrating the possibility of developing laser stimulation protocols driven by specific neural activity events in an accessible and freely available real-time tool.

6.7 Discussion

6.7.1 Singularity of the sustained and activity-dependent CW-NIR stimulation on neural dynamics

Advantages of infrared laser neuromodulation beyond its non-invasive nature include its relative simplicity regarding stimulation protocol design, good penetration depth and the possibility to implement highly selective spatio-temporal stimulation delivery. The effectiveness of future applications will depend on a clear understanding of the mechanisms of the neural dynamics modulation.

Most previous studies used protocols involving high-frequency pulsed lasers under the assumption that continuous-wave laser stimulation paradigms do not provide significant activation or neuromodulation (Cayce et al., 2014; Chernov & Roe, 2014; Goyal et al., 2012; Pan et al., 2023; J. D. Wells, M.D., et al., 2005a, 2005b). Their focus involved heating the neurons to elicit spiking activity. The laser wavelengths used were mostly in the range of 1800nm, close to a water absorption band. Here we explored a different approach, using a 830nm CW-NIR laser in sustained and activity-dependent triggered stimulation instead of pulsed illumination at fixed frequency. This setup has a promising future for clinical applications for long-term stimulation and patient-based treatments.

We assessed the action of sustained and activity-dependent CW-NIR stimulation to unveil the bio-

physical sources of the observed modulation on neuronal dynamics. We combined experimental and theoretical methods to analyze this effect. First, we quantified the change on action potential waveform dynamics and on the inter-spike intervals by comparing triplets of long intracellular recordings of control, laser stimulation and recovery. We found that sustained exposure to 830nm CW laser effectively modulated the spike waveform in a reversible manner. We showed this modulation in two different neuron types, illustrating the generalization of the effect. We observed a stronger effect on duration and repolarization, followed by a less strong change in the depolarization slope and a minimal change on amplitude. The neuron dynamics was restored after stimulation. It is important to highlight that here we presented modulation of tonic spontaneous activity, not elicitation of spiking activity as in most previous studies (Izzo et al., 2007; Rabbitt et al., 2016; Shapiro et al., 2012; J. D. Wells, M.D., et al., 2005a). We also showed a tendency to increase the spiking activity under sustained stimulation, not limited to a specific time/intensity configuration of laser pulses as it is most frequently done in the literature (Beier et al., 2014; Goyal et al., 2012; Izzo et al., 2007; Pan et al., 2023). Although there are previous studies discussing the inhibitory ability of infrared-laser illumination (Begeng et al., 2022; Duke et al., 2013; Ganguly et al., 2019a; Lothet et al., 2017), we did not find evidence of any direct CW-NIR inhibitory effect. Note that the origin of tonic spiking was affected by the intrinsic properties of the cell and the synaptic inputs within the circuit, e.g., the illuminated neuron might be triggering an inhibitory or excitatory feedback from other neurons, complicating the analysis. This explains the lack of excitation in a subpopulation in Fig. 6.8. Spontaneous neural activity and the nature of the living preparation used may naturally tend to decrease the firing rate.

6.7.2 Biophysical explanation of the CW-NIR modulation through modeling and activity-dependent stimulation

The results of sustained CW-NIR illumination alone cannot discard previously suggested mechanisms such as cytochrome oxidase (Saucedo et al., 2021; Wang et al., 2017) or calcium release from internal storage (Lumbreras et al., 2014). The fact that the illumination directly affects the spike waveform but not always translates into an increased firing rate may indicate that there is more than a single mechanism involved. Moreover, our analysis of sustained laser stimulation does not point to a slow change such as the one expected with the liberation of Ca^{2+} caused by a mitochondrial modulation (Dittami et al., 2011; Lumbreras et al., 2014), since we observed a minimal delay between the illumination onset and the modulatory effect, and the illumination cessation and the recovery. The short exposure in the activity-dependent experiment with quick response time also points to a short

timescale effect, such as a direct effect on the ionic channels.

Conductance-based models allowed us to identify the most compatible biophysical explanation to the CW-NIR modulation. We evaluated the capacitance and distinct ionic channels in the parameter space of three conductance-based models, which would be highly costly experimentally. We concluded that all candidates explored contributed to partial reproduction of the waveform modulation but none was sufficient to explain the full observed effect. Capacitance is one of the most discussed candidates (Cayce et al., 2014; Plaksin et al., 2018; Shapiro et al., 2012; Thompson et al., 2015). However, in our modeling study, capacitance alone was not able to reproduce the modulation. Although the isolated modification of any channel resulted in a limited explanation of the CW-NIR change, late activation channels such as potassium –preserving the depolarization-repolarization change relation– or high-activated calcium –necessary for shoulder shape modulation– seem to play a key role reproducing the observed effect.

Temperature-dependent simulations validated that the best explanation for the sustained laser action is a combined modulation of channels, reproducing the observed change for amplitude, duration and slopes. This supports previous studies' hypothesis that the photo-thermal interaction is key in the NIR laser effect (Albert et al., 2012; Barrett et al., 2018; Brown et al., 2020; Cury et al., 2021; Li et al., 2013; Rabbitt et al., 2016; J. D. Wells, M.D., et al., 2005a). We selectively excluded one channel from the temperature dependency at a time in the CGC-model, which cannot be performed experimentally. We found I_D and I_{NaP} channels to be critical for the activity modulation, radically changing the waveform when altering temperature dependency. Also, canceling the temperature dependency of I_{HVA} largely changed the amplitude, indicating its importance in preserving the observed amplitude-repolarization relation during the modulation.

Finally, a closed-loop protocol allowed altering the action potential at distinct generation phases. We presented a new open-source protocol for spike prediction to stimulate at precise times around the occurrence of the action potentials. The outcome of the CW-NIR effect at distinct time intervals in relation to the timing of the spike's peak highlighted the importance of the stimulus delivery time. By changing the illumination instant, we shifted the effect on the waveform shape, getting different maximum metric changes at different stages of the action potential generation.

These changes in the waveform open a discussion about the biophysical source of this effect. With short closed-loop illumination intervals ($< 60\text{ms}$), we observed a controlled modulation of neural activity smaller than the effect during the sustained laser illumination. In the open-pipette estimation, the maximum change for the steady state temperature value ($1\text{-}2^\circ\text{C}$) was reached after 1s and the change after 50ms was only of 0.1°C . This estimation was performed on the preparation's solution,

and our laser wavelength is far from the intense water absorption bands. So temperature change could be higher in the neuronal membrane, as the specific heat capacity of the water is $\sim 30\%$ larger than the estimated on the membrane (Thompson et al., 2012). This would result in a faster temperature increase under heat-inducing stimulation. Also, in the model, we observed a change similar to the experimental results with $\Delta T >= 5^\circ\text{C}$. Thus, the modulation might not be caused by simply heating the surrounding water. In the sustained stimulation, there might be additional modulation sources such as an effect on the mitochondria as it has been discussed in previous studies (Dittami et al., 2011; Lumbreiras et al., 2014; Saucedo et al., 2021), which we cannot discard as adding to the modulation of ionic channels. However, the effect observed during the activity-dependent stimulation is unlikely to have other than fast sources such as ionic-channels. A rigorous characterization of the timescale of the temperature changes induced by the CW-NIR and the associated instantaneous voltage dynamics could provide further insight on the fast and slow biophysical mechanisms underlying the waveform modulation. This is particularly relevant for the design of fast activity-dependent protocols to produce the observed effect safely with minimal biophysical perturbation. An accurate characterization of the relation between temperature and neuronal dynamics under CW-NIR stimulation requires novel highly precise protocols to measure the membrane temperature and fast non-periodic electro-optical shutters controlled by real-time software technology. This could be performed using nanothermometry by estimating the temperature change in the membrane by the emission on nanoparticles in the tissue (Hamraoui et al., 2023).

6.7.3 Applications for research and clinical use

The open-source approach described in this paper can be generalized for any animal and preparation. In addition, our protocol leaves plenty of possibilities for other closed-loop stimulation methodologies, including clinical interventions. We provided an open-access repository with the code to reuse our protocols and the module for RTXI, which can be used with any control hardware including fast electro-optical shutters.

Regarding the non-invasive nature of the CW-NIR laser effect, we could not observe any damage to the cells linked to the stimulation in our experiments. We can hypothesize that stimulation from a laser with higher power could be tolerated by neurons. The recovery of the neural dynamics after illumination does not mean that the CW-NIR laser stimulation cannot be employed to address laser-driven plasticity in protocols designed for this goal. We have shown that sustained CW-NIR laser effectively accelerates neural dynamics in single neurons affecting a combination of biophysical mechanisms. Also, our results indicate that novel research and clinical applications of the excitabil-

ity increase of laser stimulation must rely on a careful selection of the stimulus parameters and the timing of the illumination. In this context, the results of our pioneer activity-dependent infrared laser stimulation provide a novel approach to adapt the modulation of neural dynamics to specific applications, particularly in the field of personalized treatments including stimulation-driven plasticity.

CHAPTER 7

Conclusion and Discussion

During this work, we have explored with distinct complementary experimental and computational approaches the sequentiality in the neuronal dynamics, from the sequential activation of ionic channels in the generation of action potentials, to the cycle-by-cycle dynamics in CPG circuits. Here is a summary of the main results presented in this thesis (see also Fig. 7.1):

- Part 1: Sequential dynamical invariants.
 - We have illustrated the importance of the study of sequential dynamics at different description levels.
 - We have hinted the universality of sequential dynamical invariants by showing their presence in the feeding CPG of *Lymnaea stagnalis* both in experimental and modeling data, i.e., in a different animal model from the one used in the work that reported their discovery.
 - We have shown that dynamical invariants can be found in models when the circuit displays enough cycle-by-cycle variability, which can be induced by an external stimulus.
 - The models that simulated the variability under the stimulation of specific neurons predicted that the dynamical invariants changes depending on the neuron stimulated. This prediction was validated experimentally.
 - Dynamical invariants are indicators of the functional distribution of variability in the CPG.
 - Neural intrinsic variability in models is usually limited but crucial to study the sequential variability in neural dynamics.
 - It is possible to study the functional role of sequential dynamical invariants by using the

robust linear relations of neural sequence intervals to control the motor coordination of a hybrot.

- Part 2: CW-NIR laser illumination as an effective modulatory technique.
 - Sustained CW-NIR laser illumination asymmetrically accelerates action potential dynamics and the spiking rate on single neurons.
 - The preliminary results in electrically coupled neurons (a minimal circuit) show the potential of CW-NIR to modulate circuit dynamics.
 - Modifying the wavelengths of the CW-NIR laser can evoke different changes in action potential metrics. The results illustrate the importance of selecting wavelength, power and duration for a specific modulation goal.
 - A model study of the effect of CW-NIR showed that no biophysical candidate alone could fully reproduce the observed modulation and the global modulation through temperature description was the closest approximation to it.
 - The closed-loop protocol unveiled the CW-laser effect at different phases of the neuron dynamics, showing a different modulation depending on the instant of illumination.
 - The code of this closed-loop protocol was published in open-access and can be easily generalized for other neuron types and research contexts.

In chapter 5, we analyzed the sequential dynamical invariants in a CPG circuit. The goal was to prove the hypothesis presented in Elices et al., 2019 that the strong linear relationships found between some cycle-by-cycle intervals in the pyloric CPG of the *Carcinus maenas* were not a specific feature of that particular CPG, but a general phenomenon for effective autonomous motor coordination. Thus, the first result showed in 5 was **the universality of sequential dynamical invariants**, found also in the feeding CPG of *Lymnaea stagnalis*. We proved this showing their presence not only in a detailed model of the circuit, but also in experimental recordings of the CPG. In the model, we quantified the variability induced by a ramp-current in specific neurons. We explored the variability and the correlations between period and the different intervals in the cycle showing the presence of sequential dynamical invariants. **The variability distribution and, consequently, the sequential dynamical invariants change as the neuron stimulated in the model simulation changes.** This highlights the importance of the relation between the neurons in the circuit dynamics so the constrained variability results in flexibility for a cycle-by-cycle adaptation. Thus the computational model configuration and the resulting dynamics must be flexible enough to achieve this constrained variability in the simulations. We supported these results analyzing different recordings from neurons in the buccal

ganglion, that represented the circuit. We discussed in that chapter the difficulties defining the three phases of the feeding CPG in comparison with the pyloric CPG. Thus, after identifying the three phases of the circuit based on combination of interneurons and motoneurons signals, we analyzed the variability and relations between intervals cycle-by-cycle for spontaneous activity cases and current stimulation driven activity in electrophysiological recordings. We showed the intervals variability and relations in examples of spontaneous activity and **found sequential dynamical invariants in this spontaneous neural activity**. We also analyzed different cases of stimulation, first SO driven stimulation, spontaneously and by induced stimulation, and reproduced the results in the model, **showing a change in the variability distribution when the rhythm is modulated by SO**. From this premise that the rhythm is different as the source varies, we analyzed cases where the rhythm was modulated by CV1a neuron stimulation and by MLN nerve. In both cases, **the interval variability was distributed between N1 and N3 phases**.

Based on these experimental and theoretical results, we also presented in [5](#) a study on neural variability. In the modeling side, **we analyzed the importance of variability in the study of neuronal dynamics and the limitation of classical models to reproduce the intrinsic functional variability of neurons**. We compared different examples of living and modeled neurons and their variability, **showing the model limitations**. Regarding the experimental approach, we explored the possibility to translate the sequential intervals into effective robot movement. This is important in order to explain the functional meaning of this strong relationships we observed in specific intervals, that as we discussed is related to the context and the source of the rhythm. In this first prototype, **we analyzed and observed that it is possible to achieve an effective robot movement in a robot maintaining strong cycle-by-cycle linear relations**.

In the study of the sequentiality in CPGs, we saw the importance of using effective tools to alter the spontaneous neural activity noninvasively. In chapter [6](#) **we explored in detail the CW-NIR laser as a stimulation technique experimentally, theoretically and in activity-dependent protocols**. First, we show the effect of illuminating single cells and how **CW-NIR sustained illumination asymmetrically accelerates action potential dynamics and increases the firing rate on single neurons**. We tested the effect of the laser stimulation in a minimal circuit by **illuminating electrically coupled neurons, showing that the main modulation was in the illuminated neuron, slightly modifying the coupled neuron**. We also showed the preliminary results of the wavelength-effect relation, analyzing the effect in duration, amplitude and slopes with different laser wavelengths and powers, **showing a modulation of the amplitude as the laser wavelength and power increases that is not showed at low-wavelengths values**. This experimentally observed effect was dissected

through model simulations, exploring the possible candidates: ionic channels and capacitance, in conductance-based models, with and without temperature dependence description, showing that **no candidate alone could fully reproduce the observed modulation and that the global modulation through temperature description was the closest approximation to it.** Finally, we presented a **closed-loop protocol to alter the action potential at distinct sequential generation phases that can be generalized for distinct subjects and neurons.** With this stimulation protocol we unveiled the CW-laser effect at different phases of the neuron dynamics, identifying different spike waveform changes depending on the time instant of the illumination. We also supported this results with a **model simulation, tuning some of the channels only at depolarization and repolarization phases, showing the enhancement of the effect as the stimulation time changes.**

The study of temporal restrictions in the sequential activation of motor circuits can have strong implications in neurorhabilitation and in the understanding of the brain processing of the motor activation. This can unveil the key aspects of the relation between variability, robust sequentiality and flexibility that is shown in living systems, such as in CPGs. For this, it is necessary to expand the study of sequential variability in different animals but also to relate the sequential dynamical invariants to their role in the motor output, relating their activation to different contexts. This restrictions can be indicators of the state of the system and can be associated to the importance of each phase in the current moment, e.g., protraction phase in the presence of food is crucial to achieve the food ingestion as in the MLN stimulation example, while its role when the circuit is active in the absence of food it is not that important, so the variability can be distributed differently, as it was the case of the spontaneous example with a high-correlation of N3 to the period. In this direction, it is important to improve the intrinsic variability in models simulations by an extended description of chaotic dynamics of the neural activity and its expansion to more complex circuits and systems. The study of the time-interval restrictions in living circuits that produce and ensure the sequential dynamical invariants can also be translated into the design of robots with the robust motor coordination observed in CPGs. These examples will be of high interest for applications in neurotechnology and autonomous robotics design.

The laser stimulation can help to further explore this dynamics by the effective modulation. The study of this novel neuromodulatory technique might have strong implications for both research and clinical applications by its noninvasive nature. Laser stimulation has been gaining ground in the field of optical stimulation, often studied as long-wavelength pulsed laser stimulation. It is important to validate different stimulation options such as the sustained continuous-wave and activity-dependent stimulation, of high interest for personalized treatments. The protocol presented in this work might

be enhanced with a larger temporal precision, down to the nanosecond scale. This will be relevant to extrapolate it to different systems, regardless of their neural activation time scale, but also to dissect precisely the channel activation dynamics. Furthermore, a in-deep characterization of the laser illumination and its safety range of activation will be of great importance for clinical applications. In this work, we showed a strong and reversible effect, that did not damage the neurons illuminated, which indicates the power used could be increased. A precise characterization of the power tolerated by the neurons would set the safety ranges of its application. Also, the preliminary study of the wavelength-effect relation showed that it is not only important the power but the laser wavelength in terms of the effect depicted, so the analysis of the relation of the wavelength might expand this range of applications but also distinguish between other different mechanisms such as photo-electrical, photo-thermal, etc. A future line of study would also assess the effect of CW-NIR laser in circuits, based on the preliminary results, it should be possible to modify the neurons in a circuit by the stimulation of one of its neurons. This could be studied in the CPG circuits, in the case of the feeding CPG illuminating neurons that have a activator/modulatory role in the circuit such as the CGC neuron in the cerebral ganglion, away to the buccal but connected. Finally, as discussed in this work and laser neurotechnology literature, a photo-thermal effect is one of the main actuators behind the neuronal laser stimulation, however with the current tools and techniques it is not possible to have a detailed description of the change of temperature in the cell. In this line, although it is not included in this work, we have explored the possibility of a more precise estimation of the temperature change using silver nanoparticles. These particles could be directly on the membrane, reducing the area of temperature change measurement, and the variation of temperature could be estimated by their irradiation. This precise measurement of the temperature could also help improve the model simulations, with the specific change in the neurons. Also exploring the fast change observed in the activity-dependent protocol with a small change in temperature according to the pipette estimation, can help understand the source of the effect.

The study of neural sequences at multiple spatial and temporal scales can provide novel insights to relate neural dynamics and behavior. Novel neurotechnologies can contribute to identify and exploit the sequential nature of neural information processing. The results discussed in this thesis in the context of neural sequences can also have strong implications in the field of neurorrehabilitation, robotics and artificial intelligence.

CHAPTER 7: CONCLUSION AND DISCUSSION

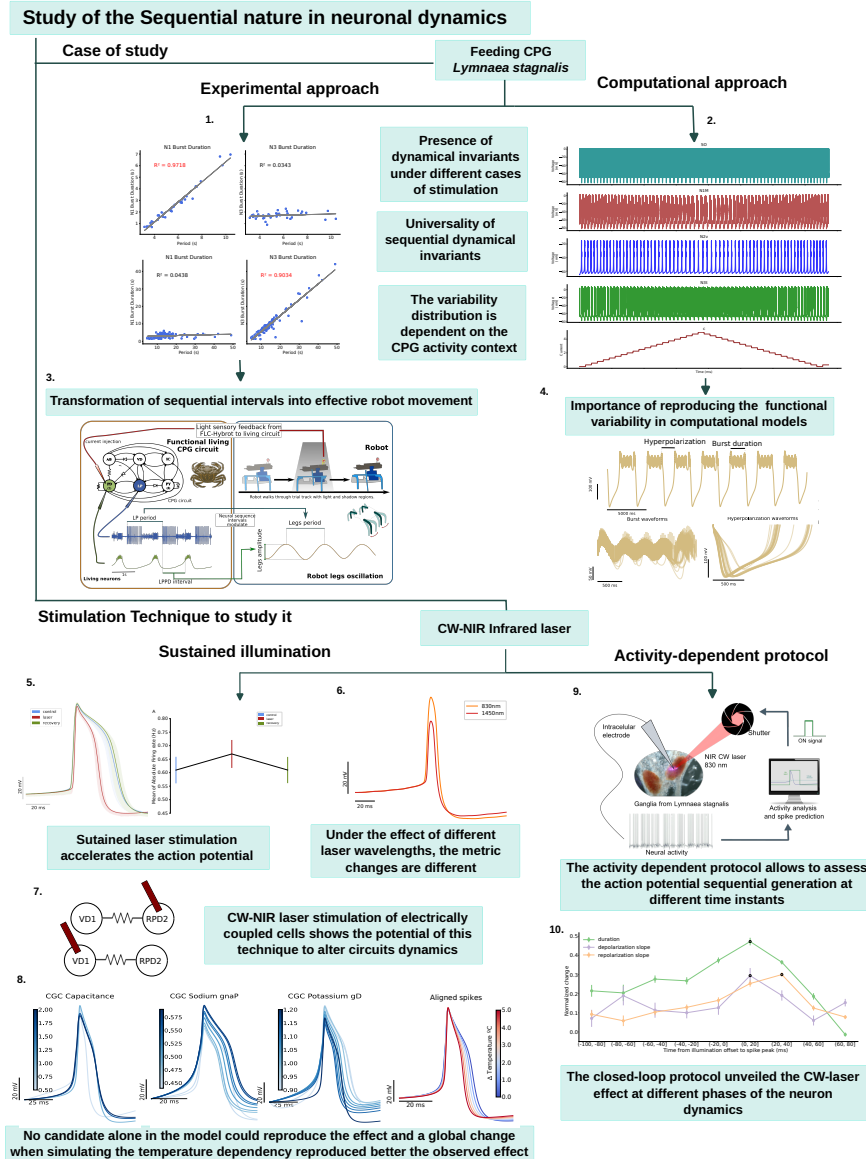


Figure 7.1: Schematic summary of the results presented in this work. In the feeding CPG of *Lymnaea stagnalis* we explored in (1) experimental and (2) computational data the presence of dynamical invariants (Secs. 5.4 and 5.3), showing strong linear relations and associating this to the possible functional role of this indicator. The experimental results were complemented exploring the transformation of (3) robot movement into effective robot movement maintaining strong linear relations (Sec. 5.6). We also showed the (4) importance of reproducing the functional variability in computational models (Sec. 5.5). As a way to modulate neural dynamics we characterized the effect of the CW-NIR laser in single neurons in a sustained and activity dependent protocol. We showed (5) the spike waveform is modified during the laser illumination, as well as the firing rate (Sec. 6.4), and discussed the effect at (6) different wavelengths (Sec. 6.4.4). We showed also (7) preliminary results in the stimulation of a minimal circuit (Sec. 6.4.3). The computational model analysis (8) revealed the combination of candidates to reproduce the effect and the importance of the temperature role (Sec. 6.5). (9) The activity-dependent protocol (10) allowed to assess the action potential generation at different phases (Sec. 6.6).

CHAPTER 8

Conclusiones y Discusión

Durante este trabajo, hemos explorado con distintos enfoques experimentales y computacionales complementarios la naturaleza secuencial de la dinámica neuronal, desde la activación secuencial de canales iónicos en la generación de potenciales de acción, hasta la dinámica ciclo a ciclo en circuitos CPG. A continuación, se presenta un resumen de los principales resultados de esta tesis:

- Parte 1: Invariantes dinámicos secuenciales.
 - Ilustramos la importancia de estudiar dinámicas secuenciales en diferentes niveles de descripción.
 - Sugerimos la universalidad de invariantes dinámicos secuenciales al demostrar su presencia en el CPG alimentario de *Lymnaea stagnalis* en datos experimentales y en simulaciones computacionales, en un modelo animal diferente al utilizado en el trabajo que reportó su descubrimiento.
 - Mostramos que los invariantes dinámicos pueden identificarse en modelos cuando el circuito exhibe suficiente variabilidad ciclo a ciclo inducida por estímulos externos.
 - Los modelos que generaban variabilidad mediante la estimulación de neurona predijeron que los invariantes cambian según la neurona estimulada. Dicha predicción se comprobó experimentalmente.
 - Los invariantes dinámicos sirven como indicadores de la distribución de variabilidad funcional en el CPG.
 - La variabilidad neuronal intrínseca en los modelos comúnmente utilizados es limitada comparada con la observada experimentalmente, sin embargo, es esencial para estudiar la dinámica neuronal secuencial.

- Demostramos el papel funcional de los invariantes dinámicos secuenciales mediante relaciones lineales robustas de intervalos temporales en la actividad neuronal para controlar la coordinación motora en un robot híbrido.
- Parte 2: Iluminación con láser CW-NIR como técnica de modulación neuronal efectiva.
 - La iluminación sostenida con láser CW-NIR acelera asimétricamente la dinámica de los potenciales de acción y aumenta la frecuencia de disparo en neuronas individuales.
 - Los resultados preliminares en neuronas eléctricamente acopladas (como circuito mínimo) muestran el potencial del láser CW-NIR para modular la dinámica en circuitos.
 - Mostramos que distintas longitudes de onda del láser CW-NIR pueden evocar diferentes cambios en las formas de onda de los potenciales de acción, resaltando la importancia de seleccionar la longitud de onda, la potencia y la duración para objetivos específicos de modulación.
 - El estudio computacional del efecto del láser CW-NIR reveló que ningún único candidato biofísico puede replicar completamente la modulación observada y la explicación más plausible es la modulación global a través del efecto de la temperatura.
 - Con el protocolo de ciclo cerrado mostramos el efecto del láser CW-NIR en varias fases de la dinámica neuronal, demostrando cambios en la modulación neuronal según el momento de la iluminación.
 - El protocolo de ciclo cerrado disponible en código abierto puede generalizarse fácilmente para otro tipo de neuronas y contextos de investigación.

En el capítulo 5, analizamos los invariantes dinámicos secuenciales en un circuito CPG. El objetivo fue demostrar la hipótesis presentada en Elices et al., 2019 de que las fuertes relaciones lineales encontradas entre algunos intervalos ciclo a ciclo en el CPG pilórico del *Carcinus maenas* no eran una característica específica de ese CPG en particular, sino un fenómeno general para la coordinación motora autónoma. Así, el principal resultado del capítulo 5 fue mostrar la **generalización de la presencia de los invariantes dinámicos secuenciales**, ya que se encontraron no solo en un modelo detallado del circuito, sino también en registros experimentales del CPG alimentario de *Lymnaea stagnalis*. En el modelo, cuantificamos la variabilidad inducida por una corriente en forma de rampa en neuronas específicas. Exploramos la variabilidad y las correlaciones entre el período y los diferentes intervalos en el ciclo, mostrando la presencia de invariantes dinámicos secuenciales. Observamos que la **distribución de variabilidad y, por lo tanto, los invariantes dinámicos secuenciales cambian según la neurona estimulada en la simulación del modelo**. Esto resalta la importancia

de la relación entre las neuronas en la dinámica del circuito, de modo que la variabilidad restringida resulta en flexibilidad para una adaptación ciclo a ciclo. Por lo tanto, la configuración del modelo computacional y la dinámica resultante deben ser lo suficientemente flexibles para lograr esta variabilidad restringida en las simulaciones. Apoyamos estos resultados analizando diferentes registros de neuronas en el ganglio bucal. Discutimos en ese capítulo las dificultades para definir las tres fases del CPG alimentario en comparación con el CPG pilórico. Así, después de identificar las tres fases del circuito basadas en la combinación de señales de interneuronas y motoneuronas, analizamos la variabilidad y las relaciones entre los intervalos ciclo a ciclo para casos de actividad espontánea y actividad inducida por estimulación eléctrica en neuronas individuales. Caraterizamos la variabilidad de intervalos y sus relaciones ciclo a ciclo en diferentes registros de actividad espontánea y **encontramos invariantes dinámicos secuenciales en la actividad neuronal espontánea**. También analizamos diferentes casos de estimulación, primero estimulación impulsada por la neurona moduladora SO, espontáneamente y por estimulación inducida, y reproducimos los resultados predichos por el modelo, **mostrando un cambio en la distribución de variabilidad cuando el ritmo es modulado por SO**. A partir de la premisa de que el ritmo es diferente según varía su fuente de activación, analizamos casos donde el ritmo fue modulado por la estimulación de la neurona CV1a y por el nervio MLN. En ambos casos, **la variabilidad de los intervalos se distribuyó entre las fases N1 y N3**.

Basados en estos resultados experimentales y teóricos, también presentamos en [5](#) un estudio sobre la variabilidad neuronal. En los modelos, **analizamos la importancia de la variabilidad en el estudio de la dinámica secuencial neuronal y las limitaciones de los modelos clásicos para reproducir la variabilidad funcional intrínseca de las neuronas**. Comparamos ejemplos de neuronas vivas y modeladas y su variabilidad, **analizando diferentes modelos y sus limitaciones**. En cuanto al enfoque experimental, exploramos la posibilidad de emplear los intervalos secuenciales de invariantes dinámicos para coordinar eficazmente el movimiento de un robot. Esto es importante para abordar el papel funcional de estas relaciones robustas que observamos en intervalos específicos, que como discutimos, están influenciadas por el contexto y el origen del ritmo. En este primer prototipo, **analizamos y observamos que es posible lograr un movimiento efectivo de un robot manteniendo estas relaciones lineales ciclo a ciclo**.

En el estudio de la secuencialidad en los CPGs, vimos la importancia de utilizar herramientas eficaces para alterar la actividad neuronal de forma no invasiva. En el capítulo [6](#), **exploramos en detalle el láser CW-NIR como técnica de estimulación de forma experimental, teórica y en protocolos dependientes de la actividad**. Primero, mostramos el efecto de iluminar células individuales y cómo la

iluminación sostenida acelera asimétricamente la dinámica del potencial de acción y aumenta la frecuencia de *spikes* en neuronas individuales. Probamos el efecto del láser en un circuito mínimo al **iluminar neuronas acopladas eléctricamente, mostrando que la principal modulación fue en la neurona iluminada, modificando ligeramente la neurona acoplada.** También mostramos resultados preliminares de la relación efecto-longitud de onda, analizando el efecto en duración, amplitud y pendientes con diferentes longitudes de onda y potencias, **mostrando una modulación de la amplitud a medida que aumenta la longitud de onda y la potencia del láser que no se observa en valores de baja longitud de onda.** El efecto observado experimentalmente en la forma de onda se diseccionó mediante simulaciones en modelos de conductancia, explorando los posibles candidatos para explicarlo: canales iónicos y capacitancia, con y sin descripción de dependencia de temperatura, mostrando que **ningún candidato por sí solo reproduce completamente la modulación observada y que la modulación global a través de la descripción de temperatura es la explicación más plausible.** Finalmente, **presentamos un protocolo en ciclo cerrado para alterar el potencial de acción en distintas fases de su generación secuencial que puede generalizarse para distintos sujetos y neuronas.** Con este protocolo de estimulación, **caracterizamos el efecto del láser CW en diferentes fases de la dinámica neuronal, identificando diferentes cambios en la onda según el momento de iluminación.** También respaldamos estos resultados con **una simulación del modelo, ajustando algunos de los canales solo en las fases de despolarización y repolarización, mostrando el aumento del efecto a medida que cambia el tiempo de estimulación.**

El estudio de las restricciones temporales en la activación secuencial de circuitos motores puede tener fuertes implicaciones en neurorrehabilitación y en la comprensión del procesamiento cerebral de la activación motora. Este análisis puede revelar los aspectos clave de la relación entre variabilidad, secuencialidad robusta y flexibilidad que se observa en sistemas vivos, como en los CPG. En este contexto, es necesario ampliar el estudio de la variabilidad secuencial en diferentes animales, pero también relacionar los invariantes dinámicos secuenciales con su papel en la salida motora, asociando su activación con diferentes contextos. Estas restricciones pueden ser indicadores del estado del sistema y pueden asociarse a la importancia de cada fase en el momento actual, por ejemplo, la fase de protracción en presencia de alimentos es crucial para la ingesta, como en el ejemplo de estimulación MLN, mientras que su papel cuando el circuito está activo en ausencia de alimentos no es tan importante, por lo que la variabilidad puede distribuirse de manera diferente, como fue el caso del ejemplo espontáneo con una alta correlación de N3 con el período. En esta dirección, es importante mejorar la variabilidad intrínseca del modelo con una descripción ampliada de la dinámica caótica de la actividad neuronal, y su expansión a circuitos y sistemas más complejos. El estudio de las restricciones entre intervalos de tiempo secuenciales en circuitos vivos que producen y mantienen

CHAPTER 8: CONCLUSIONES Y DISCUSIÓN

los invariantes dinámicos también puede trasladarse al diseño de robots que reproduzcan la robustez de la coordinación observada en los CPGs. Estos estudios son de gran interés para aplicaciones en neurotecnología y el diseño de robótica autónoma.

La estimulación láser puede ayudar a explorar más en detalle la dinámica neuronal secuencial mediante su modulación efectiva. El estudio de esta nueva técnica neuromoduladora puede tener fuertes implicaciones tanto para investigación como para aplicaciones clínicas debido a su naturaleza no invasiva. La estimulación láser ha ido ganando terreno en el campo de la estimulación óptica, a menudo estudiada como estimulación láser pulsada de longitud de onda larga. Es importante validar diferentes opciones de estimulación como la estimulación sostenida del láser CW-NIR y la estimulación dependiente de la actividad, de gran interés para tratamientos personalizados. El protocolo presentado en este trabajo podría mejorarse con una mayor precisión temporal, siendo capaz de estimular a escala de nanosegundos. Esto permitirá extrapolarlo a diferentes sistemas, independientemente de su escala temporal de activación neuronal, y también para diseccionar con precisión la dinámica de activación de los canales. Además, una caracterización en detalle de la iluminación láser y su rango de seguridad de actuación será de gran importancia para las aplicaciones clínicas. En este trabajo hemos mostrado un efecto notable y reversible que no dañó las neuronas iluminadas, lo que indica que la potencia utilizada podría aumentarse aun más. Una caracterización precisa de la potencia tolerada por las neuronas establecería los rangos de seguridad de su aplicación. Además, el estudio preliminar de la relación efecto-longitud de onda mostró que no solo es importante la potencia, sino la longitud de onda del láser en términos del efecto observado, por lo que el análisis de la relación de la longitud de onda podría ampliar este rango de aplicaciones y ayudar a distinguir las causas del efecto entre otros posibles mecanismos como los fotoeléctricos o fototérmicos. Una línea de estudio futura también podría evaluar el efecto del láser CW-NIR en circuitos, según los resultados preliminares obtenidos, ya que debería ser posible modular la actividad de un circuito mediante la estimulación de componentes individuales. Esto podría estudiarse en los circuitos de CPG, en el caso del CPG alimentario de *L. stagnalis*, iluminando neuronas que tienen un papel activador/modulador en el circuito, como la neurona CGC en el ganglio cerebral, alejada del bucal pero conectada. Finalmente, como se discutió en este trabajo y en la literatura sobre neurotecnología láser, el efecto fototérmico es uno de los principales responsables de la modulación neuronal resultante, sin embargo, con las herramientas y técnicas actuales no es posible tener una descripción detallada del cambio de temperatura en la célula. Aunque no se han incluido en este trabajo los resultados, hemos explorado la posibilidad de una estimación más precisa del cambio de temperatura utilizando nanopartículas de plata. Estas partículas podrían alojarse directamente en la membrana, reduciendo el área de medición del cambio de temperatura, y la variación de la temperatura podría estimarse a partir de su irradiación. Esta

CHAPTER 8: CONCLUSIONES Y DISCUSIÓN

medición precisa de la temperatura también podría ayudar a mejorar las simulaciones del modelo, con el dato específico del cambio de temperatura en las neuronas. También permitiría explorar el cambio rápido observado en el protocolo dependiente de la actividad que se produce con un pequeño cambio en la temperatura (según la estimación de la pipeta) y puede ayudar a comprender la fuente del efecto.

El estudio de secuencias neuronales en múltiples escalas espaciales y temporales puede proporcionar nuevas ideas para relacionar la dinámica neuronal y el comportamiento. Las nuevas neurotecnologías pueden contribuir a identificar y explotar la naturaleza secuencial del procesamiento de información neuronal. Los resultados discutidos en esta tesis en el contexto de secuencias neuronales también pueden tener fuertes implicaciones en el campo de la neurorrehabilitación, la robótica y la inteligencia artificial.

Bibliography

- Aguirre, C., Campos, D., Pascual, P., & Vázquez, L. Pattern formation and encoding rhythms analysis on a spiking/bursting neuronal network. en. *The European Physical Journal Special Topics*, 146(1). 2007. 146. (1). 169–176. ISSN: 1951-6355, 1951-6401. <https://doi.org/10.1140/epjst/e2007-00177-8>. (Cit. on p. 14).
- Albert, E. S., Bec, J. M., Desmadryl, G., Chekroud, K., Travo, C., Gaboyard, S., Bardin, F., Marc, I., Dumas, M., Lenaers, G., Hamel, C., Muller, A., & Chabbert, C. TRPV4 channels mediate the infrared laser-evoked response in sensory neurons [Publisher: American Physiological Society Bethesda, MD]. *Journal of Neurophysiology*, 107(12). 2012. 107. (12). 3227–3234. ISSN: 00223077. <https://doi.org/10.1152/jn.00424.2011>. (Cit. on pp. 114, 136, 148).
- Alonso, L. M., & Marder, E. Temperature compensation in a small rhythmic circuit [Publisher: eLife Sciences Publications Ltd]. *eLife*, 9. 2020. 9. 1–24. ISSN: 2050084X. <https://doi.org/10.7554/eLife.55470>. (Cit. on p. 138).
- Amaducci, R., Elices, I., Reyes-Sanchez, M., Garrido-Peña, A., Levi, R., Rodriguez, F. B., & Varona, P. Hybrid robot driven by a closed-loop interaction with a living central pattern generator with online feedback. 29th Annual Computational Neuroscience Meeting: CNS*2020. P207. [Related to Chapter 4]. *BMC Neuroscience*, 21. 2020. 21. 54. <https://doi.org/10.1186/s12868-020-00593-1>. (Cit. on p. 105).
- Amaducci, R., Elices, I., Reyes-Sánchez, M., Garrido-Peña, A., Levi, R., Rodriguez, F. B., & Varona, P. Controlling robotic locomotion by a closed-loop interaction with living central pattern generators. [Related to Chapter 4]. *COSYNE*. 2021. https://www.cosyne.org/s/Cosyne2021_program_book.pdf. (Cit. on p. 105)
- Amaducci, R., Reyes-Sánchez, M., Elices, I., Rodriguez, F. B., & Varona, P. RThybrid: A standardized and open-source real-time software model library for experimental neuroscience [Publisher: Frontiers Media S.A.]. *Frontiers in Neuroinformatics*, 13. 2019. 13. 1–14. ISSN: 16625196. <https://doi.org/10.3389/fninf.2019.00011>. (Cit. on pp. 114, 118).

BIBLIOGRAPHY

- Amunts, K., Knoll, A., Lippert, T., Pennartz, C., Ryvlin, P., Destexhe, A., Jirsa, V., D'Angelo, E., & Bjaalie, J. The Human Brain Project—Synergy between neuroscience, computing, informatics, and brain-inspired technologies. *PLOS Biology*, 17. 2019. 17. e3000344. <https://doi.org/10.1371/journal.pbio.3000344>. (Cit. on pp. 10, 31).
- Arichi, T., Whitehead, K., Barone, G., Pressler, R., Padormo, F., Edwards, A. D., & Fabrizi, L. Localization of spontaneous bursting neuronal activity in the preterm human brain with simultaneous EEG-fMRI. *eLife*, 6. 2017. 6. 1–14. ISSN: 2050084X. <https://doi.org/10.7554/eLife.27814>. (Cit. on p. 56).
- Bansal, A., Shikha, S., & Zhang, Y. Towards translational optogenetics [Publisher: Nature Publishing Group UK London]. *Nature Biomedical Engineering*, 7. 2022. 7. 1–21. <https://doi.org/10.1038/s41551-021-00829-3>. (Cit. on p. 113).
- Barrett, J. N., Rincon, S., Singh, J., Matthewman, C., Pasos, J., Barrett, E. F., & Rajguru, S. M. Pulsed infrared releases Ca²⁺ from the endoplasmic reticulum of cultured spiral ganglion neurons [Publisher: American Physiological Society]. *Journal of Neurophysiology*, 120(2). 2018. 120. (2). 509–524. ISSN: 15221598. <https://doi.org/10.1152/jn.00740.2017>. (Cit. on pp. 19, 37, 114, 136, 148).
- Beekharry, C. C., Zhu, G. Z., & Magoski, N. S. Role for electrical synapses in shaping the output of coupled peptidergic neurons from Lymnaea [Publisher: Elsevier]. *Brain Research*, 1603. 2015. 1603. 8–21. ISSN: 18726240. <https://doi.org/10.1016/j.brainres.2015.01.039>. (Cit. on p. 128).
- Begeng, J. M., Tong, W., Rosal, B. d., Ibbotson, M., Kameneva, T., & Stoddart, P. R. Activity of Retinal Neurons Can Be Modulated by Tunable Near-Infrared Nanoparticle Sensors [Publisher: American Chemical Society]. *ACS Nano*, 17(3). 2022. 17. (3). 2079–2088. ISSN: 1936086X. https://doi.org/10.1021/ACSNANO.2C07663/ASSET/IMAGES/LARGE/NN2C07663_0006.JPG. (Cit. on pp. 19, 37, 114, 147).
- Beier, H. T., Tolstykh, G. P., Musick, J. D., Thomas, R. J., & Ibey, B. L. Plasma membrane nanoporation as a possible mechanism behind infrared excitation of cells [Publisher: IOP Publishing]. *Journal of Neural Engineering*, 11(6). 2014. 11. (6). 066006. ISSN: 1741-2552. <https://doi.org/10.1088/1741-2560/11/6/066006>. (Cit. on p. 147).
- Benjamin, B. Y. P. R., Rose, R. M., Slade, C. T., & Lacy, M. G. Morphology of Identified Neurones in the Buccal Ganglia of Lymnaea Stagnalis. *Journal of Experimental Biology*, 80(1). 1979. 80. (1). 119–135. ISSN: 0022-0949. (Cit. on pp. 17, 35).
- Benjamin, P. R., & Pilkington, J. B. The electrotonic location of low-resistance intercellular junctions between a pair of giant neurones in the snail Lymnaea. eng. *The Journal of Physiology*, 370.

BIBLIOGRAPHY

1986. 370. 111–126. ISSN: 0022-3751. <https://doi.org/10.1113/jphysiol.1986.sp015925>. (Cit. on pp. 17, 36, 128).
- Benjamin, P. R., & Rose, R. M. Central generation of bursting in the feeding system of the snail, *Lymnaea stagnalis*. *Journal of Experimental Biology*, 80. 1979. 80. 93–118. ISSN: 00220949. (Cit. on pp. 16, 34).
- Benjamin, P. R. Distributed network organization underlying feeding behavior in the mollusk *Lymnaea* [Publisher: Springer Nature]. *Neural Systems & Circuits*, 2(1). 2012. 2. (1). <https://doi.org/10.1186/2042-1001-2-4>. (Cit. on pp. 43, 77, 78, 80, 81, 109).
- Benjamin, PR., Benjamin, P. R., & Elliott, C. J. (1989). Snail Feeding Oscillator: The Central Pattern Generator and Its Control by Modulatory Interneurons [Pages: 173–214 Publication Title: *Neuronal and Cellular Oscillators*]. (Cit. on pp. 17, 35).
- Berbel, B., Latorre, R., & Varona, P. Emergence of sequential dynamical invariants in central pattern generators from auto-organized constraints in their sequence time intervals. *Neurocomputing*. 2024. 127378. ISSN: 0925-2312. <https://doi.org/10.1016/j.neucom.2024.127378>. (Cit. on pp. 10, 30, 71).
- Bezaire, M. J., Raikov, I., Burk, K., Vyas, D., & Soltesz, I. Interneuronal mechanisms of hippocampal theta oscillations in a full-scale model of the rodent CA1 circuit. eng. *eLife*, 5. 2016. 5. e18566. ISSN: 2050-084X. <https://doi.org/10.7554/eLife.18566>. (Cit. on pp. 11, 31).
- Bickle, J. Revolutions in Neuroscience: Tool Development. *Frontiers in Systems Neuroscience*, 10. 2016. 10. ISSN: 1662-5137. <https://doi.org/10.3389/fnsys.2016.00024>. (Cit. on p. 113).
- Boyden, E. S., Zhang, F., Bamberg, E., Nagel, G., & Deisseroth, K. Millisecond-timescale, genetically targeted optical control of neural activity [Publisher: Nature Publishing Group]. *Nature Neuroscience* 2005 8:9, 8(9). 2005. 8. (9). 1263–1268. ISSN: 1546-1726. <https://doi.org/10.1038/nn1525>. (Cit. on p. 113).
- Brenner, S. THE GENETICS OF CAENORHABDITIS ELEGANS. *Genetics*, 77(1). 1974. 77. (1). 71–94. ISSN: 1943-2631. <https://doi.org/10.1093/genetics/77.1.71>. (Cit. on pp. 16, 34).
- Brierley, M., Staras, K., & Benjamin, P. Behavioral Function of Glutamatergic Interneurons in the Feeding System of *Lymnaea* : Plateauing Properties and Synaptic Connections with Motor Neurons. *Journal of neurophysiology*, 78. 1997. 78. 3386–95. <https://doi.org/10.1152/jn.1997.78.6.3386>. (Cit. on pp. 17, 35).
- Brown, W. G. A., Needham, K., Begeng, J. M., Thompson, A. C., Nayagam, B. A., Kameneva, T., & Stoddart, P. R. Thermal damage threshold of neurons during infrared stimulation [Publisher: The Optical Society]. *Biomedical Optics Express*, 11(4). 2020. 11. (4). 2224. ISSN: 2156-7085. <https://doi.org/10.1364/boe.383165>. (Cit. on pp. 19, 37, 114, 121, 148).

BIBLIOGRAPHY

- Brown, W. G. A., Needham, K., Begeng, J. M., Thompson, A. C., Nayagam, B. A., Kameneva, T., & Stoddart, P. R. Response of primary auditory neurons to stimulation with infrared light in vitro [Publisher: IOP Publishing]. *Journal of Neural Engineering*, 18(4). 2021. 18. (4). 046003. ISSN: 1741-2552. <https://doi.org/10.1088/1741-2552/ABE7B8>. (Cit. on p. 121).
- Buonomano, D. V., & Merzenich, M. M. Temporal information transformed into a spatial code by a neural network with realistic properties. eng. *Science (New York, N.Y.)*, 267(5200). 1995. 267. (5200). 1028–1030. ISSN: 0036-8075. <https://doi.org/10.1126/science.7863330>. (Cit. on pp. 7, 28).
- Burke, K. J. J., & Bender, K. J. Modulation of Ion Channels in the Axon: Mechanisms and Function [Publisher: Frontiers]. English. *Frontiers in Cellular Neuroscience*, 13. 2019. 13. ISSN: 1662-5102. <https://doi.org/10.3389/fncel.2019.00221>. (Cit. on pp. 9, 29).
- Buzsáki, G., & Tingley, D. Space and Time: The Hippocampus as a Sequence Generator [Publisher: Elsevier Current Trends]. *Trends in Cognitive Sciences*, 22(10). 2018. 22. (10). 853–869. ISSN: 1364-6613. <https://doi.org/10.1016/J.TICS.2018.07.006>. (Cit. on p. 55).
- Carter, M., & Shieh, J. C. (2015). *Guide to research techniques in neuroscience*. Academic Press. <https://doi.org/https://doi.org/10.1016/C2013-0-06868-5>. (Cit. on p. 113)
- Castillo, A., & de la Guardia, Y. Spineless solutions [Num Pages: 1888 Publisher: John Wiley & Sons, Ltd]. *EMBO reports*, 18(11). 2017. 18. (11). 1885–1888. ISSN: 1469-221X. <https://doi.org/10.15252/embr.201744113>. (Cit. on pp. 17, 35).
- Catterall, W. A., Raman, I. M., Robinson, H. P. C., Sejnowski, T. J., & Paulsen, O. The Hodgkin-Huxley Heritage: From Channels to Circuits. *The Journal of Neuroscience*, 32(41). 2012. 32. (41). 14064–14073. ISSN: 0270-6474. <https://doi.org/10.1523/JNEUROSCI.3403-12.2012>. (Cit. on pp. 10, 31).
- Cayce, J. M., Friedman, R. M., Chen, G., Jansen, E. D., Mahadevan-Jansen, A., & Roe, A. W. Infrared neural stimulation of primary visual cortex in non-human primates [Publisher: NIH Public Access]. *NeuroImage*, 84. 2014. 84. 181. ISSN: 10538119. <https://doi.org/10.1016/J.NEUROIMAGE.2013.08.040>. (Cit. on pp. 19, 37, 114, 126, 134, 146, 148).
- Chamorro, P., Muñiz, C., Levi, R., Arroyo, D., Rodríguez, F. B., & Varona, P. Generalization of the dynamic clamp concept in neurophysiology and behavior. *PLoS ONE*, 7(7). 2012. 7. (7). e40887. ISSN: 19326203. <https://doi.org/10.1371/journal.pone.0040887>. (Cit. on pp. 19, 37, 105, 113, 114).

BIBLIOGRAPHY

- Chen, W., Li, C., Liang, W., Li, Y., Zou, Z., Xie, Y., Liao, Y., Yu, L., Lin, Q., Huang, M., Li, Z., & Zhu, X. The Roles of Optogenetics and Technology in Neurobiology: A Review [Publisher: Frontiers]. English. *Frontiers in Aging Neuroscience*, 14. 2022. 14. ISSN: 1663-4365. <https://doi.org/10.3389/fnagi.2022.867863>. (Cit. on pp. 19, 37).
- Chernov, M., & Roe, A. W. Infrared neural stimulation: A new stimulation tool for central nervous system applications [Publisher: SPIE-Intl Soc Optical Eng]. *Neurophotonics*, 1(1). 2014. 1. (1). 011011. ISSN: 2329-423X. <https://doi.org/10.1117/1.NPh.1.1.011011>. (Cit. on p. 146).
- Clarke, M., Lankappa, S., Burnett, M., Khalifa, N., & Beer, C. Patients with depression who self-refer for transcranial magnetic stimulation treatment: Exploratory qualitative study. *BJPsych Bulletin*, 42(6). 2018. 42. (6). 243–247. ISSN: 2056-4694. <https://doi.org/10.1192/bjb.2018.49>. (Cit. on pp. 20, 38).
- Cogan, S. F. Neural Stimulation and Recording Electrodes [_eprint: <https://doi.org/10.1146/annurev.bioeng.10.061807.160518>]. *Annual Review of Biomedical Engineering*, 10(1). 2008. 10. (1). 275–309. <https://doi.org/10.1146/annurev.bioeng.10.061807.160518>. (Cit. on p. 113).
- Cosens, B., Thacker, D., & Brimijoin, S. Temperature-dependence of rapid axonal transport in sympathetic nerves of the rabbit. *Journal of Neurobiology*, 7(4). 1976. 7. (4). 339–354. ISSN: 1097-4695. <https://doi.org/10.1002/neu.480070406>. (Cit. on p. 138).
- Couto, J., Linaro, D., De Schutter, E., & Giugliano, M. On the Firing Rate Dependency of the Phase Response Curve of Rat Purkinje Neurons In Vitro. *PLOS Computational Biology*, 11(3). 2015. 11. (3). 1–23. <https://doi.org/10.1371/journal.pcbi.1004112>. (Cit. on p. 114).
- Cury, J., Perre, L. V., Smets, H., Stumpp, L., Vespa, S., Vanhoestenberghe, A., Doguet, P., Delbeke, J., Tahry, R. E., Gorza, S. P., & Nonclercq, A. Infrared neurostimulation in ex-vivo rat sciatic nerve using 1470 nm wavelength [Publisher: IOP Publishing Ltd]. *Journal of Neural Engineering*, 18(5). 2021. 18. (5). ISSN: 17412552. <https://doi.org/10.1088/1741-2552/ABF28F>. (Cit. on pp. 137, 148).
- Dagnew, R., Lin, Y.-Y., Agatep, J., Cheng, M., Jann, A., Quach, V., Monroe, M., Singh, G., Minasyan, A., Hakimian, J., Kee, T., Cushman, J., & Walwyn, W. CerebraLux: A low-cost, open-source, wireless probe for optogenetic stimulation. *Neurophotonics*, 4(4). 2017. 4. (4). 045001. ISSN: 2329-423X, 2329-4248. <https://doi.org/10.1117/1.NPh.4.4.045001>. (Cit. on p. 114).
- De Carlos, J. A., & Borrell, J. A historical reflection of the contributions of Cajal and Golgi to the foundations of neuroscience. *Brain Research Reviews*, 55(1). 2007. 55. (1). 8–16. ISSN: 0165-0173. <https://doi.org/10.1016/j.brainresrev.2007.03.010>. (Cit. on pp. 1, 21).
- de Castro, F. Cajal and the Spanish Neurological School: Neuroscience Would Have Been a Different Story Without Them. *Frontiers in Cellular Neuroscience*, 13. 2019. 13. ISSN: 1662-5102.

BIBLIOGRAPHY

- Retrieved October 26, 2023, from <https://www.frontiersin.org/articles/10.3389/fncel.2019.00187>. (Cit. on pp. 1, 21)
- de Castro, F., & Merchán, M. A. Editorial: The Major Discoveries of Cajal and His Disciples: Consolidated Milestones for the Neuroscience of the XXIst Century. *Frontiers in Neuroanatomy*, 10. 2016. 10. 85. ISSN: 1662-5129. <https://doi.org/10.3389/fnana.2016.00085>. (Cit. on pp. 1, 21).
- Delgado-García, J. M. Cajal and the Conceptual Weakness of Neural Sciences. *Frontiers in Neuroanatomy*, 9. 2015. 9. 128. ISSN: 1662-5129. <https://doi.org/10.3389/fnana.2015.00128>. (Cit. on pp. 1, 21).
- Dimitrijevic, M. R., Gerasimenko, Y., & Pinter, M. M. Evidence for a spinal central pattern generator in humans. *Annals of the New York Academy of Sciences*, 860. 1998. 860. 360–76. ISSN: 0077-8923. <https://doi.org/10.1111/j.1749-6632.1998.tb09062.x>. (Cit. on p. 56).
- Dimitrov, A. G., Lazar, A. A., & Victor, J. D. Information theory in neuroscience. en. *Journal of Computational Neuroscience*, 30(1). 2011. 30. (1). 1–5. ISSN: 1573-6873. <https://doi.org/10.1007/s10827-011-0314-3>. (Cit. on pp. 10, 31).
- Ding, M., PhD, & Glanzman, D., PhD. (2011). *The Dynamic Brain*. Oxford University Press. <https://doi.org/10.1093/acprof:oso/9780195393798.001.0001>. (Cit. on p. 15)
- Ding, N., Patel, A. D., Chen, L., Butler, H., Luo, C., & Poeppel, D. Temporal modulations in speech and music [Publisher: Elsevier Ltd]. *Neuroscience and Biobehavioral Reviews*, 81. 2017. 81. 181–187. ISSN: 18737528. <https://doi.org/10.1016/j.neubiorev.2017.02.011>. (Cit. on pp. 7, 27).
- Disner, S. G., Beevers, C. G., & Gonzalez-Lima, F. Transcranial Laser Stimulation as Neuroenhancement for Attention Bias Modification in Adults with Elevated Depression Symptoms. *Brain Stimulation*, 9(5). 2016. 9. (5). 780–787. ISSN: 1935-861X. <https://doi.org/https://doi.org/10.1016/j.brs.2016.05.009>. (Cit. on p. 114).
- Dittami, G. M., Rajguru, S. M., Lasher, R. A., Hitchcock, R. W., & Rabbitt, R. D. Intracellular calcium transients evoked by pulsed infrared radiation in neonatal cardiomyocytes [Publisher: J Physiol]. *The Journal of Physiology*, 589(Pt 6). 2011. 589. (Pt 6). 1295–1306. ISSN: 1469-7793. <https://doi.org/10.1113/JPHYSIOL.2010.198804>. (Cit. on pp. 114, 147, 149).
- Dragoi, G. Cell assemblies, sequences and temporal coding in the hippocampus. eng. *Current Opinion in Neurobiology*, 64. 2020. 64. 111–118. ISSN: 1873-6882. <https://doi.org/10.1016/j.conb.2020.03.003>. (Cit. on pp. 10, 30).

BIBLIOGRAPHY

- Duke, A. R., Jenkins, M. W., Lu, H., Mcmanus, J. M., Chiel, H. J., & Jansen, E. D. Transient and selective suppression of neural activity with infrared light. *Scientific Reports*, 3. 2013. 3. 2600. <https://doi.org/10.1038/srep02600>. (Cit. on p. 147).
- Eisen, J. S., & Marder, E. Mechanisms underlying pattern generation in lobster stomatogastric ganglion as determined by selective inactivation of identified neurons. III. Synaptic connections of electrically coupled pyloric neurons [Publisher: American Physiological Society]. *Journal of Neurophysiology*, 48(6). 1982. 48. (6). 1392–1415. ISSN: 0022-3077. <https://doi.org/10.1152/jn.1982.48.6.1392>. (Cit. on pp. 16, 34).
- Elias, M., Wieczorek, G., Rosenne, S., & Tawfik, D. S. The universality of enzymatic rate–temperature dependency. *Trends in Biochemical Sciences*, 39(1). 2014. 39. (1). 1–7. ISSN: 0968-0004. <https://doi.org/https://doi.org/10.1016/j.tibs.2013.11.001>. (Cit. on p. 138).
- Elices, I., Levi, R., Arroyo, D., Rodriguez, F. B., & Varona, P. Robust dynamical invariants in sequential neural activity [Publisher: Nature Publishing Group]. *Scientific Reports*, 9. 2019. 9. 9048. ISSN: 20452322. <https://doi.org/10.1038/s41598-019-44953-2>. (Cit. on pp. 10, 30, 39, 55, 56, 57, 64, 66, 71, 77, 101, 108, 152, 158).
- Elliott, C. J. H., & Andrew, T. Temporal Analysis of Snail Feeding Rhythms: A Three-Phase Relaxation Oscillator. *Journal of Experimental Biology*, 157(1). 1991. 157. (1). 391–408. ISSN: 0022-0949. (Cit. on pp. 56, 60, 66, 68, 71, 87, 108, 109).
- Elliott, C. J. H., & Benjamin, P. R. Interactions of pattern-generating interneurons controlling feeding in Lymnaea stagnalis. *Journal of Neurophysiology*, 54(6). 1985. 54. (6). 1396–1411. ISSN: 00223077. <https://doi.org/10.1152/jn.1985.54.6.1396>. (Cit. on p. 77).
- Fishbein, A. R., Idsardi, W. J., Ball, G. F., & Dooling, R. J. Sound sequences in birdsong: How much do birds really care? [Publisher: Royal Society]. *Philosophical Transactions of the Royal Society B: Biological Sciences*, 375(1789). 2019. 375. (1789). 20190044. <https://doi.org/10.1098/rstb.2019.0044>. (Cit. on pp. 7, 27).
- FitzHugh, R. Impulses and Physiological States in Theoretical Models of Nerve Membrane. English. *Biophysical Journal*, 1(6). 1961. 1. (6). 445–466. ISSN: 0006-3495. [https://doi.org/10.1016/S0006-3495\(61\)86902-6](https://doi.org/10.1016/S0006-3495(61)86902-6). (Cit. on pp. 11, 31).
- Fodor, I., Hussein, A. A., Benjamin, P. R., Koene, J. M., & Pirger, Z. The unlimited potential of the great pond snail, Lymnaea stagnalis (S. R. King, P. Rodgers, I. Irisarri, E. E. Voronezhskaya, & M.-A. Coutellec, Eds.) [Publisher: eLife Sciences Publications, Ltd]. *eLife*, 9. Ed. by King, S. R., Rodgers, P., Irisarri, I., Voronezhskaya, E. E., & Coutellec, M.-A. 2020. 9. e56962. ISSN: 2050-084X. <https://doi.org/10.7554/eLife.56962>. (Cit. on pp. 18, 36).

BIBLIOGRAPHY

- Friedenberger, Z., Harkin, E., Tóth, K., & Naud, R. Silences, spikes and bursts: Three-part knot of the neural code [_eprint: <https://onlinelibrary.wiley.com/doi/pdf/10.1113/JP281510>]. en. *The Journal of Physiology*, 601(23). 2023. 601. (23). 5165–5193. ISSN: 1469-7793. <https://doi.org/10.1113/JP281510>. (Cit. on pp. 5, 25).
- Ganguly, M., Jenkins, M. W., Chiel, H. J., & Jansen, E. D. (2016). Modeling the effects of elevated temperatures on action potential propagation in unmyelinated axons. In S. J. Madsen, V. X. D. Yang, E. D. Jansen, Q. Luo, S. K. Mohanty, & N. V. Thakor (Eds.), *Clinical and Translational Neurophotonics; Neural Imaging and Sensing; and Optogenetics and Optical Manipulation* (96901O). SPIE. <https://doi.org/10.1117/12.2211048>. (Cit. on p. 137)
- Ganguly, M., Jenkins, M. W., Jansen, E. D., & Chiel, H. J. Thermal block of action potentials is primarily due to voltage-dependent potassium currents: A modeling study [Publisher: IOP Publishing]. *Journal of Neural Engineering*, 16(3). 2019. 16. (3). 36020. <https://doi.org/10.1088/1741-2552/ab131b>. (Cit. on p. 147).
- Ganguly, M., Jenkins, M. W., Jansen, E. D., & Chiel, H. J. Thermal block of action potentials is primarily due to voltage-dependent potassium currents: A modeling study [Publisher: Institute of Physics Publishing]. *Journal of Neural Engineering*, 16(3). 2019. 16. (3). 036020. ISSN: 17412552. <https://doi.org/10.1088/1741-2552/ab131b>. (Cit. on p. 138).
- Garrido-Peña, A. (2022). *TFM 2019/20. Máster en Investigación e Innovación en Tecnologías de la Información y las Comunicaciones*. TFM. Retrieved November 24, 2023, from <https://libros.uam.es/tfm/catalog/book/1146>. (Cit. on p. 44)
- Garrido-Peña, A., Elices, I., & Varona, P. Characterization of interval variability in the sequential activity of a central pattern generator model [JCR Q2. Related to Chapter 4]. *Neurocomputing*, 461. 2021. 461. 667–678. ISSN: 0925-2312. <https://doi.org/10.1016/j.neucom.2020.08.093>. (Cit. on pp. 10, 30, 66).
- Garrido-Peña, A., Sánchez-Martín, P., Elices, I., Reyes-Sánchez, M., Berbel, B., Latorre, R., Rodríguez, F. B., & Varona, P. Exploring the ability of biophysical models to reproduce the functional variability of neurons. 32nd Annual Computational Neuroscience Meeting: CNS*2023. [Related to Chapter 4]. *InPress for Journal of Computational Neuroscience*. 2024. (Cit. on p. 105).
- Ghigliazza, R. M., & Holmes, P. Minimal Models of Bursting Neurons: How Multiple Currents, Conductances, and Timescales Affect Bifurcation Diagrams. en. *SIAM Journal on Applied Dynamical Systems*, 3(4). 2004. 3. (4). 636–670. ISSN: 1536-0040. <https://doi.org/10.1137/030602307>. (Cit. on pp. 63, 104).

BIBLIOGRAPHY

- Gleeson, P., Cantarelli, M., Marin, B., Quintana, A., Earnshaw, M., Sadeh, S., Piasini, E., Birgiolas, J., Cannon, R. C., Cayco-Gajic, N. A., Crook, S., Davison, A. P., Dura-Bernal, S., Ecker, A., Hines, M. L., Idili, G., Lanore, F., Larson, S. D., Lytton, W. W., ... Silver, R. A. Open Source Brain: A Collaborative Resource for Visualizing, Analyzing, Simulating, and Developing Standardized Models of Neurons and Circuits. *Neuron*, 103(3). 2019. 103. (3). 395–411.e5. ISSN: 0896-6273. <https://doi.org/10.1016/j.neuron.2019.05.019>. (Cit. on pp. 12, 32).
- Gonçalves, P. J., Lueckmann, J.-M., Deistler, M., Nonnenmacher, M., Öcal, K., Bassetto, G., Chintaluri, C., Podlaski, W. F., Haddad, S. A., Vogels, T. P., Greenberg, D. S., & Macke, J. H. Training deep neural density estimators to identify mechanistic models of neural dynamics (J. R. Huguenard, T. O’Leary, & M. S. Goldman, Eds.) [Publisher: eLife Sciences Publications, Ltd]. *eLife*, 9. Ed. by Huguenard, J. R., O’Leary, T., & Goldman, M. S. 2020. 9. e56261. ISSN: 2050-084X. <https://doi.org/10.7554/eLife.56261>. (Cit. on pp. 10, 31).
- Goyal, V., Rajguru, S., Matic, A. I., Stock, S. R., & Richter, C. P. Acute Damage Threshold for Infrared Neural Stimulation of the Cochlea: Functional and Histological Evaluation [Publisher: John Wiley & Sons, Ltd]. *The Anatomical Record: Advances in Integrative Anatomy and Evolutionary Biology*, 295(11). 2012. 295. (11). 1987–1999. ISSN: 1932-8494. <https://doi.org/10.1002/AR.22583>. (Cit. on pp. 19, 37, 114, 146, 147).
- Grillner, S., & Kashin, S. (1976). On the Generation and Performance of Swimming in Fish BT - Neural Control of Locomotion. In R. M. Herman, S. Grillner, P. S. G. Stein, & D. G. Stuart (Eds.), *Neural Control of Locomotion* (pp. 181–201). Springer US. https://doi.org/10.1007/978-1-4757-0964-3_8. (Cit. on p. 56)
- Hahnloser, R. H. R., Kozhevnikov, A. A., & Fee, M. S. An ultra-sparse code underlies the generation of neural sequences in a songbird. *Nature*, 419(6902). 2002. 419. (6902). 65–70. ISSN: 1476-4687. <https://doi.org/10.1038/nature00974>. (Cit. on p. 55).
- Hamill, O. P., Marty, A., Neher, E., Sakmann, B., & Sigworth, F. J. Improved patch-clamp techniques for high-resolution current recording from cells and cell-free membrane patches. eng. *Pflügers Archiv: European Journal of Physiology*, 391(2). 1981. 391. (2). 85–100. ISSN: 0031-6768. <https://doi.org/10.1007/BF00656997>. (Cit. on pp. 19, 37).
- Hamraoui, K., Torres-Vera, V. A., Zabala Gutierrez, I., Casillas-Rubio, A., Alqudwa Fattouh, M., Benayas, A., Marin, R., Natile, M. M., Manso Silvan, M., Rubio-Zuazo, J., Jaque, D., Melle, S., Calderón, O. G., & Rubio-Retama, J. Exploring the Origin of the Thermal Sensitivity of Near-Infrared-II Emitting Rare Earth Nanoparticles. en. *ACS Applied Materials & Interfaces*, 15(27). 2023. 15. (27). 32667–32677. ISSN: 1944-8244, 1944-8252. <https://doi.org/10.1021/acsami.3c04125>. (Cit. on p. 149).

BIBLIOGRAPHY

- Hariz, M., & Blomstedt, P. Deep brain stimulation for Parkinson's disease. *Journal of Internal Medicine*, 292(5). 2022. 292. (5). 764–778. ISSN: 0954-6820. <https://doi.org/10.1111/joim.13541>. (Cit. on pp. 20, 38).
- Hartline, D. K., & Maynard, D. M. Motor patterns in the stomatogastric ganglion of the lobster *Panulirus argus*. *J. Exp. Biol.*, 62(2). 1976. 62(2). 405–420. (Cit. on p. 55).
- He, B. J. Robust, Transient Neural Dynamics during Conscious Perception [Publisher: Elsevier]. English. *Trends in Cognitive Sciences*, 22(7). 2018. 22. (7). 563–565. ISSN: 1364-6613, 1879-307X. <https://doi.org/10.1016/j.tics.2018.04.005>. (Cit. on pp. 7, 27).
- Heitler, W. J., & Edwards, D. H. Effect of Temperature on a Voltage-Sensitive Electrical Synapse in Crayfish. *Journal of Experimental Biology*, 201(4). 1998. 201. (4). 503–513. ISSN: 0022-0949. <https://doi.org/10.1242/jeb.201.4.503>. (Cit. on p. 138).
- Hindmarsh, J. L., & Rose, R. M. A model of neuronal bursting using three coupled first order differential equations. *Proceedings of the Royal Society of London. Series B, Containing papers of a Biological character. Royal Society (Great Britain)*, 221(1222). 1984. 221. (1222). 87–102. ISSN: 00804649. <https://doi.org/10.1098/rspb.1984.0024>. (Cit. on pp. 11, 16, 31).
- Hodgkin, A. L., & Huxley, A. F. A quantitative description of membrane current and its application to conduction and excitation in nerve. *The Journal of physiology*, 117(4). 1952. 117. (4). 500–544. ISSN: 0022-3751. <https://doi.org/10.1113/jphysiol.1952.sp004764>. (Cit. on pp. 16, 34, 45, 132).
- Hodgkin, A. L., & Huxley, A. F. A quantitative description of membrane current and its application to conduction and excitation in nerve. *The Journal of Physiology*, 117(4). 1952. 117. (4). 500–44. ISSN: 0022-3751. <https://doi.org/10.1113/jphysiol.1952.sp004764>. (Cit. on pp. 11, 14, 31, 32, 104).
- Hodgkin, A. L., & Katz, B. The effect of temperature on the electrical activity of the giant axon of the squid. *The Journal of Physiology*, 109(1). 1949. 109. (1). 240–249. ISSN: 0022-3751. <https://doi.org/10.1113/jphysiol.1949.sp004388>. (Cit. on p. 138).
- Hooper, S. L. Phase Maintenance in the Pyloric Pattern of the Lobster (*Panulirus interruptus*) Stomatogastric Ganglion [Publisher: Kluwer Academic Publishers]. *Journal of Computational Neuroscience*, 205(3). 1997. 205. (3). 191–205. ISSN: 09295313. <https://doi.org/10.1023/A:1008822218061>. (Cit. on p. 56).
- Huerta, R., Varona, P., Rabinovich, M. I., & Abarbanel, H. D. Topology selection by chaotic neurons of a pyloric central pattern generator. *Biological Cybernetics*, 84(1). 2001. 84. (1). L1–L8. ISSN: 03401200. <https://doi.org/10.1007/PL00007976>. (Cit. on pp. 6, 7, 14, 27, 28, 56).

BIBLIOGRAPHY

- Hutt, A., Rich, S., Valiante, T. A., & Lefebvre, J. Intrinsic neural diversity quenches the dynamic volatility of neural networks. en. *Proceedings of the National Academy of Sciences*, 120(28). 2023. 120. (28). e2218841120. ISSN: 0027-8424, 1091-6490. <https://doi.org/10.1073/pnas.2218841120>. (Cit. on p. 15).
- Ivry, R. B. The representation of temporal information in perception and motor control. eng. *Current Opinion in Neurobiology*, 6(6). 1996. 6. (6). 851–857. ISSN: 0959-4388. [https://doi.org/10.1016/s0959-4388\(96\)80037-7](https://doi.org/10.1016/s0959-4388(96)80037-7). (Cit. on pp. 7, 28).
- Izhikevich, E. M. Simple model of spiking neurons. *IEEE Transactions on Neural Networks*, 14(6). 2003. 14. (6). 1569–1572. ISSN: 10459227. <https://doi.org/10.1109/TNN.2003.820440>. (Cit. on pp. 11, 31).
- Izhikevich, E. M. (2007). *Dynamical systems in neuroscience: The geometry of excitability and bursting* [OCLC: ocm65400606]. MIT Press. (Cit. on pp. 3, 23).
- Izzo, A. D., Walsh, J. T., Jansen, E. D., Bendett, M., Webb, J., Ralph, H., & Richter, C. P. Optical parameter variability in laser nerve stimulation: A study of pulse duration, repetition rate, and wavelength. *IEEE Transactions on Biomedical Engineering*, 54(6). 2007. 54. (6). 1108–1114. ISSN: 00189294. <https://doi.org/10.1109/TBME.2007.892925>. (Cit. on pp. 114, 126, 129, 147).
- Kandel, E. R., Schwartz, J. H., & Jessell, T. M. (2012). *Principles of Neural Science* (5th ed.). McGraw-Hill Education. (Cit. on pp. 3, 23).
- Katz, P. S. Evolution of central pattern generators and rhythmic behaviours. <https://doi.org/10.1098/rstb.2015.0057>. (Cit. on pp. 7, 28).
- Katz, P. S. Evolution of central pattern generators and rhythmic behaviours. 2016. <https://doi.org/10.1098/rstb.2015.0057>. (Cit. on pp. 5, 25).
- Kecskes, M., Peigneur, S., & Held, K. Editorial: Contribution of ion channels to neuropathologies. *Frontiers in Cell and Developmental Biology*, 11. 2023. 11. 1179663. ISSN: 2296-634X. <https://doi.org/10.3389/fcell.2023.1179663>. (Cit. on pp. 9, 28).
- Kemenes, G., & Elliott, C. J. H. Analysis of the feeding motor pattern in the pond snail, Lymnaea stagnalis: Photoinactivation of axonally stained pattern-generating interneurons. *Journal of Neuroscience*, 14(1). 1994. 14. (1). 153–166. ISSN: 02706474. <https://doi.org/10.1523/JNEUROSCI.14-01-00153.1994>. (Cit. on p. 109).
- Kemenes, G., Staras, K., & Benjamin, P. Multiple Types of Control by Identified Interneurons in a Sensory-Activated Rhythmic Motor Pattern. *The Journal of neuroscience : the official journal of the Society for Neuroscience*, 21. 2001. 21. 2903–11. <https://doi.org/10.1523/JNEUROSCI.21-08-02903.2001>. (Cit. on pp. 17, 36, 78).

BIBLIOGRAPHY

- Kiebel, S. J., Daunizeau, J., & Friston, K. J. A Hierarchy of Time-Scales and the Brain [Publisher: Public Library of Science]. en. *PLOS Computational Biology*, 4(11). 2008. 4. (11). e1000209. ISSN: 1553-7358. <https://doi.org/10.1371/journal.pcbi.1000209>. (Cit. on pp. 6, 27).
- Kiebel, S. J., Kriegstein, K. v., Daunizeau, J., & Friston, K. J. Recognizing Sequences of Sequences [Publisher: Public Library of Science]. en. *PLOS Computational Biology*, 5(8). 2009. 5. (8). e1000464. ISSN: 1553-7358. <https://doi.org/10.1371/journal.pcbi.1000464>. (Cit. on pp. 7, 27).
- Koch, C. (1999). *Biophysics of computation*. Oxford University Press, New York. (Cit. on pp. 3, 23).
- Komendantov, A. O., & Kononenko, N. I. Deterministic Chaos in Mathematical Model of Pacemaker Activity in Bursting Neurons of Snail, *Helix Pomatia*. *Journal of Theoretical Biology*, 183(2). 1996. 183. (2). 219–230. ISSN: 0022-5193. <https://doi.org/10.1006/jtbi.1996.0215>. (Cit. on p. 16).
- Konstantinović, L. M., Jelić, M. B., Jeremić, A., Stevanović, V. B., Milanović, S. D., & Filipović, S. R. Transcranial application of near-infrared low-level laser can modulate cortical excitability [Publisher: John Wiley & Sons, Ltd]. *Lasers in Surgery and Medicine*, 45(10). 2013. 45. (10). 648–653. ISSN: 01968092. <https://doi.org/10.1002/lsm.22190>. (Cit. on p. 114).
- Krames, E., Peckham, P. H., & Rezai, A. R. (2009). *Neuromodulation* (1st ed). Elsevier Academic Press. (Cit. on pp. 19, 38).
- Lareo, A., Forlim, C. G., Pinto, R. D., Varona, P., & Rodriguez, F. d. B. Temporal Code-Driven Stimulation: Definition and Application to Electric Fish Signaling [Publisher: Frontiers Research Foundation]. *Frontiers in Neuroinformatics*, 10(OCT). 2016. 10. (OCT). 41. ISSN: 1662-5196. <https://doi.org/10.3389/fninf.2016.00041>. (Cit. on p. 114).
- Latorre, R., Aguirre, C., Rabinovich, M. I., & Varona, P. Transient dynamics and rhythm coordination of inferior olive spatio-temporal patterns [Publisher: Frontiers]. *Frontiers in Neural Circuits*, 7(SEP). 2013. 7. (SEP). 138. ISSN: 1662-5110. <https://doi.org/10.3389/fncir.2013.00138>. (Cit. on p. 14).
- Lecoq, J., Orlova, N., & Grawe, B. F. Wide. Fast. Deep: Recent Advances in Multiphoton Microscopy of In Vivo Neuronal Activity [Publisher: Society for Neuroscience _eprint: https://www.jneurosci.org/content/Journal of Neuroscience, 39(46). 2019. 39. (46). 9042–9052. ISSN: 0270-6474. <https://doi.org/10.1523/JNEUROSCI.1527-18.2019>. (Cit. on p. 113).
- Levitin, I. B., & Kaczmarek, L. K. (2002). *The neuron: Cell and molecular biology* (3rd ed) [OCLC: 46565032]. Oxford University Press. Retrieved October 26, 2023, from <http://catdir.loc.gov/catdir/toc/fy031/2001021591.html>. (Cit. on pp. 6, 26)

BIBLIOGRAPHY

- Li, X., Liu, J., Liang, S., Guan, K., An, L., Wu, X., Li, S., & Sun, C. Temporal Modulation of Sodium Current Kinetics in Neuron Cells by Near-Infrared Laser [Publisher: Cell Biochem Biophys]. *Cell Biochemistry and Biophysics*, 67(3). 2013. 67. (3). 1409–1419. ISSN: 10859195. <https://doi.org/10.1007/s12013-013-9674-9>. (Cit. on pp. 121, 136, 137, 138, 148).
- Liang, S., Yang, F., Zhou, C., Wang, Y., Li, S., Sun, C. K., Puglisi, J. L., Bers, D., Sun, C., & Zheng, J. Temperature-dependent activation of neurons by continuous near-infrared laser [Publisher: Springer]. *Cell Biochemistry and Biophysics*, 53(1). 2009. 53. (1). 33–42. ISSN: 10859195. <https://doi.org/10.1007/s12013-008-9035-2>. (Cit. on pp. 19, 37, 114, 136, 141).
- Limousin, P., & Foltynie, T. Long-term outcomes of deep brain stimulation in Parkinson disease [Publisher: Nature Publishing Group]. en. *Nature Reviews Neurology*, 15(4). 2019. 15. (4). 234–242. ISSN: 1759-4766. <https://doi.org/10.1038/s41582-019-0145-9>. (Cit. on pp. 20, 38).
- Linaro, D., Couto, J., & Giugliano, M. Real-time Electrophysiology: Using Closed-loop Protocols to Probe Neuronal Dynamics and Beyond [ISBN: 1940-087X]. *JoVE (Journal of Visualized Experiments)*. 2015. e52320–e52320. ISSN: 1940-087X. <https://doi.org/10.3791/52320>. (Cit. on p. 114).
- Linaro, D., Storace, M., & Giugliano, M. Accurate and Fast Simulation of Channel Noise in Conductance-Based Model Neurons by Diffusion Approximation [Publisher: Public Library of Science]. en. *PLOS Computational Biology*, 7(3). 2011. 7. (3). e1001102. ISSN: 1553-7358. <https://doi.org/10.1371/journal.pcbi.1001102>. (Cit. on p. 16).
- Lothet, E. H., Shaw, K. M., Lu, H., Zhuo, J., Wang, Y. T., Gu, S., Stoltz, D. B., Jansen, E. D., Horn, C. C., Chiel, H. J., & Jenkins, M. W. Selective inhibition of small-diameter axons using infrared light [Publisher: Nature Publishing Group]. *Scientific Reports*, 7(1). 2017. 7. (1). 1–8. ISSN: 20452322. <https://doi.org/10.1038/s41598-017-03374-9>. (Cit. on p. 147).
- Lumbreras, V., Bas, E., Gupta, C., & Rajguru, S. M. Pulsed infrared radiation excites cultured neonatal spiral and vestibular ganglion neurons by modulating mitochondrial calcium cycling [Publisher: American Physiological Society]. *Journal of Neurophysiology*, 112(6). 2014. 112. (6). 1246. ISSN: 15221598. <https://doi.org/10.1152/JN.00253.2014>. (Cit. on pp. 114, 147, 149).
- Lundqvist, M., Rose, J., Herman, P., Brincat, S. L., Buschman, T. J., & Miller, E. K. Gamma and Beta Bursts Underlie Working Memory. eng. *Neuron*, 90(1). 2016. 90. (1). 152–164. ISSN: 1097-4199. <https://doi.org/10.1016/j.neuron.2016.02.028>. (Cit. on pp. 3, 24).

BIBLIOGRAPHY

- MacKay-Lyons, M. Central Pattern Generation of Locomotion: A Review of the Evidence. *Physical Therapy*, 82(1). 2002. 82. (1). 69–83. ISSN: 0031-9023. <https://doi.org/10.1093/ptj/82.1.69>. (Cit. on pp. 7, 28).
- Marder, E., & Bucher, D. Central pattern generators and the control of rhythmic movements [Publisher: Cell Press]. *Current Biology*, 11(23). 2001. 11. (23). R986–R996. ISSN: 09609822. [https://doi.org/10.1016/S0960-9822\(01\)00581-4](https://doi.org/10.1016/S0960-9822(01)00581-4). (Cit. on pp. 7, 28, 55).
- Martinez, D., Anwar, H., Bose, A., Bucher, D. M., & Nadim, F. Short-term synaptic dynamics control the activity phase of neurons in an oscillatory network. *eLife*, 8. 2019. 8. e46911. ISSN: 2050084X. <https://doi.org/10.7554/eLife.46911>. (Cit. on p. 56).
- Masquelier, T. Neural variability, or lack thereof. *Frontiers in Computational Neuroscience*, 7. 2013. 7. ISSN: 1662-5188. <https://doi.org/10.3389/fncom.2013.00007>. (Cit. on p. 15).
- Mauk, M. D., & Buonomano, D. V. THE NEURAL BASIS OF TEMPORAL PROCESSING [Publisher: Annual Reviews]. en. *Annual Review of Neuroscience*, 27(Volume 27, 2004). 2004. 27. (Volume 27, 2004). 307–340. ISSN: 0147-006X, 1545-4126. <https://doi.org/10.1146/annurev.neuro.27.070203.144247>. (Cit. on pp. 7, 28).
- McCrohan, C. R., & Benjamin, P. R. Patterns of activity and axonal projections of the cerebral giant cells of the snail, *Lymnaea stagnalis*. *Journal of Experimental Biology*, 85. 1980. 85. 149–168. ISSN: 00220949. (Cit. on pp. 17, 36).
- Minassian, K., Hofstoetter, U. S., Dzeladini, F., Guertin, P. A., & Ijspeert, A. The Human Central Pattern Generator for Locomotion: Does It Exist and Contribute to Walking? eng. *The Neuroscientist: A Review Journal Bringing Neurobiology, Neurology and Psychiatry*, 23(6). 2017. 23. (6). 649–663. ISSN: 1089-4098. <https://doi.org/10.1177/1073858417699790>. (Cit. on pp. 7, 28).
- Moulins, M., & Selverston, A. I. (1987). Introduction. In A. I. Selverston & M. Moulins (Eds.), *The Crustacean Stomatogastric System: A Model for the Study of Central Nervous Systems* (pp. 1–8). Springer. https://doi.org/10.1007/978-3-642-71516-7_1. (Cit. on pp. 7, 28)
- Neher, E., & Sakmann, B. Single-channel currents recorded from membrane of denervated frog muscle fibres. eng. *Nature*, 260(5554). 1976. 260. (5554). 799–802. ISSN: 0028-0836. <https://doi.org/10.1038/260799a0>. (Cit. on pp. 19, 37).
- Noland, L. E., & Carriker, M. R. Observations on the Biology of the Snail *Lymnaea stagnalis* appressa During Twenty Generations in Laboratory Culture [Publisher: University of Notre Dame]. *The American Midland Naturalist*, 36(2). 1946. 36. (2). 467–493. ISSN: 0003-0031. <https://doi.org/10.2307/2421516>. (Cit. on pp. 18, 36).

BIBLIOGRAPHY

- Nowotny, T., Levi, R., & Selverston, A. I. Probing the Dynamics of Identified Neurons with a Data-Driven Modeling Approach (K. J. Friston, Ed.). en. *PLoS ONE*, 3(7). Ed. by Friston, K. J. 2008. 3. (7). e2627. ISSN: 1932-6203. <https://doi.org/10.1371/journal.pone.0002627>. (Cit. on pp. 62, 104).
- Nowotny, T., & Varona, P. (2022). Dynamic Clamp Technique. In D. Jaeger & R. Jung (Eds.), *Encyclopedia of Computational Neuroscience* (pp. 1240–1243). Springer. https://doi.org/10.1007/978-1-0716-1006-0_126. (Cit. on pp. 19, 37)
- Nüsslein-Volhard, C., & Wieschaus, E. Mutations affecting segment number and polarity in Drosophila. eng. *Nature*, 287(5785). 1980. 287. (5785). 795–801. ISSN: 0028-0836. <https://doi.org/10.1038/287795a0>. (Cit. on pp. 16, 34).
- Palmu, K., Wikström, S., Hippeläinen, E., Boylan, G., Hellström-Westas, L., & Vanhatalo, S. Detection of 'EEG bursts' in the early preterm EEG: Visual vs. automated detection. eng. *Clinical Neurophysiology: Official Journal of the International Federation of Clinical Neurophysiology*, 121(7). 2010. 121. (7). 1015–1022. ISSN: 1872-8952. <https://doi.org/10.1016/j.clinph.2010.02.010>. (Cit. on pp. 3, 24).
- Pan, L., Ping, A., Schriver, K. E., Roe, A. W., Zhu, J., & Xu, K. Infrared neural stimulation in human cerebral cortex [Publisher: Elsevier]. *Brain Stimulation*, 16(2). 2023. 16. (2). 418–430. ISSN: 1935-861X. <https://doi.org/10.1016/J.BRS.2023.01.1678>. (Cit. on pp. 114, 137, 146, 147).
- Patel, Y. A., George, A., Dorval, A. D., White, J. A., Christini, D. J., & Butera, R. J. Hard real-time closed-loop electrophysiology with the Real-Time eXperiment Interface (RTXI) (T. Poisot, Ed.). *PLOS Computational Biology*, 13(5). Ed. by Poisot, T. 2017. 13. (5). e1005430. ISSN: 1553-7358. <https://doi.org/10.1371/journal.pcbi.1005430>. (Cit. on pp. 115, 116, 143).
- Paton, J. J., & Buonomano, D. V. The Neural Basis of Timing: Distributed Mechanisms for Diverse Functions [Publisher: Elsevier]. *Neuron*, 98(4). 2018. 98. (4). 687–705. ISSN: 0896-6273. <https://doi.org/10.1016/j.neuron.2018.03.045>. (Cit. on p. 55).
- Pavlidis, E., Cantalupo, G., Cattani, L., Tassinari, C. A., & Pisani, F. Neonatal seizure automatism and human inborn pattern of quadrupedal locomotion [Publisher: Elsevier B.V.]. *Gait and Posture*, 49. 2016. 49. 232–234. ISSN: 18792219. <https://doi.org/10.1016/j.gaitpost.2016.07.015>. (Cit. on p. 56).
- Pearson, K. G. (1972). *Central Programming and Reflex Control of Walking in the Cockroach* (tech. rep.) [Publication Title: Journal of Experimental Biology Volume: 56 Issue: 1 ISSN: 0022-0949]. (Cit. on pp. 7, 28).

BIBLIOGRAPHY

- Pezo, D., Soudry, D., & Orio, P. Diffusion approximation-based simulation of stochastic ion channels: Which method to use? en. *Frontiers in Computational Neuroscience*, 8. 2014. 8. ISSN: 1662-5188. <https://doi.org/10.3389/fncom.2014.00139>. (Cit. on p. 16).
- Ping, A., Pan, L., Zhang, J., Xu, K., Schriver, K. E., Zhu, J., & Roe, A. W. Targeted Optical Neural Stimulation: A New Era for Personalized Medicine. *The Neuroscientist*, 29(2). 2023. 29. (2). 202–220. <https://doi.org/10.1177/10738584211057047>. (Cit. on p. 114).
- Plaksin, M., Shapira, E., Kimmel, E., & Shoham, S. Thermal Transients Excite Neurons through Universal Intramembrane Mechanoelectrical Effects [Publisher: American Physical Society]. *Physical Review X*, 8(1). 2018. 8. (1). 011043. ISSN: 21603308. <https://doi.org/10.1103/PHYSREVX.8.011043/FIGURES/4/MEDIUM>. (Cit. on pp. 114, 134, 148).
- Potjans, T. C., & Diesmann, M. The cell-type specific cortical microcircuit: Relating structure and activity in a full-scale spiking network model. eng. *Cerebral Cortex (New York, N.Y.: 1991)*, 24(3). 2014. 24. (3). 785–806. ISSN: 1460-2199. <https://doi.org/10.1093/cercor/bhs358>. (Cit. on pp. 11, 31).
- Potter, S. M., El Hady, A., & Fetz, E. E. Closed-Loop Neuroscience and Neuroengineering [ISBN: 1662-5110]. *Frontiers in Neural Circuits*, 8(115). 2014. 8. (115). <https://doi.org/10.3389/fncir.2014.00115>. (Cit. on p. 114).
- Prather, J. F., Okanoya, K., & Bolhuis, J. J. Brains for birds and babies: Neural parallels between birdsong and speech acquisition [Publisher: Elsevier Ltd]. *Neuroscience and Biobehavioral Reviews*, 81. 2017. 81. 225–237. ISSN: 18737528. <https://doi.org/10.1016/j.neubiorev.2016.12.035>. (Cit. on pp. 7, 27).
- Preuss, T. M. Taking the Measure of Diversity: Comparative Alternatives to the Model-Animal Paradigm in Cortical Neuroscience. *Brain Behavior and Evolution*, 55(6). 2000. 55. (6). 287–299. ISSN: 0006-8977. <https://doi.org/10.1159/000006664>. (Cit. on pp. 16, 34).
- Rabbitt, R. D., Brichta, A. M., Tabatabaei, H., Boutros, P. J., Ahn, J., Santina, C. C. D., Poppi, L. A., & Lim, R. Heat pulse excitability of vestibular hair cells and afferent neurons [Publisher: American Physiological Society]. *Journal of Neurophysiology*, 116(2). 2016. 116. (2). 825–843. ISSN: 0022-3077. <https://doi.org/10.1152/jn.00110.2016>. (Cit. on pp. 121, 136, 137, 138, 147, 148).
- Rabinovich, M. I., Bick, C., & Varona, P. Beyond neurons and spikes: cognon, the hierarchical dynamical unit of thought. *Cognitive Neurodynamics*. 2023. <https://doi.org/10.1007/s11571-023-09987-3>. (Cit. on pp. 7, 27).

BIBLIOGRAPHY

- Rabinovich, M. I., & Varona, P. Discrete Sequential Information Coding: Heteroclinic Cognitive Dynamics. *Frontiers in Computational Neuroscience*, 12. 2018. 12. 73. ISSN: 1662-5188. <https://doi.org/10.3389/fncom.2018.00073>. (Cit. on pp. 7, 27, 55).
- Rabinovich, M. I., Zaks, M. A., & Varona, P. Sequential dynamics of complex networks in mind: Consciousness and creativity. *Physics Reports*, 883. 2020. 883. 1–32. ISSN: 0370-1573. <https://doi.org/10.1016/j.physrep.2020.08.003>. (Cit. on pp. 7, 27).
- Ramón y Cajal, S. (1899). *Textura del sistema nervioso del hombre y de los vertebrados*. Imprenta y Librería de Nicolás Moya. (Cit. on pp. 1, 21).
- Renart, A., & Machens, C. K. Variability in neural activity and behavior. en. *Current Opinion in Neurobiology*, 25. 2014. 25. 211–220. ISSN: 09594388. <https://doi.org/10.1016/j.conb.2014.02.013>. (Cit. on p. 15).
- Reyes, M. B., Huerta, R., Rabinovich, M. I., & Selverston, A. I. Artificial synaptic modification reveals a dynamical invariant in the pyloric CPG. *European Journal of Applied Physiology*, 102(6). 2008. 102. (6). 667–675. ISSN: 14396319. <https://doi.org/10.1007/s00421-007-0635-0>. (Cit. on pp. 10, 30, 56).
- Reyes-Sanchez, M., Amaducci, R., Elices, I., Rodriguez, F. B., & Varona, P. Automatic adaptation of model neurons and connections to build hybrid circuits with living networks. *Neuroinformatics*, 18(3). 2020. 18. (3). 377–393. ISSN: 15590089. <https://doi.org/10.1007/s12021-019-09440-z>. (Cit. on p. 118).
- Reyes-Sanchez, M., Amaducci, R., Sanchez-Martin, P., Elices, I., Rodriguez, F. B., & Varona, P. Automatized offline and online exploration to achieve a target dynamics in biohybrid neural circuits built with living and model neurons. *Neural Networks*, 164. 2023. 164. 464–475. ISSN: 0893-6080. <https://doi.org/https://doi.org/10.1016/j.neunet.2023.04.034>. (Cit. on pp. 105, 114, 118).
- Ribeiro, T. L., Jendrichovsky, P., Yu, S., Martin, D. A., Kanold, P. O., Chialvo, D. R., & Plenz, D. Trial-by-trial variability in cortical responses exhibits scaling of spatial correlations predicted from critical dynamics [Publisher: Elsevier]. English. *Cell Reports*, 43(2). 2024. 43. (2). ISSN: 2211-1247. <https://doi.org/10.1016/j.celrep.2024.113762>. (Cit. on p. 16).
- Robbins, M., Siddiqui, O., Fuchsberger, T., Goodfellow, G., Paulsen, O., Kaminski, C. F., Euser, T., & Schierle, G. S. K. OptoGenie: An open-source device for the optogenetic stimulation of cells. *Journal of Open Hardware*, 5(1). 2021. 5. (1). 2. ISSN: 2514-1708. <https://doi.org/10.5334/joh.32>. (Cit. on p. 114).

BIBLIOGRAPHY

- Romanova, E. V., & Sweedler, J. V. Animal Model Systems in Neuroscience [Publisher: American Chemical Society]. *ACS Chemical Neuroscience*, 9(8). 2018. 9. (8). 1869–1870. <https://doi.org/10.1021/acschemneuro.8b00380>. (Cit. on pp. 16, 34).
- Rose, R. M., & Benjamin, P. R. The Relationship of the Central Motor Pattern to the Feeding Cycle of Lymnaea Stagnalis. *Journal of Experimental Biology*, 80(1). 1979. 80. (1). 137–163. ISSN: 0022-0949. <https://doi.org/10.1242/jeb.80.1.137>. (Cit. on pp. 17, 35).
- Rose, R. M., & Benjamin, P. R. Interneuronal Control of Feeding in the Pond Snail Lymnaea Stagnalis: I. Initiation of Feeding Cycles by a Single Buccal Interneurone. *Journal of Experimental Biology*, 92(1). 1981. 92. (1). 187–201. ISSN: 0022-0949. <https://doi.org/10.1242/jeb.92.1.187>. (Cit. on pp. 17, 36).
- Russell, D. F., & Hartline, D. K. Bursting Neural Networks: A Reexamination [Publisher: American Association for the Advancement of Science]. *Science*, 200(4340). 1978. 200. (4340). 453–456. <https://doi.org/10.1126/science.644309>. (Cit. on pp. 3, 24).
- Saucedo, C. L., Courtois, E. C., Wade, Z. S., Kelley, M. N., Kheradbin, N., Barrett, D. W., & Gonzalez-Lima, F. Transcranial laser stimulation: Mitochondrial and cerebrovascular effects in younger and older healthy adults [Publisher: Elsevier Ltd]. *Brain Stimulation*, 14(2). 2021. 14. (2). 440–449. ISSN: 18764754. <https://doi.org/10.1016/j.brs.2021.02.011>. (Cit. on pp. 114, 147, 149).
- Schauf, C. L. Temperature dependence of the ionic current kinetics of Myxicola giant axons. *The Journal of Physiology*, 235(1). 1973. 235. (1). 197–205. ISSN: 0022-3751. Retrieved January 22, 2024, from <https://www.ncbi.nlm.nih.gov/pmc/articles/PMC1350739/>. (Cit. on p. 138)
- Schwiening, C. J. A brief historical perspective: Hodgkin and Huxley. *The Journal of Physiology*, 590(Pt 11). 2012. 590. (Pt 11). 2571–2575. ISSN: 0022-3751. <https://doi.org/10.1113/jphysiol.2012.230458>. (Cit. on pp. 10, 31).
- Selverston, A. I., Rabinovich, M. I., Abarbanel, H. D. I., Elson, R., Szücs, A., Pinto, R. D., Huerta, R., & Varona, P. Reliable circuits from irregular neurons: A dynamical approach to understanding central pattern generators [Publisher: Institute for Nonlinear Science, University of California, San Diego, 9500 Gilman Drive, La Jolla, CA 92093-0402, USA. aselverston@ucsd.edu]. *Journal of Physiology-Paris*, 94(5-6). 2000. 94. (5-6). 357–374. [https://doi.org/10.1016/S0928-4257\(00\)01101-3](https://doi.org/10.1016/S0928-4257(00)01101-3). (Cit. on pp. 7, 15, 28, 55, 56).
- Selverston, A. I., & Ayers, J. Oscillations and oscillatory behavior in small neural circuits. en. *Biological Cybernetics*, 95(6). 2006. 95. (6). 537–554. ISSN: 1432-0770. <https://doi.org/10.1007/s00422-006-0125-1>. (Cit. on pp. 7, 28).

BIBLIOGRAPHY

- Silverston, A. I., Russell, D. F., Miller, J. P., & King, D. G. The stomatogastric nervous system: Structure and function of a small neural network. *Progress in Neurobiology*, 7. 1976. 7. 215–289. ISSN: 0301-0082. [https://doi.org/https://doi.org/10.1016/0301-0082\(76\)90008-3](https://doi.org/https://doi.org/10.1016/0301-0082(76)90008-3). (Cit. on pp. 16, 34).
- Shannon, C. E. A mathematical theory of communication [Conference Name: The Bell System Technical Journal]. *The Bell System Technical Journal*, 27(3). 1948. 27. (3). 379–423. ISSN: 0005-8580. <https://doi.org/10.1002/j.1538-7305.1948.tb01338.x>. (Cit. on pp. 10, 31).
- Shapiro, M. G., Homma, K., Villarreal, S., Richter, C. P., & Bezanilla, F. Infrared light excites cells by changing their electrical capacitance [Publisher: Nature Publishing Group]. *Nature Communications*, 3(1). 2012. 3. (1). 1–11. ISSN: 20411723. <https://doi.org/10.1038/ncomms1742>. (Cit. on pp. 19, 37, 114, 126, 134, 137, 138, 147, 148).
- Shapiro, M. G., Homma, K., Villarreal, S., Richter, C.-P., & Bezanilla, F. Correction: Corrigendum: Infrared light excites cells by changing their electrical capacitance. *Nature Communications*, 8(1). 2017. 8. (1). 16148. ISSN: 2041-1723. <https://doi.org/10.1038/ncomms16148>. (Cit. on p. 134).
- Siegle, J. H., Hale, G. J., Newman, J. P., & Voigts, J. Neural ensemble communities: Open-source approaches to hardware for large-scale electrophysiology. *Current Opinion in Neurobiology*, 32. 2015. 32. 53–59. ISSN: 0959-4388. <https://doi.org/10.1016/j.conb.2014.11.004>. (Cit. on p. 114).
- Smith, S. L., Smith, I. T., Branco, T., & Häusser, M. Dendritic spikes enhance stimulus selectivity in cortical neurons in vivo. eng. *Nature*, 503(7474). 2013. 503. (7474). 115–120. ISSN: 1476-4687. <https://doi.org/10.1038/nature12600>. (Cit. on pp. 11, 31).
- Staras, K., Kemenes, G., & Benjamin, P. R. Pattern-generating role for motoneurons in a rhythmically active neuronal network. *Journal of Neuroscience*, 18(10). 1998. 18. (10). 3669–3688. ISSN: 02706474. (Cit. on pp. 42, 77, 78).
- Staras, K., Kemenes, G., & Benjamin, P. R. Electrophysiological and Behavioral Analysis of Lip Touch as a Component of the Food Stimulus in the Snail \textless\textgreater Lymnaea\textless\textgreater. *Journal of Neurophysiology*, 81(3). 1999. 81. (3). 1261–1273. ISSN: 0022-3077. <https://doi.org/10.1152/jn.1999.81.3.1261>. (Cit. on p. 92).
- Staras, K., Kemenes, I., Benjamin, P. R., & Kemenes, G. Loss of self-inhibition is a cellular mechanism for episodic rhythmic behavior. eng. *Current biology: CB*, 13(2). 2003. 13. (2). 116–124. ISSN: 0960-9822. [https://doi.org/10.1016/s0960-9822\(02\)01435-5](https://doi.org/10.1016/s0960-9822(02)01435-5). (Cit. on p. 81).
- Stephan, P. (2015). How Economics Shapes Science. Retrieved January 16, 2024, from <https://www.hup.harvard.edu/books/9780674088160>. (Cit. on pp. 17, 35)

BIBLIOGRAPHY

- Steuer, I., & Guertin, P. A. Central pattern generators in the brainstem and spinal cord: An overview of basic principles, similarities and differences. *Reviews in the Neurosciences*. 2018. ISSN: 03341763. <https://doi.org/10.1515/revneuro-2017-0102>. (Cit. on pp. 5, 25).
- Štih, V., Petrucco, L., Kist, A. M., & Portugues, R. Styra: An open-source, integrated system for stimulation, tracking and closed-loop behavioral experiments. *PLOS Computational Biology*, 15(4). 2019. 15. (4). e1006699. ISSN: 1553-7358. <https://doi.org/10.1371/journal.pcbi.1006699>. (Cit. on p. 114).
- Straub, V. A., Staras, K., Gyo'', G., Kemenes, G., Benjamin, P. R., Kemenes, G., & Endogenous, P. R. B. Endogenous and Network Properties of Lymnaea Feeding Central Pattern Generator Interneurons [ISBN: 00223077/02]. 2002. <https://doi.org/10.1152/jn.00872.2001>. (Cit. on p. 43).
- Streisinger, G., Walker, C., Dower, N., Knauber, D., & Singer, F. Production of clones of homozygous diploid zebra fish (Brachydanio rerio) [Number: 5813 Publisher: Nature Publishing Group]. en. *Nature*, 291(5813). 1981. 291. (5813). 293–296. ISSN: 1476-4687. <https://doi.org/10.1038/291293a0>. (Cit. on pp. 16, 34).
- Szücs, A., Varona, P., Volkovskii, A. R., Abarbanel, H. D. I., Rabinovich, M. I., & Selverston, A. I. Interacting Biological and Electronic Neurons Generate Realistic Oscillatory Rhythms. *Neuroreport*, 11(3). 2000. 11. (3). 563–569. ISSN: 09594965. <http://journals.lww.com/neuroreport/Fulltext/2000/02280>. (Cit. on p. 105)
- Tang, L. S., Goeritz, M. L., Caplan, J. S., Taylor, A. L., Fisek, M., & Marder, E. Precise Temperature Compensation of Phase in a Rhythmic Motor Pattern. *PLOS Biology*, 8(8). 2010. 8. (8). e1000469. ISSN: 1545-7885. <https://doi.org/10.1371/journal.pbio.1000469>. (Cit. on p. 138).
- Tatsuno, M. (Ed.). (2015). *Analysis and Modeling of Coordinated Multi-neuronal Activity* (Vol. 12). Springer. <https://doi.org/10.1007/978-1-4939-1969-7>. (Cit. on pp. 10, 30)
- Thompson, A. C., Fallon, J. B., Wise, A. K., Wade, S. A., Shepherd, R. K., & Stoddart, P. R. Infrared neural stimulation fails to evoke neural activity in the deaf guinea pig cochlea [Publisher: Elsevier B.V.]. *Hearing Research*, 324. 2015. 324. 46–53. ISSN: 18785891. <https://doi.org/10.1016/j.heares.2015.03.005>. (Cit. on p. 148).
- Thompson, A. C., Wade, S. A., Brown, W. G. A., & Stoddart, P. R. Modeling of light absorption in tissue during infrared neural stimulation. *Journal of Biomedical Optics*, 17(7). 2012. 17. (7). 0750021. ISSN: 1083-3668. <https://doi.org/10.1117/1.jbo.17.7.075002>. (Cit. on pp. 138, 149).

BIBLIOGRAPHY

- Torres, J. J., & Varona, P. (2012). Modeling Biological Neural Networks. In *Handbook of Natural Computing* (pp. 533–564). Springer. https://doi.org/10.1007/978-3-540-92910-9_17. (Cit. on pp. 11, 15, 31)
- Tsodyks, M., & Markram, H. The neural code between neocortical pyramidal neurons depends on neurotransmitter release probability. *P. Natl. Acad. Sci. USA*, 94. 1997. 94. 719–723. (Cit. on p. 15).
- Tye, K. M., & Deisseroth, K. Optogenetic investigation of neural circuits underlying brain disease in animal models. *Nature Reviews Neuroscience* 2012 13:4, 13(4). 2012. 13. (4). 251–266. ISSN: 1471-0048. <https://doi.org/10.1038/nrn3171>. (Cit. on p. 113).
- Ullén, F., Forssberg, H., & Ehrsson, H. H. Neural networks for the coordination of the hands in time. eng. *Journal of Neurophysiology*, 89(2). 2003. 89. (2). 1126–1135. ISSN: 0022-3077. <https://doi.org/10.1152/jn.00775.2002>. (Cit. on pp. 10, 30).
- Valero-Cabré, A., Amengual, J. L., Stengel, C., Pascual-Leone, A., & Coubard, O. A. Transcranial magnetic stimulation in basic and clinical neuroscience: A comprehensive review of fundamental principles and novel insights. *Neuroscience & Biobehavioral Reviews*, 83. 2017. 83. 381–404. ISSN: 0149-7634. <https://doi.org/https://doi.org/10.1016/j.neubiorev.2017.10.006>. (Cit. on pp. 20, 38, 113).
- Varona, P., Arroyo, D., Rodríguez, F. B., & Nowotny, T. (2016). Online event detection requirements in closed-loop neuroscience. In A. El Hady (Ed.), *Closed-Loop Neuroscience* (pp. 81–91). Academic Press. <https://doi.org/10.1016/B978-0-12-802452-2.00006-8>. (Cit. on pp. 114, 142)
- Varona, P., & Rabinovich, M. I. Hierarchical dynamics of informational patterns and decision making. *Proceedings of the Royal Society B*, 283(1832). 2016. 283. (1832). 20160475. ISSN: 14712954. <https://doi.org/10.1098/rspb.2016.0475>. (Cit. on pp. 7, 27).
- Vavoulis, D. V., Nikitin, E. S., Feng, J., Benjamin, P. R., & Kemenes, G. Computational model of a modulatory cell type in the feeding network of the snail, *Lymnaea stagnalis* [Publisher: Springer Nature]. *BMC Neuroscience*, 8(S2). 2007. 8. (S2). <https://doi.org/10.1186/1471-2202-8-s2-p113>. (Cit. on pp. 43, 44, 60, 68).
- Vavoulis, D. V., Nikitin, E. S., Kemenes, I., Marra, V., Feng, J., Benjamin, P. R., & Kemenes, G. Balanced plasticity and stability of the electrical properties of a molluscan modulatory interneuron after classical conditioning: A computational study. *Frontiers in Behavioral Neuroscience*, 4. 2010. 4. 19. ISSN: 16625153. <https://doi.org/10.3389/fnbeh.2010.00019>. (Cit. on pp. 14, 44, 48, 132, 137).

BIBLIOGRAPHY

- Vavoulis, D. V., Straub, V. A., Kemenes, I., Kemenes, G., Feng, J., & Benjamin, P. R. Dynamic control of a central pattern generator circuit: A computational model of the snail feeding network. *European Journal of Neuroscience*, 25(9). 2007. 25. (9). 2805–2818. ISSN: 0953816X. <https://doi.org/10.1111/j.1460-9568.2007.05517.x>. (Cit. on pp. 15, 56, 66, 104, 109).
- Vavoulis, D. V., Straub, V. A., Kemenes, I., Kemenes, G., Feng, J., & Benjamin, P. R. Dynamic control of a central pattern generator circuit: A computational model of the snail feeding network. *European Journal of Neuroscience*, 25(9). 2007. 25. (9). 2805–2818. ISSN: 0953816X. <https://doi.org/10.1111/j.1460-9568.2007.05517.x>. (Cit. on pp. 45, 46, 60, 66, 132).
- Vehovszky, Á., Szabó, H., & Elliott, C. J. Octopamine-containing (OC) interneurons enhance central pattern generator activity in sucrose-induced feeding in the snail Lymnaea. *Journal of Comparative Physiology A: Neuroethology, Sensory, Neural, and Behavioral Physiology*, 190(10). 2004. 190. (10). 837–846. ISSN: 03407594. <https://doi.org/10.1007/s00359-004-0539-y>. (Cit. on p. 43).
- Venaille, A., Varona, P., & Rabinovich, M. I. Synchronization and coordination of sequences in two neural ensembles [Publisher: Institute for Nonlinear Science. University of California, San Diego, 9500 Gilman Dr. 0402, La Jolla, California 92093, USA]. *Physical Review E*, 71(6 Pt 1). 2005. 71. (6 Pt 1). 61909. ISSN: 15393755. <https://doi.org/10.1103/PhysRevE.71.061909>. (Cit. on p. 55).
- Wachtel, H., & Kandel, E. R. A Direct Synaptic Connection Mediating Both Excitation and Inhibition [Publisher: American Association for the Advancement of Science]. *Science*, 158(3805). 1967. 158. (3805). 1206–1208. <https://doi.org/10.1126/science.158.3805.1206>. (Cit. on pp. 16, 34).
- Wang, X., Reddy, D. D., Nalawade, S. S., Pal, S., Gonzalez-Lima, F., & Liu, H. Impact of heat on metabolic and hemodynamic changes in transcranial infrared laser stimulation measured by broadband near-infrared spectroscopy. *Neurophotonics*, 5(01). 2017. 5. (01). 1. ISSN: 2329-423X. <https://doi.org/10.1117/1.NPh.5.1.011004>. (Cit. on pp. 114, 147).
- Wells, J., Kao, C., Konrad, P., Milner, T., Kim, J., Mahadevan-Jansen, A., & Jansen, E. D. Biophysical mechanisms of transient optical stimulation of peripheral nerve. *Biophysical Journal*, 93(7). 2007. 93. (7). 2567–2580. ISSN: 00063495. <https://doi.org/10.1529/biophysj.107.104786>. (Cit. on pp. 114, 129, 137).
- Wells, J. D., M.D., C. K., Jansen, E. D., M.D., P. E. K., & Mahadevan-Jansen, A. Application of infrared light for in vivo neural stimulation. *Journal of Biomedical Optics*, 10(6). 2005. 10. (6). 64003. <https://doi.org/10.1117/1.2121772>. (Cit. on pp. 114, 126, 146, 147, 148).

BIBLIOGRAPHY

- Wells, J. D., M.D, C. K., Jansen, E. D., M.D, P. E. K., & Mahadevan-Jansen, A. Application of infrared light for in vivo neural stimulation. <https://doi.org/10.1111/1.2121772>, 10(6). 2005. 10. (6). 064003. ISSN: 1083-3668. <https://doi.org/10.1111/1.2121772>. (Cit. on p. 146).
- Winlow, W., Haydon, P., & Benjamin, P. Multiple Postsynaptic Actions of the Giant Dopamine-Containing Neurone R.Pe.D.I of Lymnaea Stagnalis. *Journal of Experimental Biology*, 94. 1981. 94. <https://doi.org/10.1242/jeb.94.1.137>. (Cit. on pp. 17, 36).
- Woźniak, S., Pantazi, A., Bohnstingl, T., & Eleftheriou, E. Deep learning incorporating biologically inspired neural dynamics and in-memory computing [Publisher: Nature Publishing Group]. en. *Nature Machine Intelligence*, 2(6). 2020. 2. (6). 325–336. ISSN: 2522-5839. <https://doi.org/10.1038/s42256-020-0187-0>. (Cit. on pp. 10, 31).
- Yizhar, O., Fennel, L. E., Davidson, T. J., Mogri, M., & Deisseroth, K. Optogenetics in Neural Systems. *Neuron*, 71(1). 2011. 71. (1). 9–34. ISSN: 1097-4199. <https://doi.org/10.1016/J.NEURON.2011.06.004>. (Cit. on p. 113).
- Yuste, R., MacLean, J. N., Smith, J., & Lansner, A. The cortex as a central pattern generator. *Nat Rev Neurosci*, 6(6). 2005. 6. (6). 477–483. <https://doi.org/10.1038/nrn1686>. (Cit. on pp. 7, 27).
- Zheng, Q., Shen, J., & Xu, Y. Spontaneous Activity Induced by Gaussian Noise in the Network-Organized FitzHugh-Nagumo Model. *Neural Plasticity*, 2020. 2020. 2020. 6651441. ISSN: 2090-5904. <https://doi.org/10.1155/2020/6651441>. (Cit. on p. 16).
- Zhou, S., Masmanidis, S. C., & Buonomano, D. V. Neural Sequences as an Optimal Dynamical Regime for the Readout of Time. eng. *Neuron*, 108(4). 2020. 108. (4). 651–658.e5. ISSN: 1097-4199. <https://doi.org/10.1016/j.neuron.2020.08.020>. (Cit. on pp. 10, 30).
- Zimnik, A. J., & Churchland, M. M. Independent generation of sequence elements by motor cortex [Publisher: Nature Publishing Group]. en. *Nature Neuroscience*, 24(3). 2021. 24. (3). 412–424. ISSN: 1546-1726. <https://doi.org/10.1038/s41593-021-00798-5>. (Cit. on pp. 10, 30).
- Zrenner, C., Belardinelli, P., Müller-Dahlhaus, F., & Ziemann, U. Closed-loop neuroscience and non-invasive brain stimulation: A tale of two loops [Publisher: Frontiers Media SA]. *Frontiers in Cellular Neuroscience*, 10. 2016. 10. 92. <https://doi.org/doi.org/10.3389/fncel.2016.00092>. (Cit. on p. 114).

BIBLIOGRAPHY

APPENDIX A

Publications

Journal Publications

- Garrido-Peña, A., Elices, I., & Varona, P. Characterization of interval variability in the sequential activity of a central pattern generator model [JCR Q2. Related to Chapter 4]. *Neurocomputing*, 461. 2021. 461. 667–678. ISSN: 0925-2312. <https://doi.org/10.1016/j.neucom.2020.08.093>.
- Garrido-Peña, A., Sanchez-Martin, P., Reyes-Sanchez, M., Levi, R., Rodriguez, F. B., Castilla, J., Tornero, J., & Varona, P. Modulation of neuronal dynamics by sustained and activity-dependent continuous-wave near-infrared laser stimulation [JCR Q1. Related to Chapter 5.]. *Neurophotonics*, 11(2). 2024. 11. (2). 024308. ISSN: 2329-423X, 2329-4248. <https://doi.org/10.1117/1.NPh.11.2.024308>.

International Conference Contributions

- Amaducci, R., Elices, I., Reyes-Sanchez, M., Garrido-Peña, A., Levi, R., Rodriguez, F. B., & Varona, P. Hybrid robot driven by a closed-loop interaction with a living central pattern generator with online feedback. 29th Annual Computational Neuroscience Meeting: CNS*2020. P207. [Related to Chapter 4]. *BMC Neuroscience*, 21. 2020. 21. 54. <https://doi.org/10.1186/s12868-020-00593-1>.

- Amaducci, R., Elices, I., Reyes-Sanchez, M., Garrido-Peña, A., Levi, R., Rodriguez, F. B., & Varona, P. Controlling robotic locomotion by a closed-loop interaction with living central pattern generators. [Related to Chapter 4]. *COSYNE*. 2021. https://www.cosyne.org/s/Cosyne2021_program_book.pdf

APPENDIX A: PUBLICATIONS

- Berbel, B., Garrido-Peña, A., Elices, I., Latorre, R., & Varona, P. (2021a). Effect of Electrical Synapses in the Cycle-by-Cycle Period and Burst Duration of Central Pattern Generators [Related to Chapter 4.]. In I. Rojas, G. Joya, & A. Català (Eds.), *Advances in Computational Intelligence* (pp. 81–92). Springer International Publishing. https://doi.org/10.1007/978-3-030-85099-9_7
- Berbel, B., Garrido-Peña, A., Elices, I., Latorre, R., & Varona, P. Gap junctions shape the intervals that build robust sequences in a central pattern generator model. 30th Annual Computational Neuroscience Meeting: CNS*2021—Meeting Abstracts. P194. [Related to Chapter 4.]. *Journal of Computational Neuroscience*, 49. 2021. 49. 3–208. <https://doi.org/10.1007/s10827-021-00801-9>.
- Garrido-Peña, A., Elices, I., Levi, R., Rodriguez, F. B., & Varona, P. Experimental and computational characterization of interval variability in the sequential activity of the Lymnaea feeding CPG. 29th Annual Computational Neuroscience Meeting: CNS*2020. O11. ORAL PRESENTATION [Related to Chapter 4.]. *BMC Neuroscience*, 21. 2020. 21. 54. <https://doi.org/10.1186/s12868-020-00593-1>.
- Garrido-Peña, A., Elices, I., Levi, R., Rodriguez, F. B., & Varona, P. Universality of interval variability constraints in the sequential activity of motor circuits. [Related to Chapter 4.]. COSYNE. 2021. https://www.cosyne.org/s/Cosyne2021_program_book.pdf
- Garrido-Peña, A., Levi, R., Castilla, J., Tornero, J., & Varona, P. Effect of infrared laser stimulation in single neurons: Experimental and modeling study. 30th Annual Computational Neuroscience Meeting: CNS*2021—Meeting Abstracts. P193. [Related to Chapter 5]. *Journal of Computational Neuroscience*, 49. 2021. 49. 3–208. <https://doi.org/10.1007/s10827-021-00801-9>.
- Garrido-Peña, A., Sanchez-Martin, P., Levi, R., Castilla, J., Tornero, J., & Varona, P. Activity-dependent stimulation to assess the effect of infrared-laser stimulation in single neurons. Poster Presentation [Related to Chapter 5]. FENS. 2022. S02–556. <https://kenesvm.azureedge.net/public/general/FENS2022.pdf>
- Garrido-Peña, A., Sanchez-Martin, P., Reyes-Sanchez, M., Levi, R., Rodriguez, F. B., Castilla, J., Tornero, J., & Varona, P. Effective noninvasive neuronal waveform modulation with sustained and activity-dependent continuous-wave near-infrared laser stimulation. Poster presentation. [Related to Chapter 5.]. FENS. 2024.
- Garrido-Peña, A., Sánchez-Martín, P., Elices, I., Reyes-Sánchez, M., Berbel, B., Latorre, R., Rodriguez, F. B., & Varona, P. Exploring the ability of biophysical models to reproduce the functional variability of neurons. 32nd Annual Computational Neuroscience Meeting: CNS*2023. [Related to Chapter 4]. *InPress for Journal of Computational Neuroscience*. 2024.

APPENDIX A: PUBLICATIONS

- Garrido-Peña, A., Sánchez-Martín, P., Reyes-Sánchez, M., Castilla, J., Tornero, J., Levi, R., Rodríguez, F. B., & Varona, P. Activity-dependent infrared laser stimulation to assess its biophysical effects on single neurons. 31st Annual Computational Neuroscience Meeting: CNS*2022. F3. ORAL PRESENTATION. [Related to Chapter 5]. *Journal of Computational Neuroscience*, 51. 2023. 51. 3–101. <https://doi.org/10.1007/s10827-022-00841-9>.
- Sanchez-Martin, P., Elices, I., Garrido-Peña, A., Levi, R., Rodriguez, F. B., & Varona, P. Dynamic synchronization between electrically coupled cells of central pattern generators. 30th Annual Computational Neuroscience Meeting: CNS*2021—Meeting Abstracts. P195. [Related to chapter 4]. *Journal of Computational Neuroscience*, 49. 2021. 49. 3–208. <https://doi.org/10.1007/s10827-021-00801-9>.
- Sánchez-Martín, P., Garrido-Peña, A., Berbel, B., Rodriguez, F. B., Levi, R., & Varona, P. Influence of electrical coupling in shaping time intervals and dynamical invariants of central pattern generator sequences. 31st Annual Computational Neuroscience Meeting: CNS*2022. P109. [Related to Chapter 4]. *Journal of Computational Neuroscience*, 51. 2023. 51. 3–101. <https://doi.org/10.1007/s10827-022-00841-9>.
- Soétard, P., Amaducci, R., Sánchez-Martín, P., Reyes-Sánchez, M., Garrido-Peña, A., Levi, R., Rodríguez, F. B., & Varona, P. Dynamical principles of functional neural sequences validated in hybrid robots built with living central pattern generators. 31st Annual Computational Neuroscience Meeting: CNS*2022. P110 [Related to Chapter 4]. *Journal of Computational Neuroscience*, 51. 2023. 51. 3–101. <https://doi.org/10.1007/s10827-022-00841-9>.

APPENDIX A: PUBLICATIONS

APPENDIX B

Supplementary figures for chapter 4

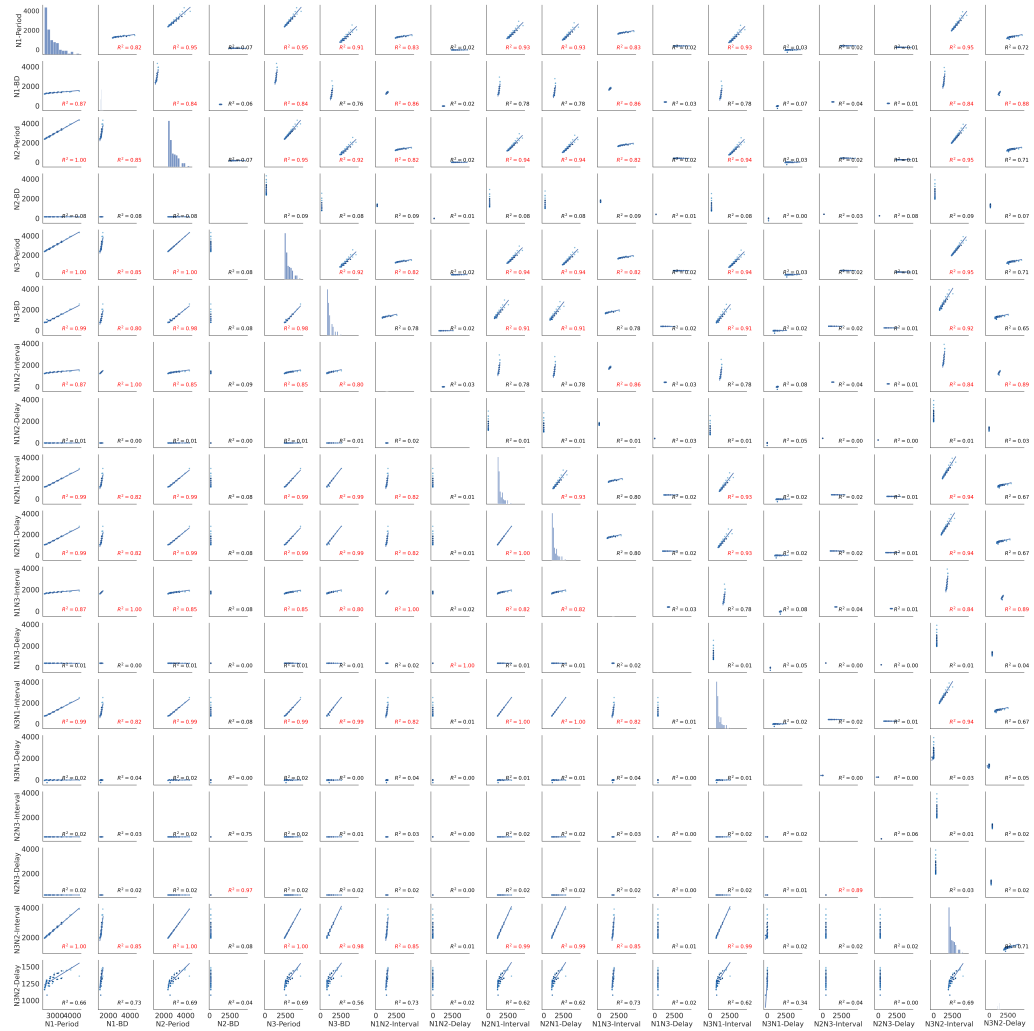


Figure B.1: N1M stimulation: Pairplot of the invariants no reset within cycles. Lower triangle represents the intervals within the same cycle. Upper triangle represents the intervals of one cycle within the next cycle.

APPENDIX B: SUPPLEMENTARY FIGURES FOR CHAPTER 4

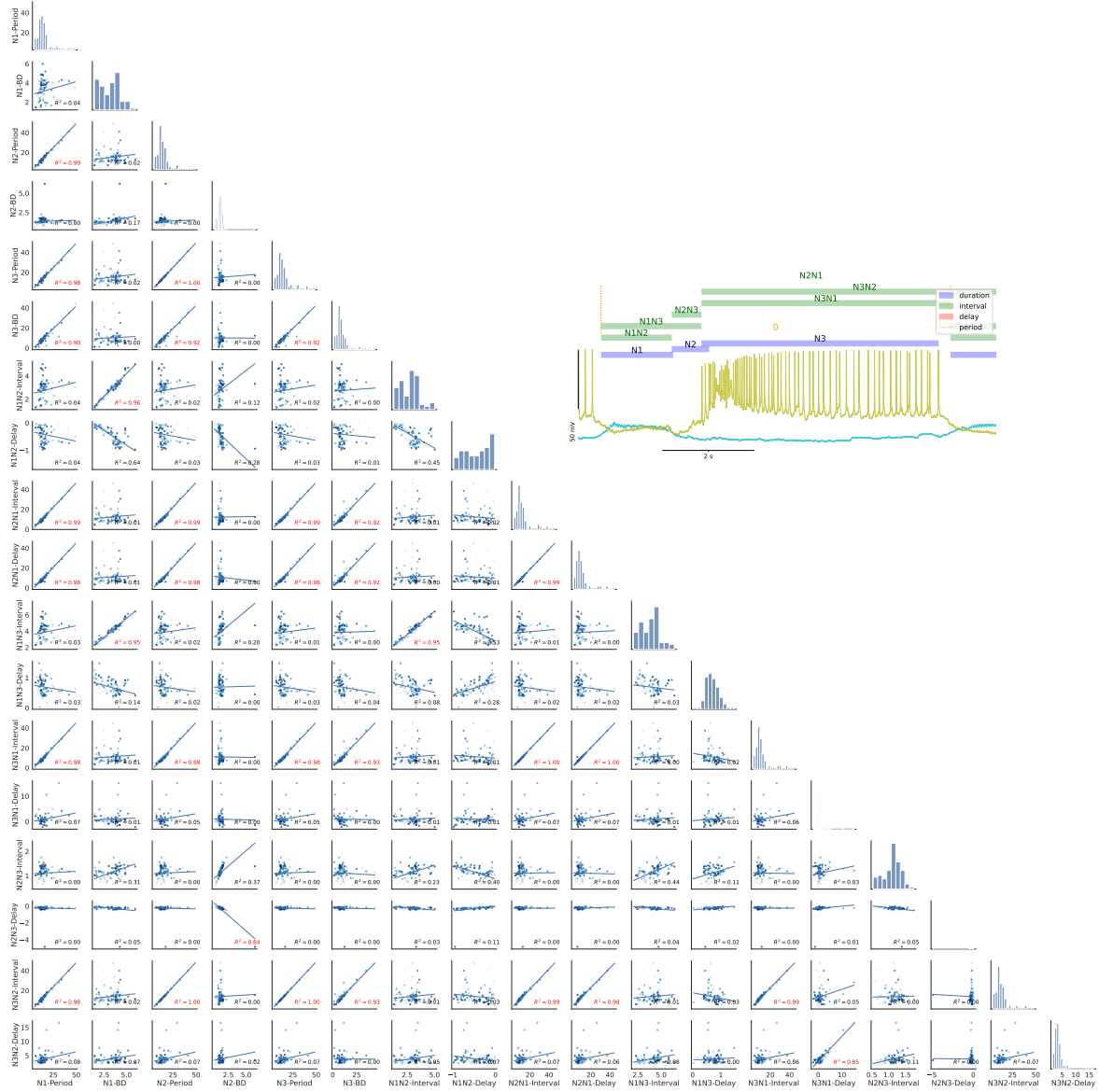


Figure B.2: Spontaneous case 1: Panel of intervals distribution and dynamical invariants for the three phases in the CPG for spontaneous activity.

APPENDIX B: SUPPLEMENTARY FIGURES FOR CHAPTER 4

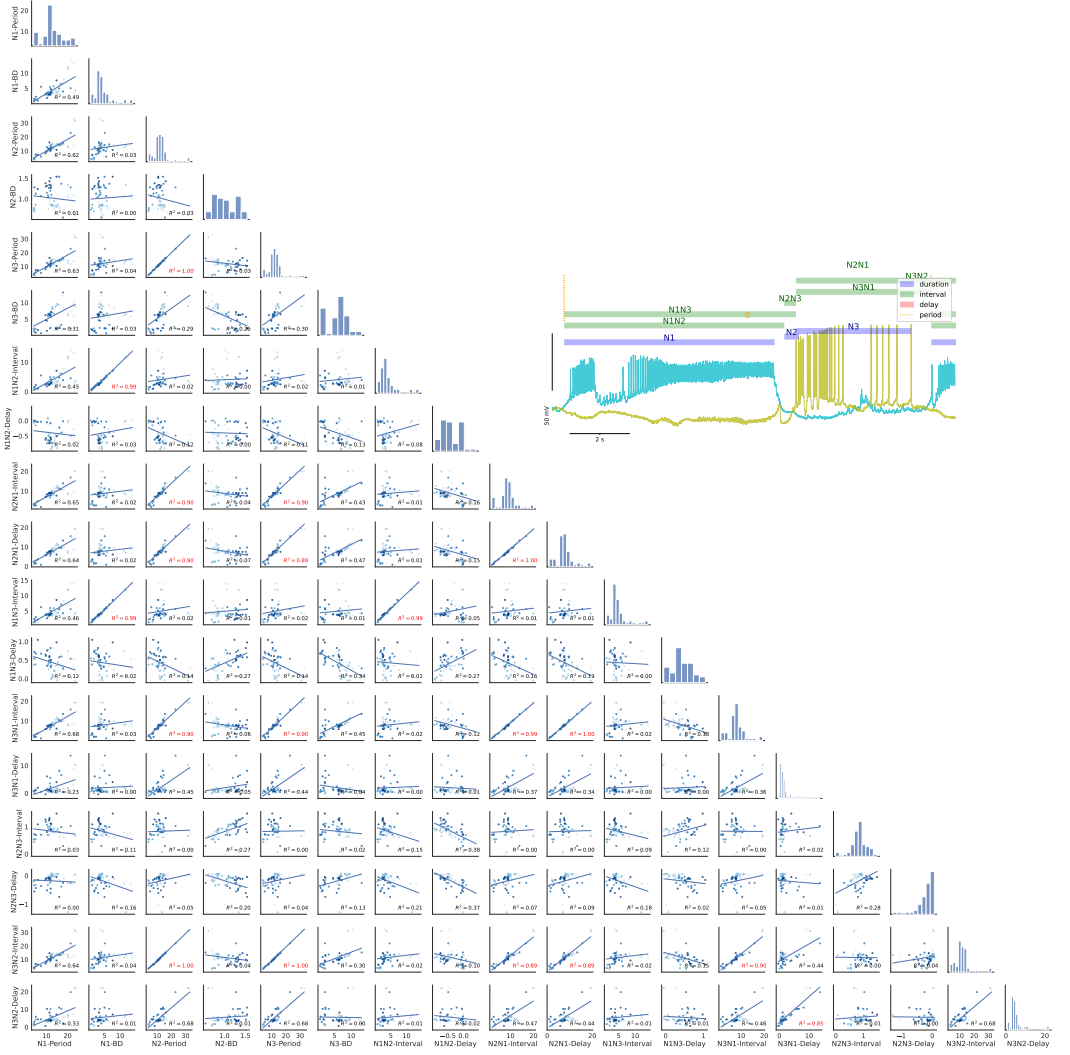


Figure B.3: Spontaneous case 2: Panel of intervals distribution and dynamical invariants for the three phases in the CPG for spontaneous activity.

APPENDIX B: SUPPLEMENTARY FIGURES FOR CHAPTER 4

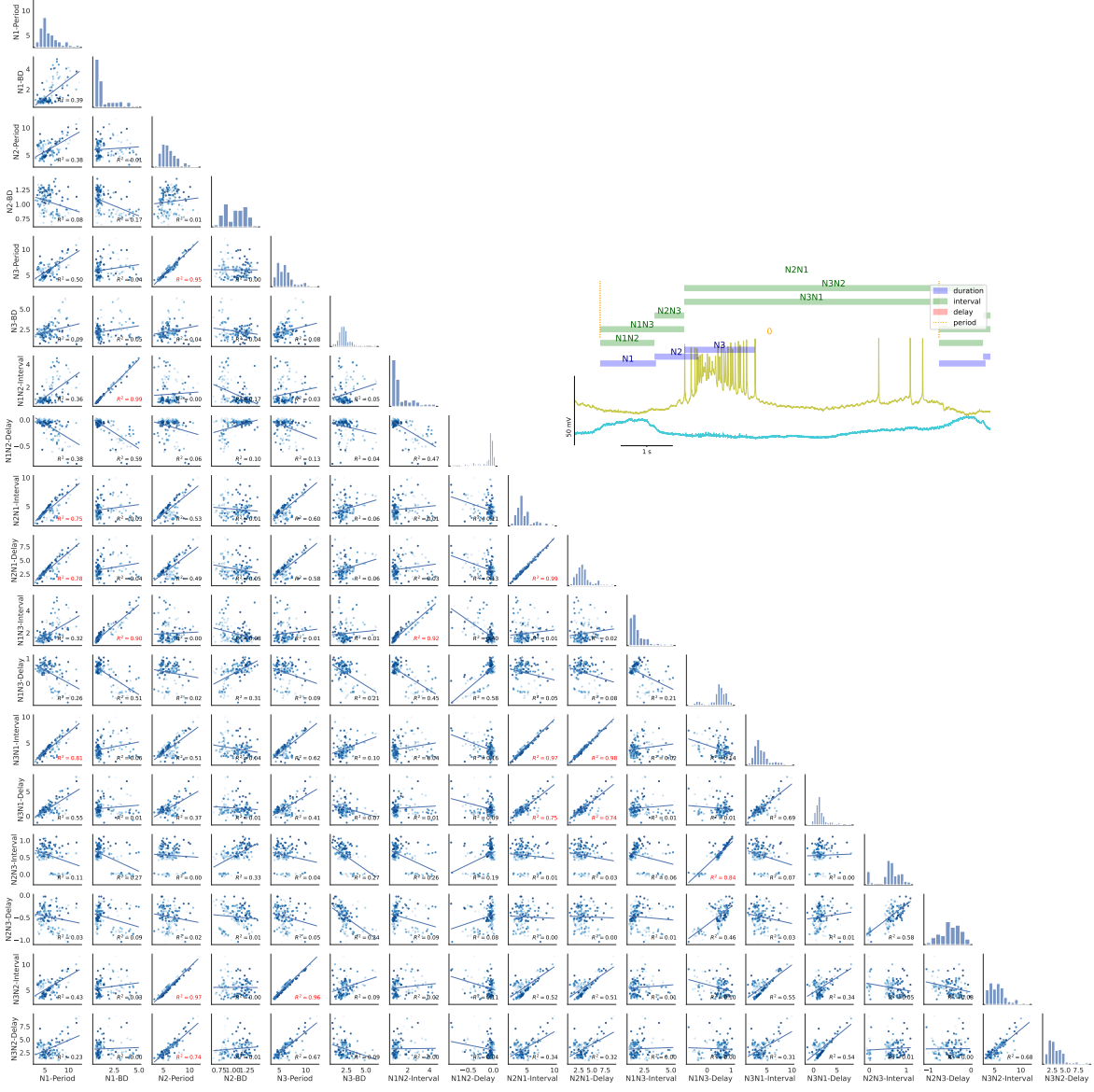


Figure B.4: Spontaneous case 3: Panel of intervals distribution and dynamical invariants for the three phases in the CPG for spontaneous activity.

APPENDIX B: SUPPLEMENTARY FIGURES FOR CHAPTER 4

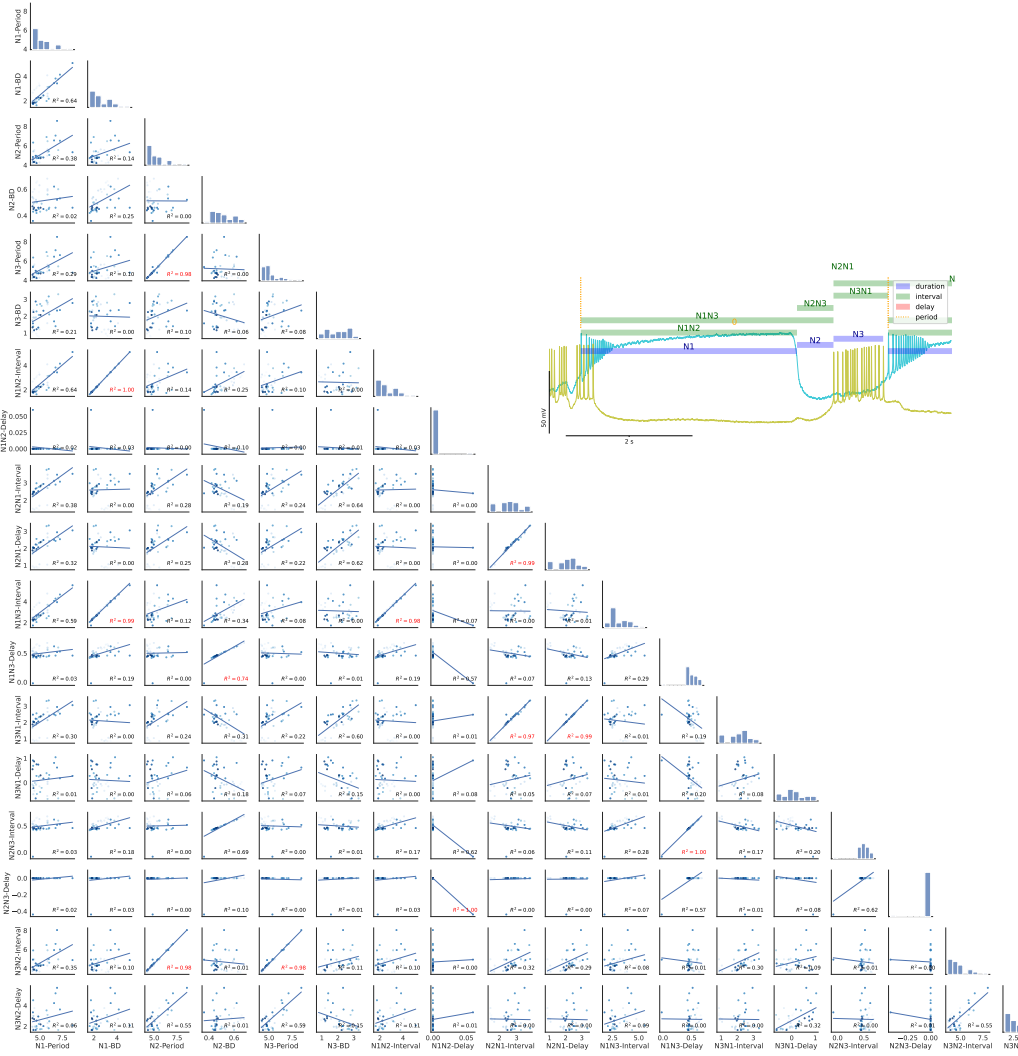


Figure B.5: CV1a driven case 4: Panel of intervals distribution and dynamical invariants for the three phases in the CPG under CV1a stimulation.

Interval	Num_Cycles	N1-BD	N2-BD	N3-BD	N1N2-Interval	N2N1-Interval	N1N3-Interval	N3N1-Interval	N2N3-Interval	N3N2-Interval	N1N2-Delay	N2N1-Delay	N1N3-Delay	N3N1-Delay	N2N3-Delay	N3N2-Delay
./prep1_2phases.ini	158.00	0.39	nan	0.04	nan	nan	0.36	0.86	nan	nan	0.16	0.69	nan	nan	0.16	0.69
./prep1_3phases.ini	158.00	0.39	0.05	0.04	0.37	0.82	0.36	0.86	0.05	0.59	0.28	0.84	0.16	0.69	0.01	0.44
./prep2_2phases.ini	91.00	0.04	nan	0.90	nan	nan	0.03	0.98	nan	nan	0.03	0.07	nan	nan	0.03	0.07
./prep2_3phases.ini	91.00	0.04	0.00	0.90	0.04	0.99	0.03	0.98	0.00	0.98	0.04	0.97	0.03	0.07	0.00	0.08
./prep3_2phases.ini	59.00	0.49	nan	0.31	nan	nan	0.46	0.68	nan	nan	0.12	0.23	nan	nan	0.12	0.23
./prep3_3phases.ini	59.00	0.49	0.01	0.31	0.45	0.65	0.46	0.68	0.03	0.64	0.02	0.64	0.12	0.23	0.00	0.32
./so_spontaneous.ini	89.00	0.73	nan	0.21	nan	nan	0.82	0.72	nan	nan	0.47	0.48	nan	nan	0.47	0.48
./so_stim_2phases.ini	41.00	0.84	nan	0.28	nan	nan	0.84	0.60	nan	nan	0.04	0.09	nan	nan	0.04	0.09
./so_stop_spontaneous.ini	10.00	0.91	nan	0.09	nan	nan	0.89	0.89	nan	nan	0.22	0.91	nan	nan	0.22	0.91
./stim_cv1a_1_2phases.ini	39.00	0.93	nan	0.05	nan	nan	0.92	0.02	nan	nan	0.00	0.03	nan	nan	0.00	0.03
./stim_cv1a_1_3phases.ini	39.00	0.93	0.00	0.05	0.93	0.03	0.92	0.02	0.00	0.02	0.00	0.02	0.00	0.03	0.00	0.07
./stim_cv1a_2_2phases.ini	43.00	0.52	nan	0.17	nan	nan	0.44	0.27	nan	nan	0.04	0.00	nan	nan	0.04	0.00
./stim_cv1a_2_3phases.ini	36.00	0.22	nan	0.52	nan	nan	0.18	0.60	nan	nan	0.02	0.06	nan	nan	0.02	0.06
./stim_cv1a_4_2phases.ini	40.00	0.62	nan	0.21	nan	nan	0.58	0.29	nan	nan	0.03	0.01	nan	nan	0.03	0.01
./stim_cv1a_4_3phases.ini	40.00	0.62	0.02	0.21	0.62	0.37	0.58	0.29	0.03	0.35	0.02	0.31	0.03	0.01	0.02	0.06
./stim_mln_2phases.ini	37.00	0.97	nan	0.03	nan	nan	0.98	0.00	nan	nan	0.63	0.04	nan	nan	0.63	0.04

Figure B.6: Table of R^2 values for the linear regression between the period and each interval for all experimental recordings showed in this section.